Mixing in the Continental slope:

study case Gulf of Cadiz

Thesis submitted in accordance with the requirements of the University of Liverpool for the degree of Doctor in Philosophy

by

Ruben Alvarado Bustos

June 2011

Abstract

Internal waves in the ocean are the principal generators of mixing in the abyssal ocean and regions of rough topography. The present research work diagnoses the influence of internal wave activity over the Continental slope in the Gulf of Cadiz. Mediterranean Outflow (MOW) and North Atlantic Central Water (NACW) are the main baroclinic flows over the study region and diapycnal mixing acts in each layer.

Semi-diurnal internal tides and a continuous MOW flow are observed on the slope. The MOW flow is persistent reaching >0.40 ms^{-1}, but varies in strength with the tides. The Internal wave field in the Gulf of Cadiz can play an important role affecting the MOW signal over the continental slope; MOW can be displaced by the internal tide. Internal waves are generated by tides and MOW flow interacting with the bottom, the two most energetic sources locally. Also MOW bottom stress provides strong diapycnal mixing, providing well-mixed conditions in the MOW. Internal tides can transfer energy on the slope and can cause turbulence. A critical slope characteristic for semidiurnal internal waves occurs over the continental slope with local background stratification where MOW travels as an undercurrent.

Diapycnal mixing is found to be enhanced inside the MOW with a diapycnal diffusivity O($7x10^{-4}$ m^2s^{-1}), and at the MOW-NACW interfaces, reaching O($2x10^{-4}$ m^2s^{-1}) for the upper interface and O($5x10^{-4}$ m^2s^{-1}) for the lower interface. Fine-structure methods are used to estimate mixing using CTD measurements; however most of the records came from temperature profiles (XBTs) and an alternative approach to diagnose the strain uses temperature profiles with inferred salinity (using temperature-salinity relations from the CTDs). Applying the strain method using temperature with inferred salinity profiles provides a plausible approximation of the strain spectrum and the mixing estimates, with uncertainties similar to those diagnosed using CTD measurements.

Mixing estimates are also diagnosed using a large scale box model, where a salinity budget is applied to study gain and loss over the Gulf of Cadiz. Box model results confirm that salinity is diapycnally transferred from the MOW layers into the neighbouring NACW layers. The advective and diffusive transfers of salt along the layer are much larger than the diapycnal transfer. The inferred diffusivities from the box model are broadly in accord with the estimates from strain.

Acknowledgements

First, I take this opportunity to thanks God for this experience and for the amazing moments I lived during this PhD program, to provide great friends during this journey and unforgettable experiences in which I learned and grew as a person. To Jesus, my brother, since the first day I prayed for walk one step at the time and you always were there, thanks.

Many thanks to my supervisors, Prof. John M. Huthnance from the National Oceanography Centre (formerly Proudman Oceanographic Laboratory) and Prof. Ric Williams from the Department of Earth and Ocean Science at the University of Liverpool. John provided guidance and advice with a lot of enthusiasm, thanks to polish me and now to have a better me; I really appreciate all his effort but most important thanks for his friendship. Ric also provided guidance and advice, he was a man of his word, I remember the first time I meet him he said something like: 'he will be the difficult part' and 'yes he was', I learn loads with his inputs and pushing this research to a great ending, also to provide opportunities within the university to interact with undergraduate students to improve my English.

I want to thank as well to the National Oceanography Centre Liverpool staff which always was there for help and advice. To Prof. Richard Hobbs (Geophysical Oceanography 'GO' leader, University of Durham) for encouraging me and provide facilities within the GO project (sorry to scratch the RRS Discovery wood-deck). To colleagues in the GO project which provided loads of comments during the workshops to improve this research as Martin Vogt, Gerd Krahmman, Isabel Ambar, Elise Quentel, Luis Geli, Grant Buffet, Patricia Silva, Nuno Serra, Martin Visbeck, Ekaterina Vsemirnova. Also to NOCL and NMF technicians for provide the measurement used in this research and for advices during the processing of the raw data. To SEMANE program for facilitate CTD data to the GO project and this work. To Mike Smithson and John Howarth for processing mooring data and advices during analysis.

Finally a big thanks to my Family back in Mexico, friends all around the world, particularly those that God gave to me here in sunny Liverpool, amazing lads and God bless the 'scousers' (even if they come from the Wirral).

This PhD was funded partly by the NEST-Adventure project GO (2007-2009) and for Mexican science council CONACYT by a doctoral scholarship (2009-2011).

Contents

Chapter 1 Turbulence and mixing on the continental slope

1.1 Introduction

Physical processes in the ocean span a broad range of spatial and temporal scales. The winds, tides and atmospheric buoyancy forcing of the ocean occur at lateral scales of O(100-1000km), driving the global overturning circulation, gyres, mesoscale eddies, coastal dynamics, and wave motion such as Kelvin, Rossby and internal waves. All these processes move energy through a cascade that ultimately leads to dissipation by frictional processes, which can happen in the interior but mainly occur at physical boundaries. The cascade is dominated by the oceanic eddy field and internal waves. Internal waves provide a clear pathway from vertical scales O(1 km), which are associated with baroclinic modes (pycnocline movement), to the fine-scale O(10 m) shear and strain that lead to instabilities and turbulence [even finer scale down to molecular ones].

The processes that dissipate energy in the ocean can have a temporal and spatial pattern; a process could start at a distant location with a distinctive oceanic forcing, but its effects could be detected in another region (e.g. internal waves can propagate in any direction). Away from the surface mixed layer, most of the ocean mixing is driven by breaking internal waves. Tides (14%) and wind (86%) are the main sources of energy for the internal wave field (*Wunsch and Ferrari*, 2004).

In the ocean, stratification provides a context for various processes; its presence or absence determines the potential for mixing mechanisms. Internal waves drive mixing acting most prominently on the stratification. This process (mixing across density contours, so affecting stratification) is known as diapycnal mixing and is the most significant diffusive process acting on the potential energy budget of the ocean interior (*Muller and Briscoe*, 2000).

1.1.1 Diapycnal mixing

The breaking of internal waves produces mixing, which then reduces stratification. Two groups of waves are generated in the deep ocean, internal tides and near-inertial internal waves. Internal tides are generated when the barotropic tide passes over rough topography; a portion of energy in the barotropic tide is lost and used by turbulence locally leading to

dissipation. In practice energy dissipation occurs in the ocean at localised regions, where turbulence is increased by orders of magnitude [the locations are known as mixing hot-spots (*Polzin, et al* 1997; *St Laurent, et al* 2002)]. Most of the internal tide energy is radiated away in the form of low mode waves, part goes to the internal wave field through internal wave-wave interactions, some may be lost through parametric subharmonic instabilities near mid latitudes and radiated away in the form of low mode waves over deep ocean topography breaking on distant continental slopes (*St Laurent and Garret*, 2002). Near inertial internal waves are generated by wind forcing of near inertial motions in the surface mixed layer (*Alford*, 2001). Also, "Beta" and eddy interactions change the horizontal wave number of internal waves and move this variance equatorward and into the pycnocline resulting in near-inertial waves (*D'Asaro*, 1985; *D'Asaro, et al* 1995). As with internal tides, high mode near-inertial waves tend to be generated and dissipated locally, while low mode waves tend to propagate across the ocean (*Alford,* 2003).

The input of energy into the ocean via tides or wind forcing generates large amplitude waves of large vertical scale. However, dissipation takes place from breaking small scale waves through shear or convective instabilities, leading to mixing associated with buoyancy fluxes altering stratification (involving a conversion of mechanical energy into potential energy). The internal wave mixing distribution is controlled by the combination of the generation pattern, wave propagation and refraction, and nonlinear interactions leading to shorter waves and wave breaking (*Gill*, 1984; *St Laurent and Garrett*, 2002).

The existing parameterizations of diapycnal mixing include a semi empirical scheme to represent the elevated mixing near internal tide generation sites; it is called the 'nearfield' problem (*St Laurent, et al* 2002). The internal tide is the starting point for diapycnal mixing parameterization due to the predictability of the tides and well developed theory for tidal baroclinic conversion (*Garrett and Kunze,* 2007), which makes estimates of the source term relatively easy. The parameterization for the energy dissipation ε is:

$$\varepsilon = \frac{qE(x,y)F(z)}{\rho} \qquad (1.1)$$

where $E(x,y) \sim \frac{1}{2}\rho_o k h^2 N |\boldsymbol{u}|^2$ is the horizontally varying internal tide energy flux [*(k,h)* are the wave number and amplitude that characterize the bathymetry, $\boldsymbol{u}$ is the barotropic tidal

velocity vector (*Jayne and St Laurent*, 2001; *Jayne* 2009)], *q=1/3* is the fraction of energy flux dissipated locally (*St. Laurent and Garrett*, 2002) [The rest of the internal wave energy (*1-q=2/3*) is presumed to radiate to the 'farfield' and contribute to the background internal wave field (*Garrett and Munk*, 1975)], $F(z) = \frac{e^{(z-H)/\zeta}}{\zeta(1-e^{-H/\zeta})}$ is the vertical structure for the dissipation rate [i.e. $F(z)$ is an exponential decay upward away from the bottom, with a vertical scale of $\zeta = 500m$ (*St. Laurent and Nash*, 2004)]. The energy dissipation ε leads to diffusivity κ by the Osborne (1980) relation:

$$\kappa = \kappa_0 + \frac{\Gamma \varepsilon}{N^2} \qquad (1.2)$$

where Γ=*0.2* is the mixing efficiency parameter, N^2 is the buoyancy gradient and κ_0 a constant background diffusivity included to account for other mixing processes.

In practice, the above parameterization model makes an attempt to account for vertical tidal mixing. The greatest weakness is that only a fraction of the internal wave energy available for mixing is represented. The unaccounted energy for mixing includes the low mode internal tides and near inertial internal waves (*Egbert and Ray*, 2000; *St Laurent, et al* 2002; *Alford*, 2003).

Another difficulty for diapycnal mixing parameterizations is the patchy nature of mixing. Elevated mixing has been found in the deep ocean above rough topography (*Naveira Garabato et al* 2004a,b; *Kunze et al* 2006). Also upper ocean diapycnal mixing has been found to have a significant impact on circulation, water properties and heat fluxes. Upper ocean mixing has a strong latitudinal dependence (*Henyey et al* 1986; *Gregg et al* 2003). Diapycnal mixing has been found to be spatially and temporally variable, which mostly is not taken into account in ocean circulation simulations (*Wunsch and Ferrari*, 2004).

1.1.2 Mixing over the Continental slopes

Internal waves provide a source of energy for turbulent diffusion at ocean margins (*Munk*, 1966). Studies suggest that enhanced dissipation occurs in regions of elevated wave energy and those are located over sloping boundaries and rough topography (*Toole, et al* 1994; *Ledwell, et al* 2000; *Toole*, 2007). Evidence of large amounts of diapycnal mixing has

been related to internal waves breaking over rough bathymetry (*Ledwell, et al* 2000). Providing evidence that confirms mechanical connections between the internal wave field and diapycnal mixing is now a key research topic in mixing studies over continental slopes.

Continental slopes can have significant topographic roughness on scales O(10 km) both along and across the slope. Continental slopes can be inefficient generators of low-mode internal tides because barotropic tidal flows are generally parallel to large scale isobaths (*Nash, et al* 2007). The important mixing mechanism over small scale topography is the presence of high mode waves generated by flow (*St Laurent and Nash,* 2004; *Garrett and Kunze,* 2007). Tidal mixing can be generated either by local generation of internal tides over small scale topography (*Legg,* 2004) or from remotely generated internal tides (*Nash, et al* 2004).

High mode waves over continental slopes are generated by energy transfer from low mode waves, part of the energy cascade process. For specific seafloor slopes, critical reflection of internal waves can lead to instabilities and subsequent mixing, very near the bottom and hundreds of metres up in the water column (*Eriksen* 1985; *Garrett* 1991). While some of the locally generated baroclinic energy is dissipated in the 'nearfield', another portion is also radiated away. The escape of waves can elevate the shear and strain farther away and enhance mixing in the ocean.

When internal waves reflect from a sloping bottom, the frequencies of the incident waves are preserved; reflection of energy rays or characteristics (see section 2.3.4) occurs about the local gravity vector (*Phillips,* 1977). Characteristics of internal tide energy can approach the slope from the ocean interior or from local generation areas at the boundary over the shelf (*Prinsenberg,* 1974). Figure (1) shows the rays or characteristics of internal semidiurnal tides approaching the continental slope.

The Gulf of Cadiz is an ocean boundary region with a continental slope with rough topography where local circulation is strongly influenced by mixing processes (*Baringer and Price,* 1997b). As shown in figure (1.1), internal semi-diurnal tides can propagate in the Gulf of Cadiz, which is to be considered here as a case study of diapycnal mixing.

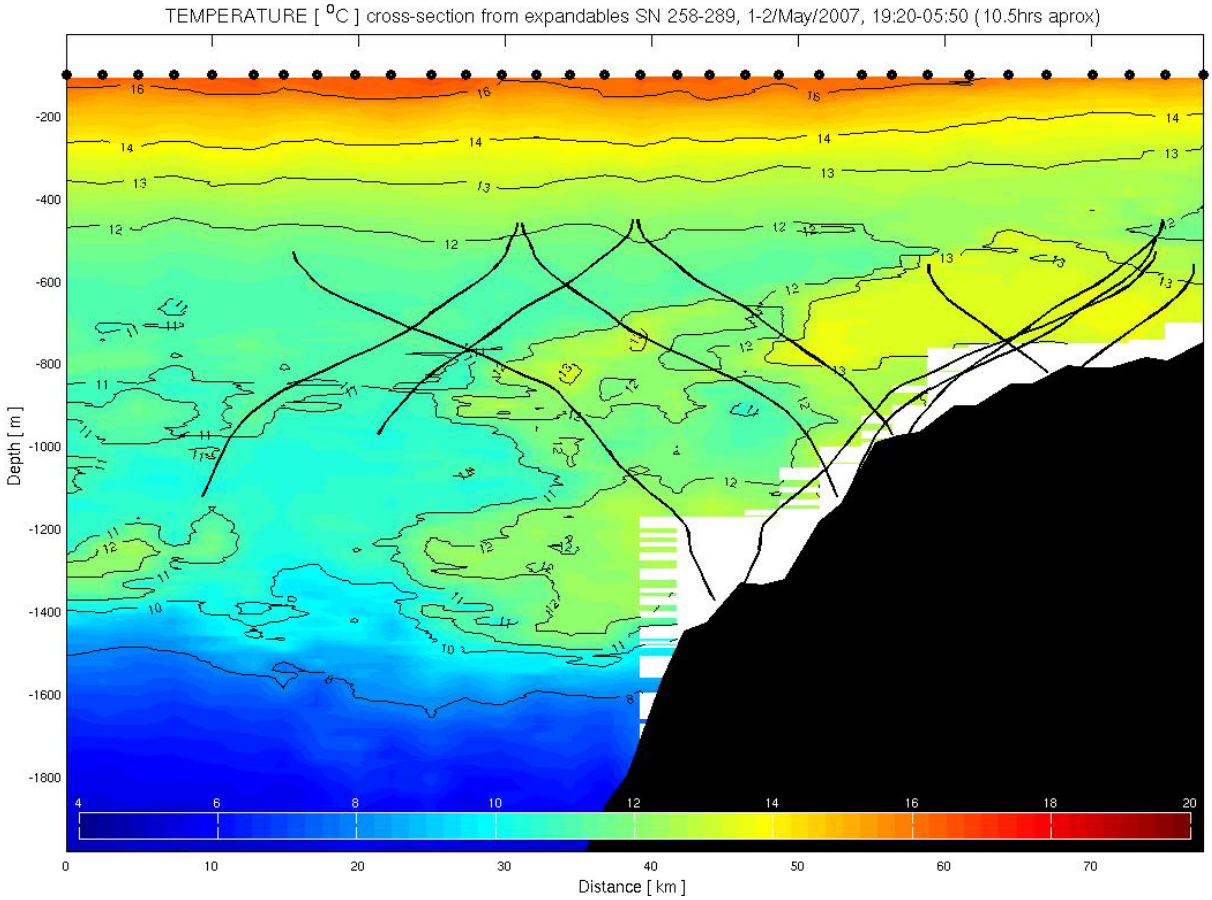

Figure 1.1: Gulf of Cadiz continental slope and internal semidiurnal tide characteristics or rays (black lines) using the background stratification (rays are located from 500m to 1400m where available stratification has conditions for propagation), and plotted against the temperature field (colour). Details of internal tide characteristic calculation are presented in section 2.3.4.

1.1.3 Gulf of Cadiz Continental Slope

The Gulf of Cadiz is located south of the Iberian Peninsula and adjacent to the north-east Atlantic (Figure 1.2). In this region, there is North Atlantic Central Water [NACW, in average upper 250m<z<500m and lower 1400m<z<bottom] on the southern (offshore) edge of the Gulf of Cadiz, Mediterranean Outflow Water [MOW, in average 500m<z<1400m] partly extends over the continental slope or northern (onshore) edge. The MOW originates from Gibraltar Strait and is affected by entrainment of fresher NACW, which reduces the salinity anomaly of the outflow (*Baringer and Price*, 1997a). Initially the MOW moves as an undercurrent to the north-west towards Cape St Vincent due to Coriolis deflection of the dense water flow to the right. The MOW passes into the Atlantic and is vertically subdivided into two main cores, as revealed by hydrological properties (*Borenas, et al* 2002): the upper core (around 800m) and the Lower core (around 1200m) move westward along the continental slope and leave the Gulf of Cadiz at Cape St Vincent in either a northward or south-westward direction (*Bower et al*, 2002).

The spreading of MOW from the Gulf of Cadiz into the rest of the Atlantic is partly achieved by mesoscale vortices with diameters of the order of 100km called Meddies, which propagate into the Atlantic and maintain their hydrographical properties (*Pingree*, 1995). Eddy formation has been detected off the south coast of Portugal within the Gulf of Cadiz, indicating the presence of meddies in the MOW cores (*Serra and Ambar*, 2002). Recent observations reveal the presence of four MOW cores inside the Gulf of Cadiz, the two "extra" to those originally proposed are a Shallow core (located between 400 and 600m) and a Deep core (with the highest density, located between 1300 and 1600m) found adjacent to Portimao Canyon (*Ambar et al*, 2008).

Observational studies have identified meddy generation areas, formation and intervals between generation episodes (*Cherubin, et al* 2000; *Borenas, et al* 2002; *Ambar et al*, 2008; *Carton, et al* 2010;). A hypothesis for MOW cores generation suggests that after MOW leaves Gibraltar Strait it is heavily influenced by mixing and dissipation, with the kinetic energy of the mean flow suggested as a source of turbulent energy for vertical mixing (*Baringer and Price*, 1997b). Bottom stress seems to be an important element in the dynamics causing the MOW to descend the continental slope (*Baringer and Price*, 1997a). Diffusivity studies over the region also suggest that lateral and vertical mixing are enhanced over the continental slope where the MOW flows, however results suggest more study is needed to quantify vertical and lateral mixing as the nearby irregular topography is likely to increase the turbulent diffusion (*Daniault et al*, 1994). There is evidence of internal waves generation and propagation along the coast of the Iberian peninsula (*da Silva et al*, 2008; *Azevedo et al*, 2006; *New and da Silva*, 2002), but their contribution as a source of energy for mixing process has not been quantified.

The separation of MOW into cores and the generation mechanism of the MOW eddies have been studied but are not fully understood. More observational work has been proposed to address the controlling mechanisms.

Internal waves are active where density gradients are strong near to continental slopes. Strong density gradients serve as pathways for internal waves but near continental slopes turbulence is present by internal wave breaking. Strong density gradients are associated with MOW interfaces between two distinctive layers of water. It is known that

inside the MOW stratification is weak and interfaces with NACW can be affected by the internal wave field.

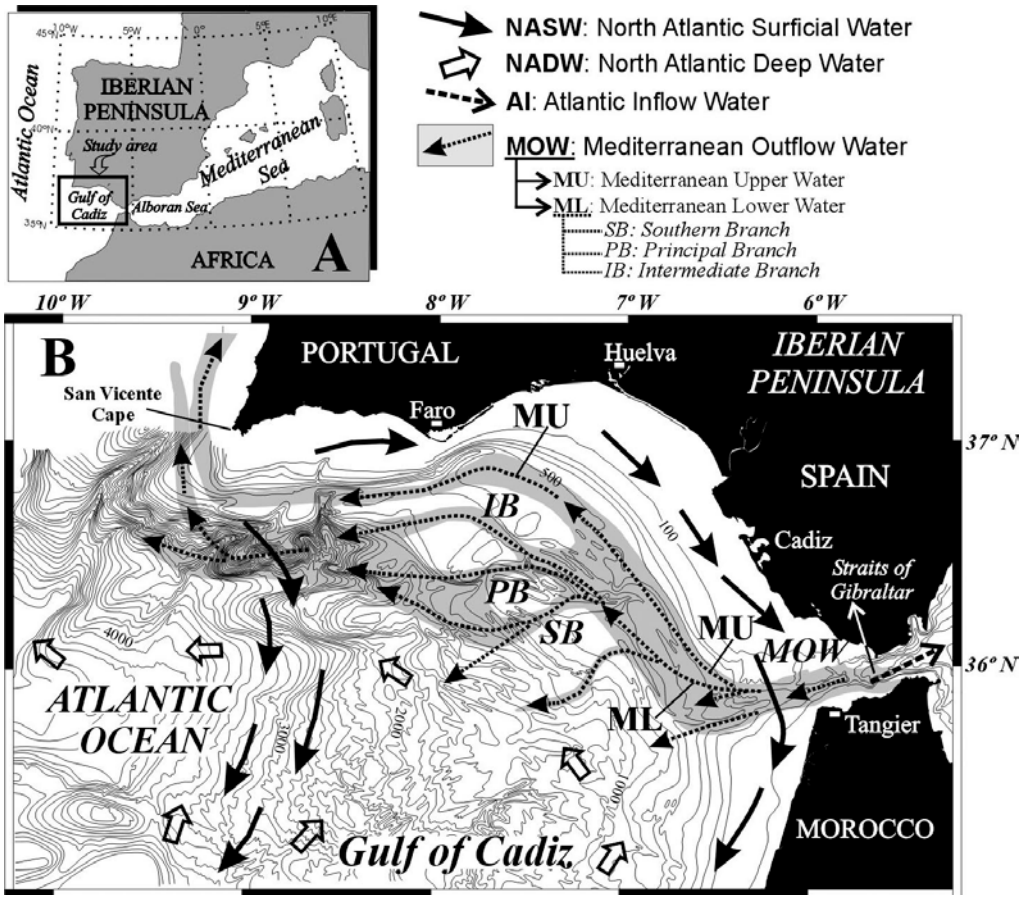

Figure 1.2: Gulf of Cadiz location and circulation pathways along and across the Continental slope (Hernandez Molina, 2003). MOW travels down/along the slope, separating at different depths into cores and Meddies. NACW interacts with MOW along its path, NACW is defined in two layers, one above and one below the MOW layer.

The contribution of salinity from the MOW in the Atlantic has been studied during the last 60 years and this contribution has a direct impact over the mid-depths of the North Atlantic (*Potter and Lozier*, 2004); they found that the MOW signal increased, becoming warmer (0.101±0.024 °C/decade) and saltier (0.0283±0.007 psu/per decade). This trend has been related with global warming changes in the Mediterranean Sea, generating warmer and saltier MOW during the last decades; however, recently minimal impact on MOW was found (*Lozier and Sindlinger*, 2009). The general agreement is that MOW has variable pathways into the North Atlantic, related with wind and buoyancy forcing variability. Lozier and Sindlinger (2009) suggested an alternative explanation for how MOW properties increased circulation changes in the North Atlantic and altered the advective-diffusive pathways of MOW. Such an explanation is now confirmed (*Bozec et al*, 2011).

1.2 Research study questions to follow

The aim of this study is the diagnosis of diapycnal mixing over the continental slope in the Gulf of Cadiz. Mixing in the water column is related to internal wave breaking and shear instabilities. Finescale structure of the water masses can be used to analyse the background stratification. The extent of mixing over the continental slope in the Gulf of Cadiz has not been completely quantified and internal wave field contribution is not clear yet.

The motivation of this study is to diagnose diapycnal mixing by using alternative available instrumentation to measure water mass properties and an approach to mixing estimates by finescale parameterizations.

The following research questions have been proposed for this study:

- In the Gulf of Cadiz, how is the internal wave activity affected by the MOW and presence of the continental slope?
- The generation of MOW cores or Meddies have not been well understood. If diapycnal mixing is playing an important role over them, how does mixing vary along the continental slope?
- How does the presence of MOW affect the diapycnal mixing, is the mixing particularly enhanced?
- Mixing is happening over the continental slope, due to density overturns or shear instabilities. How much mixing is contributed by each process?
- From a mechanical point of view, energy may be transferred over the area from the mean flow to turbulent scales or from waves remotely generated; is there evidence of energy flux onto the slope that can be discussed?
- In this region, internal waves are present, mixing is occurring and the local circulation is modified; how are these three processes connected?
- How important is diapycnal mixing in the Gulf of Cadiz versus horizontal transport processes for a salinity budget?

To address our research questions, the present work uses the Geophysical Oceanography (GO) project datasets gathered in 2007, which include conventional oceanography measurements of an on-site experiment and a historical hydrography database. In practice diapycnal mixing studies use onsite experiments focusing on diapycnal fluxes

variability. In the GO project, isothermal displacements and the spreading of MOW were measured using a large set of temperature profiles and fewer salinity profiles.

The following work addresses these aspects:

- An early analysis of hydrography and time series from available sources to provide a scenario of temporal and spatial variability of tides and density structure.
- Internal wave field analysis using available data sources for currents and waves in the Gulf of Cadiz, focusing on their spectra and variability over the slope.
- Due to the strength of the flow, the MOW can provide most of the energy for locally generated internal waves, will be expected from the current spectrum.
- Establish a plausible density ratio relationship (between temperature and salinity differences) over the Gulf of Cadiz, to identify density variability over the water column, where salinity changes will be inferred to complement the more extensive temperature profiles measurements. This will be used as evidence of the background stratification and to inspect the strain.
- Diapycnal mixing, diagnosed mostly from the strain method (*Mauritzen et al, 2002*); vertical shear and Thorpe scale methods are also used.
- Diapycnal mixing, estimated from strain method by using extensive temperature profiles measurements, used to map mixing in the Gulf of Cadiz.
- Comparison between these fine-scale parameterizations and effective values from a large scale salinity budget using a box model, to assess how robust the observational diagnostics are.

This chapter provides an overview of the general research problem. Chapter two provides the information on data sources and analysis, which address how the water mass variability relates to the MOW flow and internal wave field. Chapter three is a theoretical framework to reconstruct the density structure by using temperature profiles and inferred salinity using the extensive source of XBTs. Chapter four provides the fine structure analysis of mixing parameterisations using predominantly the strain method. Chapter five links diapycnal mixing with the internal wave field and local circulation. Chapter six compares mixing estimates from finescale parameterizations with large scale effective mixing estimates from a salinity-balanced box model. Chapter seven provides the final conclusions including water mass implications and final remarks, used to answer research questions.

1.3 Summary

Diapycnal mixing is one of many important processes which affect ocean dynamics. In the Gulf of Cadiz diapycnal mixing has not been completely addressed; the Gulf of Cadiz is now selected as a study area where mixing could be enhanced. Mixing processes have been poorly understood in the Gulf of Cadiz, many indicators of mixing contributions to generation of MOW cores and Meddies have been suggested and are now considered for diagnosis. It is important to separate processes. The Continental slope of the Gulf of Cadiz appears to be a good candidate where enhanced diapycnal mixing is taking place, and its effects are relevant to the intrusion of MOW into the Atlantic. The chapter presents an overview of the Gulf of Cadiz as the selected study area and with the objective to introduce the study area as important region where internal wave field can found to be active. Internal waves are present in oceans, and especially active over the continental slope; their breaking is considered a major cause of mixing in the oceans.

Chapter 2 Variability of the Mediterranean Overflow Water in the Gulf of Cadiz

2.1 Introduction

The Mediterranean Overflow Water (MOW) undercurrent is the most variable water mass in the Gulf of Cadiz. The MOW undercurrent is saltier (> 36) than the surrounding NACW. During its spreading phase, the properties of MOW are continuously modified. The MOW undercurrent starts at Gibraltar Strait, as a dense mass of water spreading down and along the slope where the dense plume is deflected to the right by rotational effects. As the MOW reaches Cape St Vincent, its properties are fresher due to mixing with NACW (*Ambar, et al* 2008). Strong mixing taking place inside the GC (*Baringer and Price,* 1997a,b) is probably related to flow interacting with the topographical features. The MOW undercurrent spreads from the continental slope into the Atlantic through two ways: either involving MOW cores (found over different depth ranges) or mesoscale eddies called Meddies. MOW cores are a shallow core (between 400 and 600 m), upper core (centred at 800 m), lower core (centred at 1200 m) and a deep core (between 1300 and 1600 m). Portimao Canyon, a relevant feature of Gulf of Cadiz topography, has been proposed as one area of enhanced MOW cores generation (*Ambar, et al* 2008) taking place when MOW is displaced by the internal tide suggested by observations of historical data sources (*Serra and Ambar,* 2002; *Serra et al,* 2005).

The MOW temperature and salinity relationship reveals a very distinctive core of particular values (36≤salinity≤36.8 and 10ºC≤temperature≤13ºC, mid-slope Continental slope in the Gulf of Cadiz). NACW surrounds MOW above and below, so having at least two interfaces where mixing can occur. The NACW layer above the MOW is on average saltier (> 35.8) and warmer (>10 ºC) than the NACW layer below.

Temperature and salinity can provide information on the water mass structure of the MOW, but salinity is more revealing in identifying every MOW signal. The MOW is a persistent flow and is constantly passing along and across the continental slope, although the MOW volume, flow and water mass properties can vary (*Price, et al* 1993; *Baringer and Price,* 1997a,b). The present Chapter aims to analyse the research data sources for studying cross sections in the Gulf of Cadiz.

2.2 Water masses in the Gulf of Cadiz

The present work uses datasets from the Geophysical Oceanography project (GO): first a hydrography dataset of historical experiments from the SEMANE project, and second from the GO experiment using conventional oceanographic measurements. Both projects targeted the MOW variability over the water column and mostly sampled during the summer period. The MOW undercurrent flows all year and seems to be prevalent during spring and summer seasons, due to the high rates of evaporation taking place in the Mediterranean Sea (*Baringer and Price,* 1999). Hydrographical data were measured using conventional CTD casts (Conductivity Temperature Density unit), but during the GO experiment another source of hydrography comes from temperature profiles (eXpendable Bathy Thermograph, XBT). Hydrographical data are shown by using vertical distributions over the Gulf of Cadiz. MOW signals are identified by inspecting the T/S relationship. MOW signals are presented in terms of volume fluxes passing through sections across the Gulf of Cadiz.

2.2.1 Variability from legacy/historical data (SEMANE).

SEMANE (the *Suivi des Eaux Mediterranéennes en Atlantique Nord-Est* programme) measured the currents of Mediterranean water and their variability near the continental slope of the Iberian coast. Hydrographical transects were performed across the continental slope and extended into the deep ocean (especially in the Gulf of Cadiz) to identify MOW cores and Meddies. The SEMANE research programme have reported their results with the presence of MOW cores and Meddies over the Gulf of Cadiz (*Cherubin, et al* 2000; *Carton, et al* 2010).

For the present work, SEMANE hydrographical data will be used within the Gulf of Cadiz. The SEMANE sections were taken during summer and early autumn: October 1995, May 1997, July 1999, July 2000, August-September 2000, June-July 2001, July 2002. With the aim of understanding the mixing processes and their impact on a salinity budget, three specific vertical cross section transects were analysed (along longitude 8.3° W, latitude 35.83° N and longitude 6.25° W); these transects enclose the region where the MOW undercurrent spreads from Gilbratar Strait to the roughest topographical feature, the Portimao Canyon (Figure 2.1).

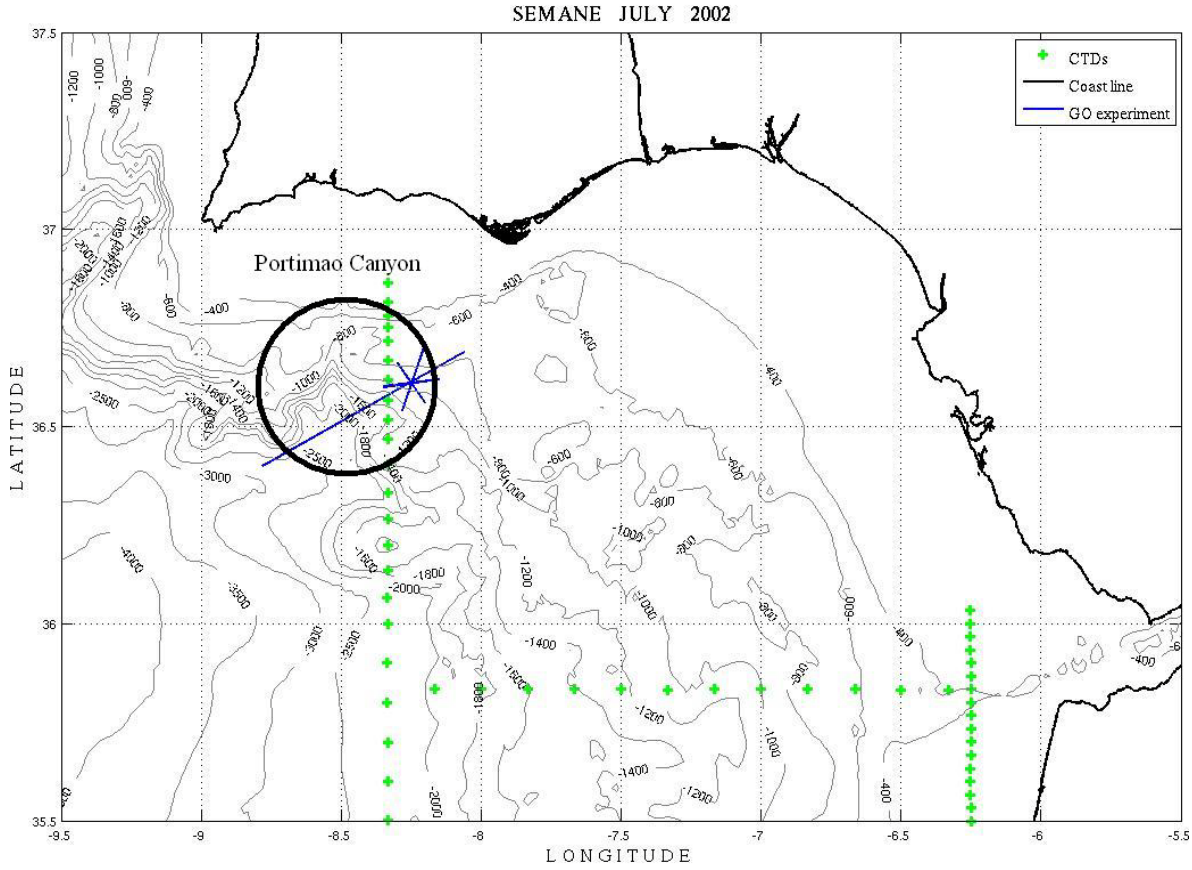

Figure 2.1: SEMANE data points (green) during July 2002; the same transects were worked throughout SEMANE in the GC. On blue lines are the sections which the GO project covered during spring 2007.

Data calibration for hydrographical profiles used in-situ measurements of salinity and temperature (analysis of water samples). Spurious points in the profiles were removed using individual inspections and a binomial filter (a fixed range of 20-40m) applied for smoothing. Final data were presented in 2db resolution (*Cherubin, et al* 2000; *Carton, et al* 2010).

Below the surface mixed layer the MOW is the most distinctive mass of water. During the spreading of the MOW along and across continental slope of the Gulf of Cadiz, there is strong mixing which changes the MOW undercurrent at Gibraltar from having a high salinity (>37.2) to a more diluted water mass (>36), although still more saline than the NACW above and below it, reinforcing the prior understanding. Figure 2.2 shows the Temperature and Salinity (TS) diagram from data surveyed during the SEMANE program at a cross section just east of Portimao Canyon (along Longitude 8.3° West). The MOW is revealed by the temperature between 10º and 13.6°C and salinity between 35.9 and 36.8 exceeding the salinity in the NACW TS relation. In comparison, the upper NACW layer has temperature and salinity close to a line from 11.5º, 35.6 to 16°C, 36.3, and the lower NACW layer has a temperature and salinity close to a line from 6º,35.1 to 10°C, 36.

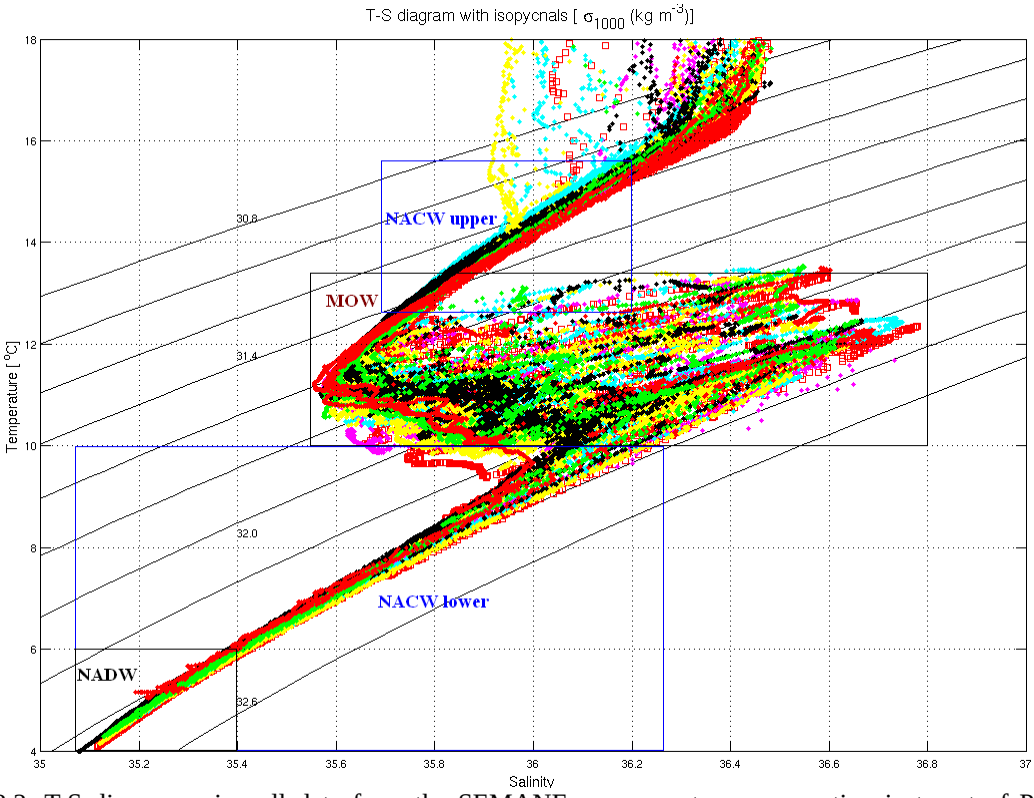

Figure 2.2: T-S diagram using all data from the SEMANE program at a cross section just east of Portimao Canyon (along Longitude 8.3° West), plotted with density referred to 1000db. SEMANE experiments (dots) involved are October 1995 (RED), May 1997 (GREEN), July 1999 (RED squares), July 2000 (BLUE), August-September 2000 (MAGENTA), June-July 2001 (YELLOW) and July (2002).

In figure 2.2, NACW is both above and below the MOW. The NACW top layer interacts with the surface mixed layer extended over a vertical scale of around 100m to 200m. The NACW bottom layer lies above the North Atlantic Deep Water (NADW) at deeper regions (*Ambar,* 2008). Overall, figure 2.2 shows vertically two thousand metres of hydrographical data. Density contours of σ_{1000} reveal isopycnals follow a stable path in the T-S diagram (which is not found using σ_0).

In figure 2.3.1 salinity countours are plotted against the salinity differences (every 10m) of each profile and potential density referenced to one kilometre. Salinity highlights the presence of the MOW in all sections. Salinity from the cross sections near to Gibraltar Strait (along Longitude 6.25° West) reveal a core of strong saline water, the MOW undercurrent, deflected to the right by the Coriolis effect, and allowing fresher NACW above to pass into the Mediterranean Sea. Another clear increase of salinity is in the surface mixed layer which covers a few tens of metres, however for the mixing interest of the MOW the focus is only with the MOW undercurrent.

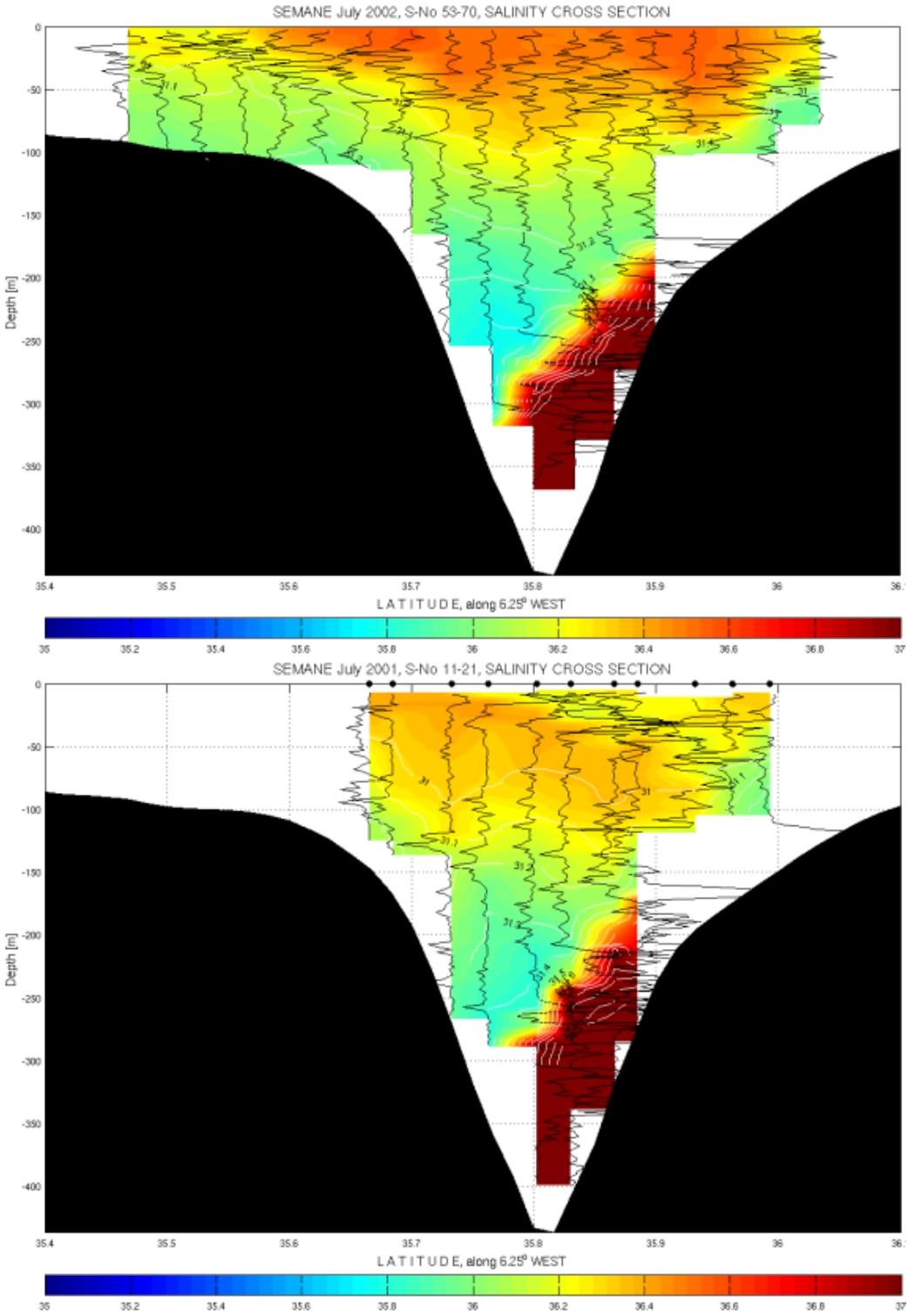

Figure 2.3.1: Salinity colour contoured cross sections along Longitude 6.25º West (East face in figure 2.1), plotted against salinity differences (every 10m) of each profile (black lines, using same scale as Latitude) and isopycnals (white lines) referred to 1000db. TOP is June 2002 and BOTTOM is June-July 2001 SEMANE experiment. *Note: for this section only 2001 and 2002 cross-sections.*

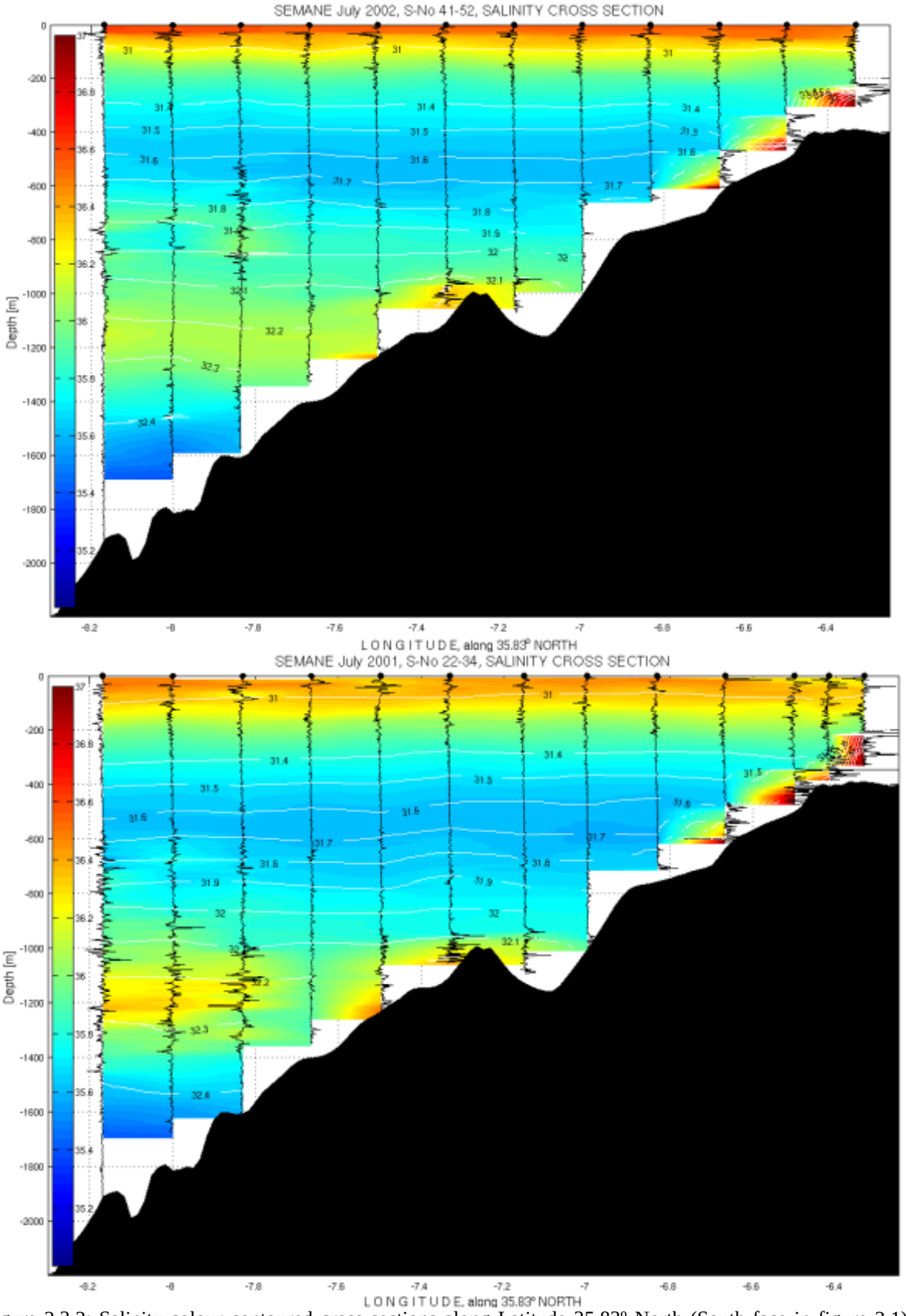

Figure 2.3.2: Salinity colour contoured cross sections along Latitude 35.83º North (South face in figure 2.1), plotted against salinity differences (every 10m) of each profile (black lines, using same scale as Longitude) and isopycnals (white lines) referred to 1000db. TOP is July 2002 and BOTTOM is June-July 2001 SEMANE experiment. *Note: for this section only 2001 and 2002 cross-sections.*

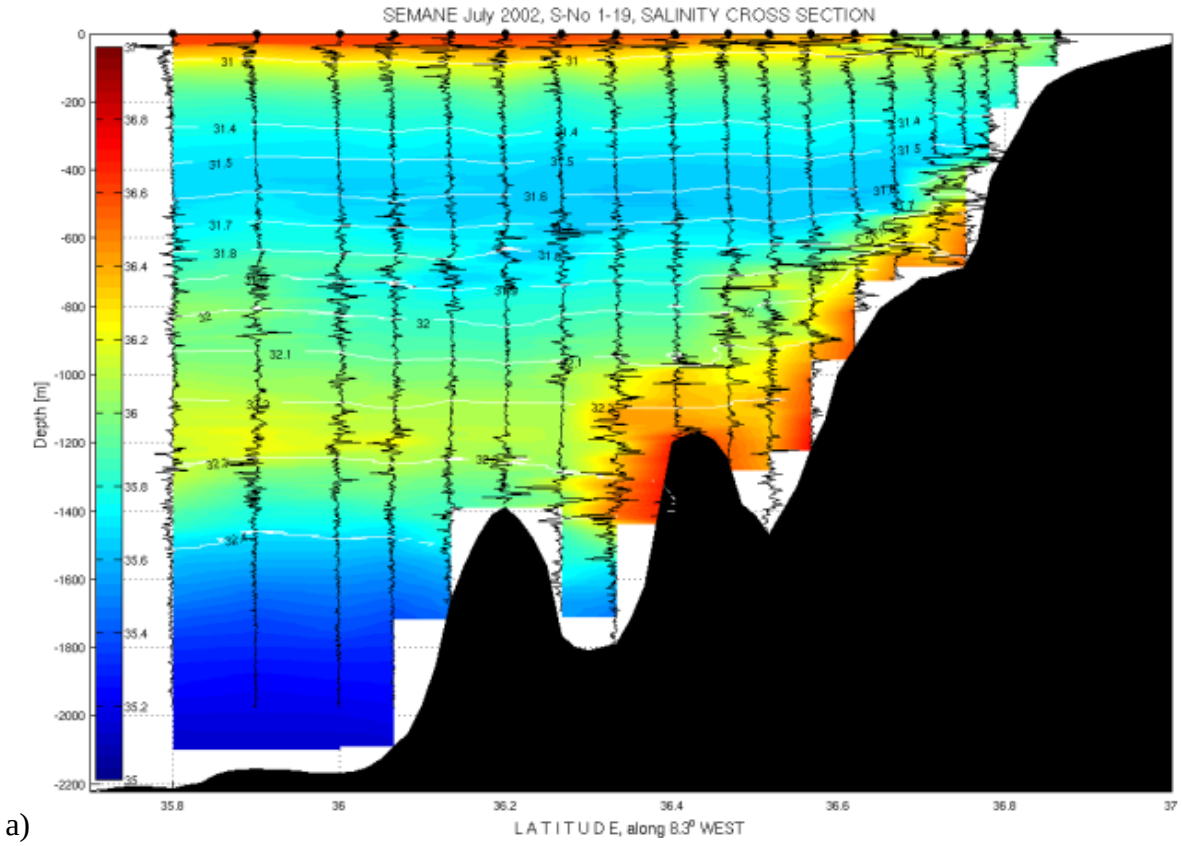

a)

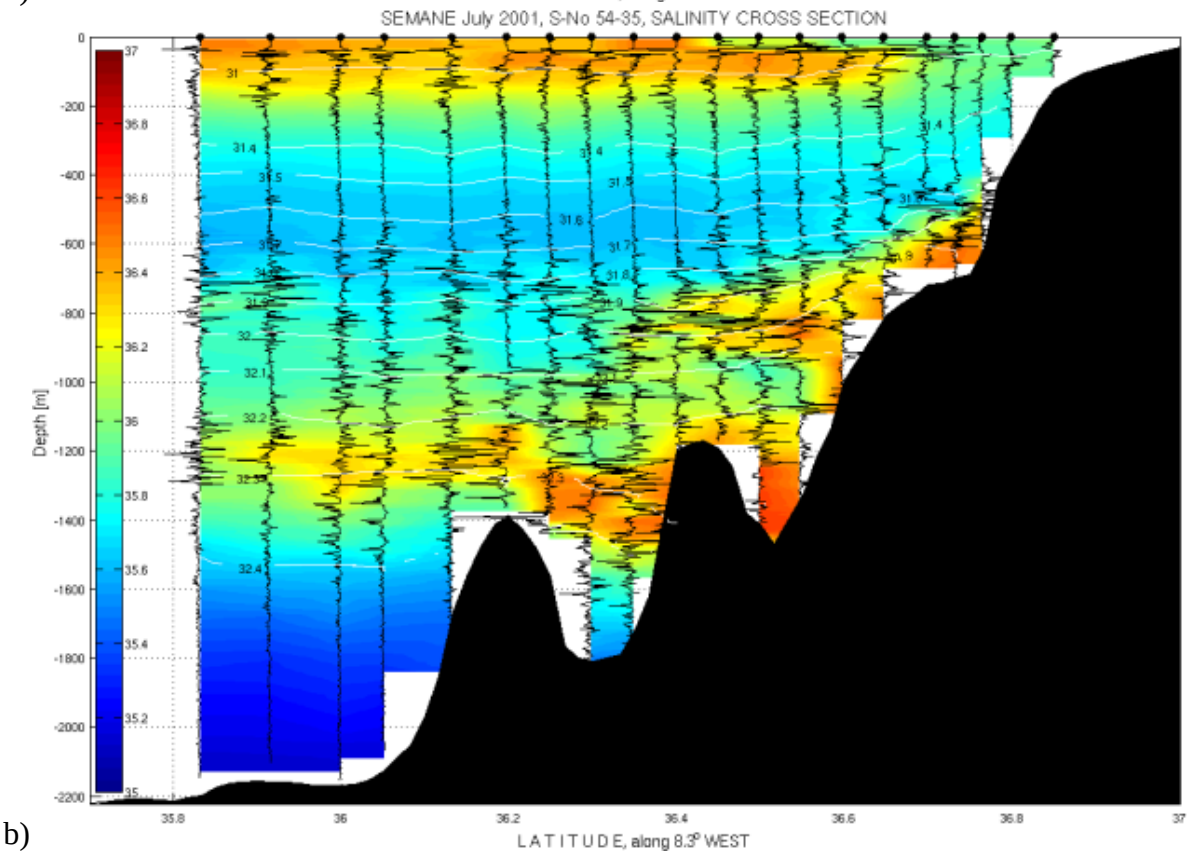

b)

Figure 2.3.3: Salinity colour contoured cross sections along Longitude 8.3° West (west face in figure 2.1), plotted against salinity differences (every 10m) of each profile (black lines, using same scale as Latitude) and isopycnals (white lines) referred to 1000db. (a) July 2002, (b) June-July 2001 (c) August-September 2000, (d) July 2000 and (e) July 1999, from SEMANE experiments. *Note: October 1995 and May 1997 do not have complete cross sections and were only used to confirm water mass properties* .

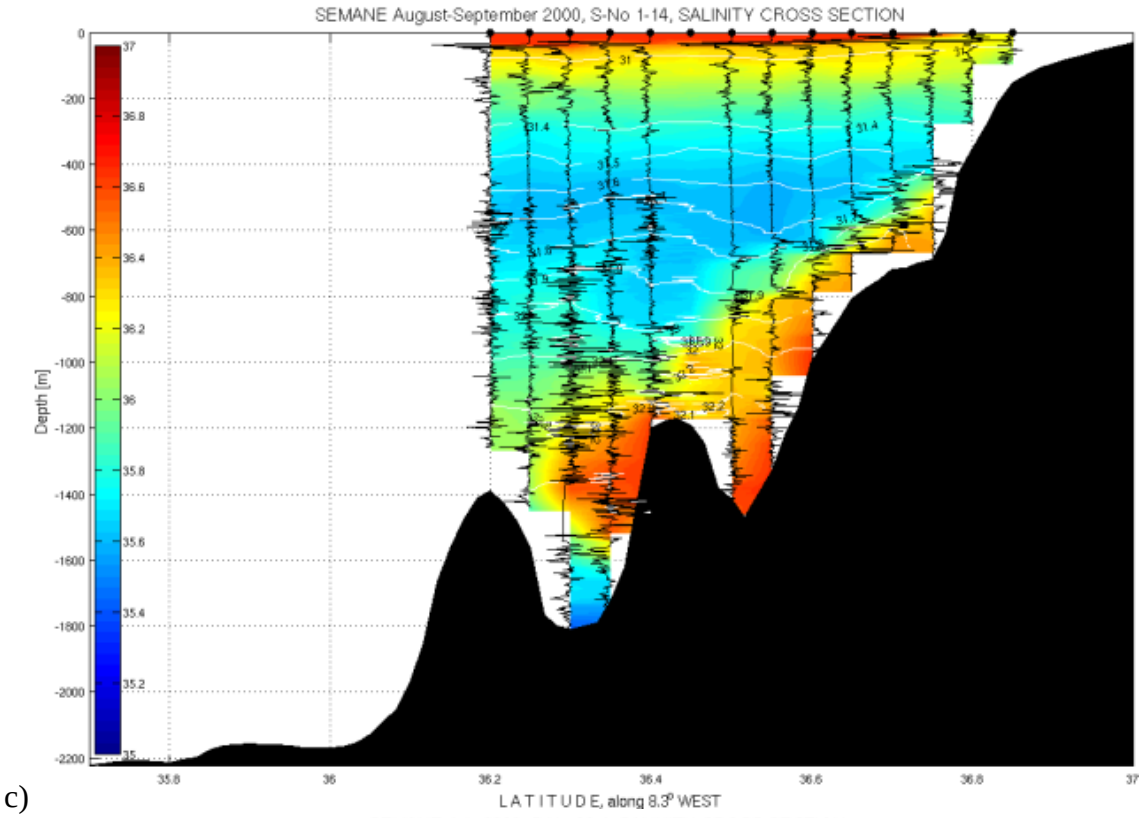

c)

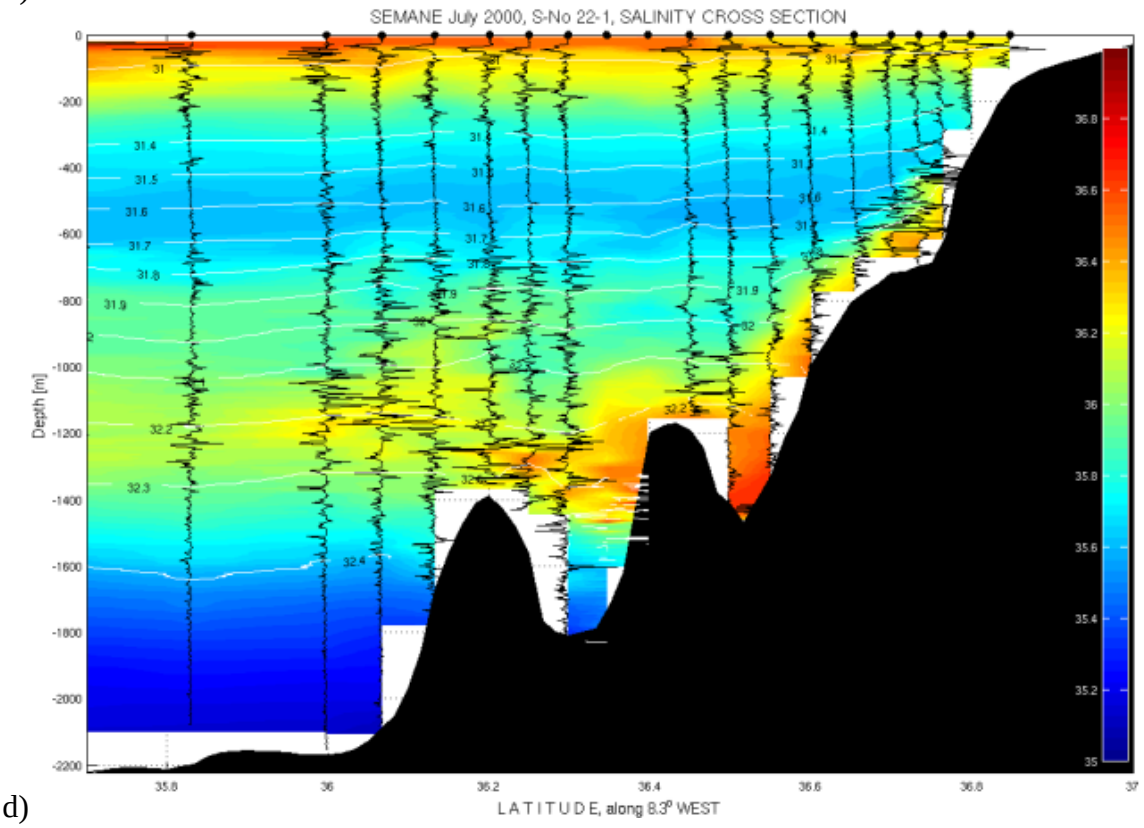

d)

Figure 2.3.3: Salinity colour contoured cross sections along Longitude 8.3° West (west face in figure 2.1), plotted against salinity differences (every 10m) of each profile (black lines, using same scale as Latitude) and isopycnals (white lines) referred to 1000db. (a) July 2002, (b) June-July 2001 (c) August-September 2000, (d) July 2000 and (e) July 1999, from SEMANE experiments. *Note: October 1995 and May 1997 do not have complete cross sections and were only used to confirm water mass properties* .

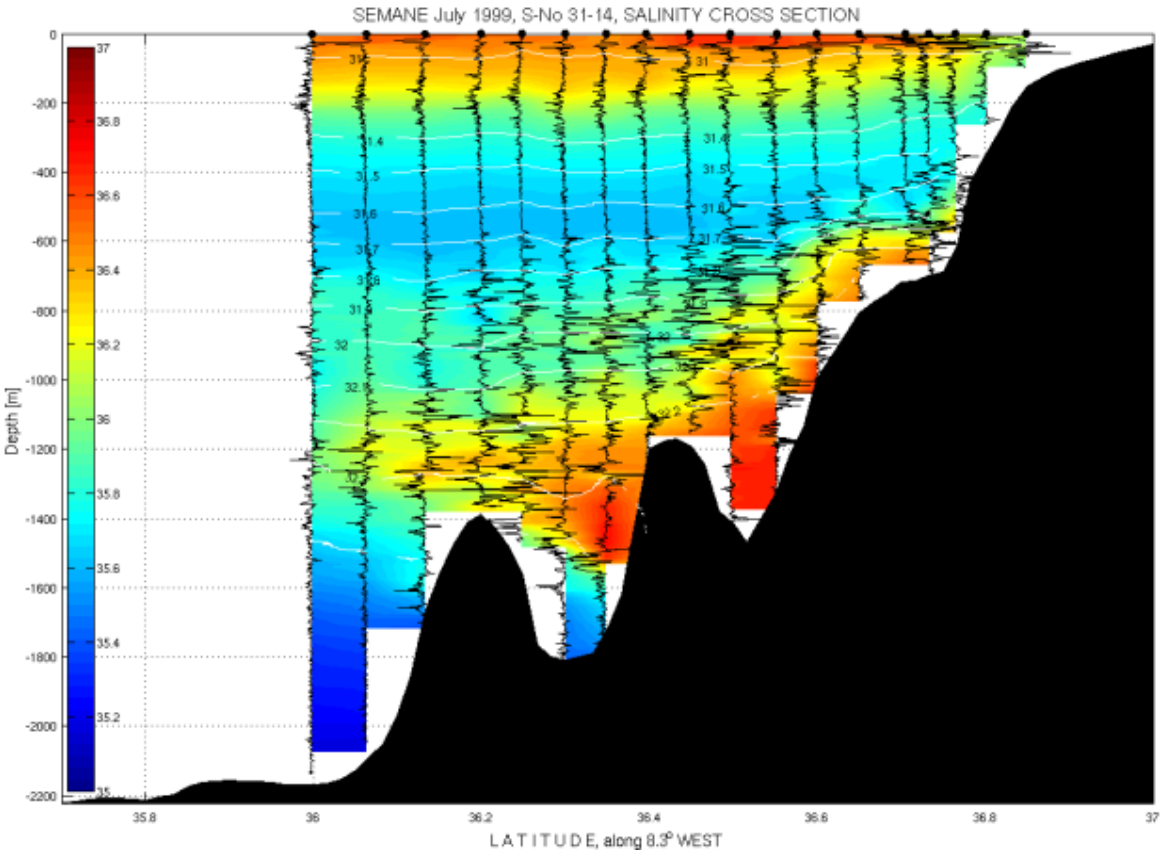

e)

Figure 2.3.3: Salinity colour contoured cross sections along Longitude 8.3° West (west face in figure 2.1), plotted against salinity differences (every 10m) of each profile (black lines, using same scale as Latitude) and isopycnals (white lines) refered to 1000db. (a) July 2002, (b) June-July 2001 (c) August-September 2000, (d) July 2000 and (e) July 1999, from SEMANE experiments. *Note: October 1995 and May 1997 do not have complete cross sections and were only used to confirm water mass properties* .

Figure 2.3.2 shows another vertical cross section which is on the south side of the study region. NACW is more predominant over the section and a strong MOW signal (S > 37.5) travelling down slope can be detected at the shallow end (which is the early stage of MOW mostly travelling northward), however this patch ends and another pacth of high salinity occurs over the outer continental slope (900m < z < 1400m). High salinity is (>35.9) found mid slope (1000m to 1200m) and at same depth at outer slope regions, this salinity is there probably due to the amount of spreading of MOW cores and Meddies from previous pulses (*Cherubin, et al* 2000; *Carton, et al* 2010). There is a clearly separated region between the surface mixed layer and MOW water, occupied by NACW with a local minimum of salinity (S < 35.8). At deeper regions (z > 1500m), below the MOW layer, salinity drops again within NACW.

Figure 2.3.3 shows five salinity cross sections at the Western side of the study region, which crosses the Continental slope towards the end of the Iberian peninsula. MOW can be found as the highest salinity (S > 36.1) at mid depths, lying alongside the continental slope.

In all the five plots, there is a clear signal of a lower (from 1000 to 1500 metres) MOW core or meddy over the outer-slope. In the 2001 datasets, there is also MOW spreading in an upper MOW core (from 700m to 900m). Surrounding the MOW layers there are well defined NACW layers with observed lower salinity (S<36).

Salinity profiles in all cross sections reveal large vertical gradients (a change of 0.2 over 10m) on the interfaces between MOW and NACW. However, there is variability in the profiles according to whether there is a strong MOW signal. Inside the MOW, salinity differences are found to be large and suggest a lot of interleaving variability. In the NACW layers, the absence of strong salinity differences suggests little interleaving.

In comparison between the cross sections [South, East and West], the highest salinity in the MOW (S > 37.5) is seen on the Eastern side (Figure 2.3.1), and the MOW over the south face is mostly fresher than both East and West faces(Figure 2.3.2) and East face is saltier than the West face (Figure 2.3.3). In a simple view, the area included by salinity from [inside of main canyon at 150m to 400m depth] East side is around ten times smaller than the West side, which may mean that MOW water increases its volume greatly in less than two hundred kilometres. To understand the amount of water passing within the MOW and NACW layers, the volume flux is calculated using geostrophic balance over the previous cross sections. The measurements of temperature and salinity on two profiles provide the information to calculate the specific volume anomalies, and their horizontal gradients are used to provide the velocity shear over the water column, assuming a level of no motion (for face South and West calculations start at 350db and for face East at 40db, where velocities were assumed to be minimal based on near-zero currents measured (Vessel Mounted and Lowered ADCPs) in the NACW upper layer down below the surface mixed layer). Also each face was separated into distinct continental slope regions (shelf, mid and outer slope; on face West due to topographical features the mid slope was divided in two canyons sections) to compare outputs from different pairs of CTD profiles as geostrophic velocities. Once velocities are obtained, the volume flux or transport ($Sv = 1 \times 10^6 m^3 s^{-1}$) is calculated for each water mass passing through each section. The uncertainties were estimated first by calculating the velocity shear with alternative profiles and comparing with interannual variability through depth, second by using an extra 0.03 m/s at each pressure level (this value was obtained from actual LADCP and VMADCP measurements at the assumed level of no motion).

In Table 2.1, the transport calculation gives the MOW transport on the East side as around 0.375 Sv on average directly into the Gulf of Cadiz; this face is small with strong velocity shear. On the South side, the geostrophic velocities have similar variability on each region over the continental slope with on average a transport of 0.31 Sv, apart from 2002 over the outer slope when the transport was 1.25 Sv. In three regions over the continental slope, the geostrophic velocity was directed northward into the Gulf of Cadiz. However, velocity flow is found to the south related to Meddies (*Cherubin, et al* 2000; *Ambar, et al* 2008; *Carton, et al* 2010).

Table 2.1: Transport results (Sv) on East and South sides using SEMANE cross sections, distance between profiles in km next to volume transport values.

SEMANE datasets	Longitude 6.25º W EAST (< 400m)	Latitude 35.83º N - SOUTH		
		SHELF (<1000m)	MID SLOPE (1000m-1500m)	OUTER SLOPE (>1500m)
June-July 2001	0.46±0.38(19.23km)	0.17±0.32(29.91km)	0.60±1.19(74.89km)	0.27±1.85(30.34km)
July 2002	0.29±0.40(18.10km)	0.21±0.32(30.20km)	0.32±2.61(75.18km)	1.25±1.79(30.00km)

Note: On Longitude 6.25º baroclinic velocities were integrated from 40db to bottom. Uncertainties come from difference of velocity shear by using different set of CTD profiles, as explained in the above text.

Table 2.2: Transport results (Sv) on West side (along Longitude 8.3º W) using SEMANE cross sections, distance between profiles in km next to volume transport values.

SEMANE datasets WEST	SHELF (< 1000m)	MID SLOPE 1st Canyon	MID SLOPE 2nd Canyon	OUTER SLOPE (> 1500m)
October 1995	-	0.95±0.49(18.22km)	0.11±1.32(21.78km)	-
May 1997	-	1.40±0.34(12.45km)	1.28±0.84(10.00km)	-
July 1999	0.30±0.22(18.32km)	1.84±0.99(22.59km)	1.70±1.58(29.25km)	1.18±0.99(15.00km)
July 2000	0.47±0.34(23.82km)	0.71±1.75(33.32km)	0.61±0.85(27.96km)	2.01±3.24(36.55km)
August-September 2000	1.19±1.10(22.17km)	1.91±0.89(16.78km)	0.91±0.40(22.35km)	-
June-July 2001	0.81±0.22(24.15km)	1.93±0.92(16.34km)	0.87±0.68(29.71km)	1.41±1.65(18.70km)
July 2002	0.57±0.34(20.67km)	0.82±0.75(18.15km)	0.76±1.96(37.49km)	0.92±2.36(29.56km)

Note: All transports were integrated from 350db to bottom, assuming weak velocities at 350db depth.

Table 2.3: Total transport (Sv) at each side of the cross sections.

Volume flux [Sv]	Gulf of Cadiz cross-section faces		
	West	South	East
June-July 2001	5.02±3.28	1.04±3.35	0.46±0.38
July 2002	3.07±5.10	1.78±4.72	0.29±0.40
1995-2002	4.44±4.13	1.41±3.97	0.37±0.39

In table 2.2 the transport calculations over the West side give the least transport on the shelf (< 1 Sv) on average from any of the four parts of this section. The mid continental slope region was separated into two sections (due two canyons, Fig 2.3.3): the shallower canyon has a large transport of >1.5Sv and the deeper canyon has a transport of >1Sv. On the mid slope combining these transport estimates gives a total transport of >2.5Sv passing through the section. On the Outer slope there is a significant tranport (> 1.3 Sv). These transports are directed to the west leaving the Gulf of Cadiz.

In summary, the transport is found (Table 2.3) on average in the East and South sides to be directed into the Gulf of Cadiz and on the West side to be directed out of Gulf of Cadiz. The estimates and implications of the transport and the water mass balance are discussed in chapters 6 and 7.

2.2.2 Variability during the GO experiment

In the spring of 2007, the EU funded Geophysical Oceanography project led an expedition to the GC to observe acoustic reflectivity in the water column. During the experiment, a set of detailed hydrographic and current measurements was made on a section which the MOW crosses on the continental slope near to the Portimao Canyon. Hydrographical measurements were mainly based on few CTD profiles and many profiles of XBT (only recording temperature), both were made frequently (1-2 hour gap, over same area) and with only a short distance (~1 km) between profiles. In figure 2.4 the experiment area and details of profiles taken during the survey are shown.

Data from hydrographical profiles (CTD casts) were calibrated against in-situ measurements of surface salinity and temperature from analysis of water samples. Spurious points in the profiles were removed using individual inspections. Data were analysed in full vertical resolution to compare CTD profiles with extensive data of temperature profiles (XBTs). Due to the spatial scatter of CTD stations, a full cross section could not be made.

A T-S diagram (Figure 2.5) from the twelve CTD casts available in the GO experiment shows a similar structure to the profiles observed in the SEMANE program historical data. MOW and NACW layers can be identified as well as the modification within the surface mixed layer.

Inside the MOW, temperature and salinity reveal strong variability, which in most cases is difficult to compare from one site to the other. However there are two permanent conditions that can be compared: the vertical salinity gradients in the transition between NACW and MOW (top interface) and between the MOW (bottom interface) and NACW again. Both interfaces contain variability and can be compared in the T-S diagram. Salinity interfaces above and below the MOW are discussed more in chapters 4, 5 and 6. The positions of these upper and lower interfaces do though vary for every profile depending on how the MOW signal is spreading near or along the continental slope.

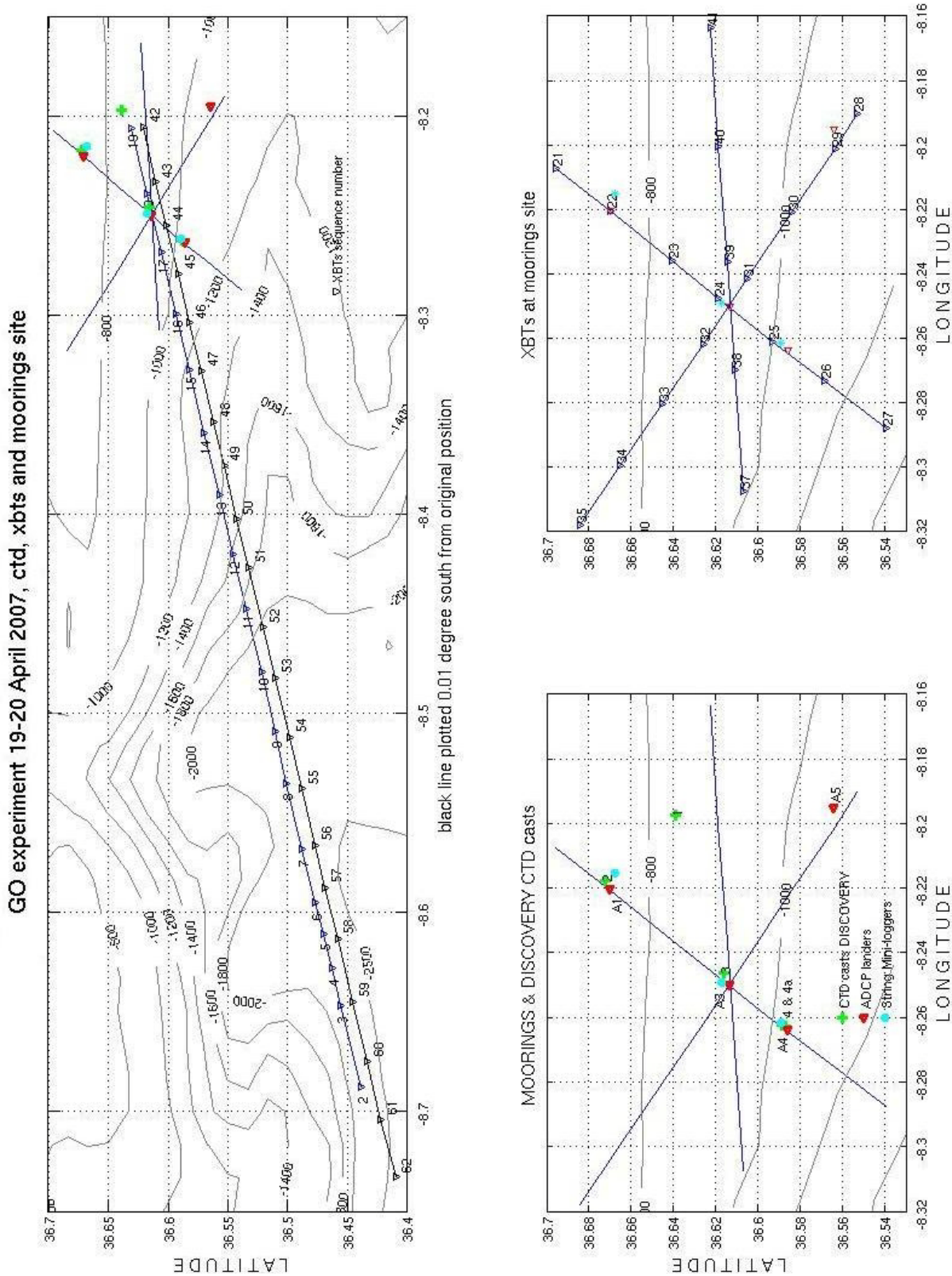

Figure 2.4: GO experiment during April to May 2007: instruments deployment. TOP plot shows a diagonal cross section with XBT positions. BOTTOM left shows where the few CTD casts were made and also some moorings were deployed. BOTTOM right shows XBTs positions over the star shape sections. All the XBTs show the sequence number on the plots following the time sequence, approximately 20 min apart for each profile. For context see Figure 2.1.

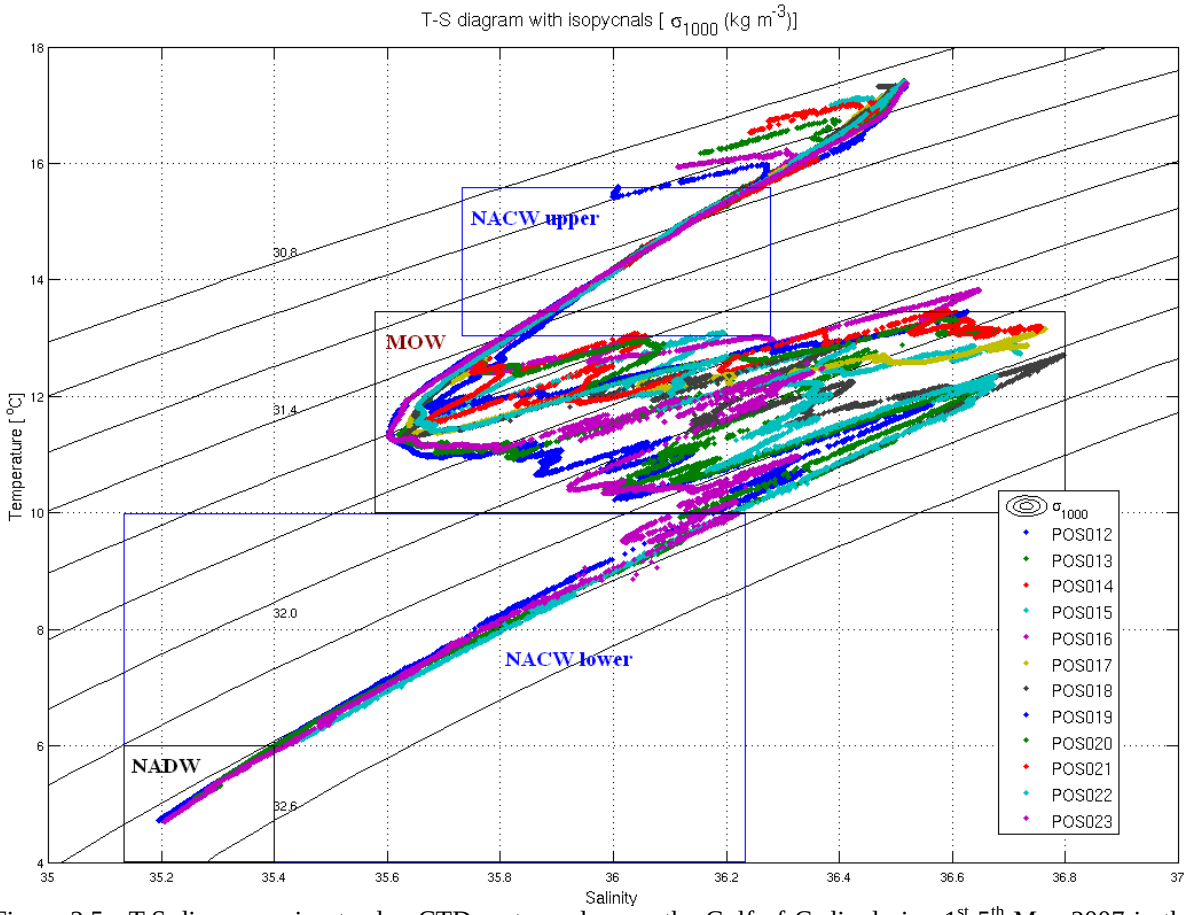

Figure 2.5: T-S diagram using twelve CTD casts made over the Gulf of Cadiz during 1st-5th May 2007 in the GO experiment, plotted against isopycnals referred to a pressure of 1000db.

2.3 Current and waves inside MOW

This section evaluates time series measurements. During the Geophysical Oceanography experiment in the Gulf of Cadiz in spring of 2007, four Acoustic Doppler Current Profiler (ADCP) landers and three Temperature mini-logger chains were deployed over the continental slope, adjacent to Portimao Canyon (*Mountfield*, 2007; *Smithson*, 2007). Time series records were taken from April 18th to May 10th 2007 (approximately 21 days). Figure 2.4 shows a map of the mooring deployments. Instruments were programmed to record a mean value every two minutes. ADCP records were processed using manufacturer routines from BINARY to ASCII (readable data). Currents were processed in components (north, east and vertical components in millimetres per second). Also every two minute record is accompanied by a backscattering strength and error values. Table 2.4 shows some specifications and record lengths from the ADCP landers.

Table 2.4: ADCP Landers specifications.

Site	Type Bins/size	Record starts (dd/m/yyyy hh:mm;ss)	Ends (dd/m/yyyy hh:mm;ss)	Position	Description/ Total depth
A1	600 kHz 30/2m	18/4/2007 06:20:00	9/5/2007 17:57:59.96	Lat 36°40.18' N Lon 8°13.22' W	Bottom frame 742 m
A3	150 kHz 60/4m	18/4/2007 10:27:37.02	10/5/2007 07:15:41.72	Lat 36°36.81' N Lon 8°15.00' W	Bottom frame 866 m
A4	150 kHz 60/4m	18/4/2007 16:20:00	10/5/2007 09:22:00	Lat 36°35.15' N Lon 8°15.82' W	Bottom frame 980 m
A5	75 kHz 30/8m	18/4/2007 18:52:00	9/5/2007 16:03:59.96	Lat 36°33.86' N Lon 8°11.71' W	Moored ADCP 1015 m

ADCP moorings at site A1 and A5 also recorded temperature and pressure time series with sensors at the top of the frame. On A3 and A4, there were only temperature sensors, but A3 gave bad data. Not all the values on the current profile were obtained, especially on the last bins (bins located far above the instrument). A lack of scattered particles and malfunction of sensors are the most common candidates for lack of data.

Temperature miniloggers were arranged in a chain of 16 instruments at intervals of 2-4 metres along mooring wires (50m length approximately). Data were used without any processing and were taken as real temperature [data were calibrated by comparing with CTD and XBT data nearby]. Two or four minute time intervals were obtained from the instruments. Some systematic errors were present in the mini logger records and some spikes were removed. Details of temperature miniloggers moorings are shown in the Table 2.5 below.

Table 2.5. Temperature miniloggers moorings details taken from GO mooring deployments report.

Site	Position	Instruments (m) above bed and time interval (min)	Record starts (dd/m/yyyy)	Ends (dd/m/yyyy)	Water Depth (m)
A1	Lat 36° 40.07' N Lon 8° 12.92' W	49(2), 41(2),37(4) 33(2),25(2),19(4),17(2), 15(4),13(2), 11(4),7(4),3(4)	18/4/2007 07:20	09/5/2007 16:40	747 m
A3	Lat 36° 37.03' N Lon 8° 14.95' W	50(2),46(4),42(2),38(4), 30(4),20(4),18(2),16(4), 12(4),8(4),4(4)	18/4/2007 12:20	10/5/2007 06:00	854 m
A4	Lat 36° 35.35' N Lon 8° 15.69' W	46(4),38(4),26(2),20(4), 18(2),16(4),14(2),12(4), 10(2),8(4),4(4)	18/4/2007 17:40	10/5/2007 06:00	978 m

All time series were analysed to study variability related with currents and waves. Several analysis methods were investigated. The first method was to apply basic statistics to inspect general statistical values and correlations between sites. The second method was to

apply a harmonic analysis to current time series to inspect the internal wave field and its relation with tidal components; finally residuals were compared against results from a low pass filter applied to current series. The third method was to apply a spectral analysis to compare the kinetic energy from currents against the Garrett-Munk spectrum (1972, 1975), which represents the variability of the internal wave field. The fourth was a diagnosis of the internal wave field using the internal wave characteristics by using background stratification. For each section here, the methodology is explained followed by the results from the analysis.

2.3.1 Time series statistics

The currents were analysed in terms of components to the North and East, for mean, minimum, maximum, standard deviation and variance. Temperature and pressure were analysed as well. Table 2.5 shows formulae for each statistical function.

Table 2.5: Formulas of the different statistical functions used on time series.

Statistical functions	Mean ($\bar{x}$)	Standard deviation (σ)	Variance (σ^2)
Formula	$\frac{1}{N}\sum_{i=1}^{N} x_i$	$\left(\frac{1}{N-1}\sum_{i=1}^{N}(x-\bar{x})^2\right)^{\frac{1}{2}}$	$\frac{1}{N-1}\sum_{i=1}^{N}(x-\bar{x})^2$

The following table (2.6) presents the statistics of the time series. ADCP time series are presented using depth average statistics. From the hydrographical sources (water mass analysis) over the moorings sites, the measured currents are mostly within the MOW undercurrent.

Table 2.6: Depth-average statistics from different instruments at each sites.

Site		Mean	Min	max	std	Var
A1	East-West (m/s)	-0.119	-0.398	0.226	0.095	0.009
	North-South (m/s)	-0.008	-0.204	0.200	0.054	0.003
	Temperature (ºC)	13.38	12.90	13.69	0.19	0.030
	Pressure (db)	754.64	752.46	757.15	0.790	0.624
A3	East-West (m/s)	-0.149	-0.483	0.189	0.100	0.010
	North-South (m/s)	0.052	-0.257	0.461	0.075	0.006
	Temperature (ºC)	13.11	12.69	13.59	0.11	0.010
A4	East-West (m/s)	-0.312	-0.673	0.065	0.100	0.010
	North-South (m/s)	0.114	-0.218	0.434	0.078	0.006
	Temperature (ºC)	12.89	12.46	13.59	0.16	0.026
A5	East-West (m/s)	-0.197	-0.432	0.053	0.078	0.006
	North-South (m/s)	0.128	-0.148	0.328	0.079	0.006
	Temperature (ºC)	12.95	12.56	13.30	0.15	0.023
	Pressure (b)	1032.30	1030.40	1034.08	0.731	0.534

Note: As explained there is no available pressure record at A3 and A4 sites. The measure of error for mean values is O(10^{-5}) due length of records (15000 samples).

From table 2.6, the current becomes stronger with water depth and is strongest at site A4. Current East-West components are the stronger and mostly to the West. Also at three different sites (A3, A4 and A5), the current is mostly to the North-West, only at site A1 is there not a clear preferred North or South. Temperature decreased with depth and the MOW overall temperature range was 12.46ºC < t < 13.69ºC. Pressure records obtained in two sites (A1 and A5) showed a variance of around half a squared decibar.

From all sites it is clear that MOW is travelling preferentially to the West to North-West around (0.20 m s^{-1}), only A1 shows a more westward direction (0.11 m s^{-1}). The fastest current speeds were detected at sites A3 and A4 (> 0.5 m s^{-1}). On average MOW passing at three different sites is around 13ºC, the highest value was found at site A1 (13.69ºC). At A1 and A5 sites, sea level variability was found to be around 4-5 db with the highest amplitude during spring tides.

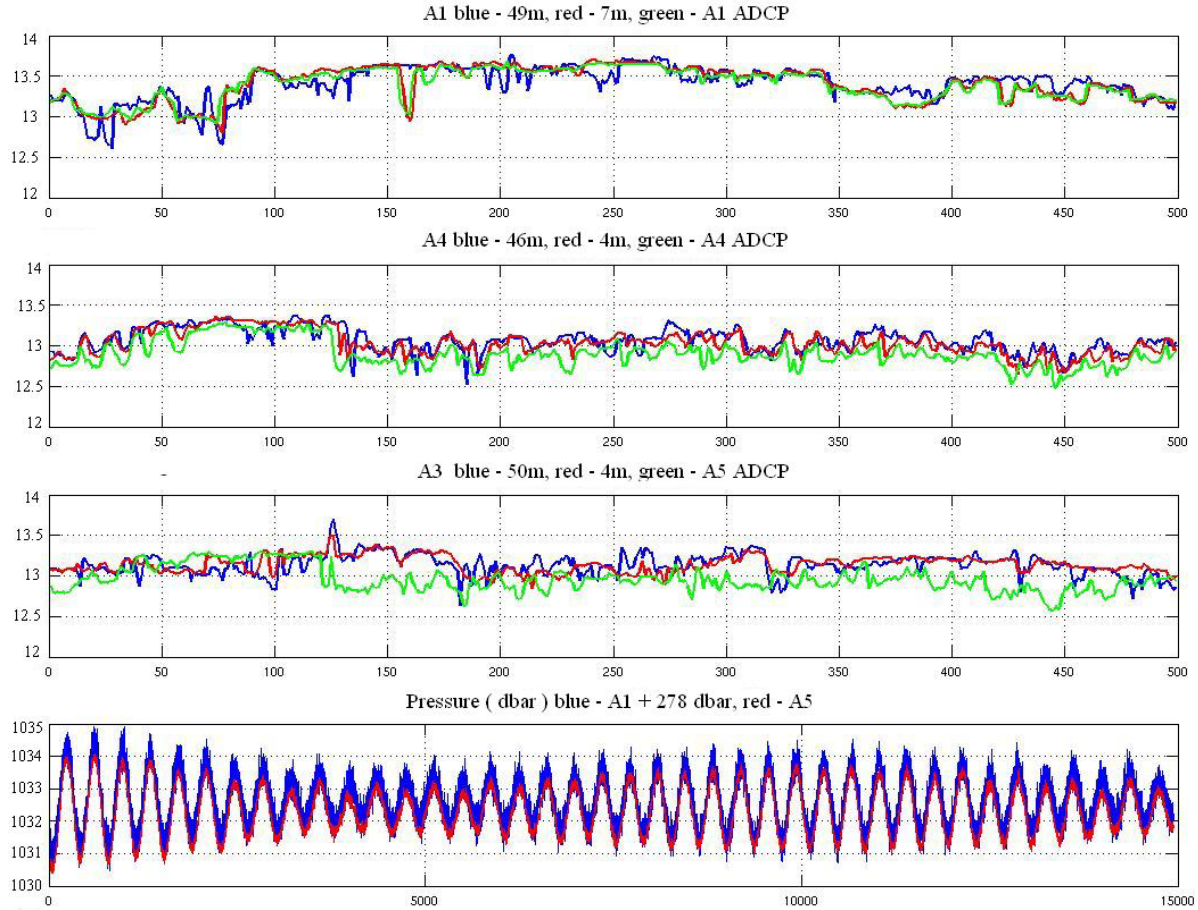

Figure 2.6: Temperature and pressure time series from ADCP (sensors at top of frame) and related temperature record from Temperature chain mini-loggers (approx. 3-4m above bed and top of the chain approx. 50m above bed). First panel at site A1, Second panel is A4 and third panel is A3 and ADCP temperature sensor at A5. All temperature records (one hour resolution) are in degrees Celsius. Fourth panel shows pressure (2 minutes resolution) time series observed at A1 and A5 sites (decibars).

Figure 2.6 shows temperature time series recorded at different sites. Temperature observed in our records is characteristic of MOW (12.6-13.6 ºC). The warmest record (> 13.5ºC) from all time series is at A1. The temperature differences between top and bottom records of the miniloggers-chain array were sometimes significant (> 0.1ºC, reaching 0.6ºC at A1). Temperature records at A4 and A5 were spatially correlated; it was not the same with A3 or A1. In comparison with the pressure records, temperature showed some tidal influence.

A Progressive Vector Diagram (PVD) is the cumulative sum of vectors plotted to show distance travelled according to the velocity measured by an instrument. In order to present PVDs from all instruments, PVDs were taken as a depth-average and plotted in colour (colour changes at three day intervals).

Figure 2.7 shows the PVDs at different sites (A3, A4 and A5) where the current is directed mostly to the North-West and is strongest at A4. Also PVDs showed that at site A1 the current is directed predominantly to the West. However during the second period of three days (red), the current direction changes more to the North-West and then after roughly five days suddenly changes to the South. The change happens after a period where the pressure variations decrease in magnitude (neap tides) and temperature showed an increase (0.3 ºC) around April 27th. The temperature records had some variability with abrupt changes on some sites (A3, A4 and A5), however those changes are not related with changes in current directions, but only with less variability.

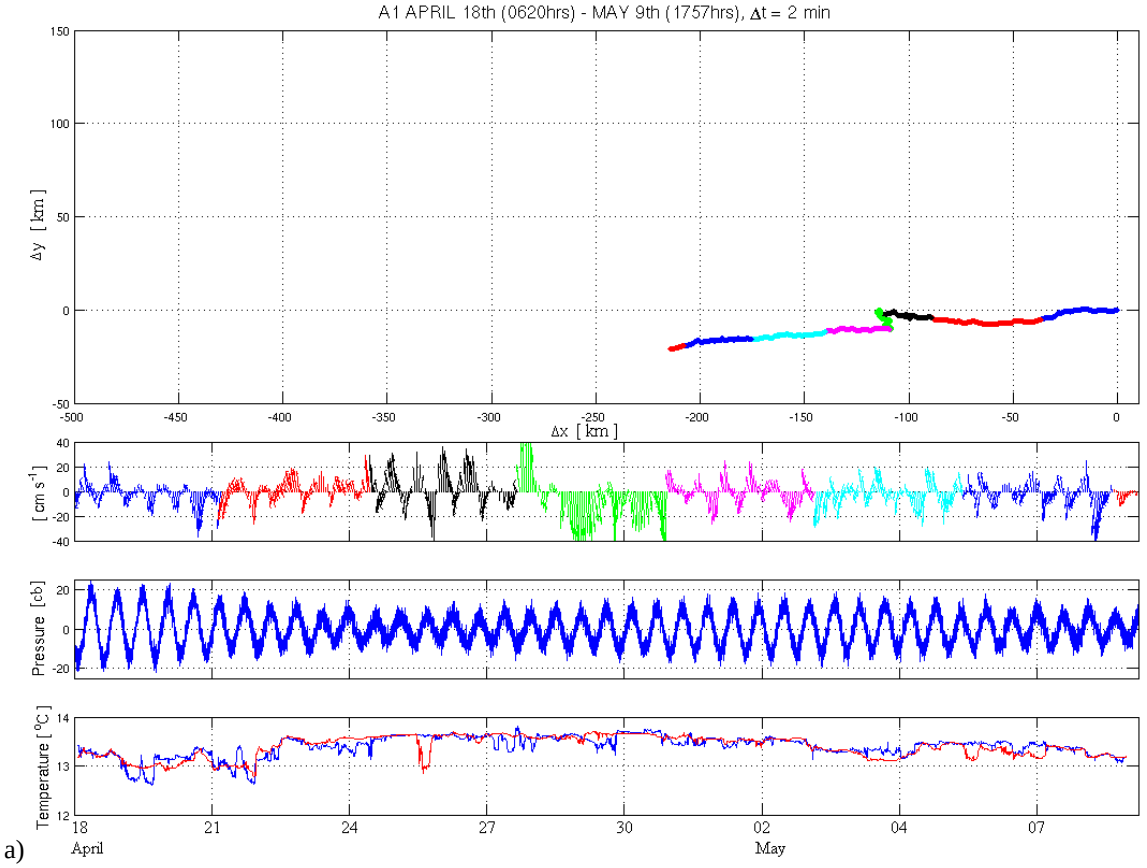

a)

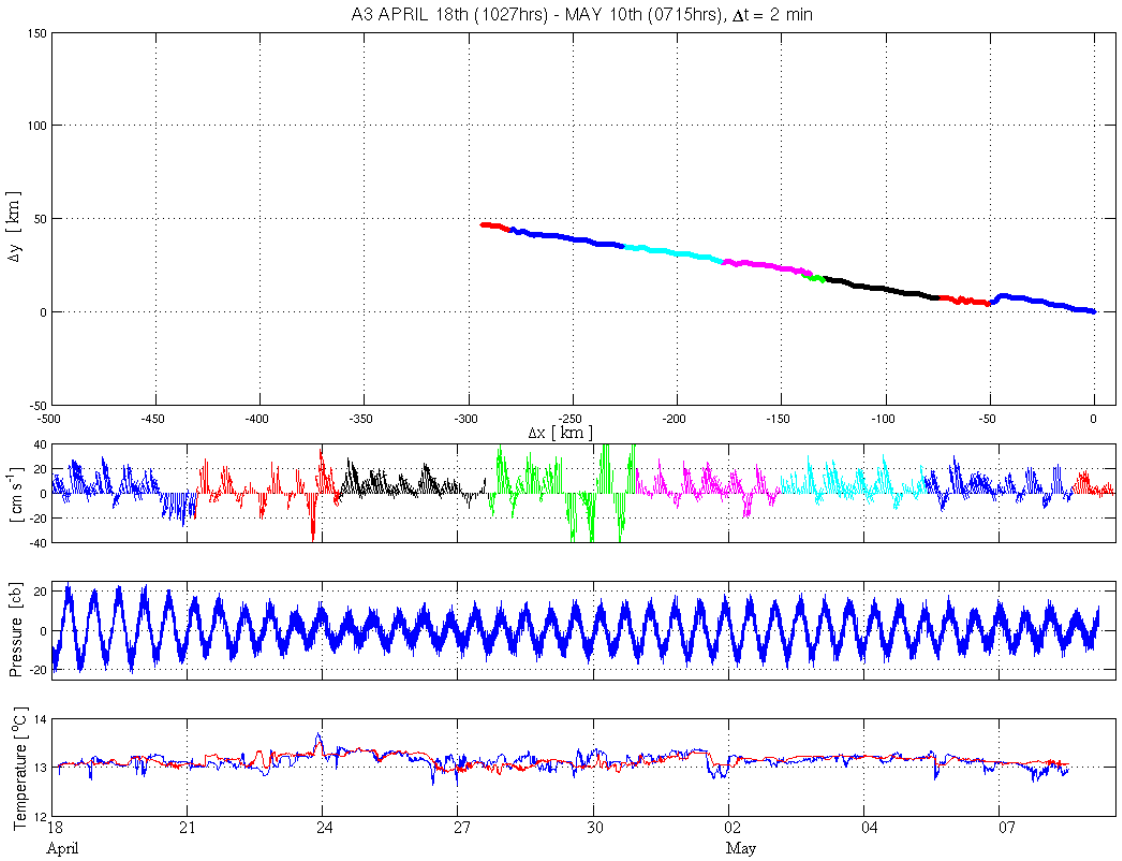

b)

Figure 2.7: Progressive vectors diagrams (PVD) from averaged ADCP are shown (coloured in 3-days range) with current (coloured arrows in cm/s, angle has been exaggerated to the North), pressure (-20< p <20 centibars) and temperature from available sensors (Blue and red lines are the first and the last miniloggers on the chain, 3 m and 50 m depth above seabed respectively). Panels refer to a) A1, b) A3, c) A4 and d) A5.

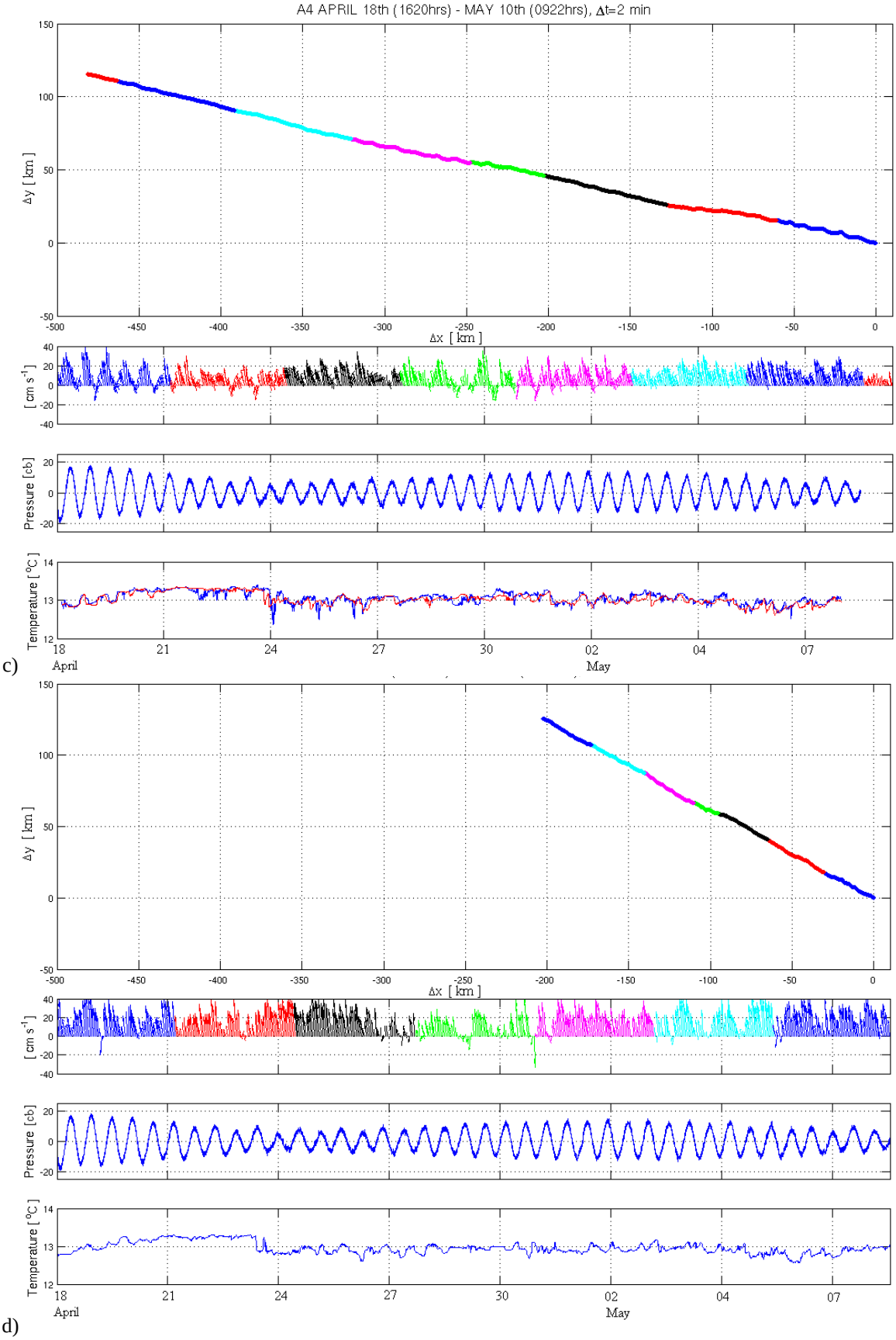

Figure 2.7: Progressive vectors diagrams (PVD) from averaged ADCP are shown (coloured in 3-days range) with current (coloured arrows in m/s, angle has been exaggerated to the North), pressure (-20< p <20, centibars) and temperature from available sensors (Blue and red lines are the first and the last miniloggers on the chain, 3 m and 50 m depth above seabed respectively). Panels refer to a) A1, b) A3, c) A4 and d) A5.

2.3.2 Correlations between mooring sites

Using temperature time series at two different locations, variability can be correlated between them. Sometimes direct correlations are not clear, however if the time series are displaced in time a lagged signal can be correlated. Using auto-covariance and cross-covariance functions, an expression for a cross correlation coefficient is:

$$\frac{C_{xy}(\tau)}{C_x C_y} = \frac{\frac{1}{N-k}\sum_{i=1}^{N-k}[x_i-\bar{x}][y_{i+k}-\bar{y}]}{\left(\frac{1}{N-k}\sum_{i=1}^{N-k}[x_i-\bar{x}]^2\right)^{\frac{1}{2}}\left(\frac{1}{N-k}\sum_{i=1+k}^{N}[y_i-\bar{y}]^2\right)^{\frac{1}{2}}} \qquad (2.1)$$

where x and y represent two selected variables and N the length of the time series. τ is the lag in time ($\tau = k\,\Delta t,\ k = 0,\ldots,M$) for k sampling increments (Δt) with $M << N$ (*Emery and Thomson*, 2001). A couple of variables can be easily correlated if they present similar changes. Temperature time series are provided from temperature mini-logger moorings and ADCP landers local sensors. All sensors were deployed within 2-4 km of each other, so big changes are not expected.

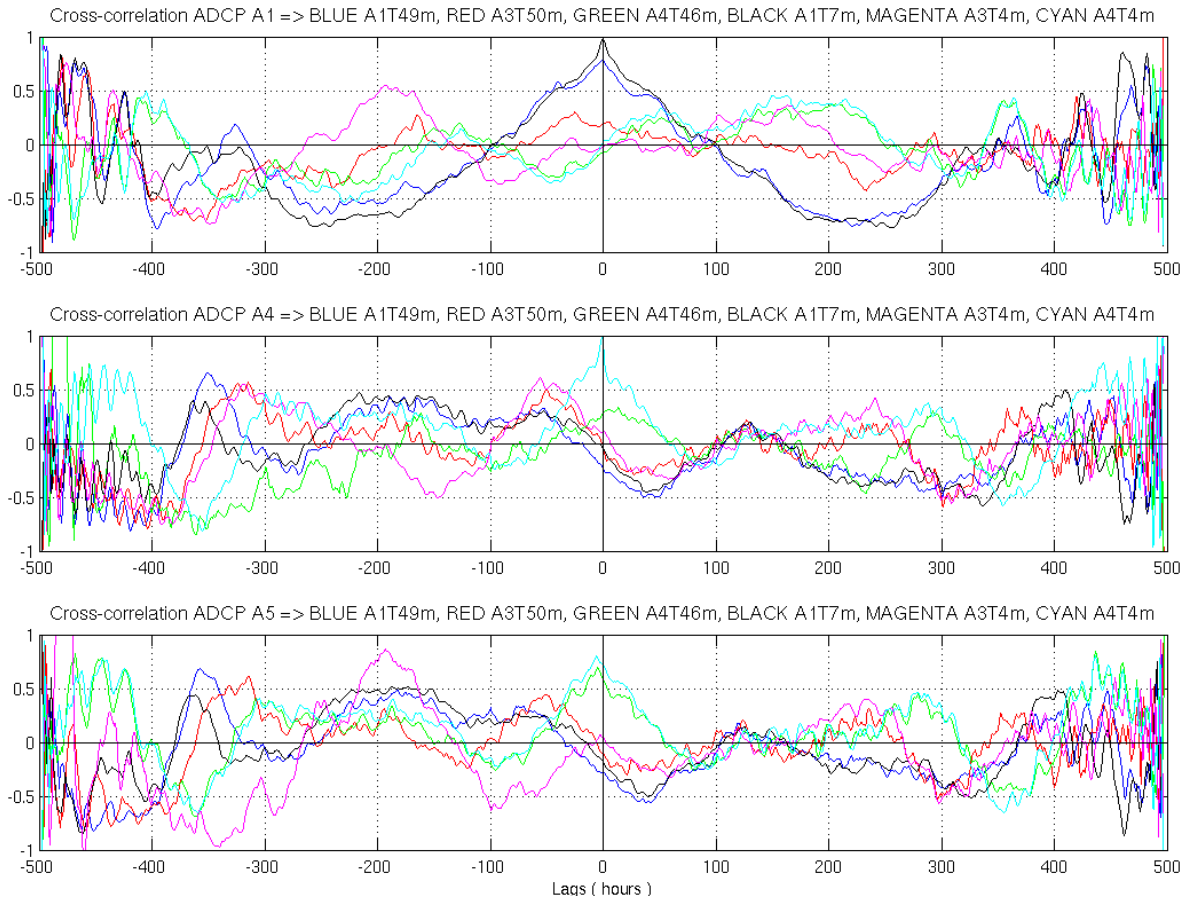

Figure 2.8: Cross correlation applied to temperature time series from ADCP sensors and minilogger-chains. The first panel uses ADCP A1 temperature sensor as first variable in the cross correlation function. The second panel is with ADCP A4 and the third panel is with ADCP A5 as first variable. Data resolution applied here is in hours.

Figure (2.8) shows different results for temperature time series cross correlation using top and bottom records at different sites. The correlation between A4 and A5 is high (~0.75) at zero lag, as mentioned before. Both sites (A4 and A5) are correlated with A3 (~0.6) and weakly (~0.35) with A1. However, the correlation between A1 and A3 is not strong (< 0.25 at zero lag). The significance of the correlation is that MOW measured by time series shows dependence on water depth. These results confirm that MOW movement inspected by water masses properties across or down slope are present but in comparison with along slope movement those can be negligible or considerable slow for some dynamics mechanisms.

2.3.3 Harmonic analysis: Tides

Any time series in the ocean reveals barotropic variability related to astronomical constituents (tides). Tides can be expressed as the sum of tidal constituents. An expression can be used to build a sum of harmonic constituents that represent a time series and can be written individually as follows:

$$Acos(wt + V - G) \qquad (2.2)$$

where A is the amplitude of the constituent, G is the phase lag, w is the angular speed and V the astronomical argument composed of combination of s (Moon's mean longitude), h (Sun's mean longitude), p (longitude of Moon's perigee), N (longitude of the Moon's ascending node) and p' (longitude of Sun's perigee). Time (t) used is elapsed time in hours. The astronomical argument is essentially to combine the factors determining phase to provide parameterization values on the day of the tidal observation (*Cartwright,* 1985). TIRA software (*Bell et al,* 2000) has been used to find tidal constituents by harmonic analysis. TIRA is basically used to study tidal constituents in sea level measurements; here it is used for current (analysed as components, separately North-South and East-West) and temperature time series.

In order to apply harmonic analysis on the time series a set of components (Z0, MSF, 2Q1, O1, K1, OO1,MU2, M2, S2, M3, M4, MS4, S4, M6, 2MS6 and 2SM6) were proposed (input file from TIRA software proposed for time series with length around 15 days). Other components were related to these in the analysis (PI1, P1, S1, PSI1 and PHI1 to K1; N2, NU2 and L2 to M2; T2 and K2 to S2; Q1 and RHO1 to O1; SIG1 to 2Q1, J1 to OO1, 2N2 to MU2). The time series length was approximately 21 days. Components with a strong signal, and residuals (time series without the contribution of tidal components solved for), were used to interpret results.

a)

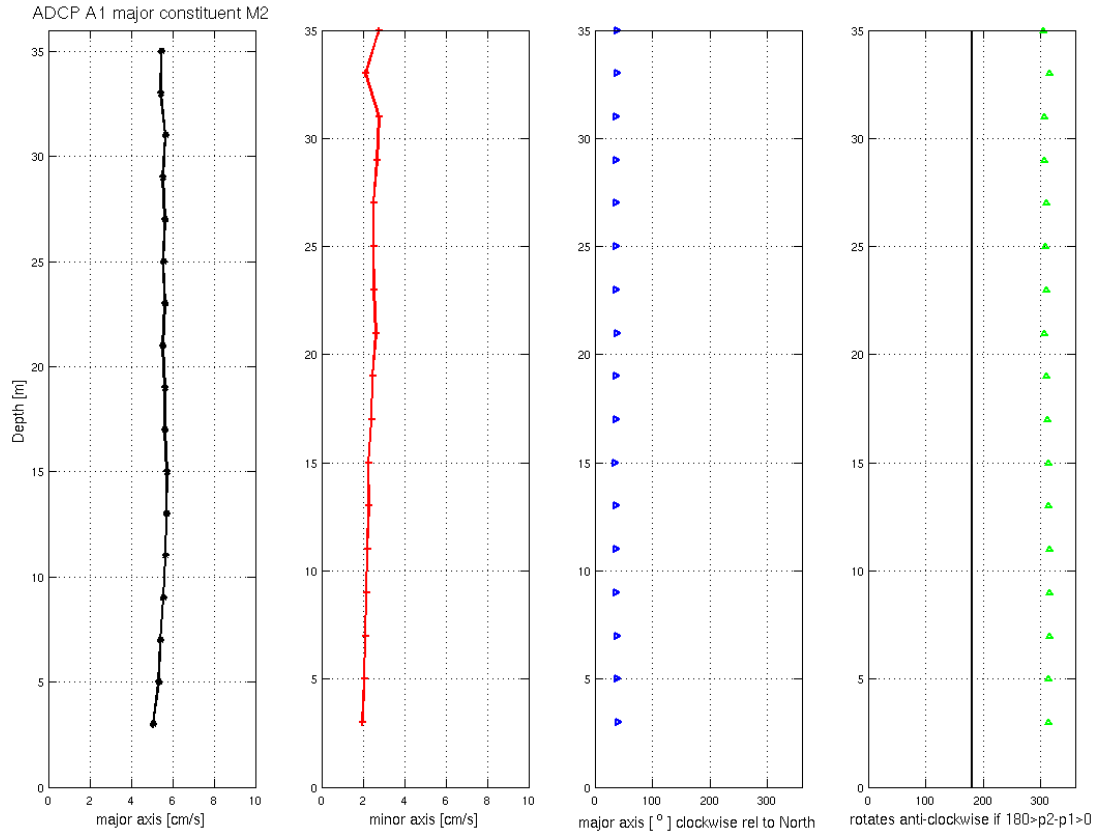

b)

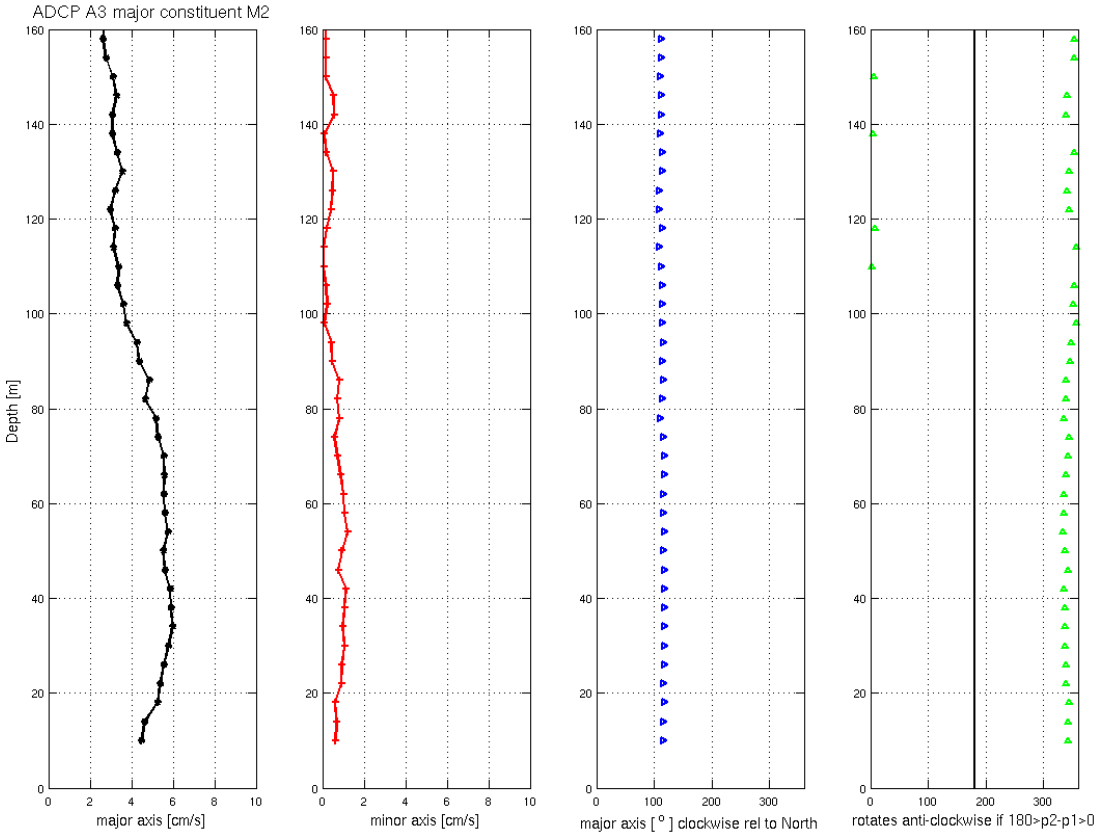

Figure 2.9: TIRA analysis results for M2 astronomical constituent. Each set of four panels shows the ellipse properties: major axis (black line, cm/s), minor axis (red line, cm/s), major axis orientation (blue line, degrees relative to the North) and rotation (green line, anticlockwise if 180º > rotation angle [p2-p1] > 0º; black line shows 180º). Panels refer to a) A1, b) A3, c) A4 and d) A5.

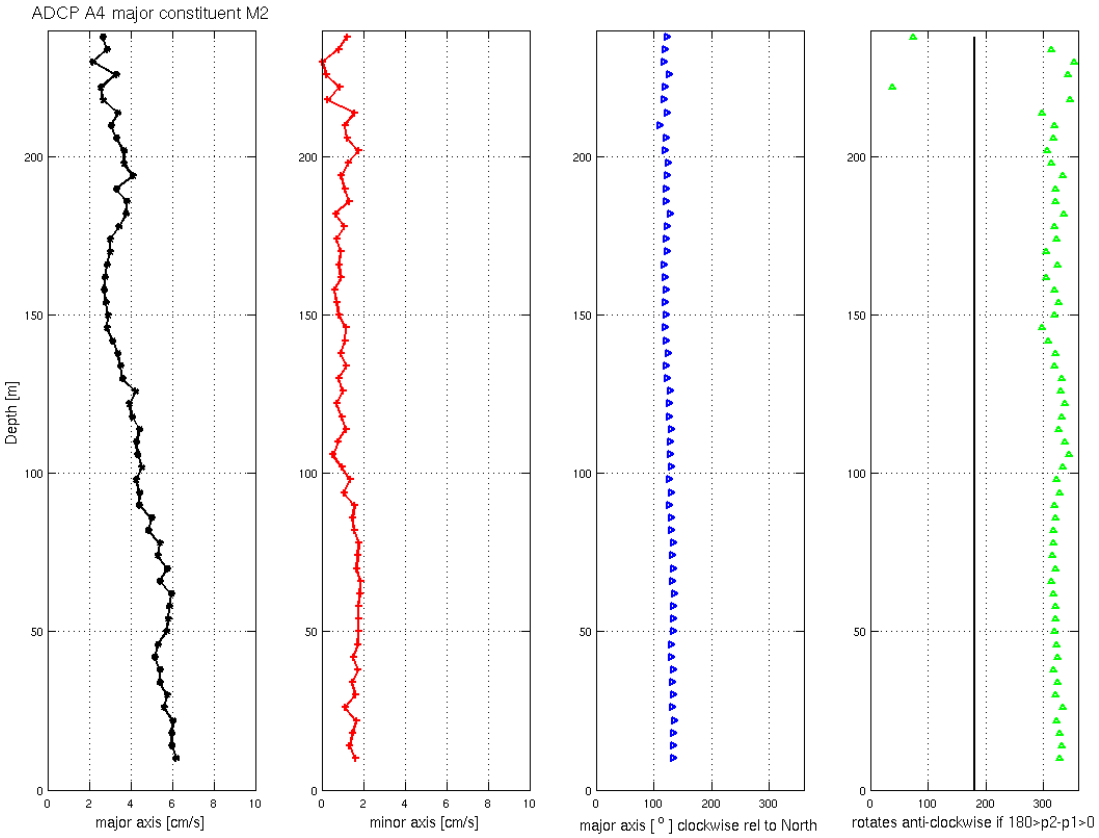

c)

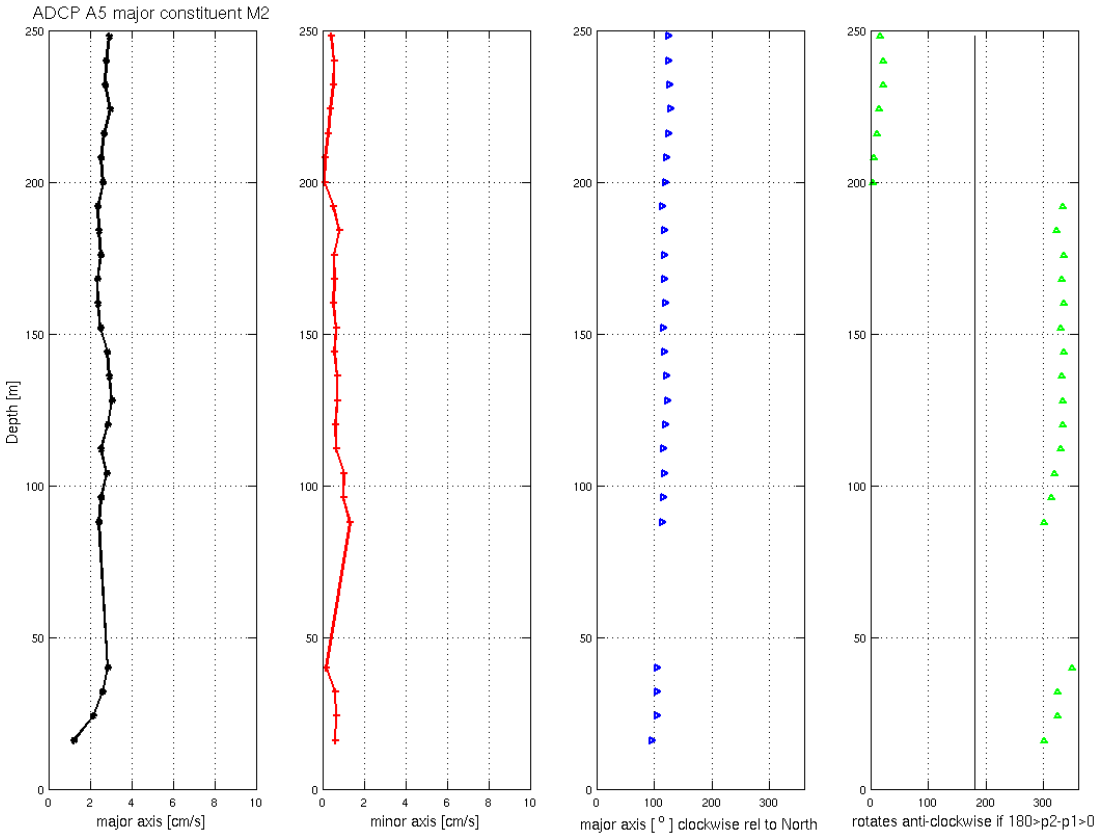

d)

Figure 2.9: TIRA analysis results for M2 astronomical constituent. Each set of four panels shows the ellipse properties: major axis (black line, cm/s), minor axis (red line, cm/s), major axis orientation (blue line, degrees relative to the North) and rotation (green line, anticlockwise if 180º > rotation angle [p2-p1] > 0º; black line shows 180º). Panels refer to a) A1, b) A3, c) A4 and d) A5.

Results from the tidal harmonic analysis are summarised here. M2 is the strongest in all series, but not as large at A5 as at the other sites, as shown in Figure 2.9. The major axis magnitude appears to be slightly different (1-3 cm/s) between the top and bottom records (except at A1), however major axis orientation is observed to be uniform in all profiles. M2 orientation is observed to be East-West (except at A1 where it is to the North-East), and with clockwise rotation. The residual from the tidal analysis was found still to contain some tidal signal and remained energetic (reaching 10 cm/s).

A low pass filter is applied, which passes low frequency signals and reduces the amplitude of signals with frequencies higher than the cutoff frequency ($f_c = 24$hrs) (*Emery and Thomson,* 2001). The filter is a Fourier transform with a finite number of coefficients and specific interval frequency ($-f_c < f < f_c$), where components with amplitudes from frequencies bigger than the cutoff frequency can be eliminated by averaging them. Filter analysis can be used to build a filter to pass a specific frequency band or bands. Low pass filtering using Fourier transforms was originally proposed by Lanczos (1956).

Residuals from low pass filtering of the currents confirm that the MOW is flowing mainly to the North-West (Figure 2.10). At A1, the residual is towards the West. In all records, the current measured over the depth range has a uniform current profile direction slightly changing near the bottom. Also currents increase with water depth and are less close to the bottom. The filtered series reveal that the record starts with the ending of a strong signal of MOW (April 19th-20th). Three days later (April 23th-25th) the strongest MOW signal occurs, sooner on records from A4 and A5 (more clearly on the bottom records). The last MOW signal is detected around April 30th with a long duration (around 9 days). Strong MOW signal have a time lag of around one day between sites A3 to A1 and A5 to A4. Strong MOW events seem to start early on deeper (A4-A5) records, however high temperature on records seems to pass (Figure 2.10) site A1. Also, not all events of high temperature are happening during strong current events at all sites.

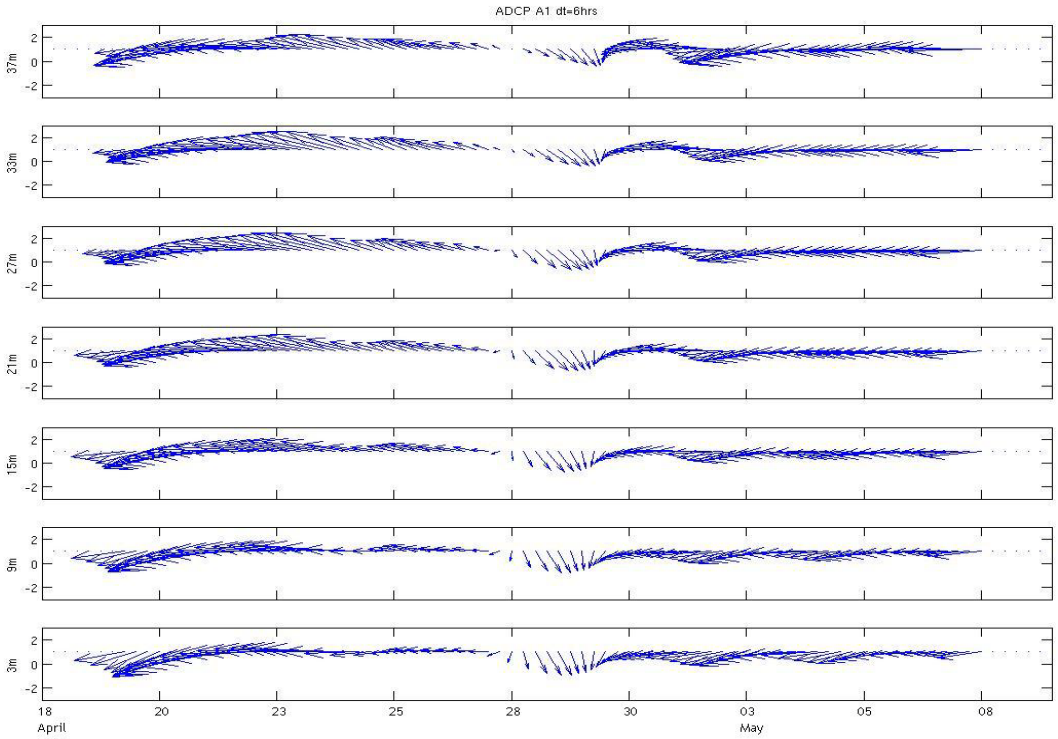

a)

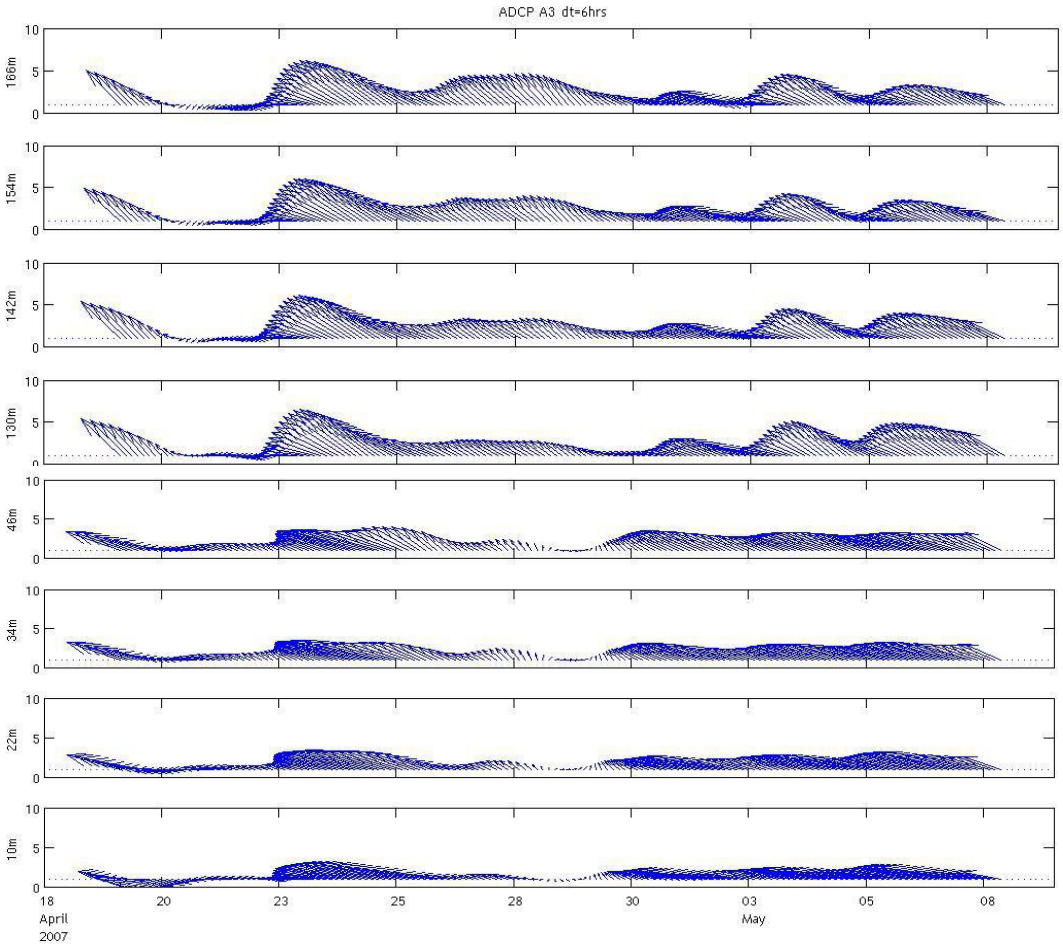

b)

Figure 2.10 Residuals (cm/s) from low pass filter applied to original ADCP time series are plotted as arrows at nominal depth above seabed (y-axis). Filter removes any signal below 24 hours period (i.e. high frequencies). A set of panels show nominal depths (metres) above seabed on the y-axes and each site has used different scale due to strength of the signal. Panels refer to a) A1, b) A3, c) A4 and d) A5.

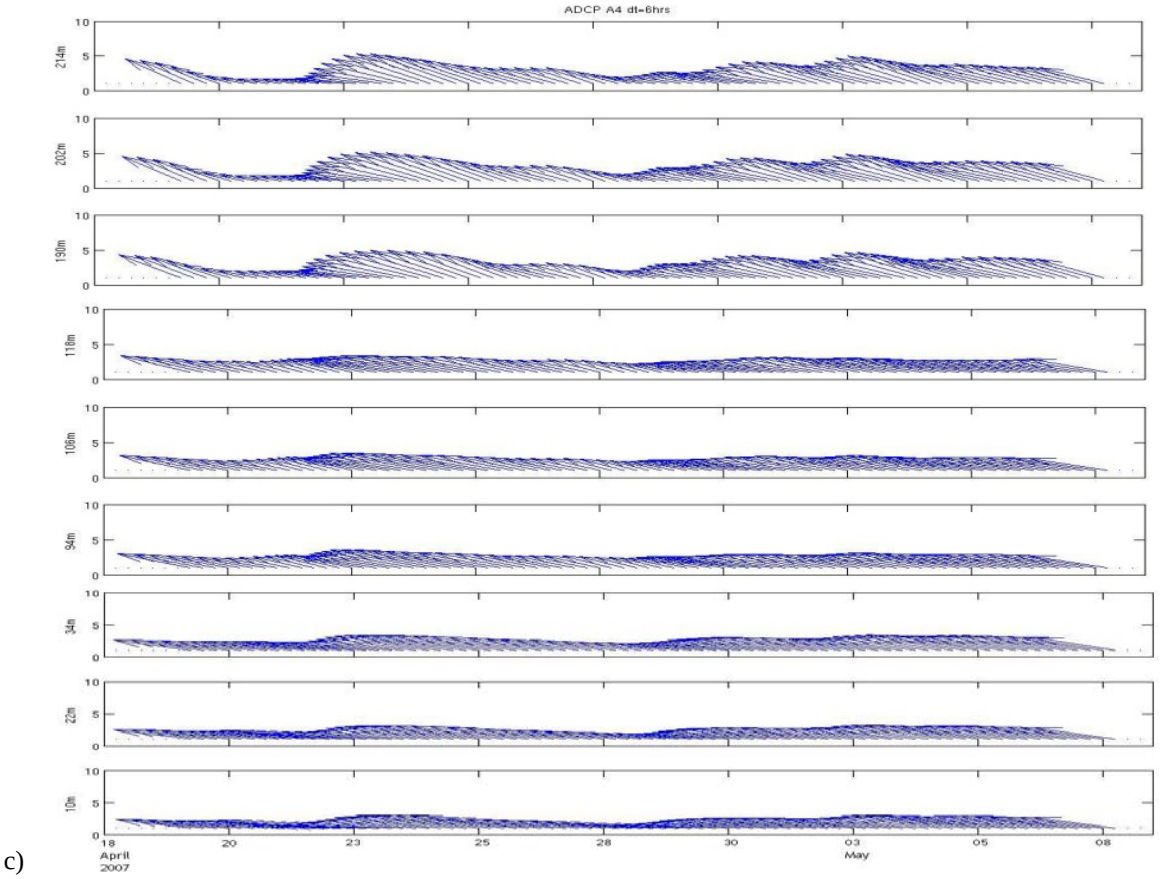

c)

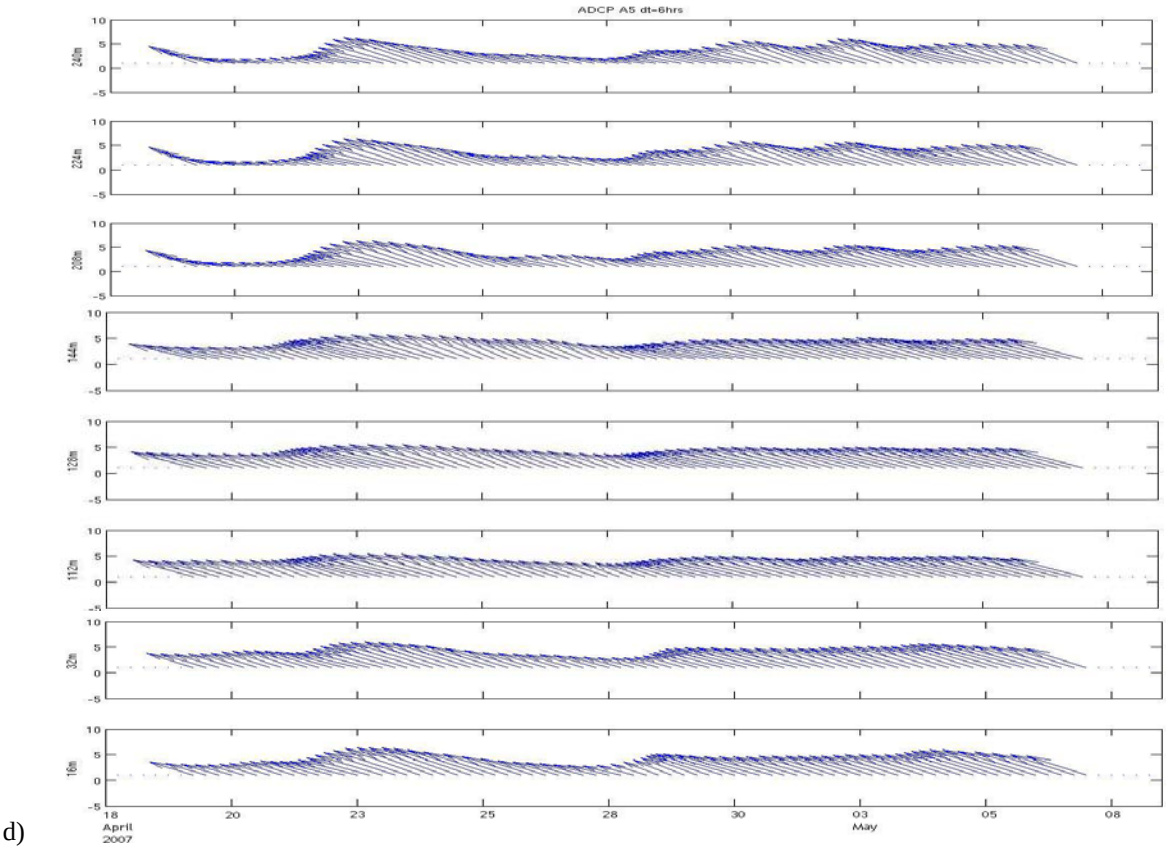

d)

Figure 2.10 Residuals (cm/s) from low pass filter applied to original ADCP time series are plotted as arrows at nominal depth above seabed (y-axis). Filter removes any signal below 24 hours period (i.e. high frequencies). A set of panels show nominal depths (metres) above seabed on the y-axes and each site has used different scale due to strength of the signal. Panels refer to a) A1, b) A3, c) A4 and d) A5.

2.3.4 Spectral analysis and GM spectrum

The present analysis transforms a discrete time series into a frequency domain using a Fourier transform. The limits of the Fourier transform are referred to the length (*N*) of the time series and it resolves frequencies over the frequency interval $-f_N \geq f_k \geq f_N$ (Nyquist frequency, $f_N = \frac{1}{2\Delta t}$). Smoothing is applied to the spectrum to highlight better statistics (but poorer frequency resolution), this smoothing is called a Hanning window (*Emery and Thomson*, 2001).

Spectra of vector time series were calculated using vector decomposition in rotary components, the current vector is represented using the complex quantity (*U(u,v) = u + iv, i* = √*-1*). For the positive angular frequency *σ* let the angular velocity ($w = \frac{2\pi n}{N\Delta t}$) be positive (*w = +σ, anticlockwise rotation*) or negative (*w = -σ, clockwise rotation*). The Fourier transform can be expressed as (*Gonella*, 1972):

$$U(w) = \frac{1}{N\Delta t}\int_0^{N\Delta t} U(t)\, e^{-iwt} dt = |U(w)|e^{i\theta_w} \qquad (2.3)$$

with $|U(w)|$ as the amplitude and θ_w phase at initial time of the complex quantity $U(w)$. In practice, *U(t)* is represented by sine and cosine Fourier coefficients corresponding to the angular frequency $\sigma = |w|$; and (2.3) is used to find the coefficients *U(w)*. Those *U(w)* coefficients are $|U_+|e^{i\theta_+}$ and $|U_-|e^{i\theta_-}$ (anticlockwise and clockwise, respectively). These coefficients have amplitudes $|U_+|, |U_-|$ and relative phases θ_+, θ_-. The combined vector from both contributions identifies an elliptical form shape (Emery and Thomson, 1998) with rotary components $S_- = |U_-|e^{i\theta_-}$ and $S_+ = |U_+|e^{i\theta_+}$.

Rotary components have been used to identify specific mechanisms. Inertial motions have clockwise rotation in the northern hemisphere. Wind stress effects as surface current can rotate similarly. At the bottom in shelf seas or over the continental slope, high energy clockwise spectrum can be found related to local circulation due to topography or pressure gradients (*Gonella*, 1972). Another factor is the difference in thickness between the clockwise and anti-clockwise boundary layer thickness, the cyclonic boundary layer is thinner so the full velocity exist closer to the bottom.

The Garrett-Munk spectrum (*Garrett and Munk*, 1972, 1975) is used as a description of the oceanic internal wave field, particularly in the deep ocean, and as a statistical description in studies of mixing parameterization (*Henyey et al*, 1986; *Polzin et al*, 1995). Energy from observed spectra is compared against the GM spectra, using two different GM spectra representations: Munk (1981) introduced a specific form of the GM spectrum used to compare with observations and Levine (2002) introduced a modification of the GM spectrum, considering changes between inertial and semi diurnal frequencies. The GM spectrum explained by Munk (1981) is usually called the continuum spectrum and describes the internal wave field in the deep open ocean. However, spectra of observations near the bottom and adjacent to rough topographies show energy peaks at tidal and inertial frequencies. This extra energy is not explained by the GM spectrum and has been a subject of discussion in recent years. Levine (2002) modified the spectrum in the tidal-inertial range using local values of inertial frequency, observed buoyancy frequency and measured kinetic energy, rather than the constant values as assumed in the GM continuum spectrum.

Figure (2.11) shows the depth-averaged spectrum at each site from the original current time series. The overall energy is high over the semidiurnal period; Semi-diurnal is strong at A5 where the inertial to diurnal frequencies energy is high or near-inertial frequency energy increased with depth. A1 has the highest energy at semidiurnal frequencies; this maybe related with the average A1 record being in shallowest water. At A1, A3, A4 and A5 the average depth of measurements is below 200m above seabed. Most of the measured spectrum has a clockwise rotation.

A comparison between the spectrum from the measurements and the GM spectrum is made, over a frequency range from inertial to M4 astronomical component frequencies (suggested here to avoid white noise). The GM spectrum (green line, Figure 2.11) slope (-2) modified by Levine (2002) is included here to compare spectrum energy with an observed level of energy for continental slopes (850 J m^3). A depth-averaged spectrum revealed a similar slope, only differing at A5 where the energy is found to be higher than GM slope. The reason to compare spectral energy with the GM spectral energy is that if the GM spectrum slope is not found then energy decay may be related with the production of turbulence. With tidal effects, it is known that a fraction of tidal current energy is used for turbulence production. However without tidal effects internal wave energy may be used for turbulence production.

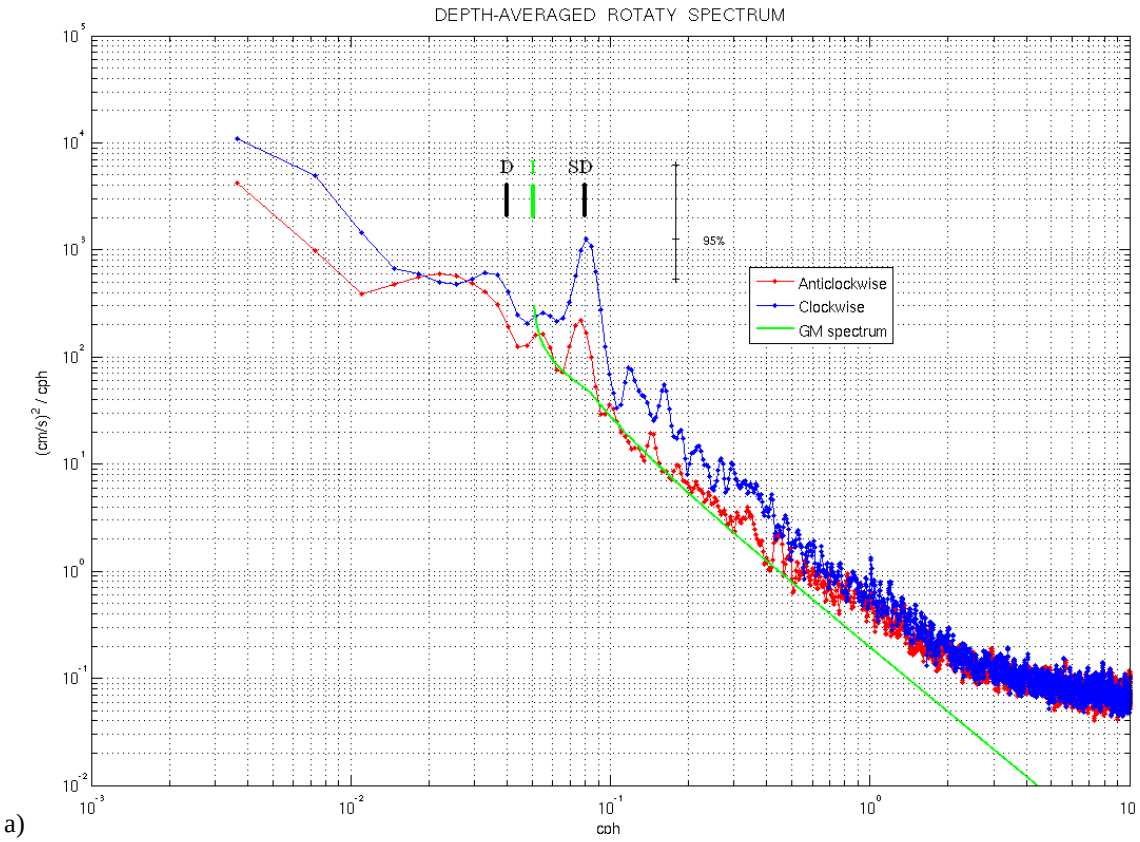

a)

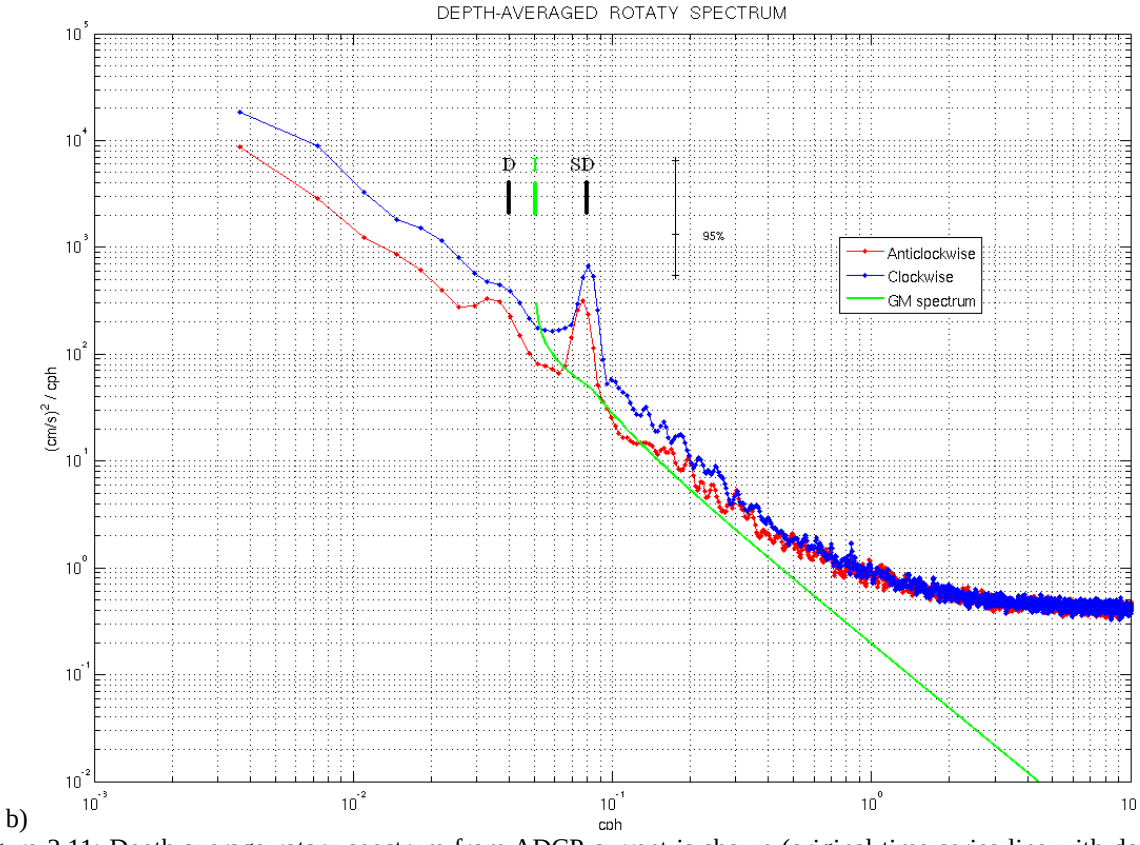

b)

Figure 2.11: Depth-average rotary spectrum from ADCP current is shown (original time series line with dots), with their rotary components (RED – anticlockwise and BLUE - clockwise). Confidence interval is calculated by using the Chi-square distribution at 95%. Also the GM spectrum modified by Levine (2002; green line) is used to compared with observations. Panels refer to a) A1, b) A3, c) A4 and d) A5.

c)

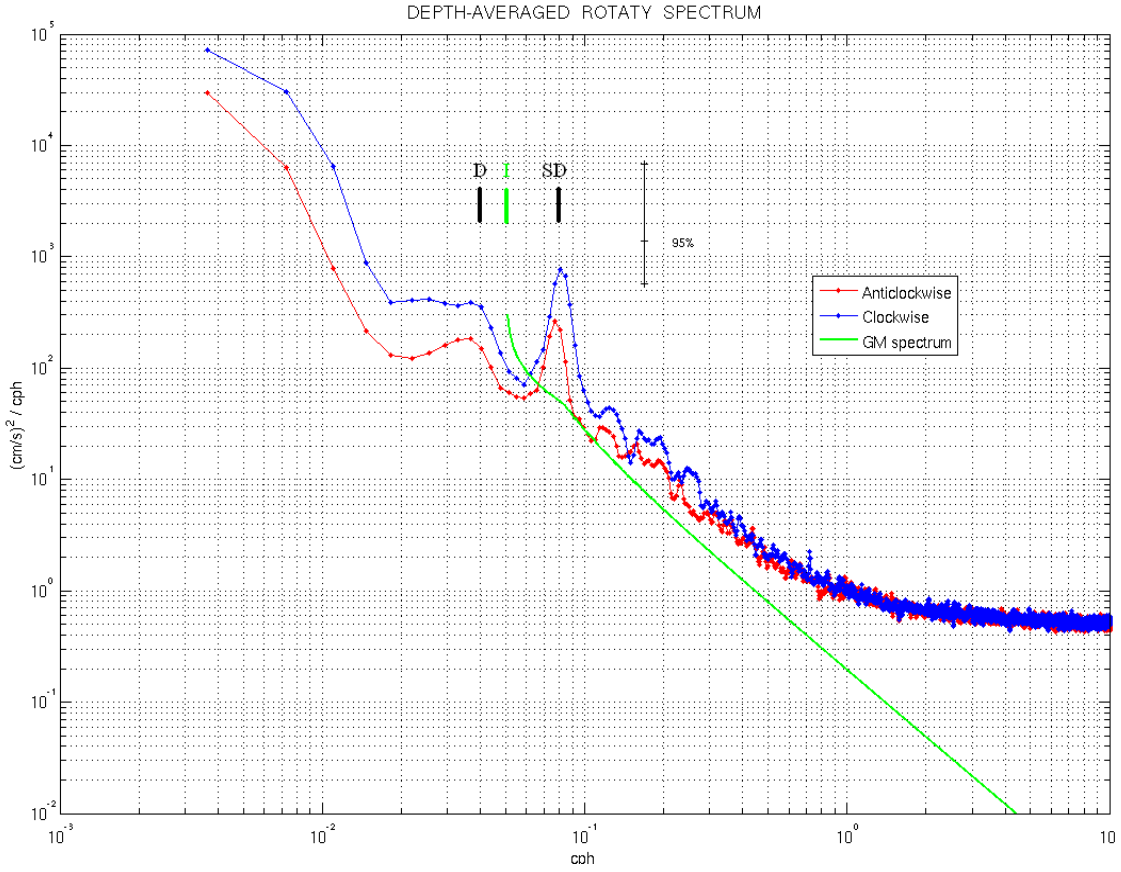

d)

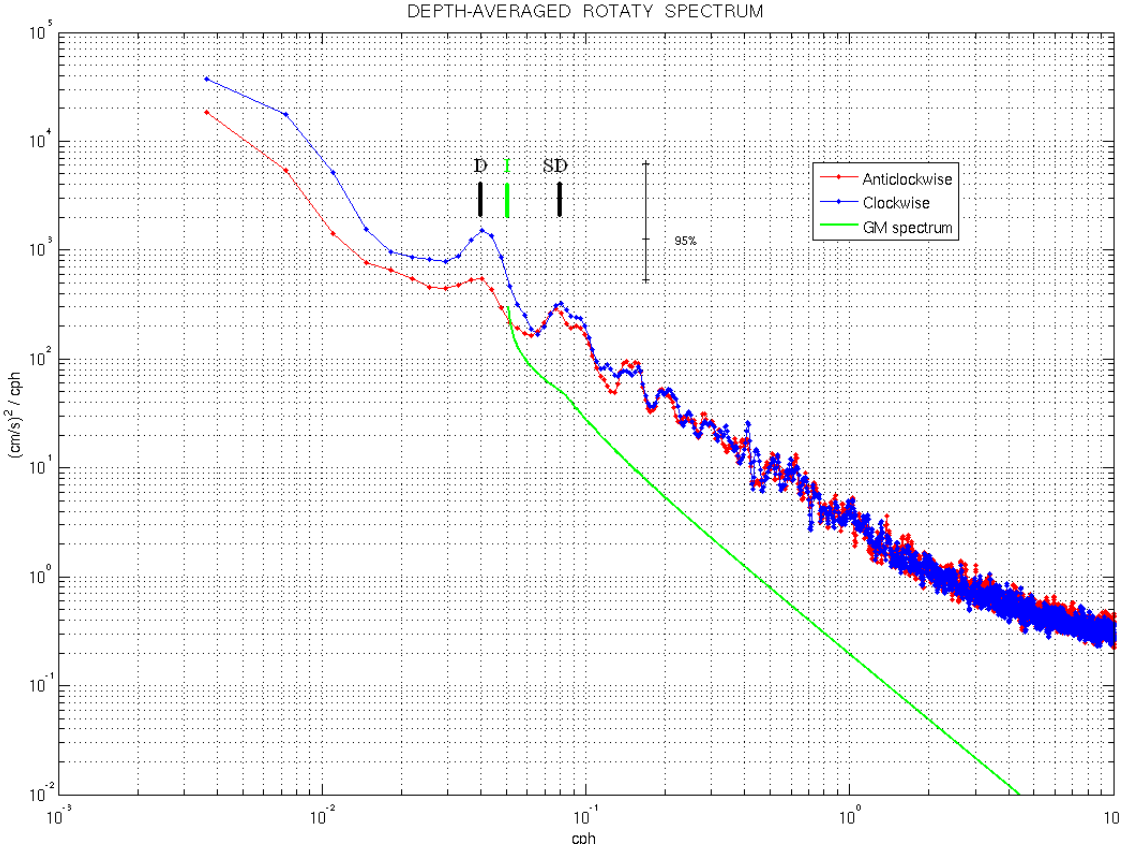

Figure 2.11: Depth-average rotary spectrum from ADCP current is shown (original time series line with dots), with their rotary components (RED – anticlockwise and BLUE - clockwise). Confidence interval is calculated by using the Chi-square distribution at 95%. Also the GM spectrum modified by Levine (2002; green line) is used to compared with observations. Panels refer to a) A1, b) A3, c) A4 and d) A5.

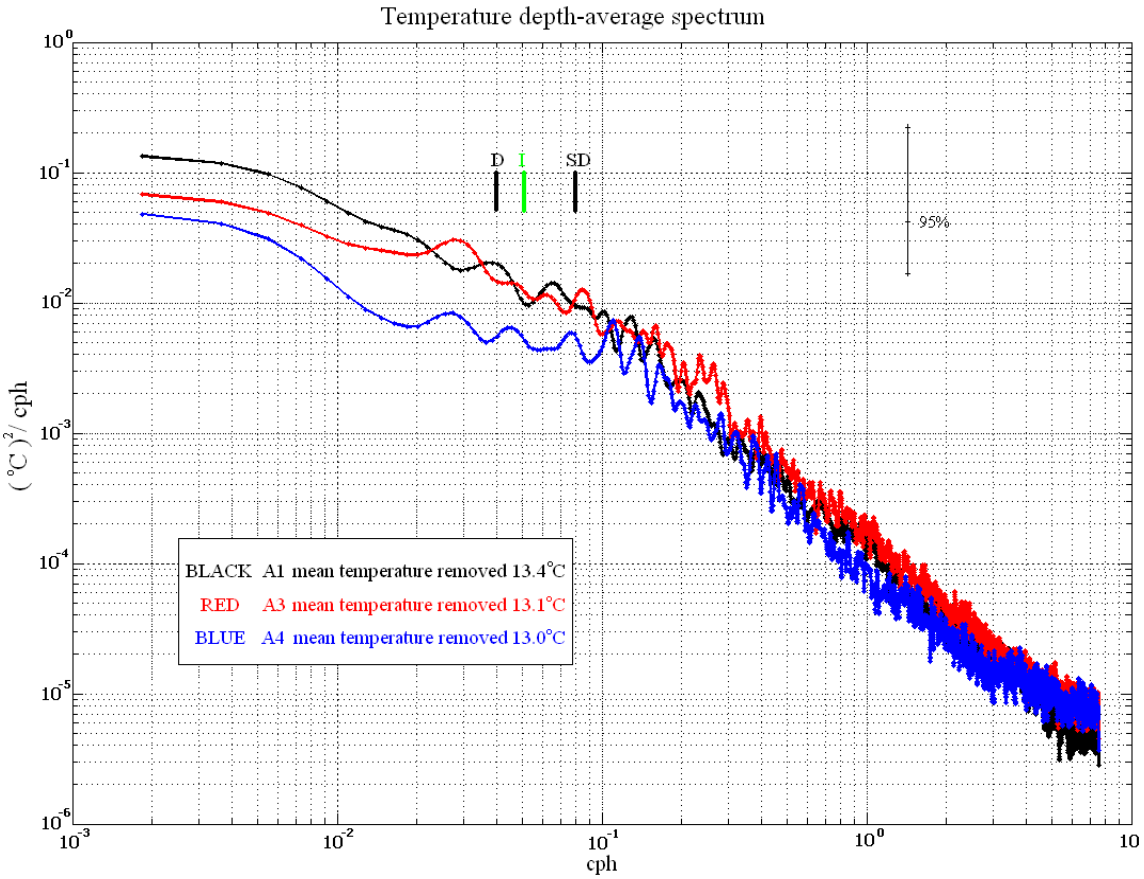

Figure 2.12: Depth-average spectra from Temperature time series are presented. Mean values had been removed from temperature records. Confidence interval is calculated by using the Chi-square distribution at 95%.

Temperature depth-average spectra were obtained as well (Figure 2.12). At A1, considerable energy is found at inertial and lower frequencies where the slope was around minus two (observed semidiurnal frequencies to high frequencies). At A3, energy can be identified around semidiurnal frequencies. And on A4, high energy is detected side of M3 astronomical component. In both A3 and A4, there is a spectrum with a slope of minus two over the same frequency range as observed in A1. A slope of minus two is related to the temperature being influenced by the internal wave field over the observed frequency range (inertial to M4, however this can be found down spectra to higher frequencies).

2.3.5 Internal wave characteristics

Internal wave characteristics are the slope of the plane of motion and of energy propagation. In practice internal wave is diagnosed using background stratification with latitudinal dependence. Baines (1973) use a relationship for mapping the internal wave over a frequency band ($f < w < N$), is expressed as follows:

$$c = \sqrt{\frac{(w^2 - f^2)}{(N^2 - w^2)}} \qquad (2.4)$$

where $N(s^{-1})$ is the buoyancy frequency ($N^2 = -\frac{g}{\rho}\frac{\partial \rho}{\partial z}$, g is the gravity constant; N is explained more extensively in chapters 3 and 4) and is used as a measure of stratification, $f(s^{-1})$ is the inertial frequency at the specific latitude and $w(s^{-1})$ is the wave frequency. Value *c* is the tangent of the angle (from horizontal) of internal tide motion. When an internal wave approaches a bottom with slope *γ*, an internal wave can be reflected and preserves its original frequency. Three reflection conditions can be identified using the ratio *γ/c*, if *N* is constant over the water column (*Cacchione,* 2002). A wave can be reflected travelling towards shallow regions (*γ/c < 1*, subcritical or transmissive), or reflected backwards or towards deep regions (*γ/c > 1,* supercritical or reflective); or wave energy can go to turbulence because the parallel bottom and internal wave motion gives strong motion (*γ/c = 1*, critical). The slope characteristics are used to inspect changes in stratification over the water column (*Cacchione,* 1974) by using the dominant M2 tidal frequency.

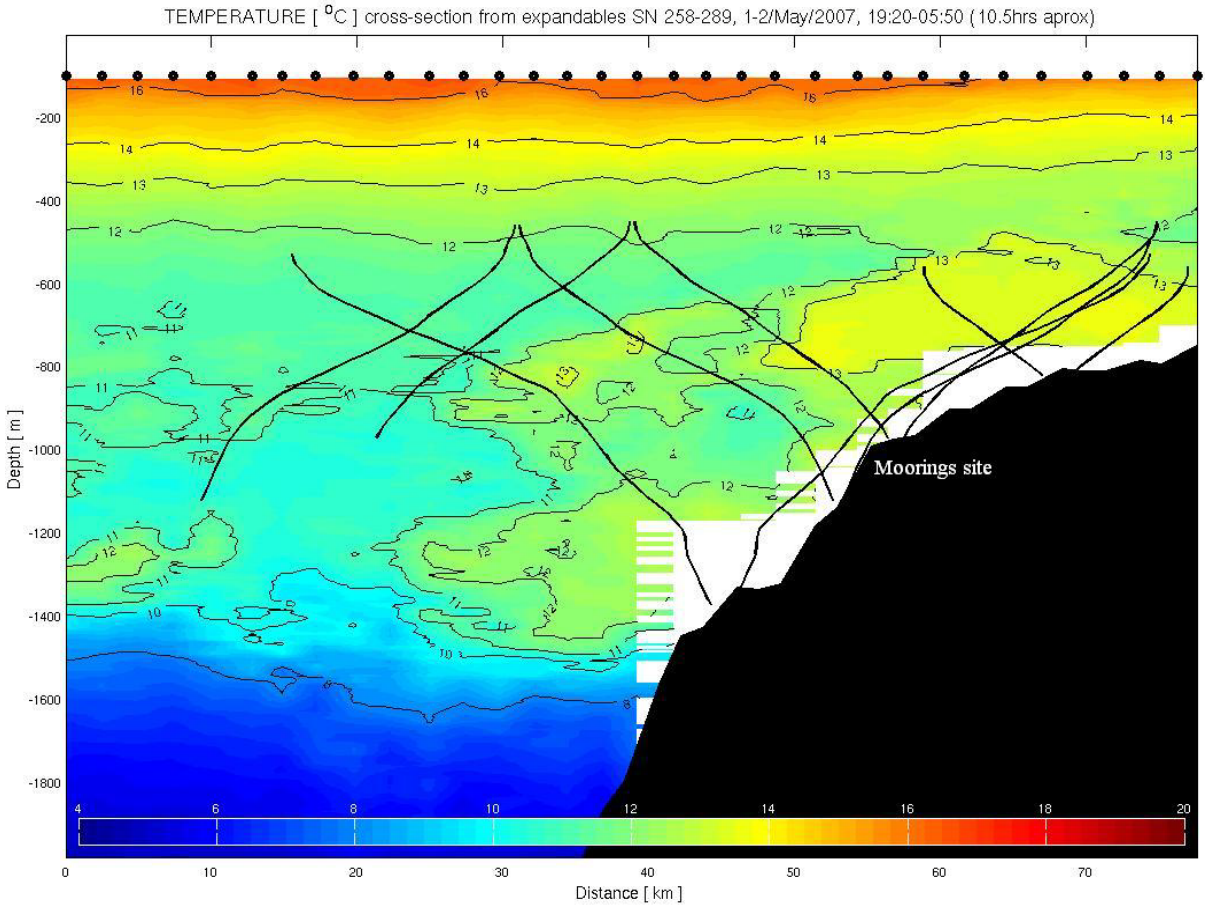

Figure 2.12: Internal wave characteristics rays (black lines) for the M2 internal tide plotted against temperature contours using background stratification from CTD casts. Note: Internal wave rays were plotted by using some profiles of N^2 but conditions for critical slope can be found along the continental slope at mid -depths and some rays were selected over the regions where moorings were deployed.

Figure (2.12) shows internal wave ray analysis for the M2 frequency. There is a critical slope at mid depths (900m-1200m), which have high bottom velocities and bottom shear stress for M2 tides. There is a subcritical slope in shallower waters (< 900m) which suggests that energy may propagate onto the Continental Shelf. In deeper waters or down slope (>1300m, where lower MOW and NACW is located), there is a supercritical condition (waves reflected), but which is confined to a small region and confirmed from a few measurements of stratification below 1800m. The critical slope was detected where strong tidal (M2) currents (> 0.05 m/s, at A3 and A4) run alongside the steep topography.

2.4 Discussion

The presence of MOW shows in the data. MOW travels along and down the slope and before arriving at the West sections (hydrographical measurements from SEMANE program) increases its volume around ten times with diluted salinity (S >36), consistent with salinity found in the GO project. From volume fluxes and confirmed by current measurement near to the West cross section, most of the water mass (salt) which comes from the East side (Gibraltar Strait) is lost from the West confirming the travelling path suggested in the literature.

When the MOW signal is penetrating into the deeper regions can be contained in cores or meddies, and is surrounded by NACW still reveals a distinctive water mass composition. The water mass signal (T-S diagrams) reveals spreading along isopycnals, as well as diapycnal mixing. Inside the MOW, water masses variability can be large as shown in the interannual variability from records.

MOW currents preferentially are directed along slope rather than penetrating down slope into the Atlantic. Measured currents inside the MOW were strong. There is a strong tidal influence near the bottom. In comparison with the pressure records, mostly current and also some signals in temperature records also suggest MOW signal is locally modulated by tides.

Tides are present inside the MOW and M2 is the strongest tidal constituent. Results suggest that M2 could affect the whole MOW layer and probably nearby NACW. However results from Harmonic analysis showed that tides only decrease and increase the MOW flow speed within the water column (or reverse the MOW flow to West and North-West). The

internal wave field is highly active, as shown by comparison with the GM spectrum, which means not only that the semidiurnal tide is energetic but also the rest of the spectrum from tidal and inertial forcings.

Results from current measurements when MOW signal increase in speed were compared with observed current from some time series study over the Gulf of Cadiz. Grundlingh *et al* (1981) reported MOW signals where increases in temperature on some occasions are accompanied by an increase of current speed [because of the length (~3 days) of their time series they did not see spring-neap effect].

2.5 Summary

In spring 2007 during the Geophysical Oceanography experiment, Current Profiler landers and temperature minilogger moorings were deployed accompanied by water mass measurements in the Gulf of Cadiz. Also an historical source of water mass properties was available from the SEMANE programme. MOW and NACW were analysed and their presence quantified. Currents and temperature records were analysed using basic statistics and their time series correlation as well as spectral and Tidal (Harmonic) analysis. Time series are mainly inside MOW, which has high speed (40 cm/s) during some strong outflow events and a preferential direction to the North-West (West in the shallowest record). Current time series showed tides with a dominant M2 component. Temperature time series showed significant tidal influence. Currents and Temperature were found to be correlated (A3, A4 and A5, not A1) at semidiurnal frequency. Water masses properties and their variability are not completely explained here; the next chapter will provide more about water mass properties focusing on the MOW structure and stratification.

Chapter 3 Intrusions and Temperature-Salinity relation

3.1 Introduction

In the present chapter, we investigate the water mass variability in the MOW. MOW has a loose temperature-salinity signal, and every MOW trace has a slightly different pattern in the Salinity-Temperature diagram (see Chapter 2). The main reason for a loose relationship is due to the varying amount of salt in the MOW, during its spreading along the continental slope (westward).

Interleaving of salinity and temperature takes place in the MOW vertical structure. Temperature and Salinity diagrams were plotted with isopycnals referred to a preferred depth (pressure). Potential density needs to be quantified carefully and referred to the local pressure to avoid misinterpretation (in literature not always corrected *Ambar, et al* 2008).

The aim of the present chapter is to study the water column in the Gulf of Cadiz using available data sources. However there is another problem to target in the research: the few sources of CTD data and extensive temperature profiles (XBTs). The objective is to construct salinity from temperature profiles in order to look at water masses and profiles fine structure. Here ways are explored to infer the salinity to then exploit the XBT data further.

3.2 TS relation in the Gulf of Cadiz, stability and instabilities

Temperature and Salinity structure through the water column is the key point of the present research. Figure (3.1) shows the temperature from 12 CTD casts from the GO experiment taken along the GC continental slope (less than 2000m depth). Inside the MOW, temperature variability can be found with the presence of interleavings, some of them are well defined as MOW cores or Meddies in water-mass structure, and others occupy small depth ranges (< 10m). Above and below the MOW layer, the NACW layer can be observed without the presence of salinity or temperature interleavings; the temperature decreases downwards gradually. Temperature can be found without variability (no interleavings), inside the MOW in the middle of cores or Meddies, or in between cores or Meddies.

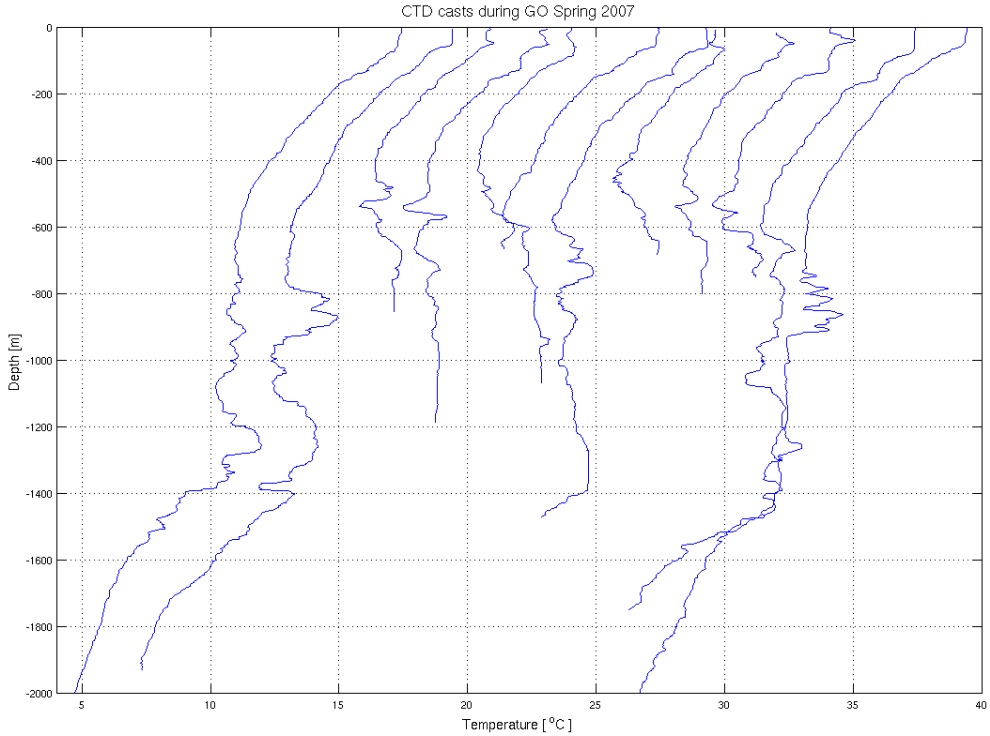

Figure 3.1: Temperature profiles from 12 CTD casts available from the GO experiment. Profiles were plotted displaced two units from each other, starting with the profile at the left hand side.

Salinity profiles shown in figure (3.2) from the same CTD casts in the GO experiment can be found with interleavings similar to those in temperature profiles. MOW cores or Meddies structure can be highlighted more by using the salinity profiles.

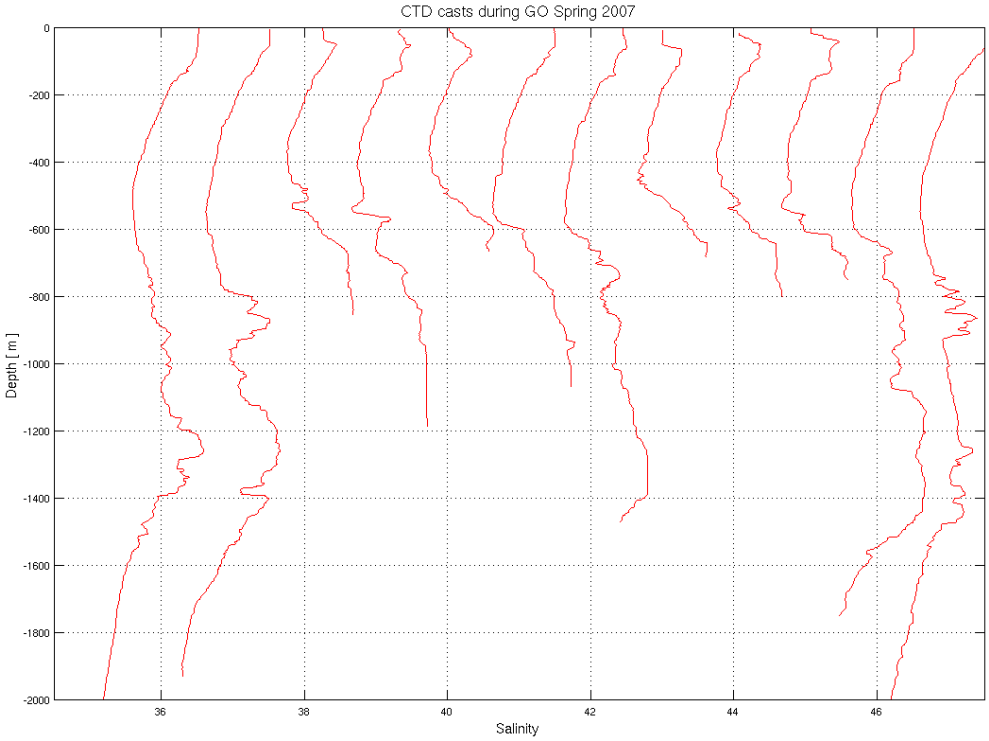

Figure 3.2: Salinity profiles from 12 CTD casts available from the GO experiment. Profiles were plotted displaced two units from each other, starting with the profile at the left hand side.

MOW cores or Meddies, visualised from temperature and salinity profiles, can be present and both contributions define the water mass structure. Both contributions have the same behaviour inside the MOW interleavings: when temperature decreases downwards, salinity does as well, and when temperature increases downwards salinity does as well.

Potential density (ρ) can be calculated (*UNESCO formulas, CSIRO software for MATLAB 1992*) using a pressure reference of 1000 decibar. The main reason for choosing 1000 decibar reference was the presence of large depth range sections of density instabilities [where salinity and temperature have a loose relationship]. The miss interpretation of potential density calculation is due to the nonlinear terms in the equation of state for potential density which tends under estimate density increments downwards. Also equation cannot solve density calculation from distant points giving some reference of instability and it is necessary to calculate potential density at local pressure (CSIRO software manual). Figure (3.3) shows the potential density profiles with the expected increase in density with depth. MOW cores or Meddy structure cannot be easily identified from the potential density.

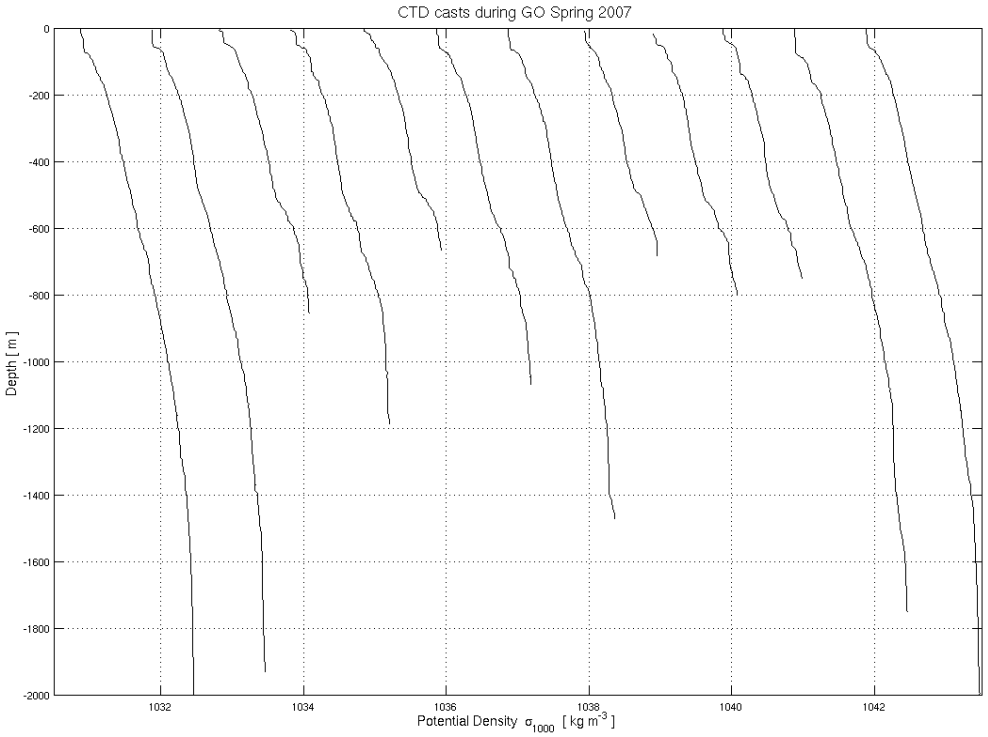

Figure 3.3: Potential density profiles referred to 1000db pressure, from 12 CTD casts available from the GO experiment. Profiles were plotted displaced a unit from each other, starting with the profile at the left hand side.

Stratification or potential density gradient vertical variability can be diagnosed in figure (3.4) from the squared buoyancy frequency ($N^2 = -\frac{g}{\rho}\frac{\partial \rho}{\partial z}$, g is the gravity constant).

Rapid changes in buoyancy frequency (on a scale of 10m) can be observed throughout the water column and particularly around the depth (400m – 1500m) where MOW is located; N^2 is more variable in MOW than in NACW.

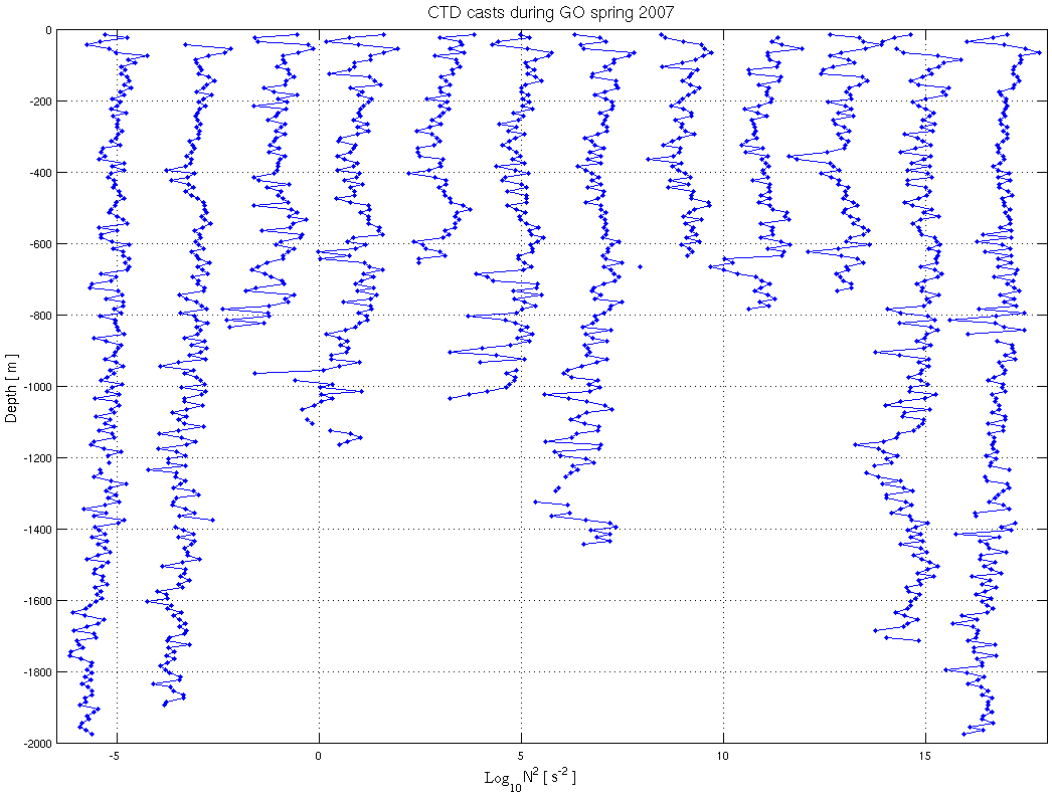

Figure 3.4: Squared buoyancy frequency ($Log_{10}\ N^2$) from 12 CTD casts available from the GO experiment, using a potential density gradient calculated from potential density differences over 10m. Profiles were plotted displaced two units from each other, starting with the profile at the left hand side.

The squared buoyancy frequency is also estimated (Figure 3.5) by using a depth-range 320db to provide a smooth profile (see Chapter 4 for more discussion). Stratification over the outer slope region (>1500m) decreases monotonically from the surface to the NACW layer. However, stratification increases on the upper interface of MOW and NACW, and then stratification continues decreasing (but not uniformly) inside the MOW [500m to 1500m depth]. In the bottom interface of MOW and NACW stratification increases again. In the mid slope, a similar behaviour is found in comparison with the outer slope from the surface to the NACW layer, at the top MOW-NACW interface stratification increases, and then decreases inside the MOW, but in the present case stratification decreases uniformly. On the shelf, stratification shows similar behaviour from surface to bottom; again at the top MOW-NACW interface the stratification has an increase. MOW signals can differ from one to another (as seen in chapter 2 with SEMANE inter-annual sections) and the temperature and salinity with a loose relationship can have sometimes a stable and sometimes an unstable profile. To

evaluate stratification, other sources of water structure information will be studied, using the more extensive XBT temperature profiles.

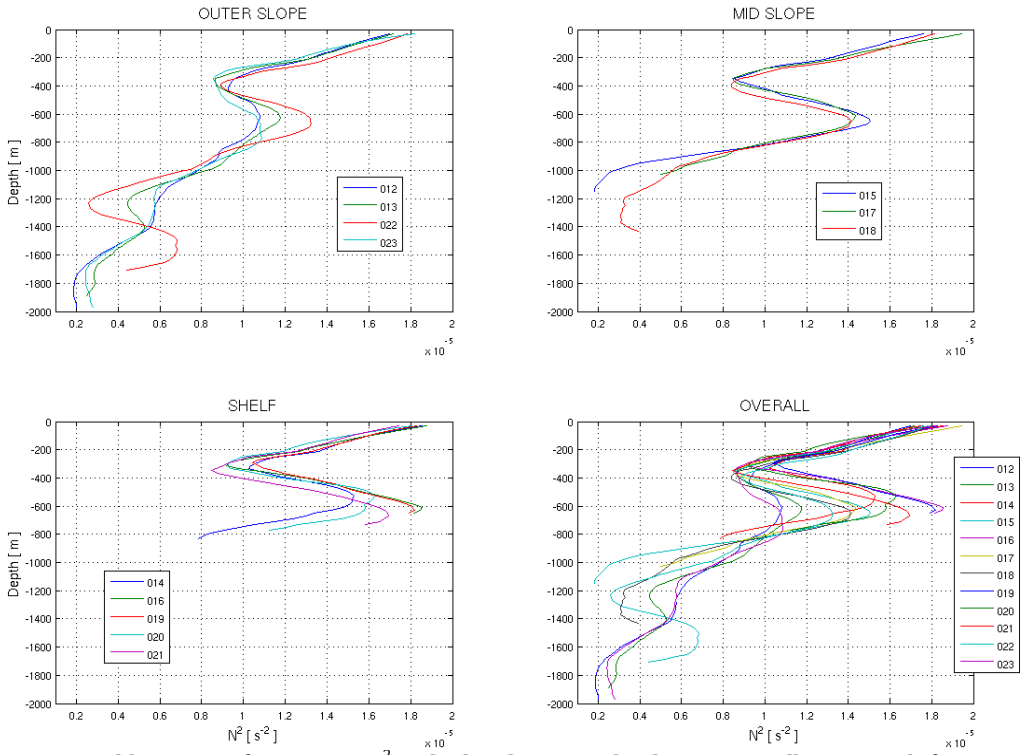

Figure 3.5: Squared buoyancy frequency (N^2) calculated using a depth range 320db to smooth for 12 CTD casts available from the GO experiment. Profiles were plotted using different depth regions. (TOP LEFT outer slope, TOP RIGHT mid slope, BOTTOM LEFT shelf and BOTTOM RIGHT overall over the continental slope.

Over the large scale (185km x 105km x 2 km depth) of the Gulf of Cadiz, the salinity and temperature reveal the stratification. However, due to the loose nature of the MOW temperature-salinity no steady relationship could be found. The next point to discuss will be density stability or instability inside the MOW and how salinity and temperature behave in the MOW cores or Meddies.

During the same period that the CTD casts were taken, there was a more detailed sampling of temperature profiles (XBTs), providing a unique snapshot of the MOW undercurrent. Figure (3.6) shows a series of cross sections from temperature profiles taken in the Gulf of Cadiz; in 24 hours, five cross sections were made. Other cross sections (Chapter 2, SEMANE program) reveal a MOW signal passing through the selected area. Accompanying the present set of temperature profiles (61 XBTs), other cross section data were available (in total around 500 probes were taken during the GO experiment).

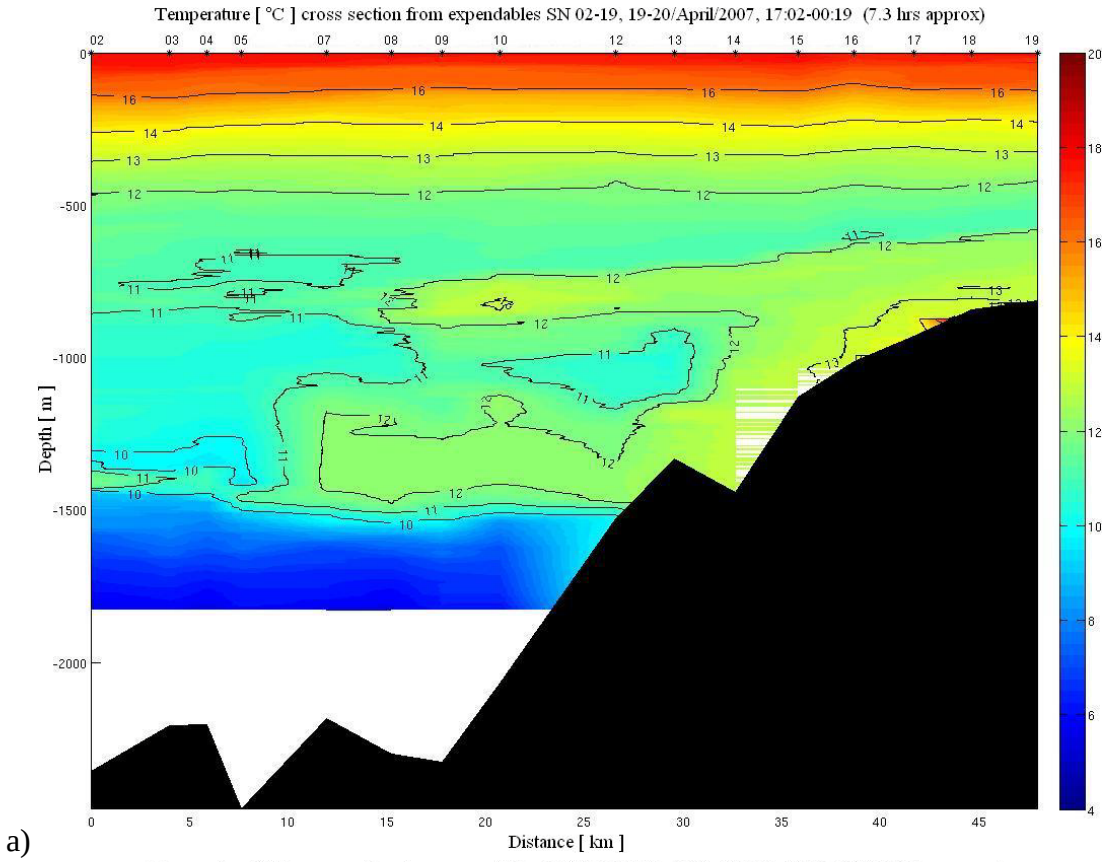

a)

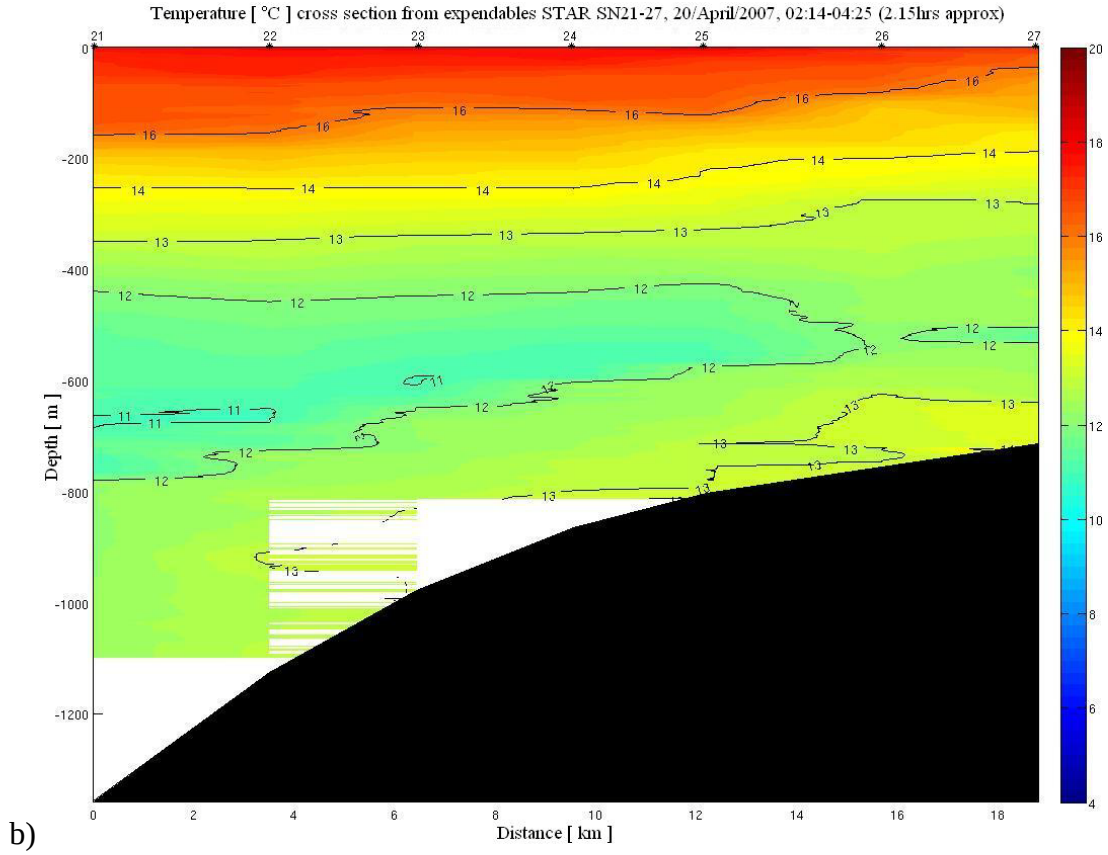

b)

Figure 3.6: Temperature cross sections from XBT profiles taken during a day in the GO experiment over the GC. a) first temperature cross section, b) second temperature cross section, c) third temperature cross section, d) fourth temperature cross section and e) fifth temperature cross section. Sketching map where data acquisition took place is Figure 2.4 - Chapter 2. Gaps between temperature measurements from XBT resolution which are used to provided more data for the water column.

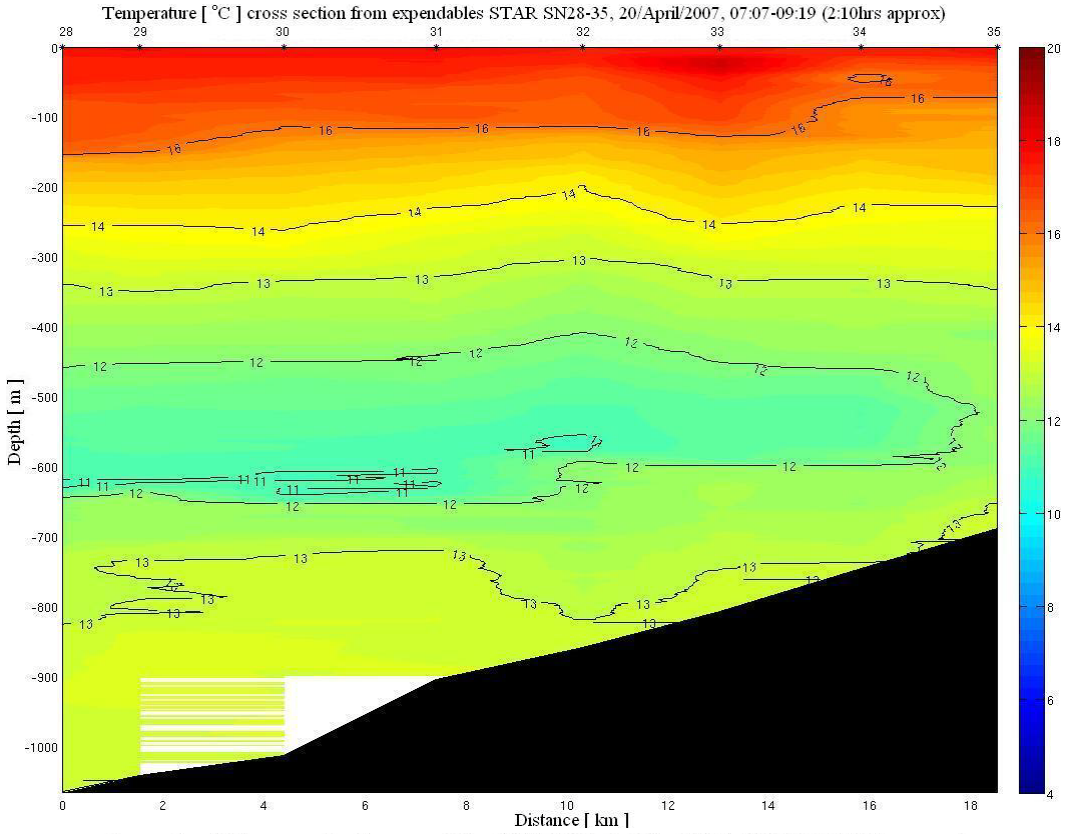

c)

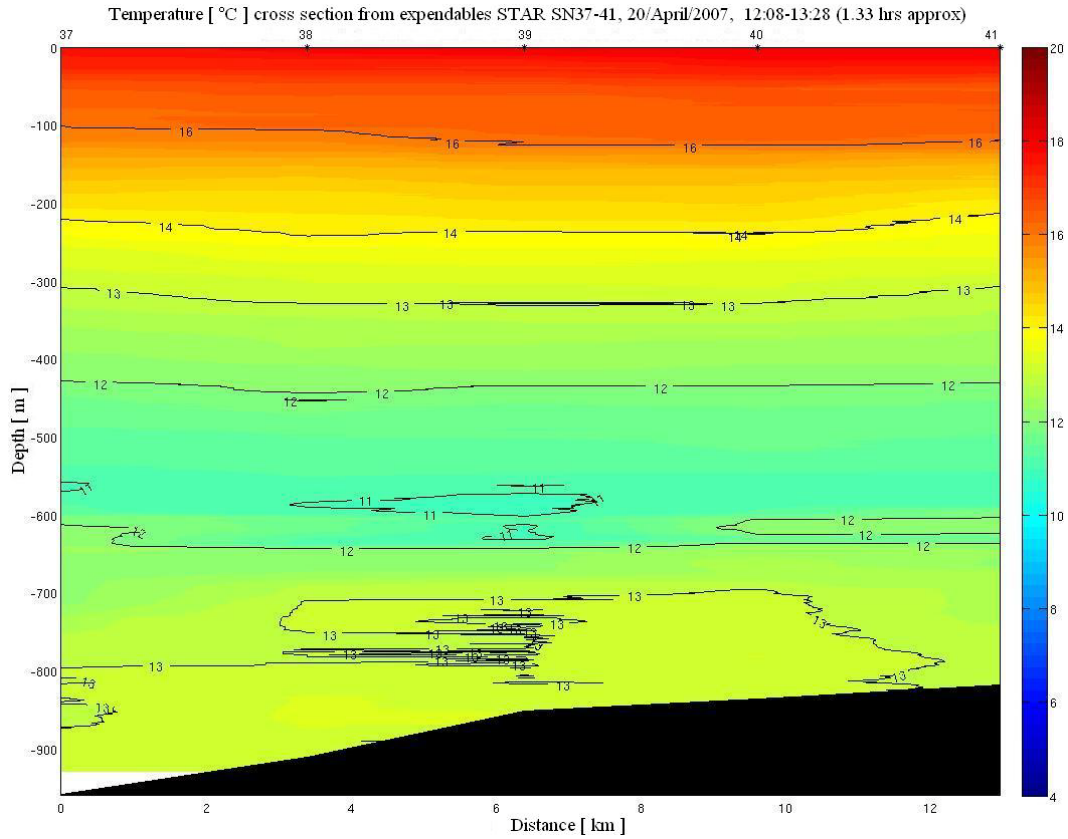

d)

Figure 3.6: Temperature cross sections from XBT profiles taken during a day in the GO experiment over the GC. a) first temperature cross section, b) second temperature cross section, c) third temperature cross section, d) fourth temperature cross section and e) fifth temperature cross section. Sketching map where data acquisition took place is Figure 2.4 - Chapter 2. Gaps between temperature measurements from XBT resolution which are used to provided more data for the water column.

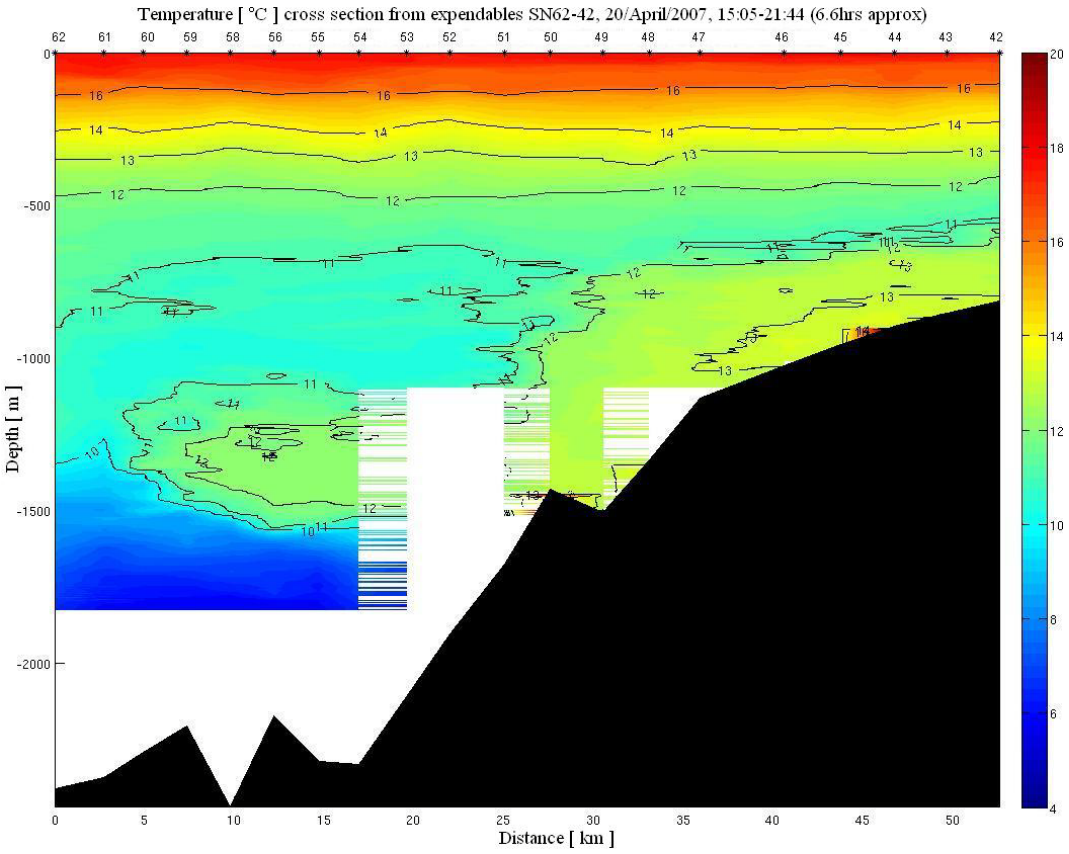

e)

Figure 3.6: Temperature cross sections from XBT profiles taken during a day in the GO experiment over the GC. a) first temperature cross section, b) second temperature cross section, c) third temperature cross section, d) fourth temperature cross section and e) fifth temperature cross section. Sketching map where data acquisition took place is Figure 2.4 - Chapter 2. Gaps between temperature measurements from XBT resolution which are used to provided more data for the water column.

3.3 Inferring salinity from temperature profiles

Käse *et al.* (1996) describe a method to infer salinity depth-by-depth, to associate with XBT profiles, using temperature and salinity differences between two or more CTD profiles. However, their emphasis was on lateral differences in density, in particular for dynamic computations (of geostrophic velocity). They state that their method is most appropriate where properties change smoothly and monotonically between the CTD stations, and that there should be no intrusions of water of different origin.

We have indeed found that intrusions can give problems with the Käse *et al.* (1996) approach. If the vertical gradient of temperature is atypically reversed, then the typical density ratio or temperature-salinity relation can imply a density inversion (static instability) where this is not in fact the case. This might not be important for dynamic computations from lateral density differences, but is important in relation to seismic imaging from spatial changes of density and sound speed, and for interests in inter-leaving and mixing.

At any one depth, two or more horizontally-separated CTD stations determine a relation between temperature and salinity: by linear interpolation if only two stations; by linear regression if three or more. The different temperatures and salinities at the CTD stations ought to span the range of values found in the XBT profiles where the method is applied. Then the inferred salinity S if the XBT profile temperature is T (at the given depth):

$$S = S_R + (T - T_R)\frac{\delta S}{\delta T} \qquad (3.1)$$

where S_R, T_R are from a reference CTD profile (most obviously the nearest) and $\delta S/\delta T$ is the slope of the temperature-salinity relation (interpolation or regression line).

If density is the main interest, the temperature-salinity relation and (3.1) have equivalents in terms of the density ratio

$$r = \frac{\alpha}{\beta}\frac{\delta T}{\delta S} \qquad (3.2)$$

where $\alpha = -\rho^{-1}\partial\rho/\partial T$ and $\beta = \rho^{-1}\partial\rho/\partial S$ are expansion coefficients for temperature and salinity. Here α and β are positive, hence r is positive if $\delta S/\delta T$ is positive, e.g. for varying proportions of warm, salty Mediterranean Water.

Käse *et al.* (1996) note restrictions: (a) no intrusions of distinct water of different origin in which r differs; (b) the CTD profiles should span a range of values sufficient for a robust estimate of r; (c) use of linearity – cabbeling effects must be unimportant. It is (a) which most concerns us here.

Figure 3.7 shows three successive XBT profiles spanning the upper Mediterranean Water in the Gulf of Cadiz, and an adjacent CTD profile. At 627 m depth, XBT profile 298 has a sharp temperature decrease downwards. The successive profiles strongly suggest that such occurrences are real although only forming a small minority of the profile. Otherwise, in 600-650 m, temperature in the profiles typically increases downwards, as the proportion of warm salty Mediterranean increases.

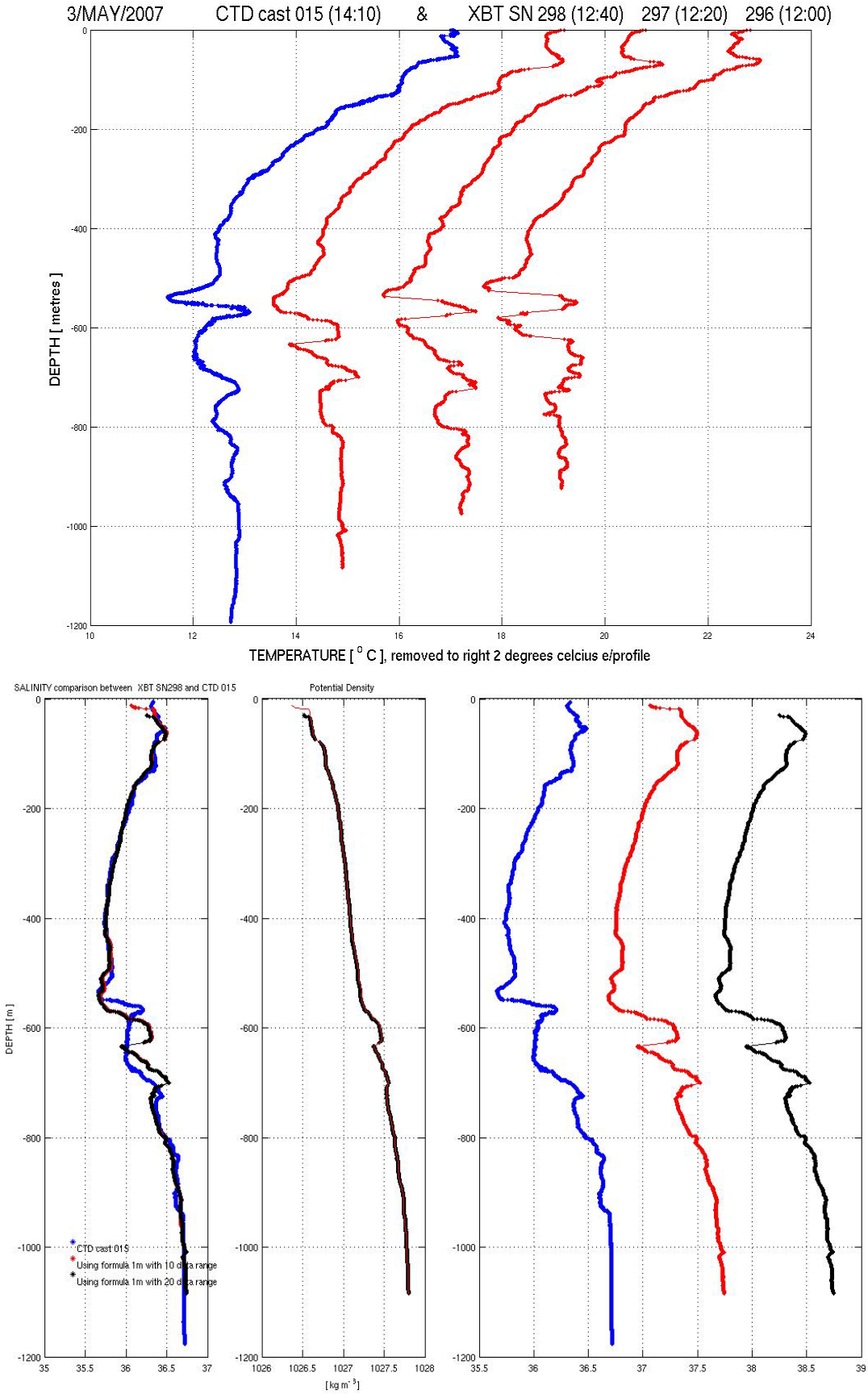

Figure 3.7: Successive XBT profiles and nearby CTD profile, Gulf of Cadiz, 3 May 2007. Upper panel – temperature; lower panel – salinity (LEFT) and potential density (CENTRE) for CTD (blue) and XBT 298 [inferred (RIGHT); 10 m (red) and 20 m (black) depth intervals to estimate $\delta S/\delta T$].

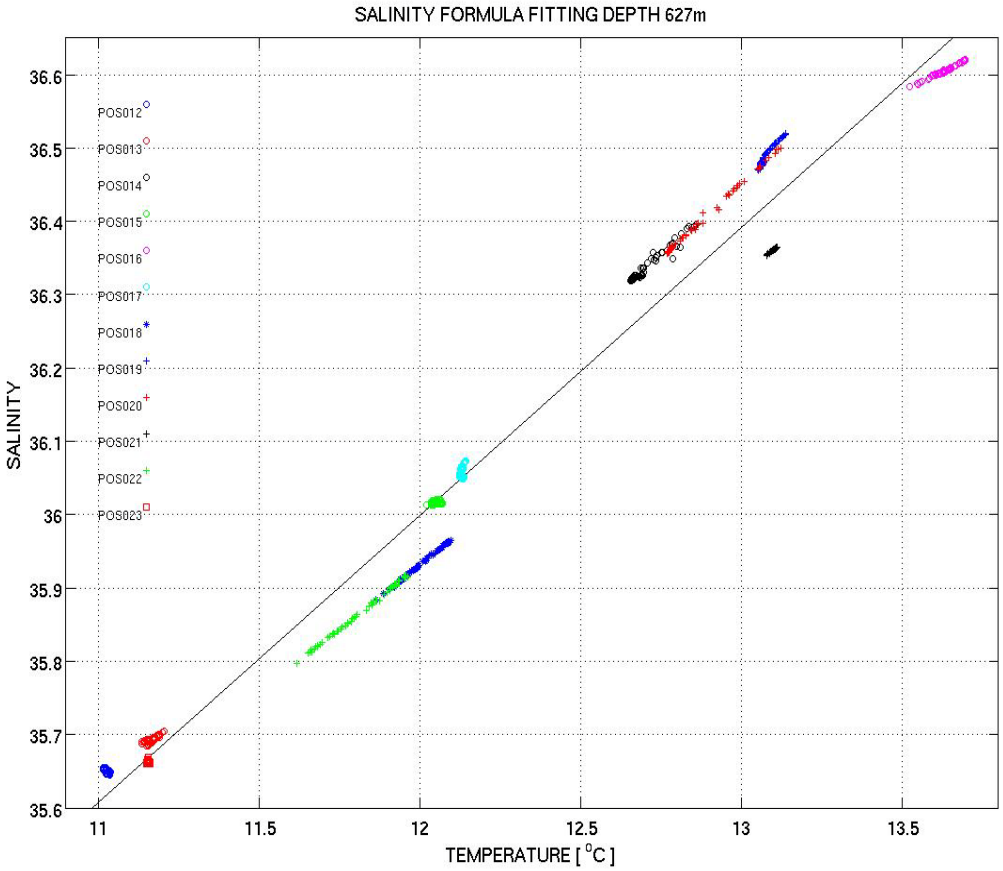

Figure 3.8: Salinity and temperature from 12 CTD profiles, and best-fit regression line (slope $\delta S/\delta T$). The data shown are in a depth range 20 m centred on 627 m.

Correspondingly, salinity increases with increasing temperature – laterally and vertically – as is clear in figure 3.8. Here the best-fit regression line slope $\delta S/\delta T$ is clearly controlled by the separation between the different CTD profiles. This represents the *horizontal* variation as emphasised in Käse *et al.* (1996). Nevertheless, almost the same temperature-salinity slope shows in many individual CTD profiles in figure 3.8, notably those with the greatest spread of temperature and salinity. The spread of temperature and salinity in individual CTD profiles represents *vertical* variation in the short range about 627 m shown in figure 3.8. On the basis that the majority of the vertical profiles are statically stable, this (common) slope corresponds to $r < 1$.

Thus application of (equation 3.1) to XBT profile 298 near 627 m depth implies a sharp decrease of salinity downwards, matching the temperature decrease, as shown in figure 3.7. This is almost independent of the depth interval (10 m or 20 m) used to estimate $\delta S/\delta T$. Because $r < 1$, the salinity decrease suffices to introduce a density inversion (static instability; figure 3.7).

This inversion is spurious. In the depth range of figure 3.8, CTD profiles POS015 (shown), POS013 and POS016 (not shown) are those in which temperature decreases with depth. The temperature-salinity slope in these individual profiles is noticeably different; their individual *vertical* variation has $r > 1$. Hence, where XBT temperature decreases downwards, inferring salinity by (3.1) with $\delta S/\delta T$ dominated by (horizontal and vertical) variations with $r < 1$ is not appropriate; it imposes $r < 1$ and static instability on the vertical profile. Instead, the *vertical* variation should be based on CTD profiles where temperature likewise decreases downwards (and typically has $r > 1$ for static stability). This is the basis of our approaches as follows.

3.4 Different approaches for inferring salinity

The essence is to separate profile segments where temperature decreases downwards from those where temperature increases downwards. Using figure 3.8 as an illustration, we separate the CTD profiles (POS013, 015, 016; "PD") where temperature decreases downwards from those (all the other profiles; "PI") where temperature increases downwards (in the small depth interval considered).

For temperature decreasing downwards, salinity is regressed against temperature using profiles PD jointly. The individual profile segments in PD are normalised by subtracting their individual means of temperature *T* and salinity *S*. Thereby all the profile segments are centred on the origin in the regression and only the slopes (equivalent to *r*) and lengths of the individual segments contribute to the outcome of the regression.

For temperature increasing downwards, salinity is likewise regressed against temperature using profiles PI jointly, again subtracting their individual means *T* and *S*.

We have distinct values of *r* or equivalently of $\delta S/\delta T$, for temperature decreasing downwards ($\delta S/\delta T_D$) and for temperature increasing downwards ($\delta S/\delta T_I$). The values of $\delta S/\delta T$ are themselves functions of depth with resolution according to the depth interval used for the regression. Then we increment salinity *S* according to the increment of temperature *T* in the XBT profile. Thus

$$S = S_{z_0} + \int_{T(z_0)}^{T(z)} \left[\left(\frac{\delta S}{\delta T_D} \right) \delta T_D + \left(\frac{\delta S}{\delta T_I} \right) \delta T_I \right] \qquad (3.3)$$

where

Z_0 is a reference depth to start the integration (as discussed below)

δT_D = 0 (if temperature increases downwards), δT (if temperature decreases downwards)

$\delta T_I = \delta T$ (if temperature increases downwards), 0 (if temperature decreases downwards)

δT is the increment of XBT temperature over the XBT depth increment δz.

The integration is best started at a depth *Z0* where the salinity variability is minimal (or at least the salinity is accurately determined by the temperature). Thus salinity is estimated by (3.3) at any other depth of the XBT profile.

The Gulf of Cadiz provides a good location to test these suggested approaches because (i) there are significant reversals of temperature gradient down the water column, especially at the top of the Mediterranean Water (where the problem of spurious density inversion was encountered), (ii) the salinity (and temperature) vary minimally at a depth of 400 m, below seasonal variability and above Mediterranean Water influence, and (iii) there is again a well-defined temperature-salinity line below the Mediterranean Water at 1700-2000 m depth. Any systematic error during the integration from 400 m to 1700/2000 m over testing conditions should be apparent in a discrepancy in the salinity at the end of the integration.

Accumulated errors in the estimated salinities derive from (3.3) and include the following. Error E_0 in S_{Z0} should be minimised by choice of a depth *Z0* where salinity has minimal variability or is determined accurately. Errors Δz in XBT recording of depth z result in mis-attribution of the recorded temperature and hence salinity to the wrong depth, hence errors $E_Z = \Delta z|\partial T/\partial z|, \Delta z|\partial S/\partial z|$ where the gradients are evaluated at the depth in question. Errors in XBT temperature are potentially significant, especially with the relatively coarse typical resolution 0.01°C. However, the cumulative contribution to the integral in (3.3) is limited, as follows. Suppose that $\delta S/\delta T$ were uniform and could therefore be taken outside the integral in (3.3). Then the cumulative error E_T due to the temperature increments is limited by the error in overall temperature difference ΔT between the ends of the integration range, i.e. the accuracy of the XBT temperature over this range. Hence $E_T = \Delta T\ \delta S/\delta T$. (The estimate would be greater in the unlikely event that variations in $\delta S/\delta T$ correlate with errors

in δT). Errors in $\delta S/\delta T_D$, $\delta S/\delta T_I$ can be estimated from the spread of the regression coefficients; they are multiplied by the respective increments δT so that the incremental errors E_r in the integral are δT (error in $\delta S/\delta T$).

If these contributions are independent, then the overall error variance is estimated as

$$E_0^2 + E_z^2 + E_T^2 + \sum E_r^2 = E_0^2 + \left(\Delta z \left|\frac{\partial S}{\partial z}\right|\right)^2 + \left(\Delta T \frac{\delta S}{\delta T}\right)^2 + \sum(\delta T)^2 \, var\left(\frac{\delta S}{\delta T} error\right) \qquad (3.4)$$

Evaluation depends on information derived from the particular XBT and CTD profiles used.

3.4.1 Salinity estimations with CTD test

The Selective Regression approach has been applied using 12 CTD profiles from the Gulf of Cadiz in May 2010. These 12 profiles were regarded as a test for the method (the salinity profile being known from the CTD data) using the other 11 profiles data to regress for $\delta S/\delta T$ at each depth. δS/δT was calculated at every metre in depth, using the CTD casts available resolved to 0.1 db (to provide enough data for the regression). Data from each profile were used over a range 20 m to -20 m relative to the depth in question. [Use of a depth range < 40 m will increase variability of the derived values $\delta S/\delta T$]. Within the 40 m depth range for the calculation, temperature in any one profile may decrease or increase downwards at different depths. Hence each 40 m depth range was divided into eight segments of 5m; these segments were classified as temperature increasing or decreasing downwards on the basis of their top-to-bottom temperature difference. These ranges (40 m, 5 m) strike a balance between desired fine resolution and stability of the derived $\delta S/\delta T$. [Due to rapid changes in gradients over the transition between NACW and MOW (400 m – 800 m depth), a reduced depth range (10 m to -10 m relative to the target depth, divided into eight segments of 2.5 m) was used for the regressions; the depth ranges 40 m, 20 m were chosen in relation to the average size of rapid changes in temperature gradients].

Figure 3.9 shows the resulting coefficients δS/δT when temperature is decreasing ($\delta S/\delta T_D$) and increasing ($\delta S/\delta T_I$) downwards. For stability, $\delta S/\delta T_D$ ($\delta S/\delta T_I$) should be less than (greater than) δS/δT for constant density. In the CTD casts, there are local density instabilities. To provide robust values for δS/δT a minimum number of CTD casts is required (four here), and sufficient depth range for each estimate (40m here).

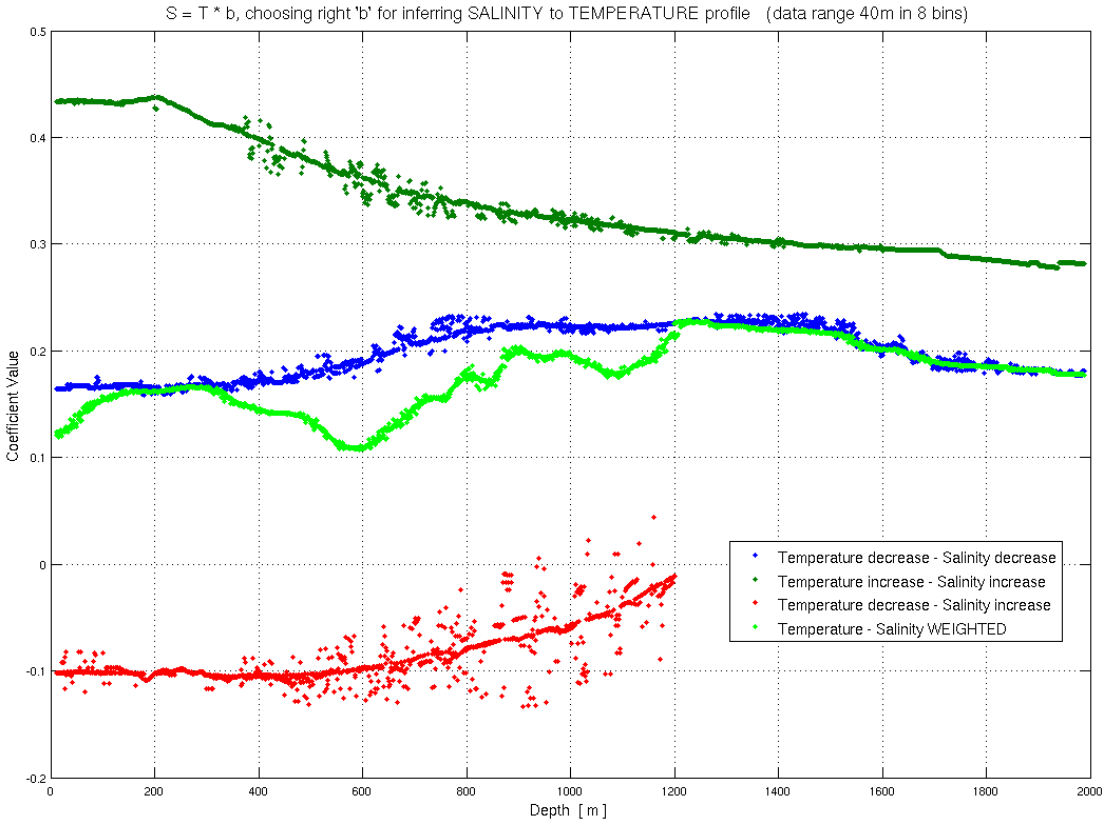

Figure 3.9: Coefficient values for $b = \frac{\delta S}{\delta T}$ (40m) using CTD casts and outliers removed (to provide a clear trend for this value). Light green data weighted from blue and red lines by number of occurrences.

The inferred profiles, obtained by integrating (3.3) down from 400 m depth after selective regression, gave a bias to low salinity with increasing depth (in tests on CTD casts where salinity is known). This bias was observed mainly at depths 400m to 800m, the transition region between NACW and MOW, especially where total water depth is greater off-shelf over the outer continental slope (Figure 3.10). This bias was a surprise for a method considered potentially deficient in having built-in stability. However, the MOW is salty and warm and interleaves with the NACW in the transition region (Ambar *et al*, 2008), but heat is much more diffusive than salt. Hence there are small depth intervals in many profiles where temperature may decrease downwards but salinity increases downwards. This is not allowed for by the procedure with two regression coefficients $\delta S/\delta T_D$, $\delta S/\delta T_I$; both represent compensating temperature and salinity influences on density. Hence downward increases of salinity, where temperature decreases downwards, cause the true profile to have greater salinity at depth than the profile inferred from (3.3).

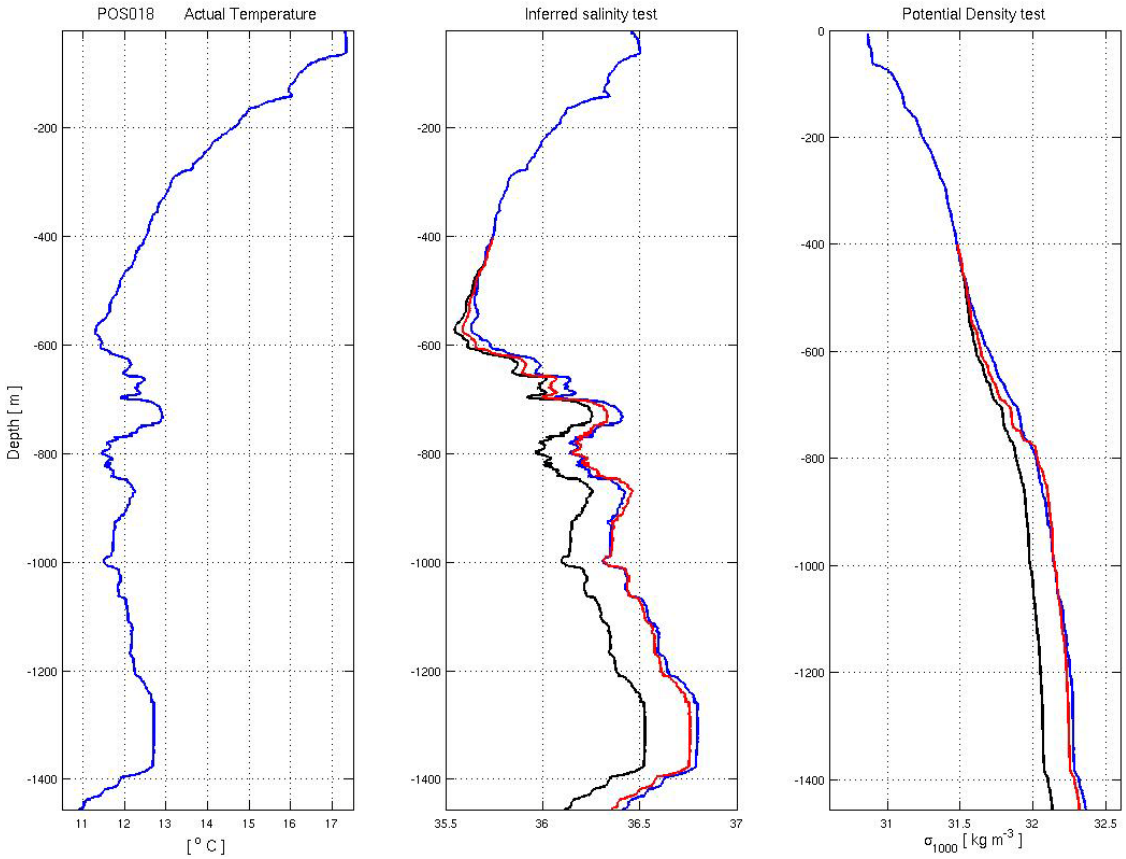

Figure 3.10. CTD cast POS018 temperature, salinity and potential density (in left, centre, right panels respectively). Blue line – as measured. Black – salinity inferred using $\delta S/\delta T_D$, $\delta S/\delta T_I$ only. Red – salinity inferred using also $\delta S/\delta T_D{}^+$.

A coefficient $\delta S/\delta T_D{}^+$, for temperature decreasing downwards with salinity increasing downwards, can be obtained in (40 m) depth ranges where CTD profile (5 m) sub-ranges have these trends in sufficient numbers for regression. Figure 3.9 shows many such depths (between 400m to 1200m) where $\delta S/\delta T_D{}^+$ has been calculated on this basis. However, $\delta S/\delta T_D{}^+$ cannot be calculated continuously through depth. All of the CTD profiles show some cases of $\delta S/\delta T_D{}^+$ between 400m and 800m, depending on their location over the continental slope. The depth range over which $\delta S/\delta T_D{}^+$ was found was about 150 m for the "continental shelf" (i.e. in total water depth < 1000 m, 5 CTD casts), 250 m for the "mid-slope" (total water depth between 1000 m and 1500 m, 3 CTD casts) and about 400 m for the "outer slope" (total water depth > 1500m, 4 CTD casts) approximately.

However, there is then a question of how or when to apply $\delta S/\delta T_D{}^+$ rather than $\delta S/\delta T_D$. Two approaches have been tried with some success in removing the bias, see Figure 3.10. (i) $\delta S/\delta T_D{}^+$ was applied when temperature decreased downwards and salinity increased downwards in CTD profile sub-ranges (2.5 m) comprising at least a quarter of the total with

temperature decreasing downwards (this is about the proportion in the overall water column; Figure 3.10). (ii) A weighted average of $\delta S/\delta T_D{}^+$ and $\delta S/\delta T_D$ was applied according to their respective number of occurrences in the CTD profiles' sub-ranges. The overall bias outcomes for (i) and (ii) are very similar (not shown). Although (i) and (ii) largely remove the bias to low salinity with depth, application of $\delta S/\delta T_D{}^+$ (even fractionally as in ii) results in a spurious large local density gradient, unless concident with temperature decreasing downwards and salinity increasing downwards in the actual profile. The application of (i) or (ii) gives errors in statistics of $\partial\rho/\partial z$. If finestructure statistics are the objective, case (ii) was found preferable (see section 3.5 Discussion).

To summarize the present diagnosis, three different approaches to the integration are:

- Case I. Using only $\frac{\delta S}{\delta T_D}$ and $\frac{\delta S}{\delta T_I}$ obtained when temperature and salinity both increase or both decrease downwards. This is the simple case
- Case II. Using $\frac{\delta S}{\delta T_I}$ when temperature increases downwards; when temperature decreases downwards, use (i) $\frac{\delta S}{\delta T_D^+}$ when the number of CTDs profile subranges with (temperature decreasing downwards and) salinity increasing downwards exceeds a threshold ratio (e.g. a quarter), and $\frac{\delta S}{\delta T_D}$ otherwise
- Case III. Using $\frac{\delta S}{\delta T_I}$ when temperature increases downwards; when temperature decreases downwards, use (ii) a weighted average between $\frac{\delta S}{\delta T_D^+}$ and $\frac{\delta S}{\delta T_D}$ according to the number of appearances in CTD profile subranges (Figure 3.9, light green).

Figure 3.11 illustrates the possibilities for two profiles having conditions of temperature and salinity increasing or decreasing downwards. The issue comes when temperature is decreasing downwards and selection of an appropriate coefficient $\delta S/\delta T_D$ or $\delta S/\delta T_D{}^+$ is needed according to whether salinity increases or decreases downwards. This condition can be found at similar depths in two profiles but with different salinity behaviour, the cases of coefficients selection (above) for when temperature is decreasing downwards is a reliable application for integrate salinity.

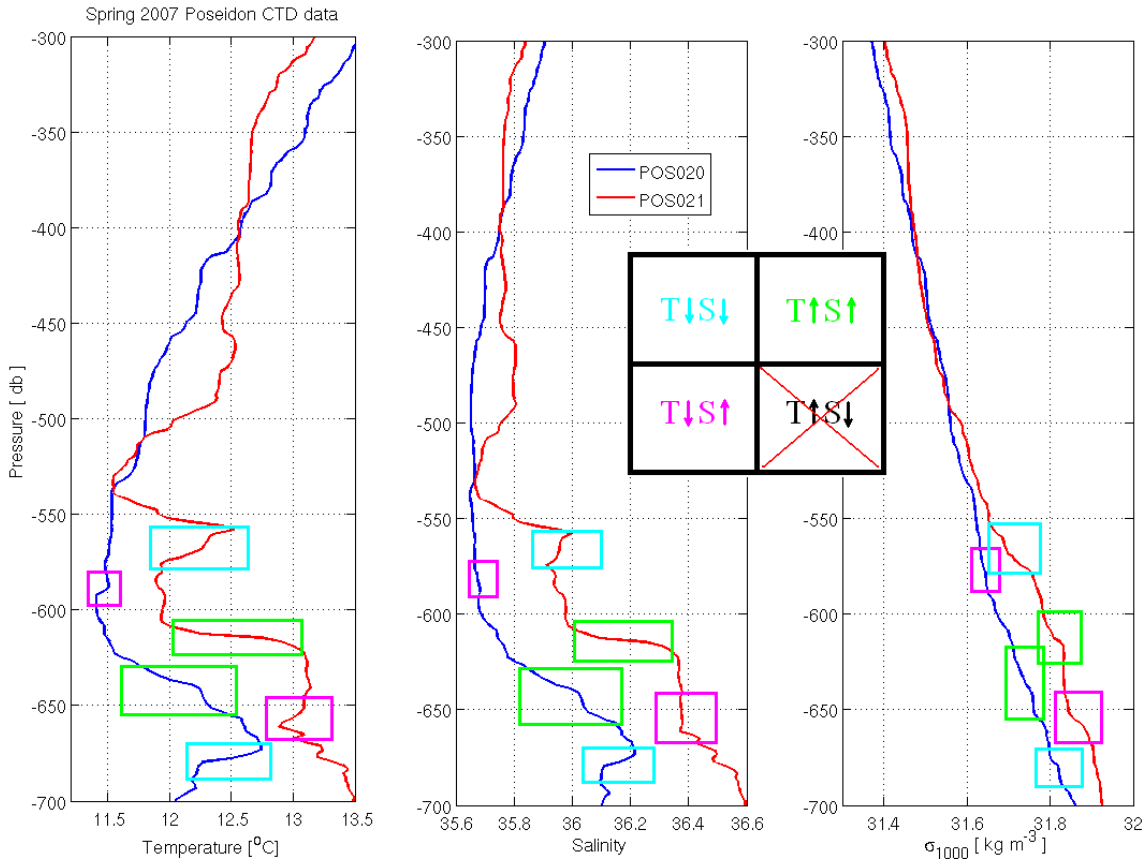

Figure 3.11: Colour coding sketch on two CTD profiles with conditions of temperature and salinity increasing or decreasing downwards. Cyan boxes show regions where temperature and salinity decrease, Magenta boxes also show temperature decreases but salinity increases, and finally Green boxes shows where temperature and salinity are increasing downwards. Temperature increase and salinity decrease implies unstable density; in CTD profiles this might be present as density overturns, however our method does not reproduce them.

Figure 3.12 shows one profile of each region ("shelf", "mid-slope", "outer slope"), comparing inferred with actual salinity, and likewise potential density using all approaches. A stable density profile is obtained. However, salinity still mis-matches around MOW depths. Various components of error and overall error variance are presented in Table 3.1.

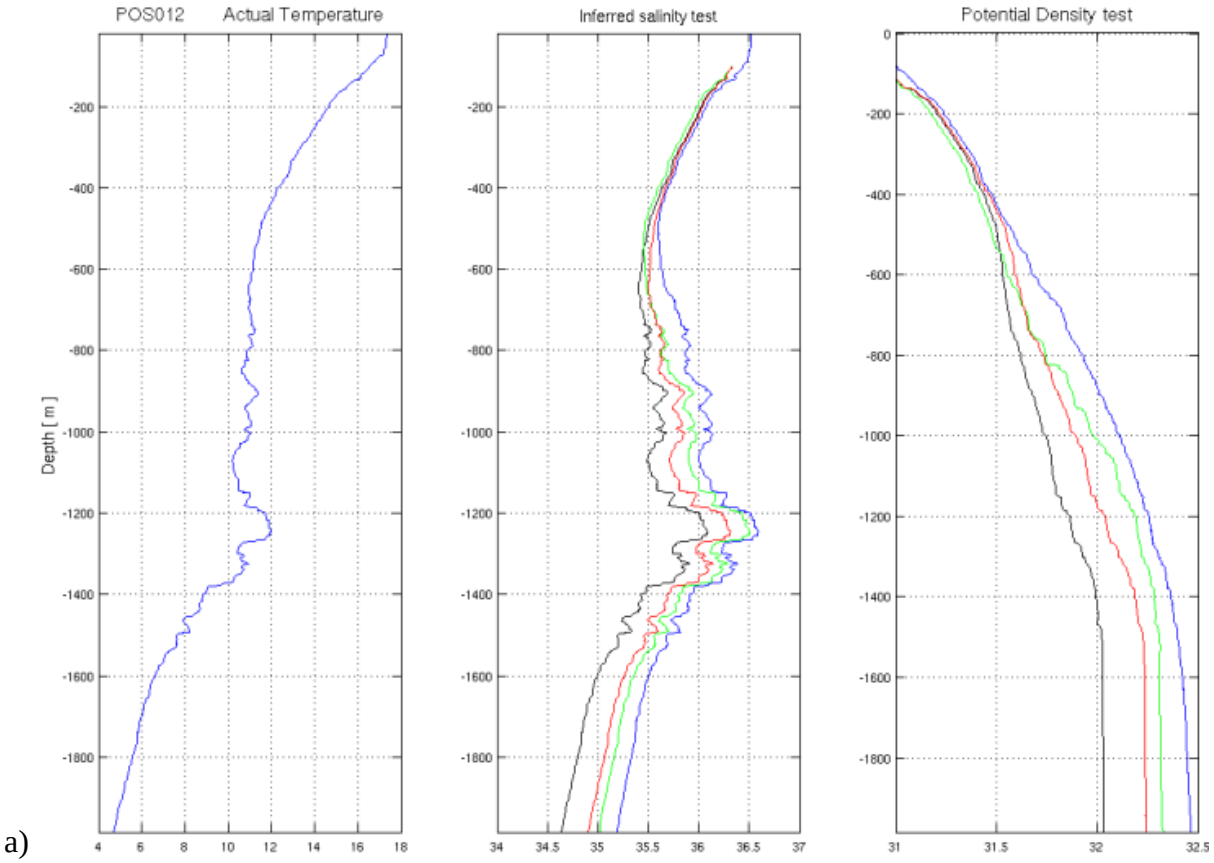

a)

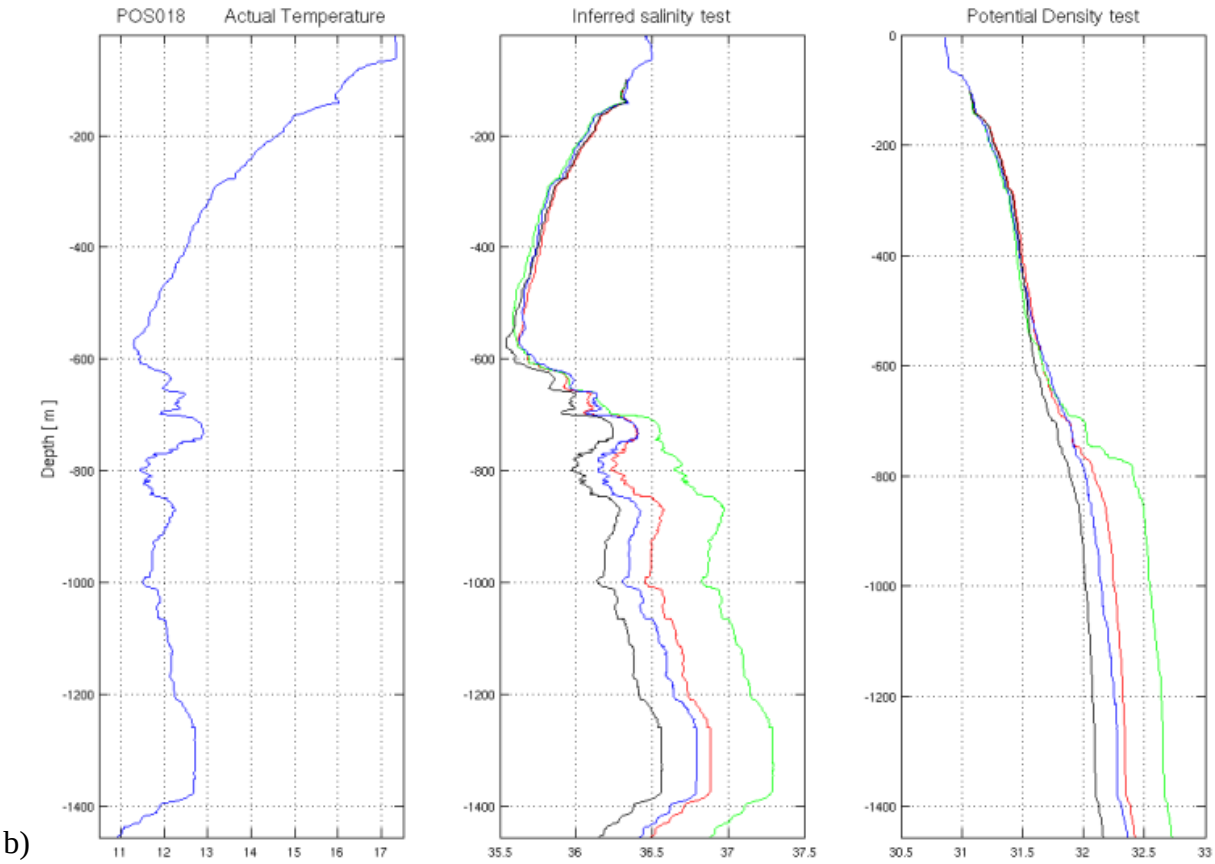

b)

Figure 3.12: Salinity integration method applied to three temperature profiles in the CTD test at different regions of the continental slope (Outer slope (a), Mid slope (b) and (c) Shelf). Each approach is applied to temperature profiles (left) to infer salinity (middle) and then to obtain potential density (right) referred to σ_{1000}. Integration methods for salinity are case I (BLACK), case II (GREEN), case III (RED) and CTD data (BLUE).

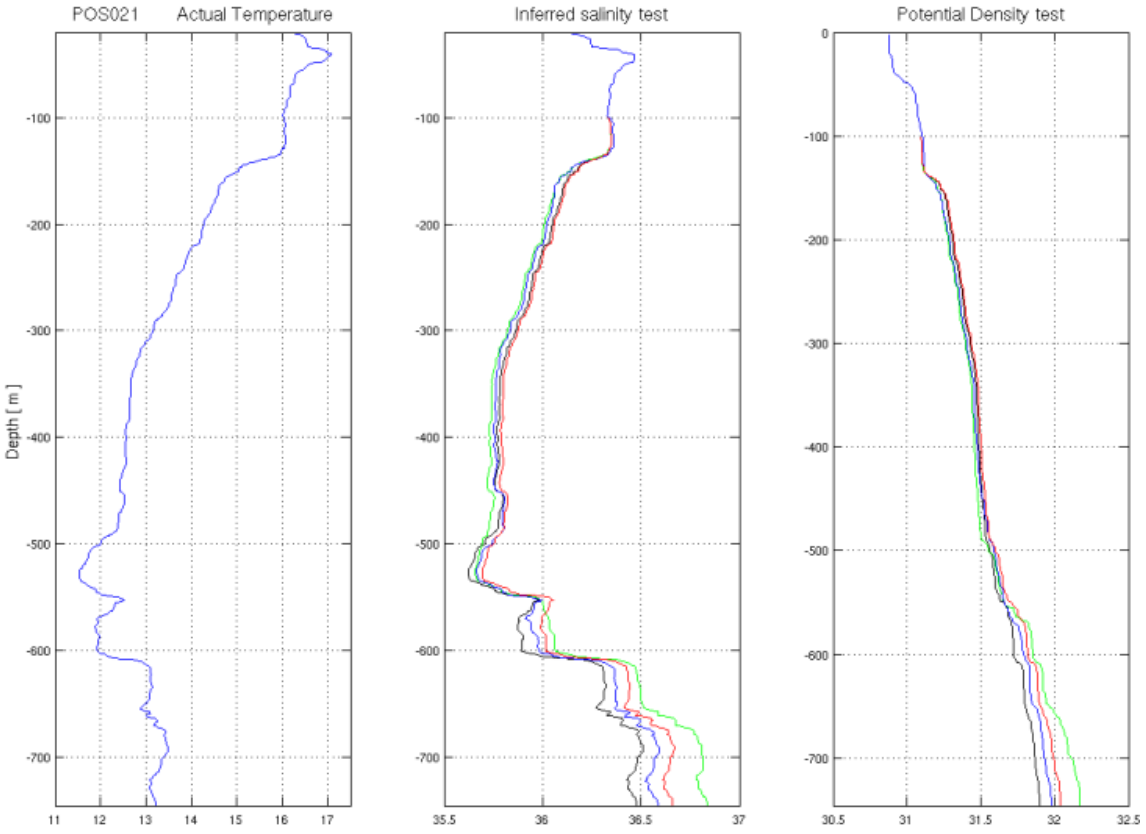

c)

Figure 3.12: Salinity integration method applied to three temperature profiles in the CTD test at different regions of the continental slope (Outer slope (a), Mid slope (b) and (c) Shelf). Each approach is applied to temperature profiles (left) to infer salinity (middle) and then to obtain potential density (right) referred to σ_{1000}. Integration methods for salinity are case I (BLACK), case II (GREEN), case III (RED) and CTD data (BLUE).

Table 3.1: Errors in salinity inferred by (3.3) for each slope sector as defined in section 3.4. (In Figure 3.11: Outer-slope POS012, mid-slope POS018, shelf POS021)

Continental region	E_0^2 ($x10^{-3}$)	E_z^2 ($x10^{-3}$)	E_T^2 ($x10^{-3}$)	ΣE_r^2 ($x10^{-3}$)	Overall error variance ($x10^{-3}$)
Outer-slope	0.71465	0.049	0.00791	0.94113	1.7127
Mid-slope	0.71465	0.049	0.00031	0.10039	0.8643
Shelf	0.71465	0.049	0.00133	0.11278	0.8778

Uncertainties in regression coefficients were large where calculations used few CTDs present at each depth. Errors from the initial integration depth (Z_0) were large, i.e. the choice of depth where salinity has minimal variability was not tight enough (originally 400m, alternative 200m). Errors from temperature data are minimum over mid-slope when the NACW lower layer is approached, however at greater depths the temperature difference increases as seen over the outer-slope. Errors from $\delta S/\delta T$ were larger on the outer continental slope with maximal and varying influence of NACW.

Figure (3.12) shows the results of inferring salinity from the temperature profiles using the CTD test. Salinity inferred using case I, shows the same structure as for temperature, but in comparison with actual salinity, the inferred profiles tend to progressively separate with depth. The misfit in salinity profiles is due to the actual salinity sometimes increasing downwards where temperature decreases downwards. Only the reconstructed salinity profile from the shelf is very close. The inferred potential density profile is as expected completely stable. Salinity inferred using case II is closer to the actual salinity in some profiles and in others is found to exceed the CTD salinity. However, when potential density is calculated, the misfit in salinity leads to 'jumps' in the potential density profile, making it steeper but still stable. Salinity inferred from case III is found to be very similar to the actual salinity. The weighted average approach provides closer density profiles in the CTD test.

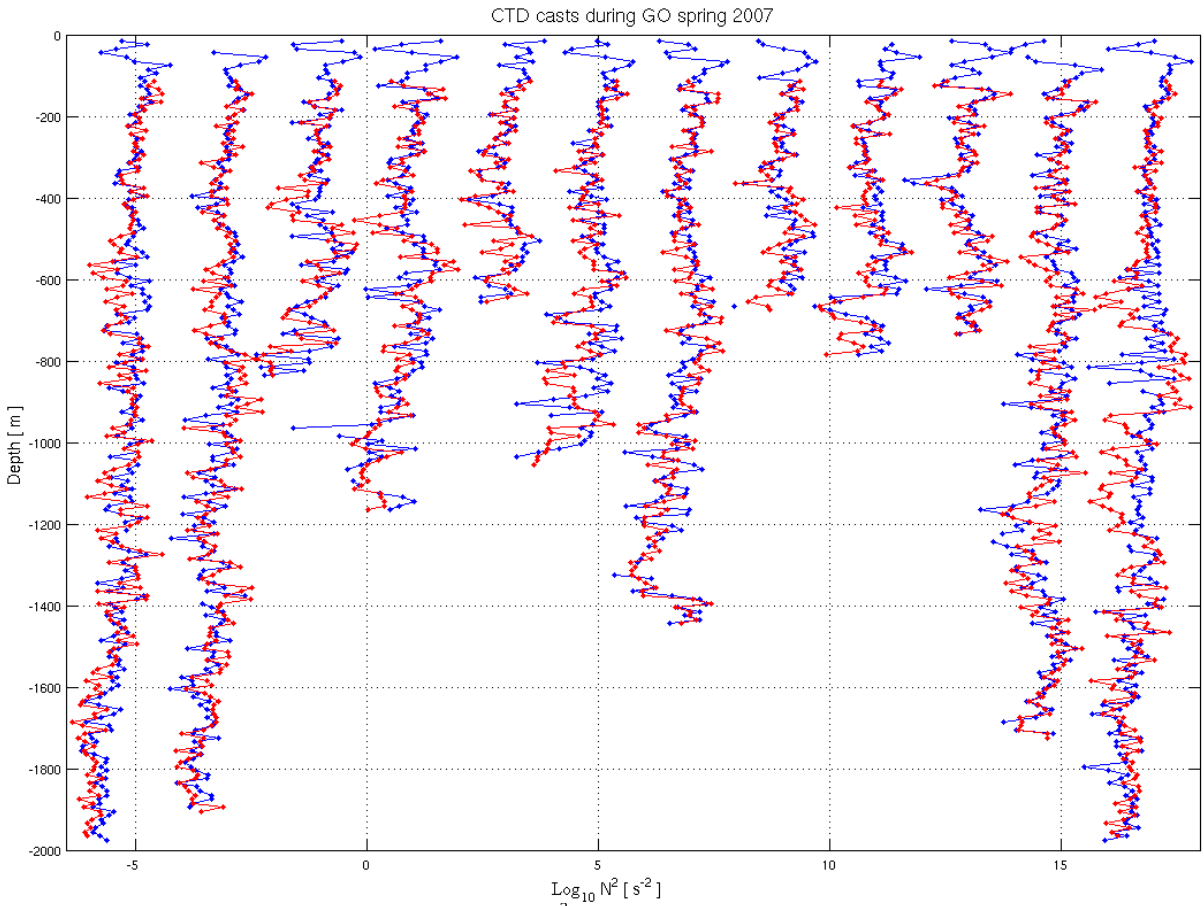

Figure 3.13 Squared buoyancy frequency ($Log_{10}\ N^2$) from actual salinity (BLUE) and salinity inferred (RED) with case III from 12 CTD casts available from the GO experiment, using a potential density gradient calculated from potential density differences over 10m. Profiles were plotted displaced two units from each other, starting with the profile at the left hand side.

Figure (3.13) shows the squared buoyancy frequency profiles from applying the CTD test to the 12 CTD casts. A plausible inferred stratification can be obtained from using the inferred salinity on the large vertical scale (>100m), however over small vertical scales (<100m) stratification can be found to differ from the actual profiles.

3.5 Discussion

Salinity can be inferred using different approaches (Cases I, II, III in section 3.4.1) to reconstruct the vertical structure from the temperature variability. All the approaches can infer salinity with a stable density profile but not matching the actual salinity. If the purpose of the research will be to analyse shelf water column conditions where salinity seems to behave the same as temperature, and to avoid any excess salinity, case I is the option. If the purpose of the research is to have the closest inferred salinity to the actual profile, at any sector of the continental slope, then the option is case II. However, if the purpose is to reproduce the density gradient with inferred salinity at all regions over the continental slope with a good approximation, the option is case III (Figure 3.14).

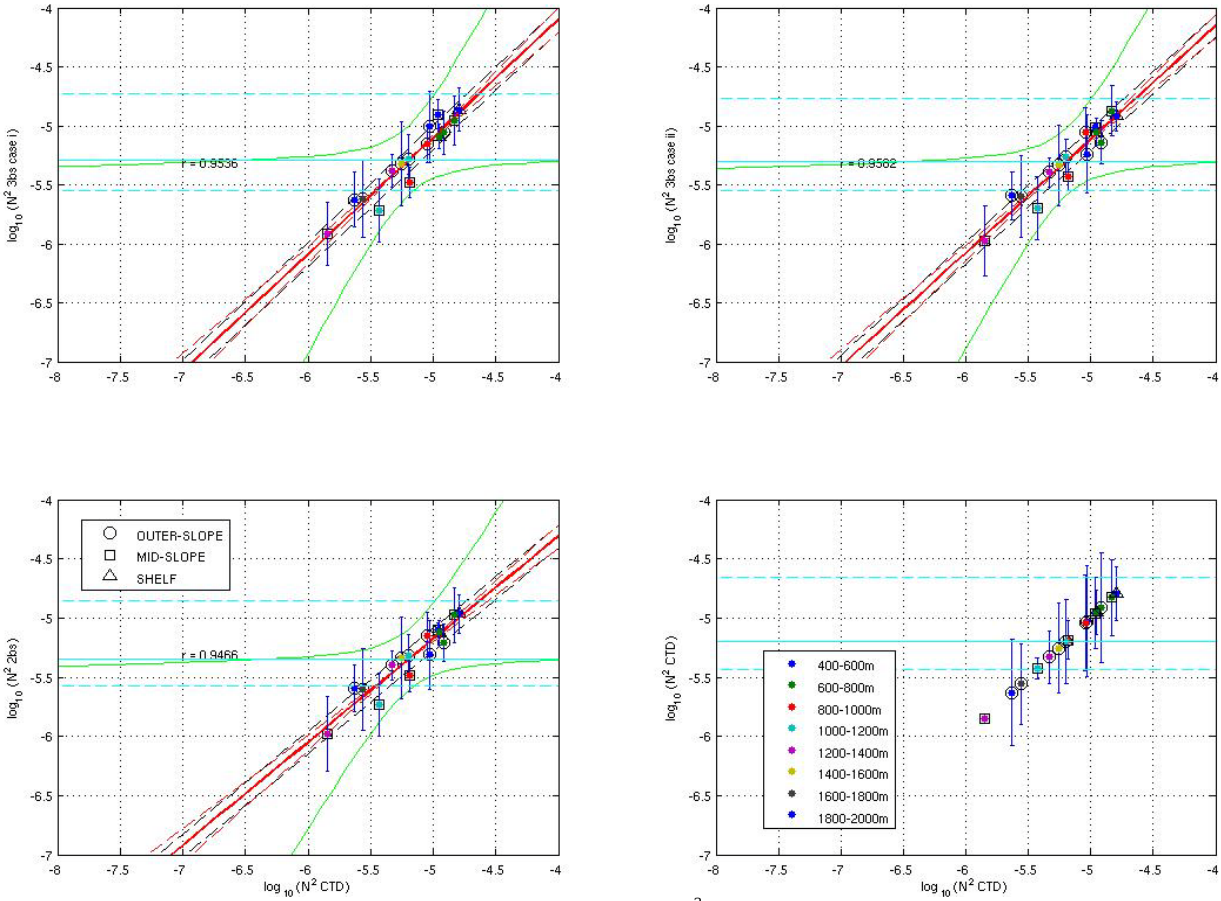

Figure 3.14: Statistics of squared buoyancy frequency ($Log_{10}\ N^2$), using all the salinity integration methods at different depths and regions over the continental slope. Case I (TOP left), case II (TOP right), case III (BOTTOM left) and actual CTD (BOTTOM right). Statistics of a weighted linear fitting are fitting standard error (black lines), slope and intercept standard error (red), slope error confidence interval (green curves) and chi-squared distribution (cyan lines).

Reconstructing the density gradient using inferred salinity can be done using any of the approaches. Salinity gradients can be used to analyse the vertical structure, in this work, without having the exact salinity. Different profiles are similar to each other over deep regions where the interfaces of MOW and NACW layer are present rather than within the MOW layer. The closest reconstruction of the density gradient is found over the NACW water, probably due to its unvarying stratification.

Vertical variability of $\delta S/\delta T$ can differ according to context (depths corresponding to water masses). In the Gulf of Cadiz varying proportions of MOW imply rapid changes of vertical temperature and salinity gradients; at such depths a correspondingly smaller depth range was used to regress for $\delta S/\delta T$. Applications over the seasonal thermocline (for example) may likewise need to consider the depth range used in regression for $\delta S/\delta T$.

All approaches can infer salinity over regions where temperature is either increasing or decreasing downwards in large scale (>100m), as through MOW-NACW interfaces. Here our aim is to reconstruct a density field where the internal wave field is active. Inside the MOW a well inferred salinity can be approximated. In Chapter 4 the reconstructions of stratification and will be used to assess how much mixing occurs. The sensitivity of the mixing estimates to the methodology will be assessed in Chapter 4.

3.6 Summary

A description of the water mass properties through the water column is studied by following the structure of temperature profiles through the MOW. Using a set of 12 CTD casts with available salinity and temperature a method to infer salinity to associate with temperature profiles from XBTs is developed with different approaches. The aim is to use the extensive available temperature profile data to construct background stratification. Approaches to infer salinity from temperature profiles were discussed by their uses and applications. A weighted average density ratio for salinity integration is found to be the optimal choice to infer the density gradient and compare with CTD profiles. Error estimates over reconstructed density profiles confirm that the suggested method is the best choice to diagnose the interfaces between NACW and MOW. For water mass, T and S are better than density and vertical variability in the water column; some discussion is presented here.

Chapter 4 Diapycnal mixing analysis

4.1 Introduction

In this chapter, different methods to diagnose diapycnal mixing are analysed: the Thorpe scale, vertical shear and strain methods. The available conventional oceanographic data from the GO experiment were used to study diapycnal mixing in two steps. The first step was to apply the above methods using CTD casts. The second step was to apply the strain method to the more extensive temperature profiles (XBTs) with inferred salinity calculated in Chapter 3. Uncertainties are also discussed, particularly those arising from the strain method using temperature profiles with inferred salinity. Also mixing is related with the internal wave field analysed in Chapter 2.

Practical parameterizations of internal wave induced mixing have been largely based on empirical statistical approaches. Dynamically-based mixing parameterisations which represent a large percentage of wave breaking have been developed with the use of novel techniques with conventional oceanography (*Polzin et al,* 1996; *Mauritzen, et al* 2002, *Naveira-Garabato, et al* 2004a,b; *Kunze, et al* 2006). Wave breaking can be divided into strongly and weakly nonlinear types, which take place in different places, governed by different dynamics and represented by different parameterizations. Strong nonlinear processes can dominate dissipation over local regions, being orders of magnitude larger than the background dissipation, while weakly nonlinear processes can dominate dissipation over most of the ocean.

4.2 Diapycnal mixing theory

Strong nonlinear wave breaking often occurs with a tidal flow approaching isolated ridges, with mixing occurring through internal hydraulic jumps (*Legg and Klymak,* 2008). The hydraulic jump can be viewed as a wave which is arrested; it occurs when a wave's horizontal phase speed (limited by vertical length scale) is not as fast as the peak tidal flow, in the presence of steep topography. Efforts to predict internal tide energy flux using theoretical approaches (*Llewellyn Smith and Young,* 2002; *St Laurent and Nash,* 2003) have a function for vertical wave numbers (*Klymak and Legg,* 2010).

Weakly nonlinear wave breaking is related to small vertical scales and the way in which waves interact. A generic equation to describe a wave-wave interaction spectrum (*McComas and Muller,* 1981) is:

$$\frac{\partial A}{\partial t} + \nabla_r \cdot \left(C_g + \bar{u}\right) + \nabla_P \cdot RA = T_r + S_o - S_i \qquad (4.1)$$

in which r is a spatial coordinate, p is the wave number vector, $A(k,x,t)=E/\omega$ the action density spectrum, $E = E_k + E_p$ the energy density, E_k and E_p kinetic and potential contributions to the energy density, ω the intrinsic frequency, $C_g = \nabla_P \omega$ group velocity, $\bar{u}$ subinertial currents, R refractive effects associated with spatially inhomogeneous stratification and subinertial currents, T_r transfers of action, S_o interior sources and S_i interior sinks (dissipation) [Not all terms are defined here and need further definition according to context]. The equation is known as the radiation balance equation which describes the temporal and spatial evolution of internal waves by generation, propagation, refraction by mesoscale inhomogeneities, nonlinear interactions and dissipation.

The important term here is T_r which represents the rate of energy cascade from large to small (vertical scales), and then governs the rate of energy available from small scales for turbulent mixing. The different forms of dissipation scaling have resulted in different approaches to describe the controlling physics. McComas and Muller (1981) summarize the resonant interaction approach, which considers energy transfer as a sum of triple interactions between internal waves. Polzin (2004) developed a heuristic cascade closure scheme that represents the 'continuous downscale transfer rate', $T_r \approx \frac{\partial F(m,\omega,\varphi)}{\partial m}$ and associated dissipation rate $\varepsilon = \int_f^N \int_0^{2\pi} F(m,\omega,\varphi) d\omega d\varphi$, where the downscale transfer of energy $F(m,\omega,\varphi)$ may be supplemented by transfer in frequency space and redistribution in azimuthal direction φ (here m is vertical wavenumber and ω is frequency). Fine-scale parameterizations (*Polzin et al*, 1996; *Mauritzen, et al* 2002, *Naveira-Garabato, et al* 2004a,b; *Kunze, et al* 2006) depend on the functional form of F. This approach depends on the turbulent production and dissipation balance ($P = \varepsilon + \kappa_z N^2$, P is turbulent production, κ_z see chapter 1).

This fine-scale parameterisation approach to internal wave breaking depends on a statistically stationary internal wave field. The turbulent dissipation (ε) and diapycnal buoyancy flux associated with mixing ($\kappa_z N^2$) balance turbulence production to the downscale energy transport from internal wave-wave interactions. Finescale parameterization

is commonly applied to vertical profiles to diagnose mixing rates (*Polzin et al*, 1996; *Mauritzen, et al* 2002, *Naveira-Garabato, et al* 2004a,b; *Kunze, et al* 2006). Those approaches are normalized by the predicted Garrett-Munk (1972, 1975) model of the background internal wave field with stratification decreasing monotonically downwards. Recent work (*Mackinnon and Winters*, 2005) demonstrates that an initial narrow-band wave-field (noise added) tends to transfer energy towards smaller scales to fill out a Garrett-Munk spectrum, until a steady state is achieved.

4.3 Analysis methods

Diapycnal mixing analysis is based on perturbations of stratification due to the presence of internal waves. Two mixing parameters used to study the mixing are the turbulent kinetic energy (TKE) dissipation rate (power per unit mass) and diapycnal diffusivity (squared distance per unit time). Here, we examine commonly applied diapycnal mixing methodologies, the Thorpe scale, Vertical shear and strain. Each method looks for internal wave interactions with stratification. The Thorpe scale method analyses the presence of density overturns generated by internal waves on density gradients. The fine-scale parameterisation methods analyse the variability of the vertical column shear and strain affected by internal waves.

The presence of the MOW in the Gulf of Cadiz leads to a particular range of temperature (10ºC - 14ºC) and Salinity (35.6 – 36.8 salinity units) scatter on T-S diagrams. Analysis of each profile suggests that stable density conditions can be found, even though there is a loose relationship between Salinity and Temperature. Inspecting the T-S scatter with respect to σ_θ suggested instabilities. However, using a potential density referenced to an interior pressure (1000db) over the TS diagram provides good evidence on stability.

Potential density (kg/m³) was calculated (using σ_θ, σ_{1000} and σ_{2000}) for each profile in order to inspect vertical variability. Firstly, using data at one decibar resolution (and then full resolution) after water mass processing using CTD seabird routines, results revealed the presence of potential density spikes. Spikes were associated with salinity sampling due to a lag in the sensor (it takes 0.07s for every measure to reach the conductivity electrodes). In order to remove spikes an algorithm was built and applied to full resolution data. For full resolution (24 samples per second) potential density was calculated and spurious data were

removed using a first threshold of 2 standard deviations over 250 points (removing the larger spikes, 125 points above and below). A second pass was applied using a similar threshold to remove any large spike still remaining from the first run. No numerical value was replaced at depths where data were removed.

4.3.1 Thorpe Scale

Potential density processed at full CTD resolution (24 samples per second) was used to construct a rearranged profile which is monotonically stable. This density profile without instabilities is then compared against the original profile. The vertical distance from the original to the rearranged location of a density measurement is called the Thorpe displacement (*Thorpe*, 1977). An overturn is identified when in a vertical segment the sum of the Thorpe displacements becomes zero. Then the Thorpe scale (L_T) is calculated as the root mean square of Thorpe displacements within each overturn (Dillon, 1982).

Using the definition of the Ozmidov length scale $L_O = (\varepsilon / N^3)^{\frac{1}{2}}$ (Ozmidov, 1965) and the empirical ratio of L_O / L_T = 0.8 (Dillon, 1982), TKE dissipation rate can be written as $\varepsilon = 0.64\, L_T^2\, N^3$ and diapycnal diffusivity as κ_z = 0.2ε/N = 0.128 L_T^2 N (Osborn, 1980). Galbraith and Kelly (1996) suggest that a test needs to be applied to avoid instrument noise being interpreted as overturns. A Run Length test looks for the number (n) of sequential Thorpe displacements with the same sign; the test uses a probability relation $\left((\sum_1^\infty 2^{-n} n^2)^{\frac{1}{2}} = \sqrt{7}\right)$ expected for random uncorrelated data (Timmermans et al, 2003), which suggest a minimum 7 sequential Thorpe displacements with the same sign for a density overturn or instability. A criterion of seven points can be used in the test; however Johnson and Garrett (2004) suggest that in regions of strong stratification the criterion can be reduced to six or less.

Figure 4.1 shows that density overturns were detected by using a reordered potential density profile. Over the outer slope profile shown (CTD P012), density overturns are found all down the water column and the biggest (>6m) are inside the MOW. In the Mid slope profile (CTD P018), density overturns are fewer in the NACW layer and prevail inside the MOW with the biggest (>10m) in the water column. Over the Shelf (profile CTD P021), the presence of density overturns can be observed all down the water column but they are intense

inside the MOW, also some big overturns (>4m) can be found in the surface mixed layer. The Thorpe scales show that strong salinity interleaving increases the presence of density overturns; suggesting that at interfaces with the MOW density overturns increase with the biggest overturns inside the MOW.

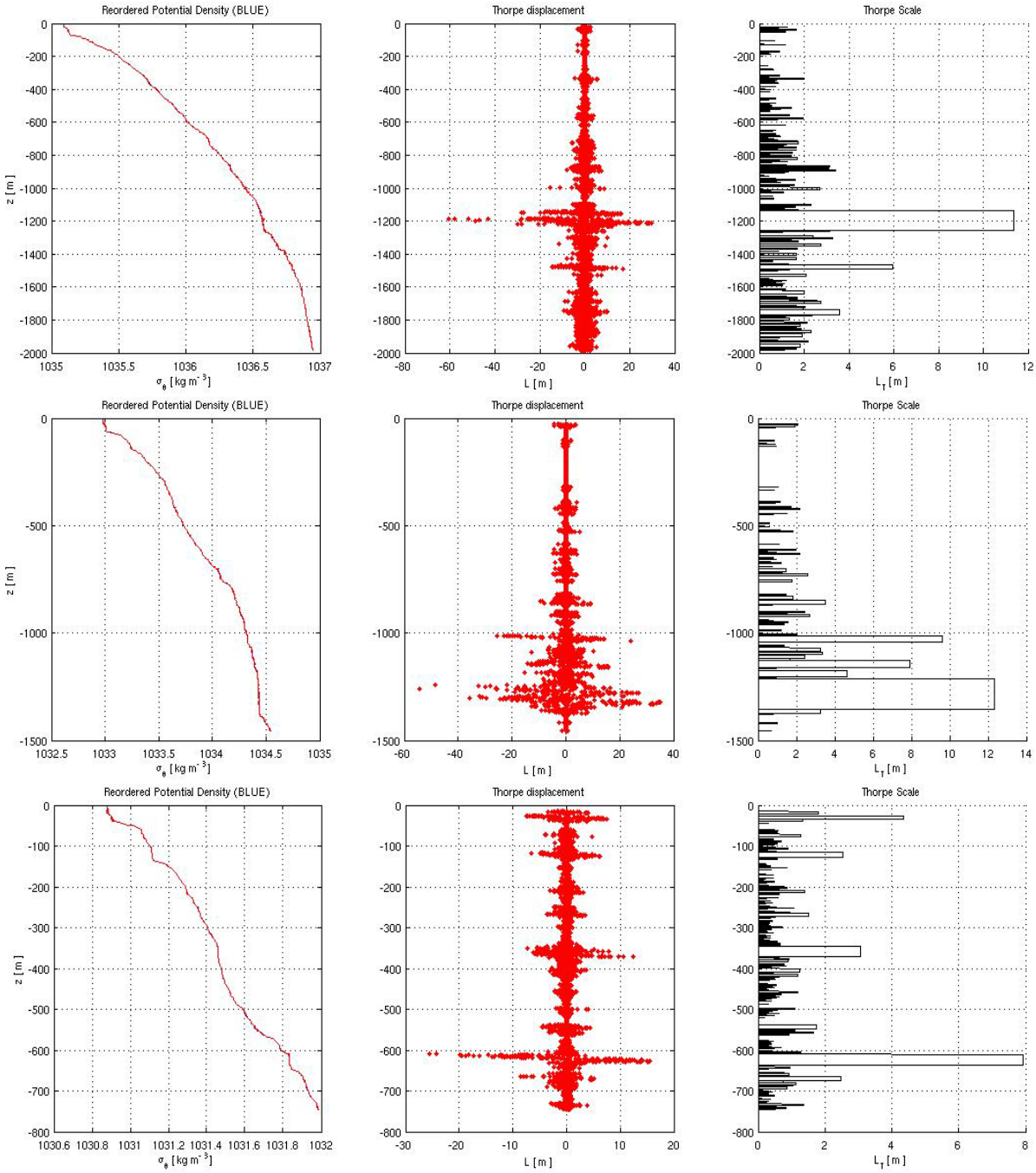

Figure 4.1: Results from Thorpe scale analysis applied to the GO dataset: reordered potential density (left hand side column), Thorpe displacement (middle column) and Thorpe scale over vertical segment (right hand side column). TOP row CTD P012, MIDDLE row CTD P018 and BOTTOM row CTD P021.

Table 4 summarizes the results from applying the Thorpe scale method to all the CTD casts; mixing parameterizations are summarised by presenting a depth-average. Overturns

were compared using CTD profiles with full resolution and with one decibar resolution, revealing similar results; most of the overturns detected were found to be larger than one metre. The presence of big overturns is evidence of strong mixing activity against the local stratification and leads to large estimates of mixing.

Mixing parameterizations from the Thorpe scale analysis reveal that enhanced mixing is taking place over the regions around the continental slope of the Gulf of Cadiz. On average mixing was found to be strong as depth-averaged over the mid-slope (ε >8.34x10^{-9} W kg^{-1}; K_z >6.67x10^{-4} m^2 s^{-1}), and considerable (ε >2.78x10^{-9} W kg^{-1}; K_z >2.39x10^{-4} m^2 s^{-1}) over the shelf and outer slope. Not only the presence of big overturns contributes to the large mixing parameters, but also the abundance of density overturns (>1m), mostly in the MOW.

Table 4.1: Results from the Thorpe scale analysis applied to the available CTD casts data using 0.1 metres of vertical resolution. N, ε and K_z are presented as depth averages.

Casts	Initial depth	Vertical resolution	Overturns size (mean)	Overturns size (max)	N [10^{-3} s^{-1}]	ε [10^{-9} Wkg^{-1}]	K_z [10^{-4} m^2 s^{-1}]
P12	6 m	0.2 m	1.4 m	7.1 m	1.80 ±0.78	1.31±2.34	5.64±1.89
P13	10 m	0.1 m	0.9 m	18.2 m	2.01 ±0.87	8.47±1.78	4.26±1.43
P14	5 m	0.1 m	0.7 m	8.6 m	2.21 ±0.56	4.52±1.21	2.08±0.87
P15	10 m	0.3 m	2.1 m	21.2 m	1.98 ±0.65	2.81±3.01	6.98±2.65
P16	5 m	0.1 m	0.5 m	4.6 m	2.26±0.43	2.66±1.31	0.80±0.59
P17	5 m	0.1 m	0.6 m	9.0 m	2.11±0.78	3.61±2.16	1.74±1.56
P18	10 m	0.3 m	1.8 m	12.3 m	1.93±0.76	1.43±3.45	8.85±2.92
P19	18.5 m	0.1 m	0.6 m	16.1 m.	2.34±0.54	3.63±1.41	2.02±0.76
P20	18.5 m	0.1 m	0.6 m	3.5 m	2.12±0.36	3.11±1.56	1.04±0.80
P21	5 m	0.1 m	0.6 m	7.9 m	2.15±0.54	4.21±1.45	1.59±1.02
P22	5 m	0.1 m	0.8 m	15.3 m	2.10±0.76	5.09±2.31	2.46±1.71
P23	5 m	0.1 m	0.8 m	18.4 m	2.04±0.89	6.41±2.65	4.47±2.00

Note: Uncertainties are factor 3 predicted for method.

4.3.2 Vertical shear and strain

Fine-scale parameterization methods are based on nonlinear internal wave-wave interaction theories (*McComas and Muller,* 1981; *Henyey et al,* 1986) of transferring energy downscale from internal waves into turbulence production. The downscale transport depends on N^2 and on fine-scale shear and strain spectral densities (as validated by *Gregg,* 1989; *Polzin et al,* 1995). The background Lowered ADCP vertical shear ($\sqrt{u_z^2 + v_z^2}$) and CTD strain $\left(\frac{N^2 - \langle N^2 \rangle}{\langle N^2 \rangle}\right)$, (based upon isopycnal displacements) are used to build the vertical

wavenumber spectral densities. TKE dissipation rate ε is estimated by the following formulae (*Polzin et al*, 1995; *Mauritzen et al*, 2002; *Gregg et al*, 2003; *Naveira Garabato et al*, 2004a,b):

$$\varepsilon_{strain} = \varepsilon_o G\left(\frac{f}{N}\right)\frac{N^2}{N_o^2}\,\frac{\langle\xi_z^2\rangle^2}{\langle\xi_{zGM}^2\rangle^2}\,F(R_w) \qquad (4.2)$$

$$\varepsilon_{shear} = \varepsilon_o G\left(\frac{f}{N}\right)\frac{N^2}{N_o^2}\,\frac{\langle V_z^2\rangle^2}{\langle V_{zGM}^2\rangle^2}\,F(R_w) \qquad (4.3)$$

where ε_0 ($7.8\text{x}10^{-10}$ W kg^{-1}), f_{30} ($7.29\text{x}10^{-5}$ s^{-1}, at critical latitudes) and N_o ($5.24\text{x}10^{-3}$ rad s^{-1}) are constants from the GM spectrum. $\langle V_z\rangle$ and $\langle \xi^2{}_z\rangle$ are the variances of the measured vertical shear and strain (shear is normalized by N); $\langle V_{zGM}^2\rangle$ and $\langle\xi_{zGM}^2\rangle$ are the variables' variances predicted by the modified GM model. $F(R_w)$ and $G(\frac{f}{N})$ are two correction functions (Polzin et al, 1995; Naveira Garabato et at, 2004a,b):

$$F(R_w) = \frac{1}{a\sqrt{2R_w}}\left[-R_w + 1 + a^2 + \{(R_w - 1 - a^2)^2 + 8R_w a^2\}^{\frac{1}{2}}\right]^{\frac{1}{2}} \qquad (4.4)$$

$$G\left(\frac{f}{N}\right) = \frac{f\,\cosh^{-1}\left(\frac{N}{f}\right)}{f_{30}\cosh^{-1}\left(\frac{N_o}{f_{30}}\right)} \qquad (4.5)$$

with $a = \frac{f}{N}$ and $R_w = \left(\frac{\langle V_z^2\rangle}{N^2\langle\xi_z^2\rangle}\right)$ which is the shear and strain ratio. For the GM model, $R_w = 3$ and $F(R_w) = 1$.

Spectra were computed using overlapping segments (of 320m for each 100m estimate, discussed in sections 4.4 and 4.5). Shear and strain variances were integrated over a selected wavelength band (from 320m to 60m, see section 4.4). Results could change by modifying these parameters by a factor of ten. Here, shear and strain estimates were calculated using similar relations as in other mixing studies (Naveira Garabato, 2004a,b): for segments a depth range of 320m can represent the surrounding variability from the average size of MOW structures; the minimum wavelength was 60m [to cover minimum M2 vertical amplitude]. Uncertainties for regions over the continental slope come from standard deviations of mixing estimates. The total uncertainty in fine-scale parameterisation of TKE dissipation rate (ε) is estimated to be a factor of three (*Polzin, et al* 2002) and the diapycnal diffusivity within a factor of four, including the uncertainty in mixing efficiency.

For N^2, a vertical range of 20 m is often used, however vertical variability can be found on scales smaller than this range. On the other hand, using a vertical bin of five metres range or smaller, N^2 would be evaluated on the scale of density instabilities. Using ten metres range, strain can explain most of the variability. For $<N^2>$, in practice a choice of four to five hundred metres range is often made. In this study, a representative value of $<N^2>$ is related strongly to the vertical length scale of MOW cores or meddies. On the Gulf of Cadiz Continental Shelf, the MOW undercurrent and cores can reach a thickness of two or three hundred metres. Over the mid and outer slope, the MOW cores thickness is around three to four hundred metres. Here, we choose a vertical bin ($<N^2>$) of three hundred metres as a standard size for strain calculation.

Figure (4.2) compares the results from applying the Vertical shear and strain methods to a set of three CTD profiles. Each profile shows that shear and strain do not follow similar variability which preludes a resultant mismatching between mixing parameterizations. In the deep CTD profile POS012, vertical shear and strain present fast changes over regions where MOW is present (800m-1400m). Around 1200m depth, a salinity core is present (around 100m thick) and the strain shows two peaks in magnitude at the edges of the salinity core with a minimum inside the core, whereas the vertical shear here is uniform over 200m depth range. However some similarities can be observed around 600m to 800m (top interface; an increase of vertical shear and strain), also at 1400m to 1600m a decrease of variability in both contributions. At the mid slope (POS018), similar variability (at 500m to 800m depth, top interface) of vertical shear and strain can be found. Also, inside the MOW around 1200m to 1400m depth, there is a salinity core in which strain has a minimum and vertical shear remains strong, showing that strain and shear have discrepancies inside MOW.

In the CTD cast POS021 on the shelf, vertical shear and strain are correlated over the upper interface (MOW at 500m to 700m). Also correlation between shear and strain can be found over the NACW lower layer. Error between fine-scale parameterization methods exceeds uncertainties (mostly inside MOW and the surface mixed layer).

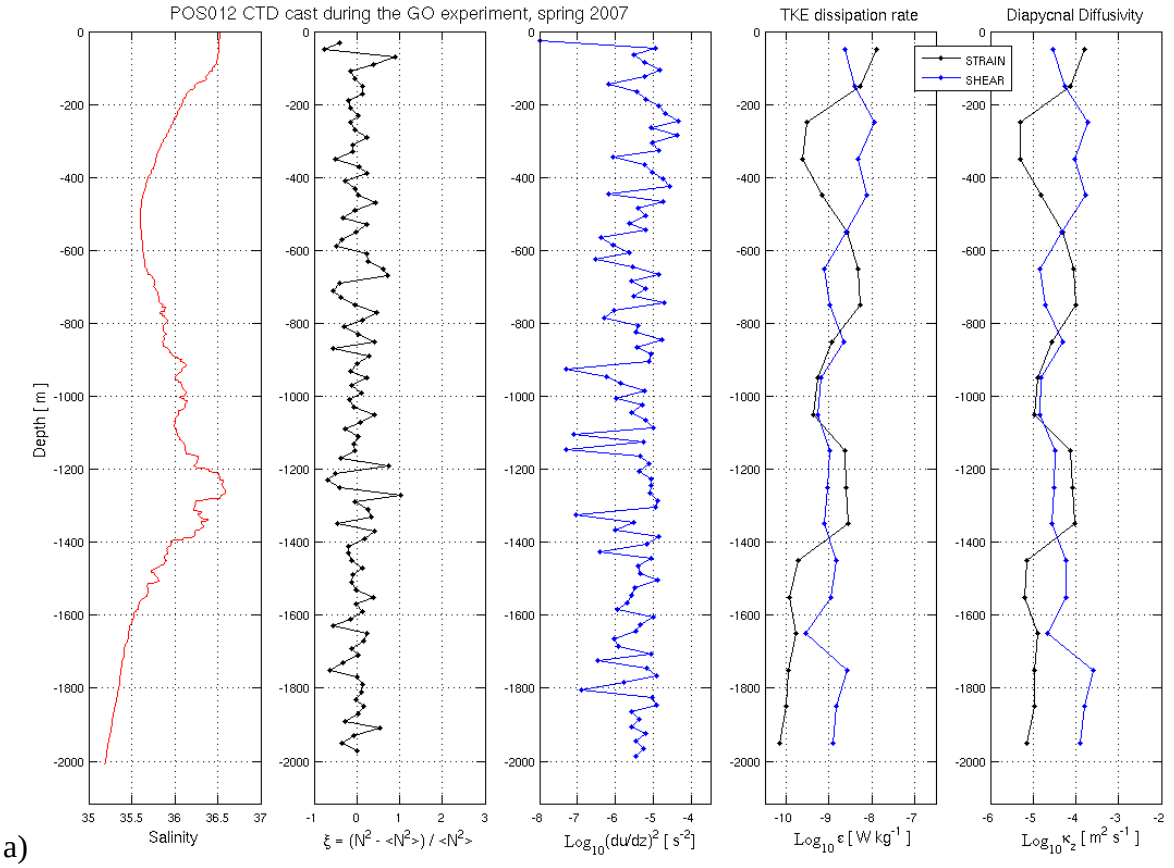

a)

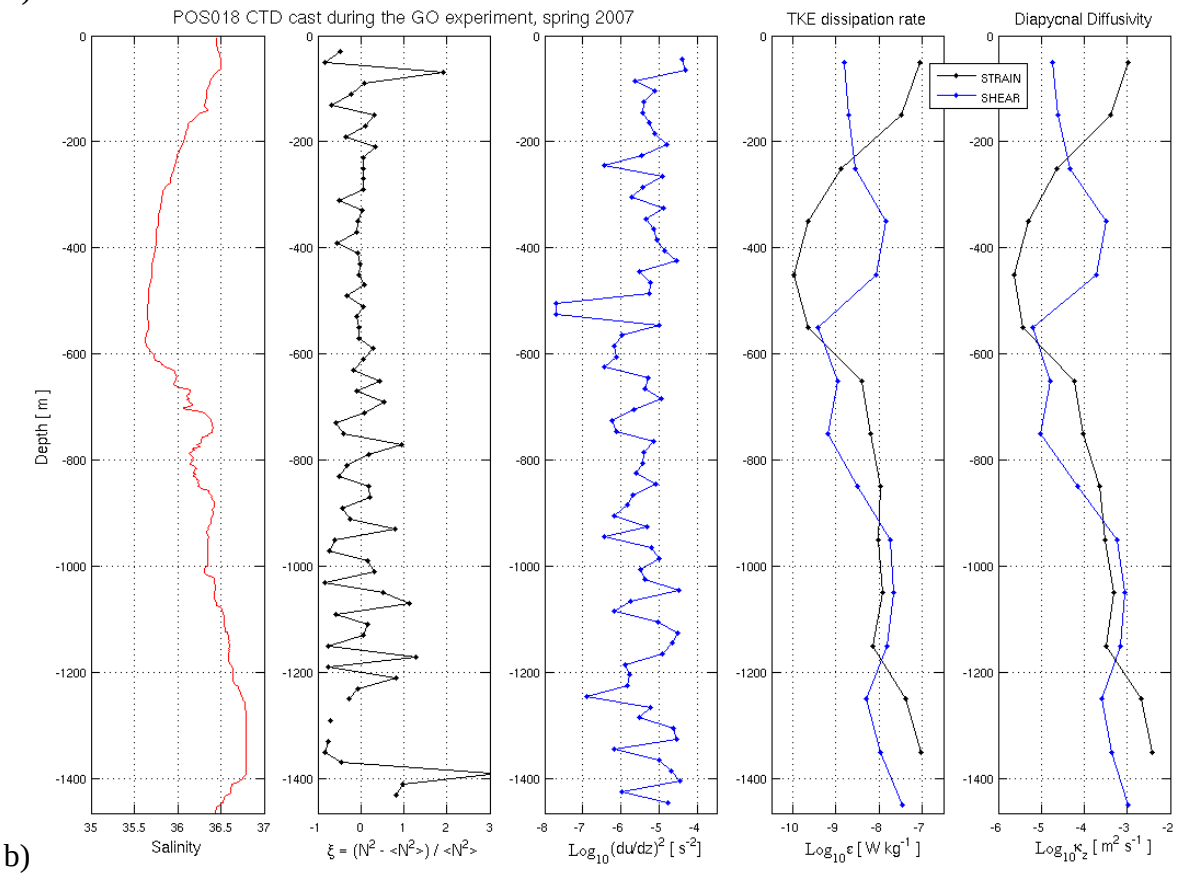

b)

Figure 4.2: Fine-scale parameterization analyses applied to a group of three CTD casts from the GO experiment during spring 2007. a) POS012 outer slope, b) POS018 mid-slope and c) POS021 shelf. From left to right the panels show salinity profiles, strain using N^2, vertical shear, calculated TKE dissipation rate (ε) and Diapycnal Diffusivity (κ_z).

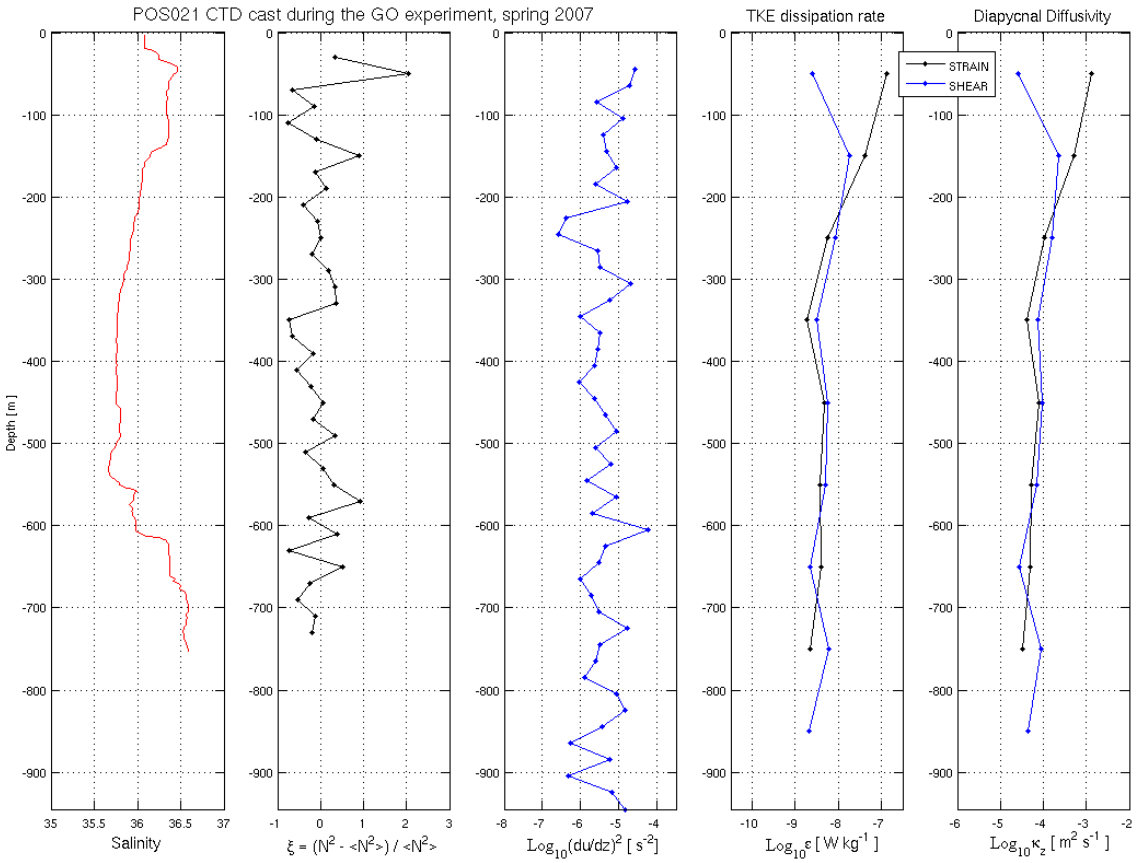

c)

Figure 4.2: Finescale parameterization analyses applied to a group of three CTD casts from the GO experiment during spring 2007. a) POS012 outer slope, b) POS018 mid-slope and c) POS021 shelf.. From left to right the panels show salinity profiles, strain using N^2, vertical shear, calculated TKE dissipation rate (ε) and Diapycnal Diffusivity (κ_z).

4.3.3 Comparisons of methods to estimate mixing

In summary density overturns and fine-scale parameterizations were applied using available CTD casts in three regions (Outer slope, mid-slope and shelf). Mixing estimates were averaged to compare variability by using statistical approach (every 100m) with the related error (standard deviation).

Figure (4.3) shows results of averaging mixing estimates over the continental slope regions; it is found that the mixing estimates can differ and mismatch can be present. Shelf mixing estimates from the three approaches (Thorpe scale, shear and strain) are found to be in agreement at the MOW-NACW interface (300m to 500m); over the rest of the water column agreement is rarely found. Over the mid slope, there is more agreement between the mixing estimates in the MOW, especially at the MOW-NACW interface (400m to 700m, across the slope); this agreement is not found inside the NACW upper layer (200m – 300m) – the vertical shear estimate differs. Over the outer slope, there was good (less than a factor of 2)

agreement in mixing estimates over the MOW-NACW interfaces (both upper, 400m to 700m, and lower, 1400m to 1700m). Agreement was not good (bigger than factor of 4) inside the MOW (shelf 500m to 800m; mid-slope 1000m to 1200m; outer slope 700m to 1400m) due to the different variability present due the presence of MOW cores or meddies. In general, the Thorpe scale (blue-red) and strain (cyan-magenta) methods usually have more agreement with each other and occasionally they agree with the vertical shear (green-yellow). Thorpe scale (blue-red) and vertical shear (green-yellow) method do not agree through the water column (shelf - NACW upper layer at 250m, MOW at 650m; mid slope – NACW upper layer at 200m to 400m; outer slope – all over inside MOW) and mismatch between estimates exceeds their formal uncertainties.

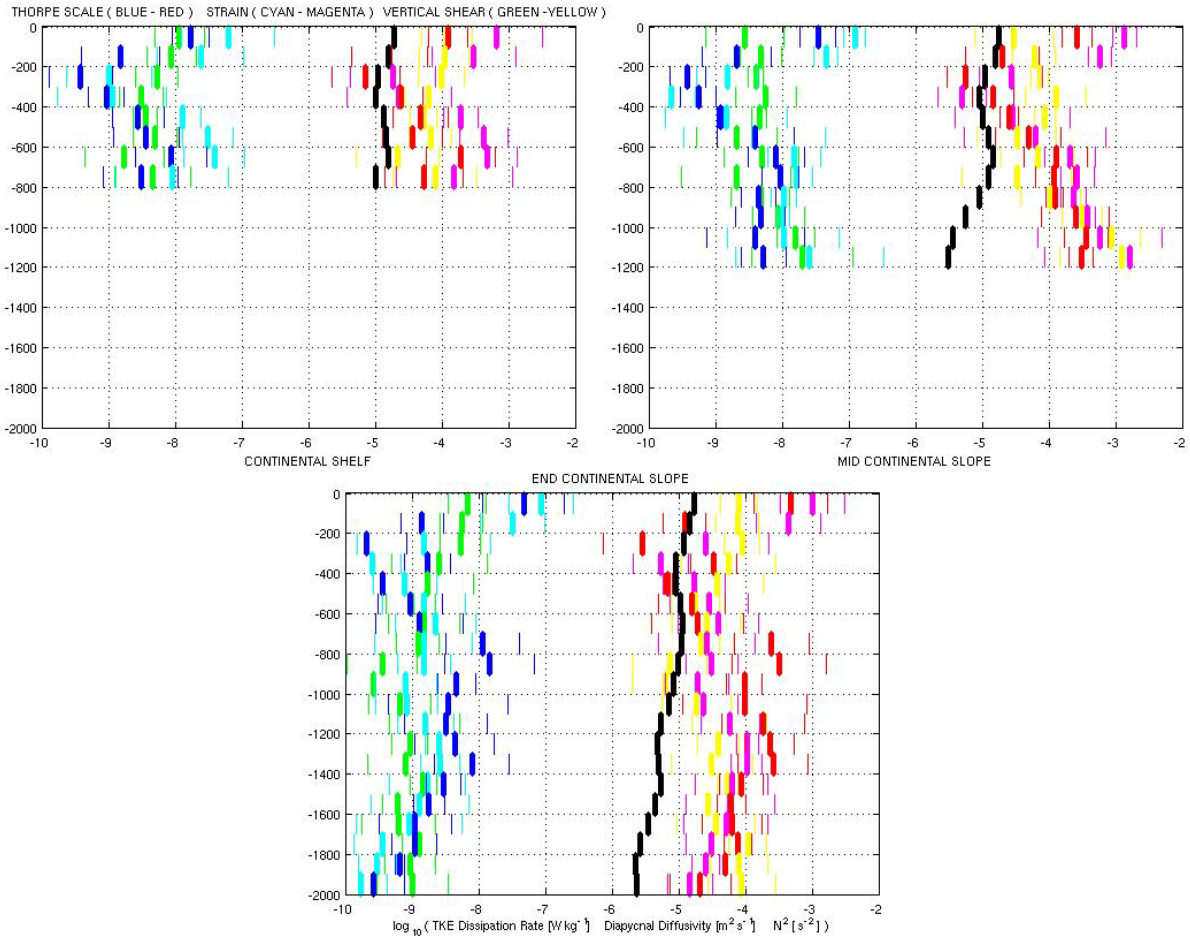

Figure 4.3: TKE dissipation rate and diapycnal diffusivity (thick coloured lines) averaged (100m depth range; Log_{10} scale for all variables) for the three different mixing methods at different continental slope regions (TOP LEFT shelf, TOP RIGHT mid slope and BOTTOM outer slope). Black line is the background stratification (N^2). Uncertainties are the expected factor of three or four for all mixing estimate approaches (thin coloured lines).

4.4 Implications of Mixing analysis over temperature profiles

In the previous section, three different methods were applied to CTD profiles to estimate diapycnal mixing. These finescale parameterizations agree in some parts of the

water column, particularly the MOW-NACW interfaces. However, to provide a robust value of mixing in a wider domain it is necessary to inspect other parts of the water-mass profiles. In this work, a particular problem is the lack of more extensive CTD data. Following Chapter 3, we now consider whether mixing estimates can be made using the more extensive XBT data.

Two important values to inspect prior to any further calculations are N^2 and $<N^2>$. These values can differ due to the presence of large-scale (Cores and Meddies) and small-scale (interleaving structures) MOW variability. Bray and Fofonoff (1981) suggested that N^2 and $<N^2>$ needed to be representative of the study area and compared with historical information. To determine the local average of N^2 to be used in the strain calculation it is important to consider the following. Strain methodology inspects the variability of the density gradient by using the squared buoyancy frequency (N^2) at different depth ranges; one is estimated locally (10m-40m) and the other one ($<N^2>$) is estimated from density difference over a much larger range (300m-500m). Fine-scale parameterization methods inspect the internal wave field spectrum, by normalizing against the Garrett-Munk model, in which N^2 is supposed to decreases monotonically downwards. However, here N^2 does not decrease monotonically downwards. Errors can be inferred by assuming, if N^2 is misinterpreted any mixing estimate value could increase by a factor of four () over the strain calculation. When the strain is calculated over an adequate vertical range for N^2, it is necessary to consider that the strain spectrum will be calculated over internal waves for which the wavelength exceeds the size of the salinity gradient misinterpretations.

Temperature profiles alone can provide additional information to analyse the strain of the water column. The strain is estimated from the temperature profile using the vertical derivative of vertical displacements and their spectra are used to calculate mixing estimates (Eriksen, 1980). The method has been applied over vertical sections where linear average temperature gradients are found (Dengler, 2002). In this study, strain from temperature profiles has been inspected using different approaches. The presence of temperature interleaving structures (related with the MOW) does not provide linear average gradients. Also, temperature can be found to be vertically decreasing non-monotonically (NACW-MOW interfaces and inside MOW) and the resulting strain then was unrealistic (with spikes from very small temperature gradients). However, salinity can be inferred from the

temperature profiles and combined to provide a stable density structure, and then the resulting strain can be analysed. The methodology is set out below.

4.4.1 Strain analysis over temperature profiles with inferred salinity and CTD test

The inferring salinity method has an in-built tendency to form stable density profiles, so that Thorpe-scale analysis, depending on overturns, is inapplicable for estimating turbulence. However, an alternative way to use fine structure for estimates of turbulence through the water column is via strain inferred from the density profile, in comparison with the background stratification ($N^2/\langle N^2\rangle$ - *1, Mauritzen et al*, 2002; also section 4.3.2). A strain test was applied using the three different approaches (Case I, II, III) to reconstruct salinity and hence density.

Figure 4.4 shows regression of the strain calculated from reconstructed density against strain calculated from the actual CTD data. Comparisons between the approaches showed that, without $\delta S/\delta T_D^+$ or when using it as in case II, the density profile is more or less "steppy" than that calculated from the actual CTD data. Using $\delta S/\delta T_D^+$ as in case III to reconstruct density, the resulting strain is better correlated with that calculated from the actual CTD data. These results encourage mixing analysis by consideration of strain, using salinity inferred by the method of section 3.4 with additional use of $\delta S/\delta T_D^+$ as in case III.

Using the case III approach (weighted average; section 3.4.1) to infer salinity and provide an N^2 profile, figure 4.5 shows the results of applying the strain method over three different CTD profiles [the CTD test]. Strain is found to be in a plausible agreement by using the case III approach. The three CTD profiles show that using a stable density ratio can provide an estimate of density gradient variability. If we are interested in an optimal match between the strain estimates, it is useful to focus on the MOW-NACW interfaces. The next step is to calculate the strain spectrum and identify the likely skill for mixing parameterizations and the resulting errors.

Density structure from temperature profiles with inferred salinity is found to be very similar to the original truth (density gradient correlation around $r=0.8$, between actual CTD and temperature profile with inferred salinity). It is essential prior any further applications or

calculations to test the strain method applied to inferred profiles by using the CTD test. Vertical variability of strain is found to be similar over vertical regions. However, in some regions strain is not well recovered due to salinity misinterpretation from the inference method. In chapter 3, the presence of salinity misinterpretation from the inference method and variance $0(10^{-4})$ was discussed over stratification. The CTD test of the strain estimates shows clearly where errors can be found, some of them are clear spikes in the profiles and others are identified.

Criteria used for removing spurious trends or spikes in a strain profile are based on the local vertical distributions (100m data range) found in the CTD test, in terms of whether the value exceeds two to three times the standard deviation. A local vertical average for standard deviation is preferred instead of a whole-column average, because strain variability is different in different depth ranges. The local vertical averaging range is 300m which is characteristic of MOW cores and meddies.

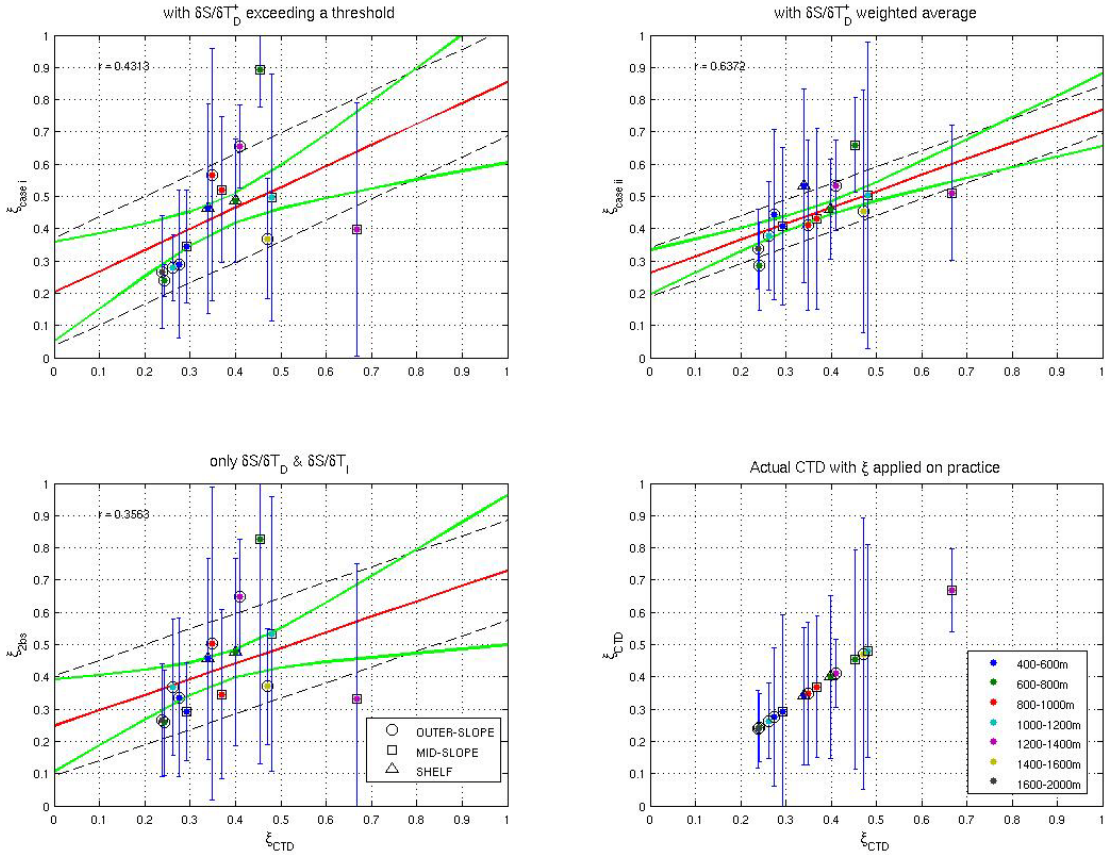

Figure 4.4: Strain calculated from reconstructed density *versus* strain calculated from the actual CTD data. The different points are for the various continental slope regions and depth ranges, averaged over the relevant CTD profiles. The two lower panels are: left using only $\delta S/\delta T_D$ and $\delta S/\delta T_I$ (case I), and right actual CTD. The two top panels are for reconstruction using also the coefficient $\delta S/\delta T_D{}^+$, left case II and right case III. Statistics of a weighted linear fitting are fitting standard error (black dashed lines), weighted mean value (red lines) and slope error confidence interval (green curves).

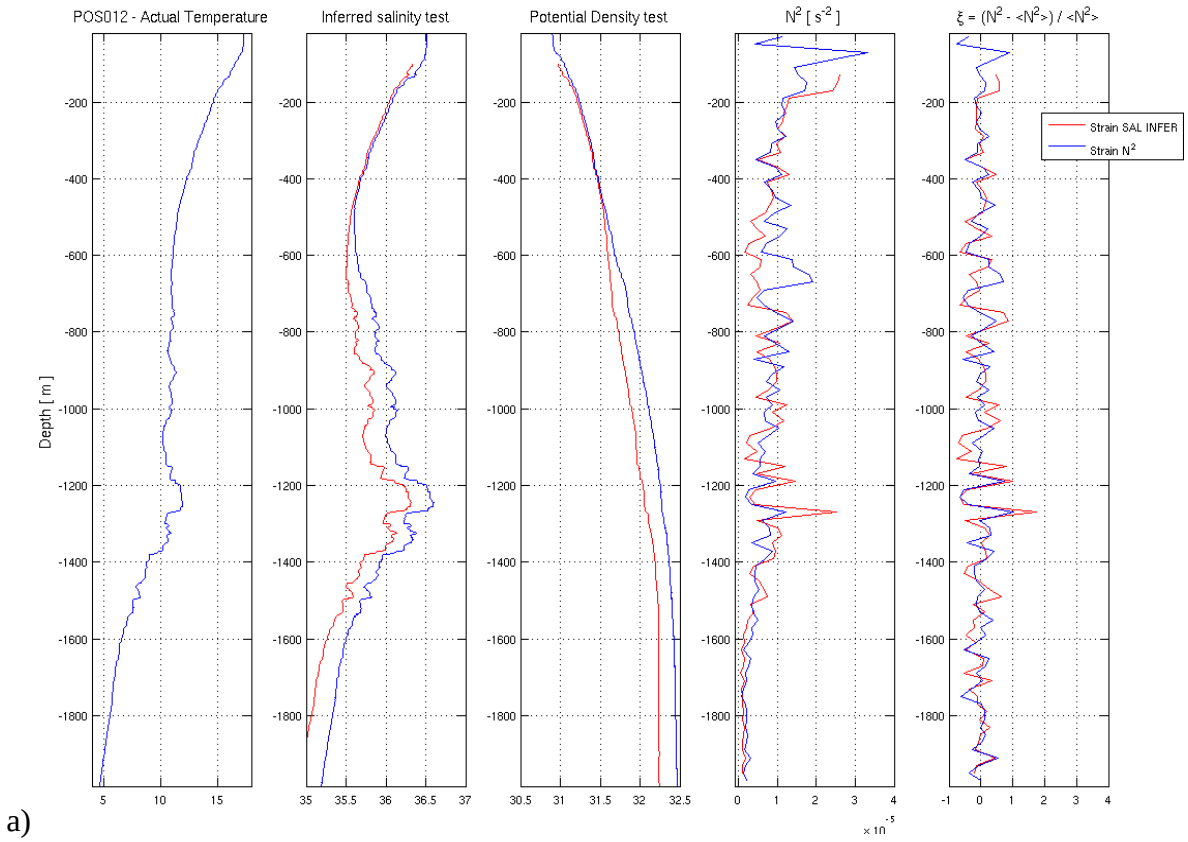

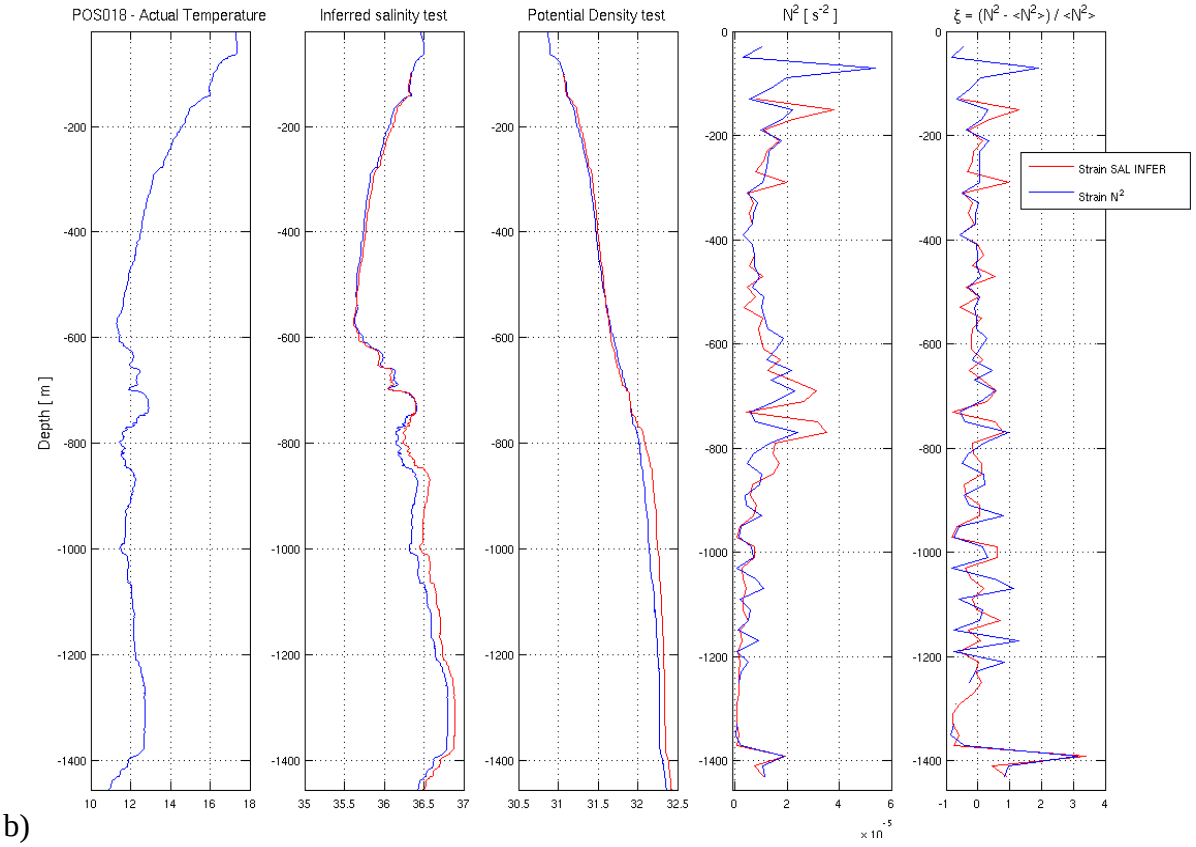

Figure 4.5: Strain calculation applying the CTD test (BLUE, actual CTD; RED, inferred salinity) to three CTD casts from the GO experiment, spring 2007, a) POS012 outer slope, b) POS018 mid slope and c) POS021 shelf. From left to right panels show temperature profile, salinity profiles, potential density profiles, N^2 profiles and strain profiles.

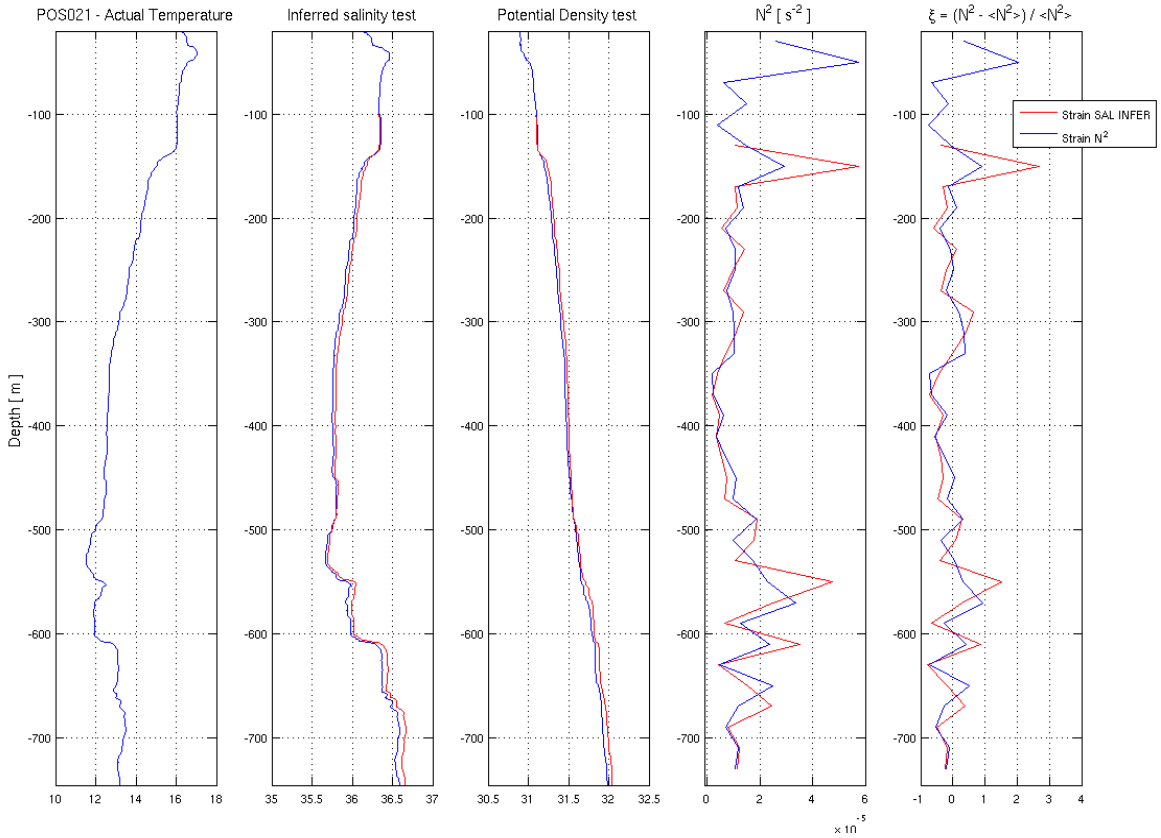

c)

Figure 4.5: Strain calculation applying the CTD test (BLUE, actual CTD; RED, inferred salinity) to three CTD casts from the GO experiment, spring 2007, a) POS012 outer slope, b) POS018 mid slope and c) POS021 shelf. From left to right panels show temperature profile, salinity profiles, potential density profiles, N^2 profiles and strain profiles.

In our method, uncertainties are around a factor of four mostly from salinity misinterpretation affecting the calculated strain. While the misfit can be minimised by removing larger spikes, there is still an error from remaining spikes with small magnitude. Spikes can be viewed as errors where gradients are incorrectly estimated. Strain is used in mixing estimate equations with a power of four, which means that any strain spike is magnified four-fold. However, using overlapping and local-average statistics improves the mixing estimates.

Table 4.2: Overall factor errors from K_z at all depths with calculation every 100m and 160m data range (see text)

Depth		Outer-Slope			Mid-Slope			Shelf			Overall		
N² / <N²>		300m	400m	500m	300m	400m	500m	300m	400m	500m	300m	400m	500m
All depths	10m	5.09	5.43	6.41	5.43	6.53	7.57	5.17	7.12	10.45	5.13	5.61	6.72
	20m	4.17	4.38	5.08	5.45	6.69	7.37	5.56	8.87	9.74	4.40	5.12	5.70

Table 4.3: Overall factor errors from K_z at all depths with calculation every 100m and 160m data range (see text) removing spurious individual values of strain around 100m data range and bigger than two standard deviations.

Depth		Outer-Slope			Mid-Slope			Shelf			Overall		
N² / <N²>		300m	400m	500m	300m	400m	500m	300m	400m	500m	300m	400m	500m
All depths	10m	3.68	3.88	4.60	9.97	16.18	17.07	4.93	7.18	10.77	4.63	5.78	6.77
	20m	4.13	4.63	5.44	3.44	4.64	5.14	4.94	8.68	10.14	3.94	4.77	5.43

Table 4.4: Variance (Log_{10}) of differences between K_z estimates (every 100m) at all depths and removing spikes bigger than 2std.

Depth		Outer-Slope			Mid-Slope			Shelf			Overall		
N^2 / $<N^2>$		300m	400m	500m	300m	400m	500m	300m	400m	500m	300m	400m	500m
All depths	10m	-7.92	-7.57	-7.27	-7.01	-6.74	-6.31	-6.85	-6.33	-5.95	-6.94	-6.17	-6.14
	20m	-8.04	-7.60	-7.37	-6.69	-6.61	-6.44	-7.14	-6.51	-6.19	-7.00	-6.02	-6.01

Table 4.5: Variance (Log_{10}) of differences between K_z estimates (every 100m) at all depths and removing spikes bigger than 2std, removing spurious individual values of strain around 100m data range and bigger than two standard deviations.

Depth		Outer-Slope			Mid-Slope			Shelf			Overall		
N^2 / $<N^2>$		300m	400m	500m	300m	400m	500m	300m	400m	500m	300m	400m	500m
All depths	10m	-8.28	-7.85	-7.46	-7.37	-7.33	-7.10	-6.98	-6.53	-6.23	-6.57	-5.63	-5.28
	20m	-8.06	-7.63	-7.39	-8.05	-8.51	-8.08	-7.12	-6.70	-6.45	-7.25	-6.07	-6.07

Tables 4.2 and 4.3 show the results of applying the CTD test and different ranges for calculating N^2 and $<N^2>$, as errors in K_z estimates. N^2 was calculated using 10m and 20m data ranges to consider the smallest scale for finestructure similar to salinity interleaving found in MOW. Errors are shown as factors relative to values using CTD salinity. Table 4.2 (no spike removal) shows that over the three regions the smallest factor is found with N^2 calculated over 20m and $<N^2>$ calculated over 300m and this is confirmed in the Overall entries. Table 4.3 (spike removal) shows similar results for N^2 and $<N^2>$ but the error factor can decrease in some cases. Looking at the actual values of K_z and using (Log_{10} of) the variance of estimates in Tables 4.4 and 4.5 the largest negative number will provide the smallest difference (due to the Log_{10}). Tables 4.4 and 4.5 confirm previous results that it is best to use N^2 calculated over 20m and $<N^2>$ calculated over 300m for application to the extensive temperature profile sources (XBTs). In Table 4.3, assessments showed that the best option provides confidence within a factor of 3.94 for mixing estimates.

This strain methodology was applied to XBT profiles over water column. Figure 4.6 shows the results of applying the strain method to a series of XBTs near a CTD cast (POS012). The inferred diapycnal diffivity (K_z) from both data sources only differs by factor of two for the nearest XBT temperature profile and around a factor of four for a more distant one. A wider assessment of the inferred diapycnal diffusivities for the available XBT data in the Gulf of Cadiz is presented in Chapter 5 (next).

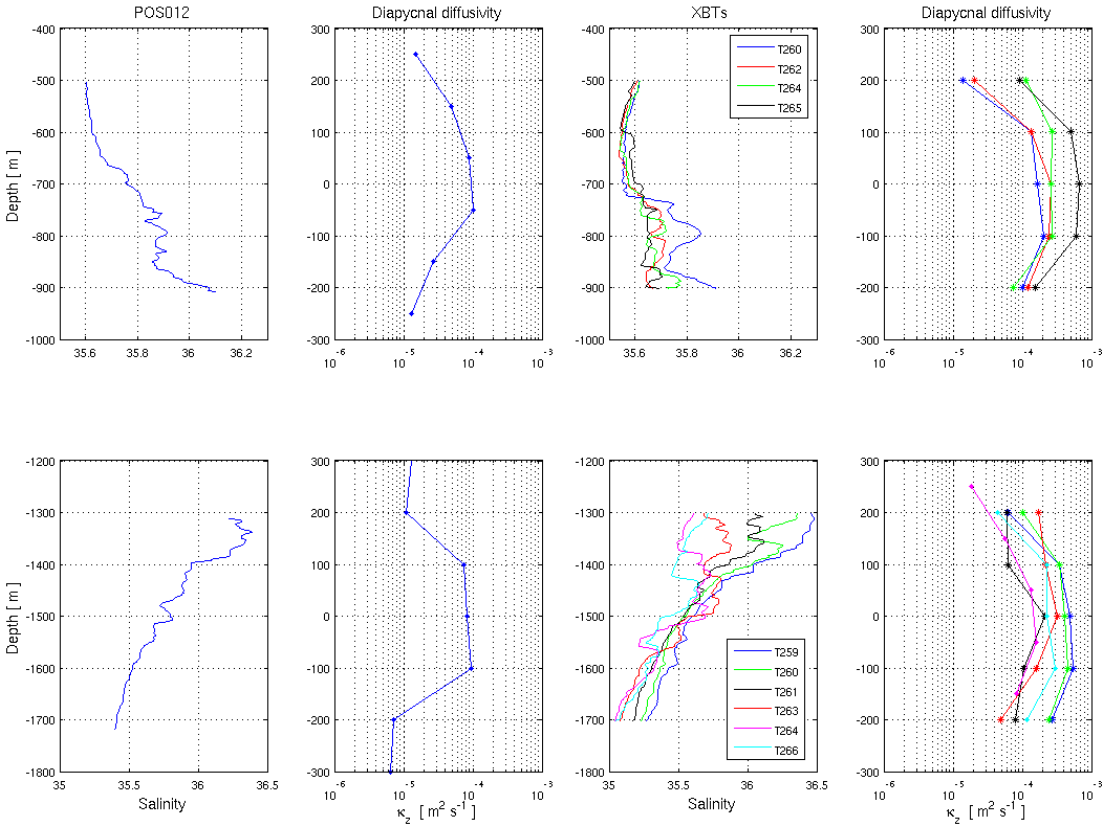

Figure 4.6: Diapycnal diffusivity results of applying the strain method to a CTD cast (POS012) and nearby XBTs. The TOP row shows the results from the depth range spanning the upper MOW-NACW interface, and the BOTTOM row shows results from the lower interface. From left to right, panels show CTD casts salinity and diapycnal diffusivity (κ_z), then XBTs inferred salinity and the resultant diapycnal diffusivity (κ_z).

4.5 Discussion

Different methodologies for estimating mixing are found to differ on fine scales, but reasonable agreement is found over the MOW-NACW interfaces. Tables 4.6 to 4.8 show the results from the mixing-estimation methodologies at different regions over the continental slope.

Table 4.6: Mixing parameterisations results: averages over the shelf (<1000m).

MOW & NACW Interface	Thorpe scale		Vertical shear		Strain		Strain (XBTs)	
	ε (x10^{-9}) W kg^{-1}	κ_z (x10^{-4}) m^2 s^{-1}	ε (x10^{-9}) W kg^{-1}	κ_z (x10^{-4}) m^2 s^{-1}	ε (x10^{-9}) W kg^{-1}	κ_z (x10^{-4}) m^2 s^{-1}	ε (x10^{-9}) W kg^{-1}	κ_z (x10^{-4}) m^2 s^{-1}
Upper	5.21±2.34	0.82±0.55	6.08±3.22	0.95±0.56	17.40±4.56	2.12±1.03	19.02±5.01	3.24±1.67
Lower	-	-	-	-	-	-	-	-

Note: Upper interface varies in depth from shelf to outer slope, from around 400m to 700m. Lower interface is more steady around 1400m to 1600m

Table 4.7: Mixing parameterisations results: averages over the mid slope (1000m to 1500m).

MOW & NACW Interface	Thorpe scale		Vertical shear		Strain		Strain (XBTs)	
	ε (x10^{-9}) W kg^{-1}	κ_z (x10^{-4}) m^2 s^{-1}	ε (x10^{-9}) W kg^{-1}	κ_z (x10^{-4}) m^2 s^{-1}	ε (x10^{-9}) W kg^{-1}	κ_z (x10^{-4}) m^2 s^{-1}	ε (x10^{-9}) W kg^{-1}	κ_z (x10^{-4}) m^2 s^{-1}
Upper	8.73±2.01	2.23±1.01	7.66±3.12	1.39±0.54	22.03±5.45	4.23±2.31	31.45±11.01	5.14±2.31
Lower	-	-	-	-	-	-	-	-

Table 4.8: Mixing parameterisations results: averages over the outer slope (>1500m).

MOW & NACW Interface	Thorpe scale		Vertical shear		Strain		Strain (XBTs)	
	ε (x10^{-9}) W kg^{-1}	κ_z (x10^{-4}) m^2 s^{-1}	ε (x10^{-9}) W kg^{-1}	κ_z (x10^{-4}) m^2 s^{-1}	ε (x10^{-9}) W kg^{-1}	κ_z (x10^{-4}) m^2 s^{-1}	ε (x10^{-9}) W kg^{-1}	κ_z (x10^{-4}) m^2 s^{-1}
Upper	4.70±1.74	0.62±0.48	4.68±1.89	0.59±0.14	5.25±2.31	0.85±0.43	8.83±3.45	2.34±0.94
Lower	5.63±2.43	0.87±0.60	5.87±2.87	0.93±0.82	16.04±5.13	1.25±0.73	20.97±6.78	3.73±1.13

Note: Standard deviation from averages was found to be around a factor of 2-3 for CTD casts and XBTs sources.

The Thorpe scale method applied to the CTD casts revealed the presence of large (>10m) density overturns and significant amounts of mixing. The vertical shear and strain methods applied to CTD casts likewise estimated enhanced mixing. However, due to the lack of coverage in the CTDs, the water mass variability and mixing cannot reliably be mapped over the region.

There was a good agreement in the mixing estimates for the MOW-NACW interfaces from all methods. On average the lower interface has the largest values of mixing parameters due to strong salinity gradients. The lower interface showed a permanent strong gradient O(10^{-3} salinity m^{-1}) which also can be found at the upper interface. In chapter 5 (next), the relation between density and salinity gradients and the presence of mixing is discussed.

Mixing estimates from XBT sources showed comparable results, due the short spatial and time separation between them; water mass structure was found to be very similar to that in the CTD casts. On the other hand, XBTs still show some discrepancies in mixing estimates, which confirms the large variability in time and space that MOW has.

4.6 Summary

In this chapter, three different methods of estimating diapycnal mixing are analysed: the Thorpe scale, Vertical shear and strain methods. The available conventional oceanographic data from the GO experiment were used to study diapycnal mixing in two steps. Firstly, apply these three methods using CTD casts. Secondly, use more extensive temperature profiles (XBTs) and infer salinity, then apply the strain method to estimate diapycnal mixing. Mixing estimates from strain method can provide values to be compared, a discussion is presented. Uncertainties are also discussed, particularly those originating from the strain method using temperature profiles with inferred salinity.

Chapter 5 Mixing, Internal waves and Local Circulation

5.1 Introduction

The purpose of the present Chapter is to explain the interplay of the local circulation, internal wave field and diapycnal mixing. Results of each topic were presented in previous chapters; now the different analyses are brought together for the Gulf of Cadiz: the evidence of MOW structures, the influence of the internal wave field and the implied finescale mixing are addressed all together.

From the literature, the MOW undercurrent is known to travel along the continental slope from Gibraltar Strait to Cape St Vincent, increasing in volume by ten times with diluted salinity. The MOW is made up either of detailed cores or Meddies. The increase in volume has been related to the intense vertical and lateral mixing, which has been diagnosed observationally (*Price, et al* 1993; *Baringer and Price*, 1997a,b) but poorly quantified. The MOW cores and Meddy structures are generated by MOW displacements by the internal tide and their final fate is controlled by vertical mixing (*Serra and Ambar*, 2002; *Serra et al* 2005). However, models of MOW undercurrent have been applied using imposed values for vertical mixing (due to the lack of measurements).

In this chapter is presented a regional map of mixing in cross sections where a MOW signal and NACW layers are present. Diapycnal mixing will now be estimated and mapped by using the extensive XBT temperature profiles with inferred salinity. Also alternative energy sources from wind and bottom stress are considered to quantify the amount of turbulence provided by them. Finally a mechanistic overview of mixing and energy sources is presented and discussed.

5.2 Diapycnal mixing along/across the Gulf of Cadiz Continental slope

The internal wave field has been analysed (Chapter 2) using current time series and local stratification for a depth range of 700m to 1000m over the region through which the MOW spreads, over the continental slope in the Gulf of Cadiz. The MOW undercurrent is influenced by tides, particularly M2, while never stopping. The MOW undercurrent continuously flows at deeper moorings (800m, 900m, 1000m approx) with high speed (0.2-0.4 m/s). However, in one observation in the shallowest (700m approx) mooring, the MOW

undercurrent flows southward during neap tides. Also the vertical shear structure is influenced by tides, mostly over the shelf. At the same location of the time series measurements, the MOW stratification is found to be highly variable.

Mixing diagnostics found diffusivity estimates to be larger ($5x10^{-4}$ -$1x10^{-3}$ m^2 s^{-1}) at interfaces. This enhanced mixing occurs mostly over the mid-slope of the continental slope (where there is broad agreement between the estimates from the different mixing analyses). Over the outer slope and shelf, mixing can be enhanced but not as much as mid-slope. Internal wave characteristics analysis, for the M2 frequency (at mid-slope) with the observed background stratification, found critical conditions over the mid slope, which were confirmed by the presence of strong currents at the M2 tide frequency.

Diapycnal mixing over the outer slope and shelf was found to be enhanced ($1x10^{-4}$ - $5x10^{-4}$ m^2 s^{-1}) but significantly less than over the mid slope. The internal tide characteristics show critical slope conditions over the mid slope, which were confirmed by the time series records of tidal current speed which was found to be the strongest over this domain (0.05-0.1 m^2 s^{-1}, at 700m depth approx). On the outer slope, conditions for supercritical slopes were found in deeper regions (>1500m).

Either over the mid slope, the outer slope or shelf, the mixing parameterization estimates suggested significant mixing at the MOW-NACW interfaces. This diagnostic is supported by using only CTD profiles. Historical data reveal the presence of these interfaces defined mostly by the salinity contrast between layers, rather than their density contrast. Based on salinity profiles, the interfaces between layers have the strongest gradients O(10^{-2} - 10^{-3} salinity per metre). The strength of the gradients can vary as is revealed by the historical data and the sampling from the GO experiment. MOW interfaces can be detected from inferred salinity using temperature profiles (XBTs). In chapter 4, estimates of mixing were obtained only using temperature profiles with inferred salinity with an error factor 3-4.

A regional view of mixing is made using the XBTs cross sections taken over the Gulf of Cadiz (Figure 5.1, summarised in Chapter 2 and 3), including four sections: one main section over the seismic line and three cross sections forming a star shape, mostly over the shelf. Temperature profiles were used with inferred salinity calculated with the optimal

choice (weighted average for $\delta S/\delta T_D$, chapter 3), providing a stable profile at MOW interfaces. The strain method is used to calculate the regional mixing along the sections.

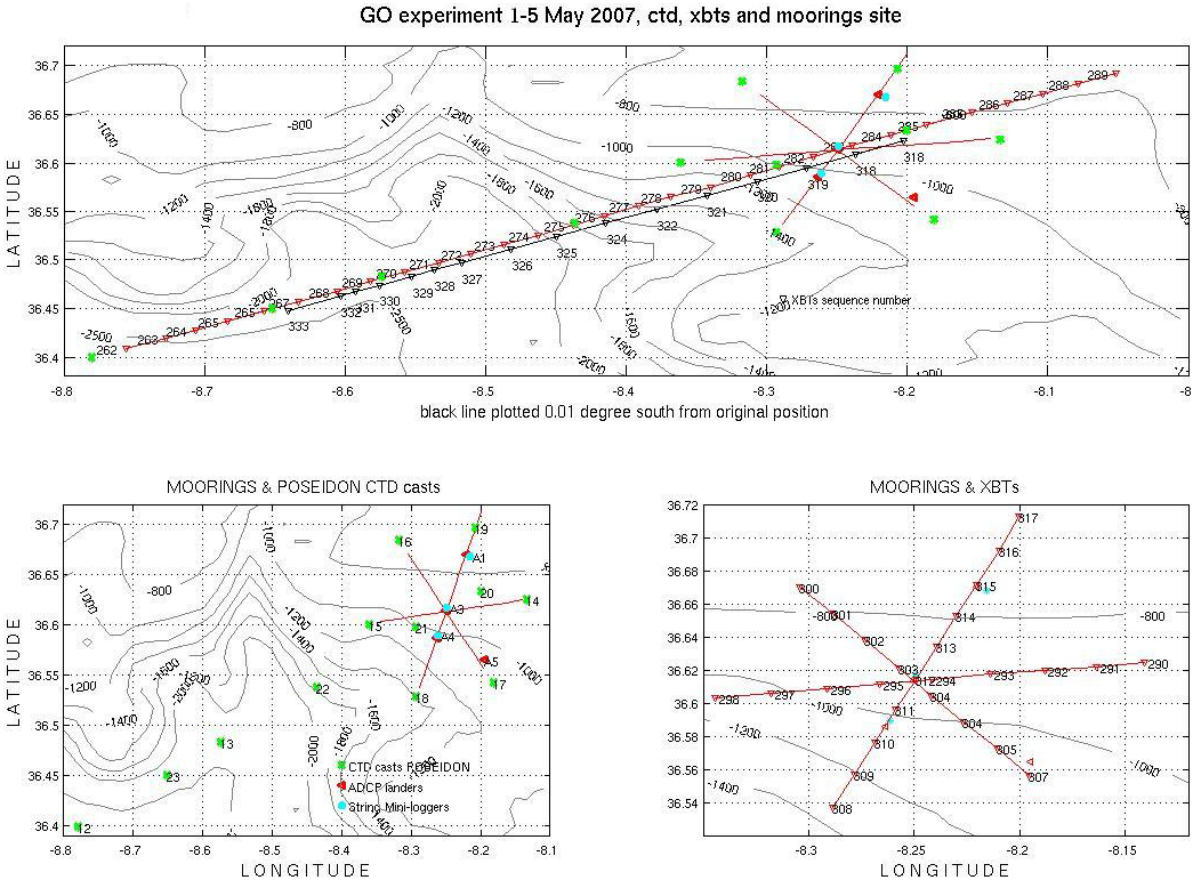

Figure 5.1: XBTs data location map during the GO experiment in Spring 2007. TOP plot: XBTs deployed over the main seismic line over the continental slope (one cross section eastwards and another westwards). BOTTOM: left hand side, data source location of CTD casts and moorings; right hand side, star shape cross sections where XBTs were taken.

Figure 5.2 shows the sections of TKE dissipation rate and diapycnal diffusivity diagnosed in the GO experiment (1-5 May 2007). Both calculations are directly related (summarised in chapter 4). Salinity contours highlight the location of the MOW; the TKE dissipation rate at MOW interfaces is large $O(10^{-7}$ W $kg^{-1})$, also at fronts at mid-depths (600m-1500m). Along the outer slope also, enhanced TKE dissipation reaches $O(10^{-7}$ W $kg^{-1})$ associated with MOW detached from the slope. Enhanced diapycnal diffusivity is found at water mass interfaces [$O(5x10^{-4}$ $m^2s^{-1})$], along the front at mid-depths [$O(6x10^{-4}$ $m^2s^{-1})$], and also within the MOW detached from the slope [$O(3x10^{-4}$ $m^2s^{-1})$]. Mixing parameterizations reveal increased mixing always in the mid-slope and shelf, where the water-mass interfaces are related to the strong salinity gradients extending from the mid-slope to the shelf. Over the shelf, the salinity gradient is less strong $O(10^{-4}$ salinity per metre) but estimates of enhanced mixing can be found.

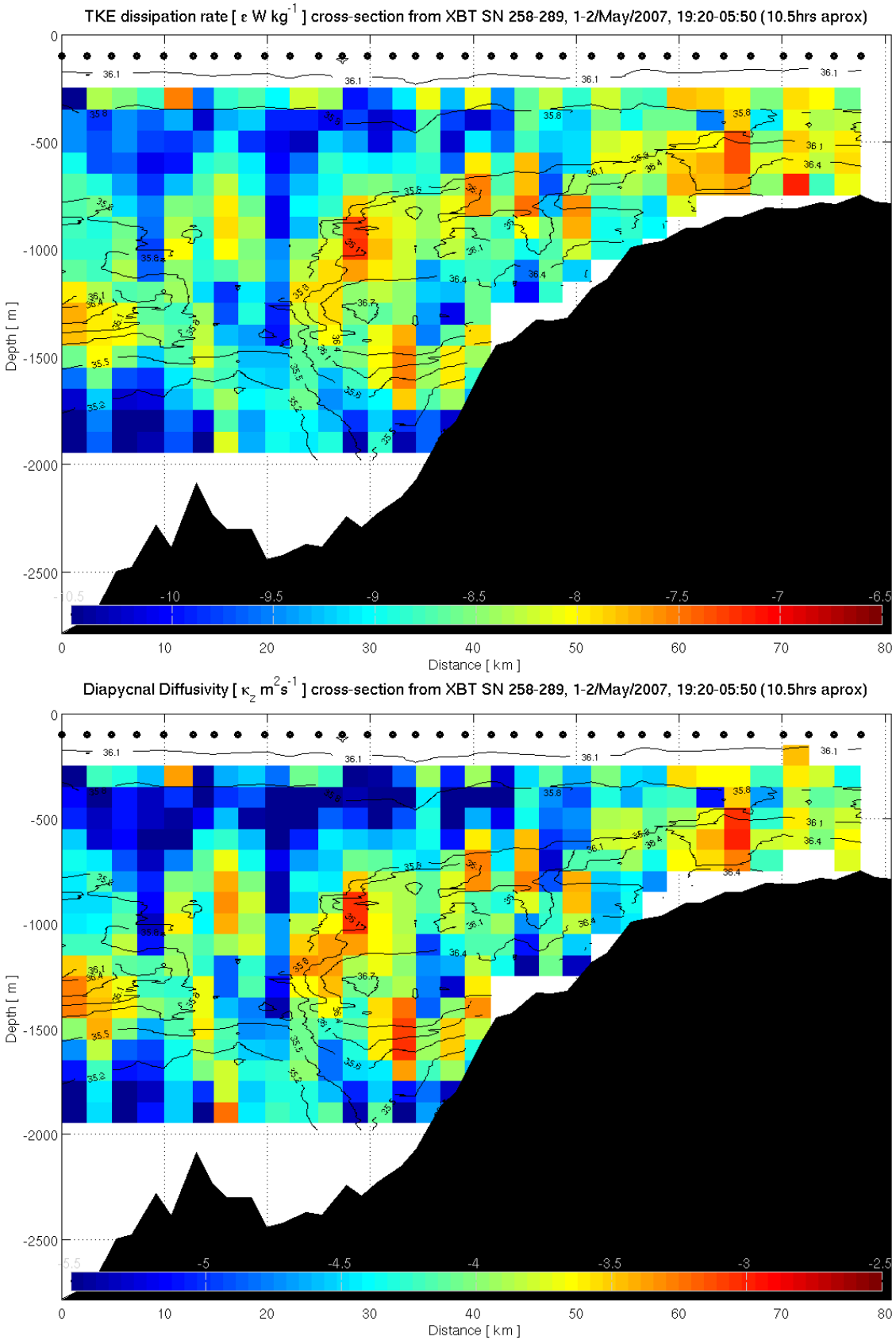

Figure 5.2: Estimates of mixing using finescale parameterizations with XBTs profiles and inferred salinity, with salinity contoured in the background. TOP panel: TKE dissipation rate [Log_{10} (W kg^{-1})] cross section over the main seismic line during the GO experiment. BOTTOM panel: diapycnal diffusivity [Log_{10} (m^2s^{-1})] along the same cross section calculated using *Osborne* (1980) parameterization.

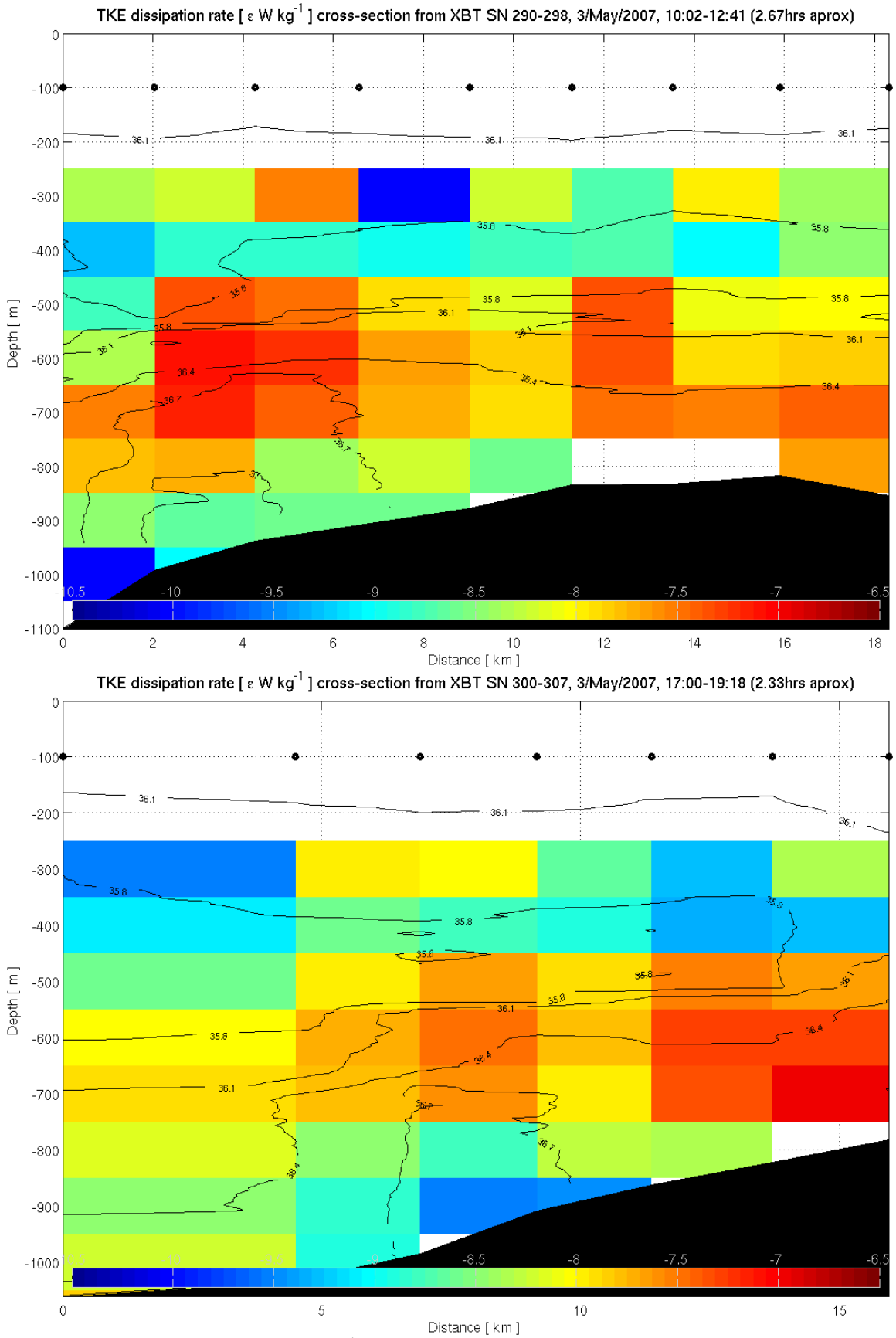

Figure 5.3: TKE dissipation rate [ε W kg^{-1}] cross sections calculated using data from XBTs over the STAR shape lines during the GO experiment.

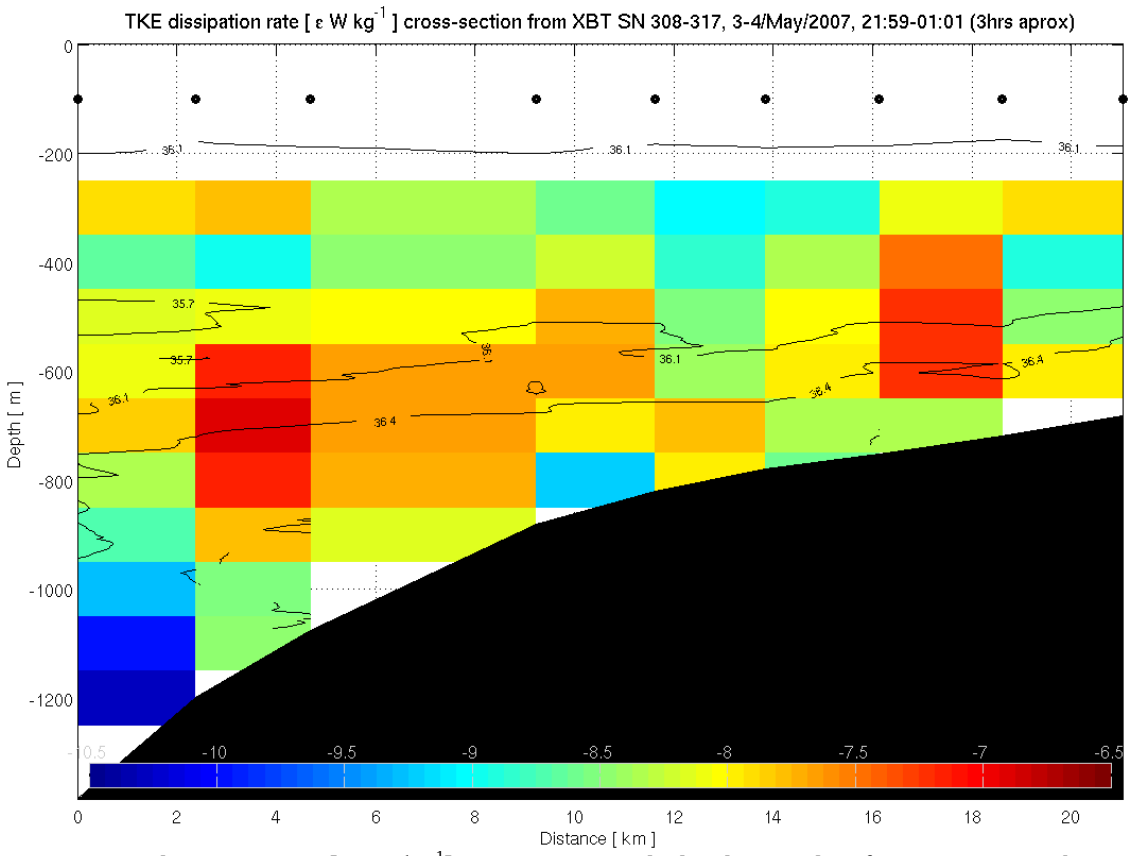

Figure 5.3: TKE dissipation rate [ε W kg^{-1}] cross sections calculated using data from XBTs over the STAR shape lines during the GO experiment.

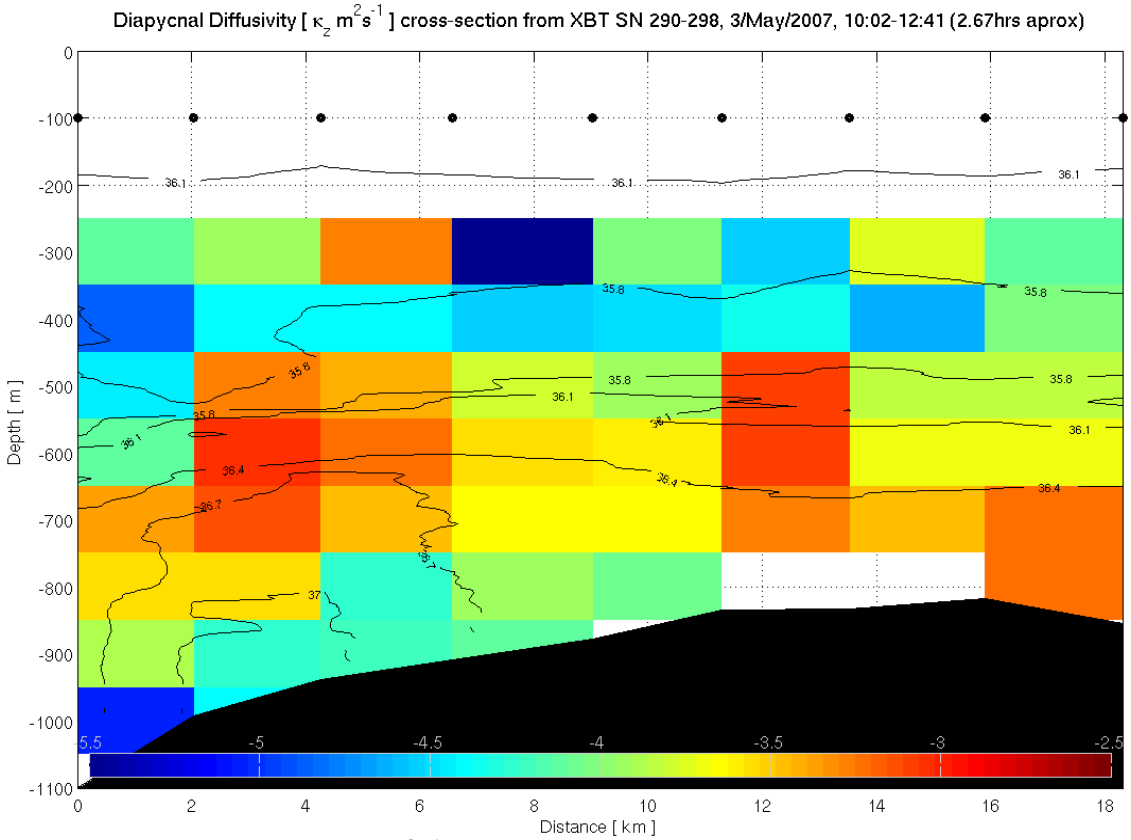

Figure 5.4: Diapycnal diffusivity [κ_z m^2s^{-1}] cross sections calculated using data from XBTs over the STAR shape lines during the GO experiment.

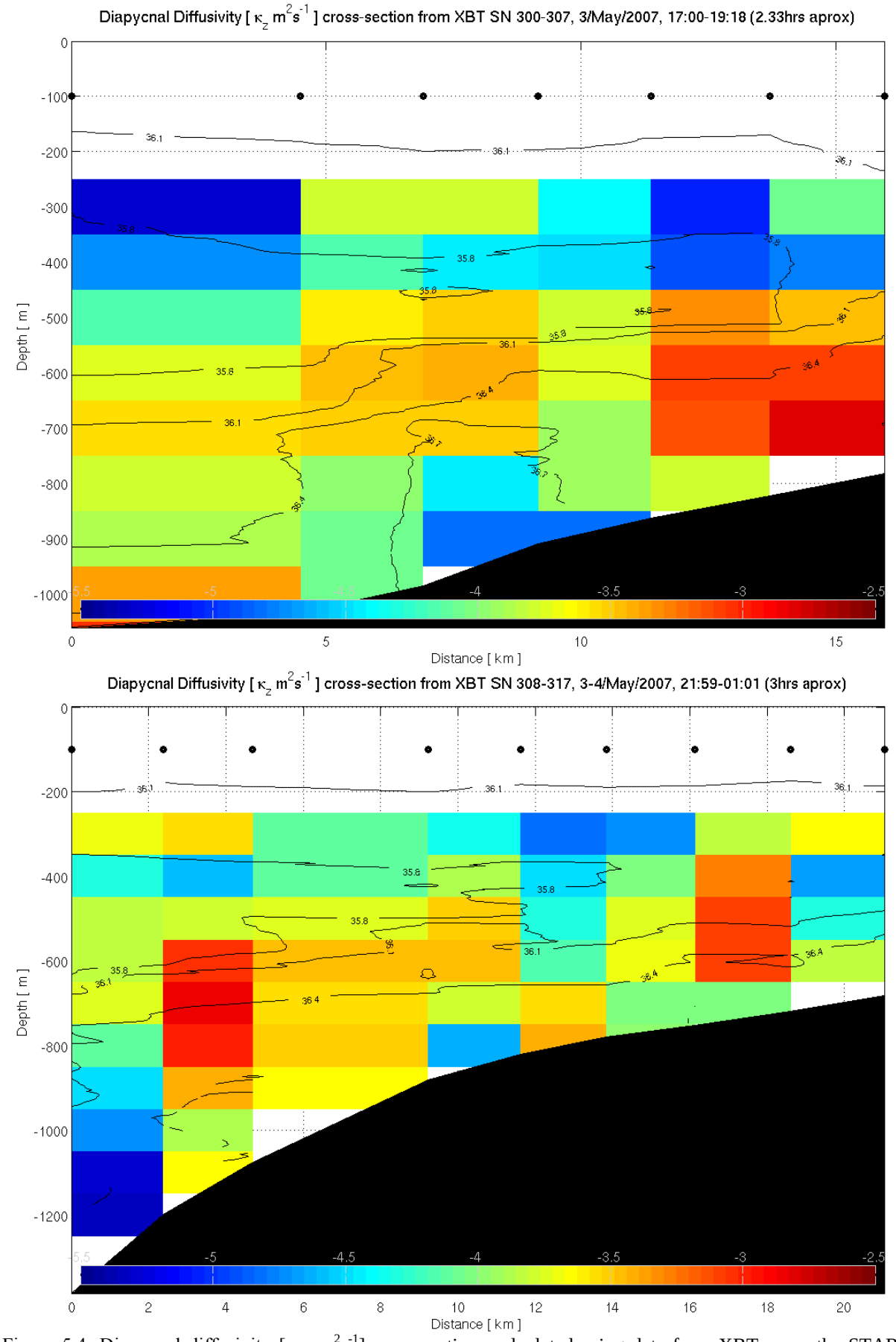

Figure 5.4: Diapycnal diffusivity [κ_z m^2s^{-1}] cross sections calculated using data from XBTs over the STAR shape lines during the GO experiment.

Figures 5.3 and 5.4 shows the cross sections of TKE dissipation rate and diffusivity along the star shape lines over the mid-slope and shelf. Three cross sections reveal that over the interface highlighted by salinity contours, the TKE dissipation is relatively enhanced O($3x10^{-7}$ W kg^{-1}). The present sections follow one another in less than a semidiurnal cycle. In relation to the previous plot the elapsed time is around three quarters of a day. In all the sections, the diapycnal diffusivity is found to be large over the mid slope and shelf [O($8x10^{-4}$ m^2s^{-1})]. The salinity gradient over the interfaces is also relatively strong, O(10^{-3} salinity per metre). These mixing estimates can be compared directly with those obtained using CTD profiles because they were made for the same days, however the regional patterns of mixing estimates are less correlated because the MOW signal varies so fast, even in less than an hour at similar positions along the Continental Slope.

Figures 5.5 and 5.6 shows the estimates of diapycnal diffusivity calculated using finescale parameterization for XBT profiles with inferred salinity from the GO experiment during 19-20 April 2007. The MOW structure in figure 5.5 is found to be more extended towards the outer slope than in other cross sections. There is large diapycnal diffusivity at the upper interface [O($2x10^{-4}$ m^2s^{-1})], lower interface [O($5x10^{-4}$ m^2s^{-1})], at the front over the outer slope [O($3x10^{-4}$ m^2s^{-1})], and considerable patchy mixing inside the MOW [O($8x10^{-4}$ m^2s^{-1})]. This MOW structure differs in detail from that observed ten days later (c.f. Figure 5.2). Figure 5.5 also shows the mixing estimates for the repeated section; a MOW structure is highlighted by salinity contours. The MOW signal is expanded in the outer-slope lower interface and the upper interface is detected at around 700m as in previous cross sections. Diapycnal diffusivity is found to be large at the upper interface over the mid slope [O($3x10^{-4}$ m^2s^{-1})] and outer slope [O($5x10^{-4}$ m^2s^{-1})], at the front over the outer slope [O($3x10^{-4}$ m^2s^{-1})], and there is some patchy mixing inside the MOW reaching values O($>7x10^{-4}$ m^2s^{-1}). In both plots of Figure 5.5, the diagnosed mixing decreases towards the shelf or shallower region, with the exception of a couple of profiles (Figure 5.5 upper). Three cross sections (Figure 5.6) were made in a star shape between the previous sections and results revealed that diapycnal diffusivity is enhanced O($2x10^{-4}$ m^2s^{-1}) at the MOW-NACW interface, while some enhanced mixing occurred towards the shelf as in Figures 5.2, 5.3. These cross sections were made during less than a diurnal cycle. All the sections (Figures 5.2 to 5.6) occurred during spring tides.

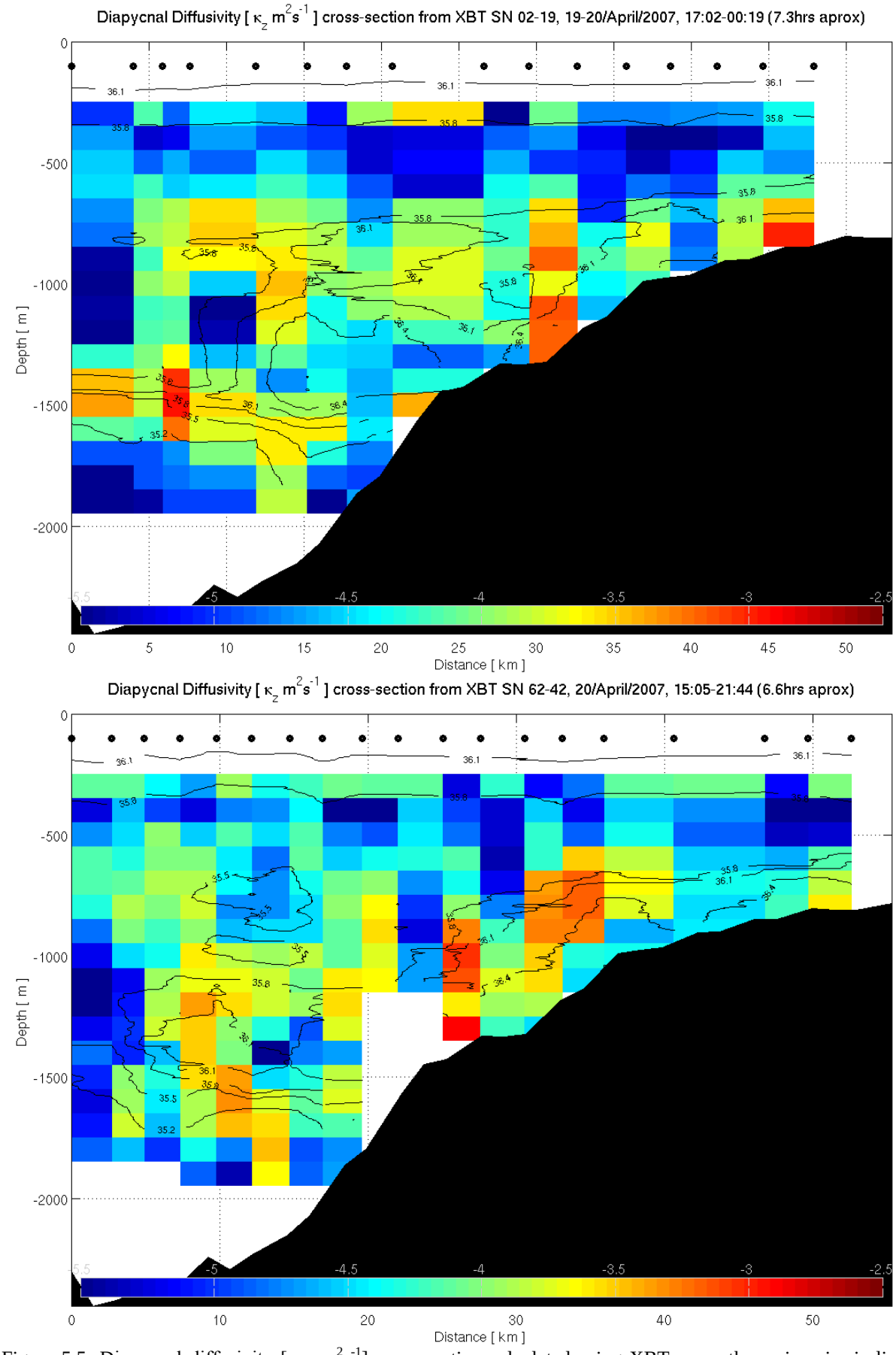

Figure 5.5: Diapycnal diffusivity [κ_z m^2s^{-1}] cross section calculated using XBTs over the main seismic line during the GO experiment.

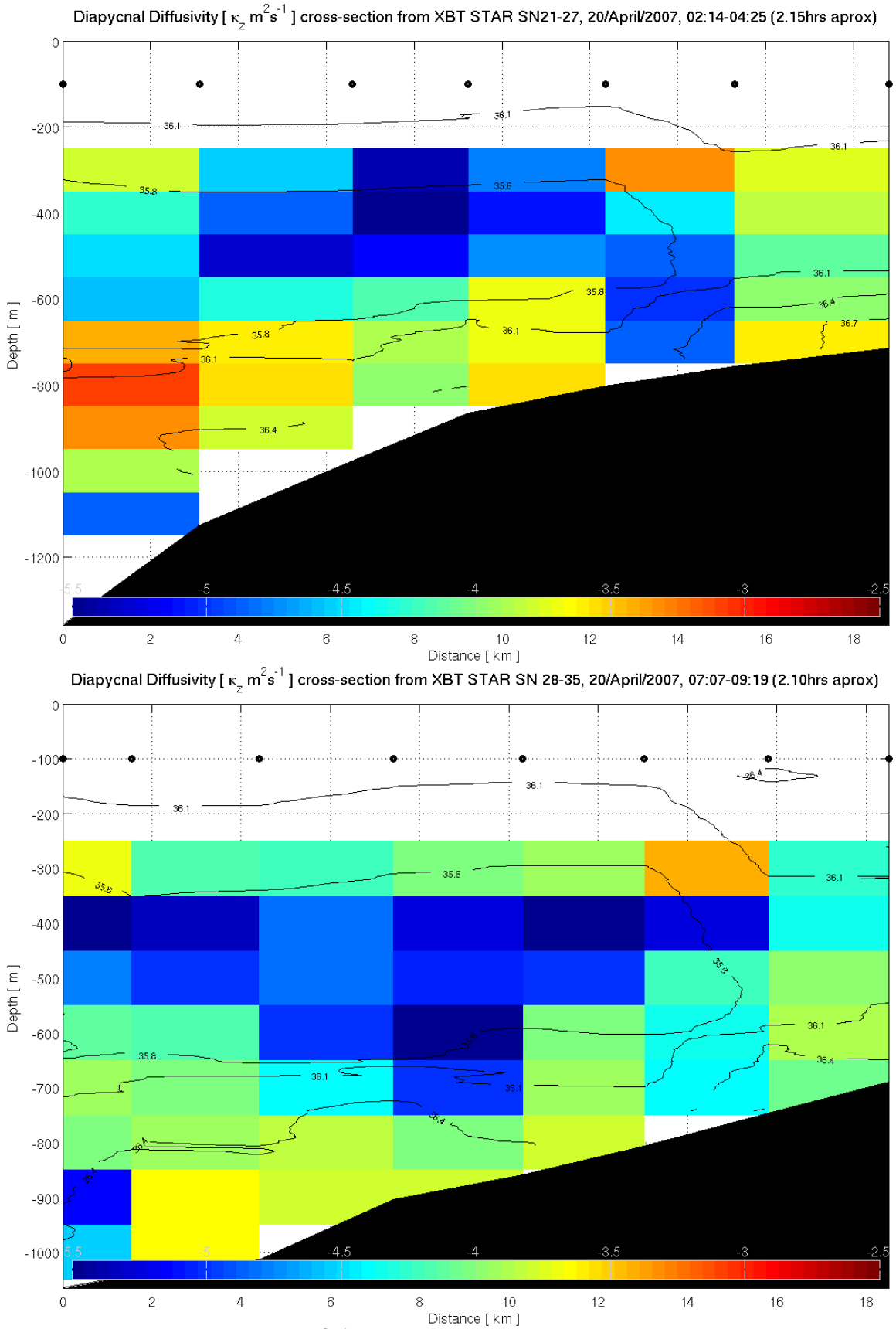

Figure 5.6: Diapycnal diffusivity [κ_z m^2s^{-1}] cross sections calculated using XBTs over the STAR shape lines during the GO experiment.

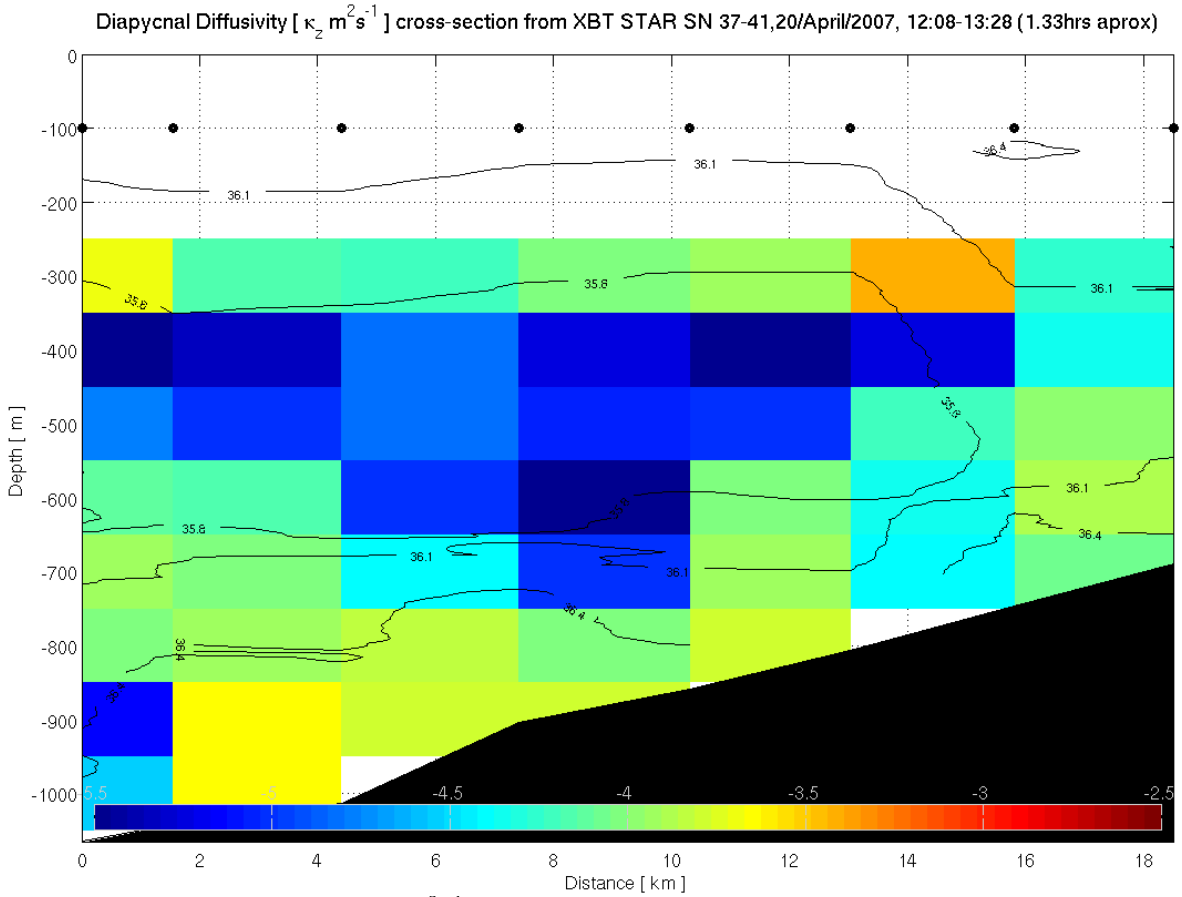

Figure 5.6: Diapycnal diffusivity [κ_z m^2s^{-1}] cross sections calculated using XBTs over the STAR shape lines during the GO experiment.

Two more cross sections (Figure 5.7) providing mixing estimates were available over the main seismic line, revealing two different MOW structures. In both cases, diapycnal diffusivity was found to be large on the upper interface [$O(3x10^{-4}$ m^2s^{-1})], lower interface [$O(5x10^{-4}$ m^2s^{-1})], at the front over the outer slope [$O(6x10^{-4}$ m^2s^{-1})], and considerable [$O(10^{-4}$ m^2s^{-1})] inside the MOW across the slope.

In all the cross sections, it is clearly seen that there is less mixing in the NACW layer. There is though enhanced diapycnal diffusivity $O(2x10^{-4}$ m^2s^{-1}) above the NACW in the surface mixed layer, as well as over the shelf, reaching $O(4x10^{-4}$ m^2s^{-1}). Due to the presence of the NACW layer and the lack of mixing there, the interactions between the surface mixed layer and the MOW undercurrent are relatively weak.

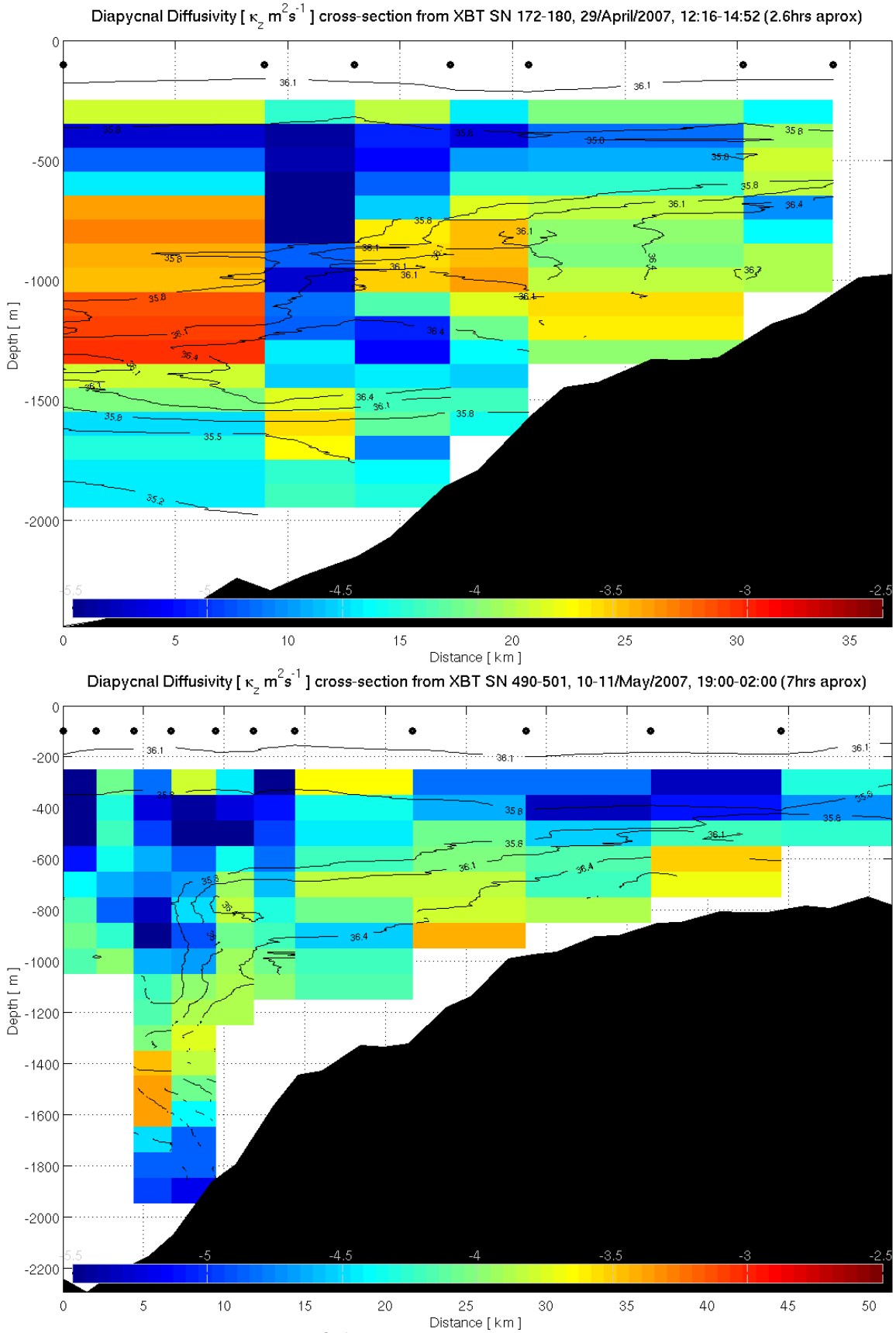

Figure 5.7: Diapycnal diffusivity [κ_z m^2s^{-1}] cross sections calculated using XBTs over the main seismic line. TOP was done on 29 April, between figures 5.5 and 5.2. BOTTOM was done on 10-11 May, 9 days after Figure 5.2.

On the mid-slope and shelf, tidal processes can become more important and affect the strength of turbulence. The MOW current is expected to experience strong bottom friction, particularly at the early stage of travelling down the slope. There is also more turbulence at shallow depths over the shelf.

5.3 Surface and Bottom stress

In this section, the influences of boundary stresses are discussed. External forces can either provide energy to the system or act to dissipate the motion. Using Ekman layer analysis, energy from wind and tidal currents was considered.

Ocean currents interact with the boundaries at the surface and bottom where effects of friction can be seen in the current shear. In both, surface and bottom, stresses act and affect the boundary layer. With the earth's rotation this region is known as an Ekman layer and can be seen in the ocean as a deflection of the current shear. Figure 5.8 shows the evidence in speed and current direction (mostly clockwise) of an Ekman layer modulated by barotropic flow [some events are highlighted as the strongest change of current direction, however the spiral can be found in smaller scale (<10m)], at other sites the evidence of Ekman spiral was found to be even larger (>50m). Also, evidence comes from the time series analysis (Chapter 2) over the tidal analysis phase and low-frequency spectrums.

From the perspective of the ocean currents, they experience surface and bottom stress from the winds and topography. These forces at the boundary alter the shear and effects of one layer can be observed on adjacent layers. A stress at the boundary can induce an Ekman spiral, the sense of rotation of the spiral depends on the position of the boundary layer. Stress in the ocean is expressed as:

$$\tau = \rho A_Z \frac{\partial u}{\partial z} \qquad (5.1)$$

where A_Z is the eddy viscosity. A stress at a boundary can be represented by:

$$\tau = \rho C_D U^2 \qquad (5.2)$$

where C_D is the drag coefficient (obtained experimentally) and U represents the speed of the forcing agent relative to the ocean current. Over the surface, wind stress can be expressed

using $\tau_a = \rho_a C_a W^2$ ($\rho_a = 1.3$ kg m^{-3} is the air density, C_a air drag coefficient and W is the wind speed). On the bottom, tidal currents stress can be represented using $\tau_b = \rho_w C_b U_b^2$ ($\rho_w = 1030$ kg m^{-3} is a reference water density at the bottom, C_b bottom drag coefficient and U_b is the observed current speed near to the bottom). These air and tidal stress expressions *(N m^{-2})* have been widely used (*Gill*, 1982; *Pond et al*, 1983). Also the stress can be represented as a "friction velocity" U_* defined as $U_* = \sqrt{C_D U_b^2}$.

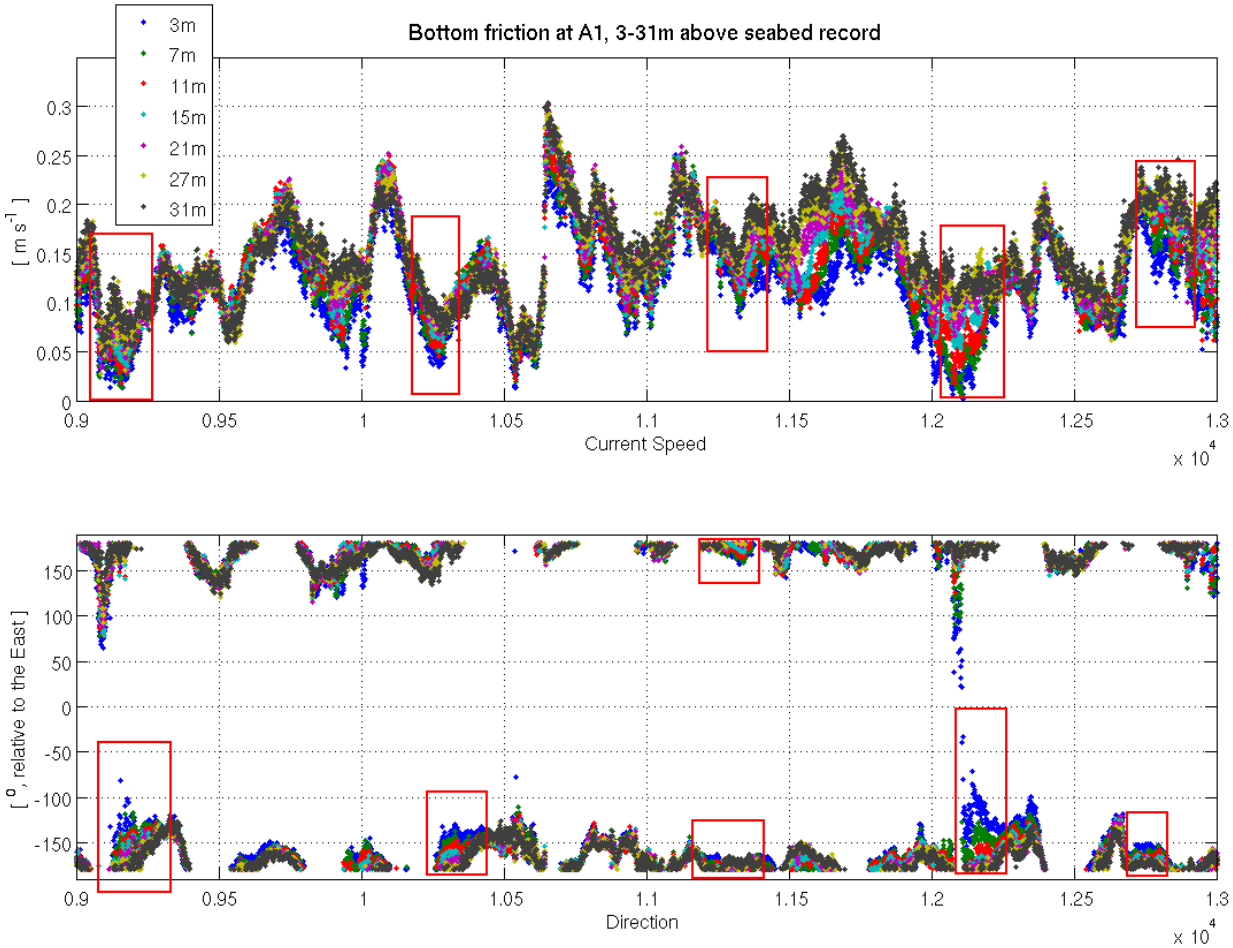

Figure 5.8: Bottom records from ADCP mooring (A1) showing (Sample number 9000-13000, related to April 30th – May 6th 2007) the evidence of current speed and direction of an Ekman layer (red boxes, some strong events).

The tidal stress of the bottom boundary affects the current shear; this can be studied with near-bottom records of current velocity. This bottom boundary shear has been studied (Gill, 1982); the shear affects the velocity over layer above sea bed as a sign of been stopped by stress. The layer below the main Ekman layer [on smaller scale, few metres] is known as logarithmic layer where turbulent friction greatly exceeds the Coriolis force.

The bottom stress is usually evaluated near to the bottom speed (3m in practice). Another expression to be used as the layer of influence of Coriolis parameters is the Ekman transport and can be expressed by:

$$Q_E = \frac{\tau}{\rho_w f} \qquad (5.3)$$

with $f = 0.87 \times 10^{-4}$ at Latitude 35.6º.

Figure 5.9 shows the results from the surface Ekman layer analysis: wind speed is gradually increasing and is strong during the second half of the time series, predominantly north-westerly, and from 400hrs changes to south-westerly. Considerable effects from surface winds were present at least for six days (144 hours) over the strong wind period. Ekman transport reaches its maximum magnitude (2.5 m^2s^{-1}) in the second half of the time series. The large Ekman layer in the surface effect can be reflected in an increase of transport. Also, energy dissipation or turbulence can be present affecting the local stratification.

Studies over our study (GO experiment) area suggested that MOW flow was found to speed up when the wind was strong and it was assumed that meteorological forcing plays an important role over the MOW signal (*Grundlingh et al*, 1981). In our records the strong wind signal (300hrs to 500hrs, around the April 28th to May 9th) happens when some cross sections of XBTs were made (Figure 5.2, 5.3 and 5.4). The salinity contours suggest that a big MOW signal is passing the area and measurements (Figure 2.7) suggest high MOW velocity during the same period (>0.30 ms^{-1}). If wind is accelerating the MOW flow down and along the slope the interaction happens at an early stage when MOW is on the shelf and closer to the surface.

The logarithmic layer was calculated only at A1 [A1 first bin at 3m above seabed; the measurements from other sites were not very close to bottom, first bin at 10m above seabed]. The friction velocity value was found to be large (>0.015 ms^{-1}) during some events [z_o<0.5m, comparable with values found in the literature O(>0.3m) of large layering effect]. A1 was the site with the weakest current from the whole moorings set; the current speed was found to be stronger at other sites (A3, A4 and A5) by comparing currents measurements at 10m above seabed.

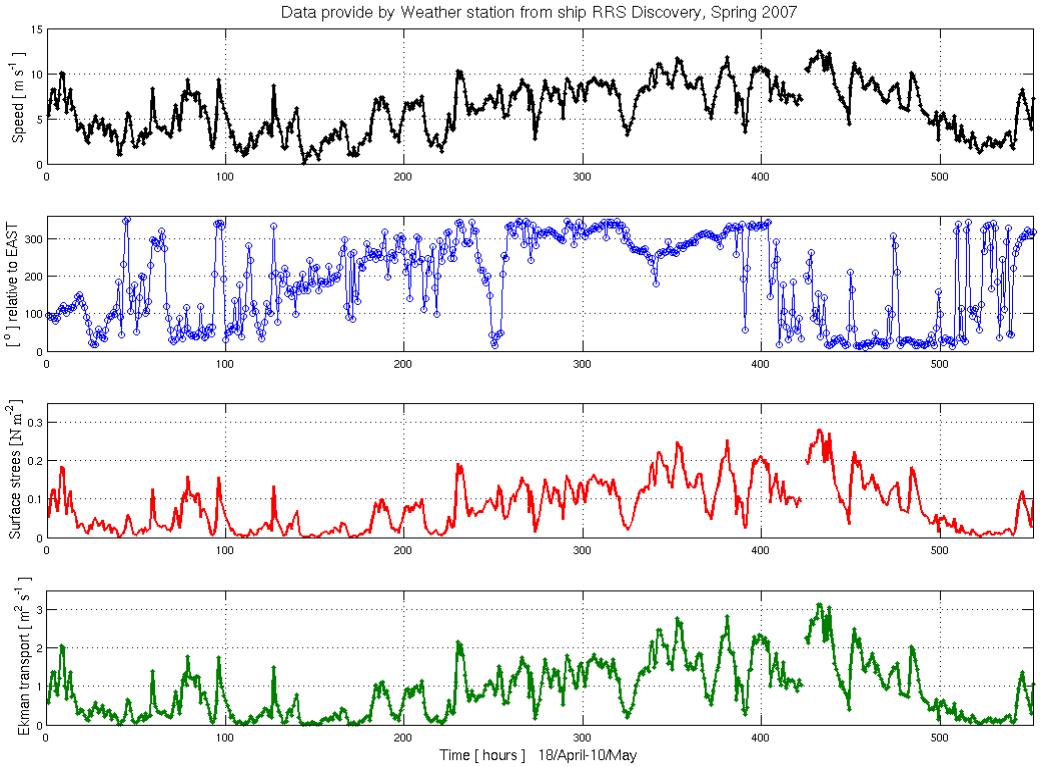

Figure 5.9: Ekman layer analysis results for surface stress using data provided from RRS Discovery during the GO experiment. TOP panel wind speed, TOP-MIDDLE panel wind direction, BOTTOM-MIDDLE panel calculated surface stress and BOTTOM panel calculated Ekman transport.

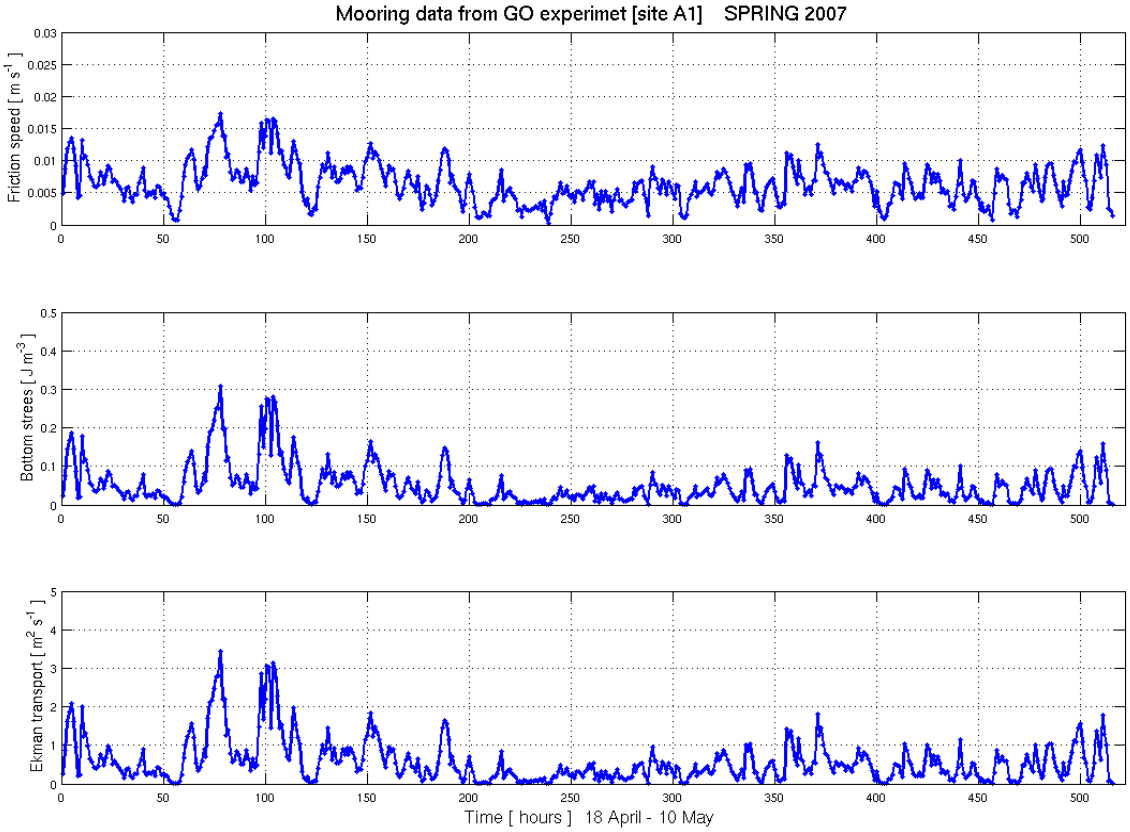

Figure 5.10: Ekman layer analysis results for bottom stress using data from A1 site ADCP mooring located on the continental slope during the GO experiment. TOP panel calculated friction velocity, MIDDLE panel calculated bottom stress and BOTTOM panel Ekman transport.

Figure 5.10 shows the results of the bottom Ekman layer analysis; friction velocity was found to be large (>0.01m/s). From site A1 was possible to do this analysis, however from other sites (A3, A4 and A5) it is known that records nearby bottom were stronger (> 0.5 m s^{-1}, other sites) and bottom stress can be found to be even stronger than observed at A1. Results shown that between 3-4 days after the records start strong (>0.25 N m^{-2}) bottom stress was found and some relevant peaks (>0.1 N m^{-2}) were observed the last 6 days [when strong wind was presented, look Figure 5.9]. A1 record is where M2 was found to be the strongest (0.05 m s^{-1}), however the influence of tides is strong at every site. Figure 5.9 showed some effects of layering affecting more than 50m, if the Ekman layer is thick the transport at sites (A3, A4 and A5) can be large (> $3m^2s^{-1}$). Records show that bottom stress can have strong energy source for turbulence (> 0.25 N m^{-2}), and bottom stress effects on MOW can be stronger (e.g. providing conditions of well-mixed water or displacement of MOW structures) than effects of the surface input.

5.4 Discussion

The MOW undercurrent experiences enhanced diffusivity at its surrounding interfaces, even in the front over the outer slope. The strongest mixing is detected over the mid-slope and is related with the strong salinity gradients. The MOW is separated from the surface by the NACW layer and is separated from the bottom by NACW over the outer slope.

Similar values of diapycnal diffusivity are found throughout the MOW. For the upper interface, there are different regions across the continental slope: diapycnal diffusivity can reach O($7x10^{-4}$ m^2s^{-1}) where the salinity gradient is O(10^{-3} salinity per metre) at mid-slope. In all other regions, salinity gradients O(10^{-4} salinity per metre) can be found with similar diapycnal diffusivity values O($2x10^{-4}$ m^2s^{-1}). For the lower interfaces over the study area and near to the continental slope where the salinity gradient is O(10^{-3} salinity per metre), diapycnal diffusivity can reach O($5x10^{-4}$ m^2s^{-1}). MOW interface depths can differ from one section to another, especially over the outer slope. Over the mid-slope to shelf, a similar salinity gradient O(10^{-3}-10^{-4} salinity per metre) as lower interface, can be found during measurement period from the XBTs cross sections snapshots (~28hrs).

Diapycnal diffusivities at the MOW front over the outer slope reach on average large values of O($5x10^{-4}$ m^2s^{-1}). Mixing is taking place when a MOW core or Meddy is penetrating the Atlantic, the internal wave breaking take place in each MOW signal. The horizontal salinity gradient is largest at the front O(10^{-4} salinity per metre; Figure 5.2, 5.5,5.7). Buoyancy forces and diapycnal mixing drive the MOW into the Atlantic, but MOW is constantly modified along the continental slope due to the salinity gradients present. If the salinity gradient is not as strong as O(10^{-4} salinity per metre) at the front, MOW water mass structure will be internally compressed (vertically) as a core and models predict that MOW will be vertically separated by the internal tide (*Nuno Serra and Ambar*, 2002; *Nuno Serra et al* 2005).

Salinity gradients are strong, conditions for enhanced mixing take place and larger estimates of mixing can be expected. The presence of critical slope conditions over the slope (Figure 5:11, summarised in chapter 2) suggests that bottom currents are strong due to the actual stratification from the MOW, but stratification varies across the slope and critical slope conditions can vary from shelf to mid slope.

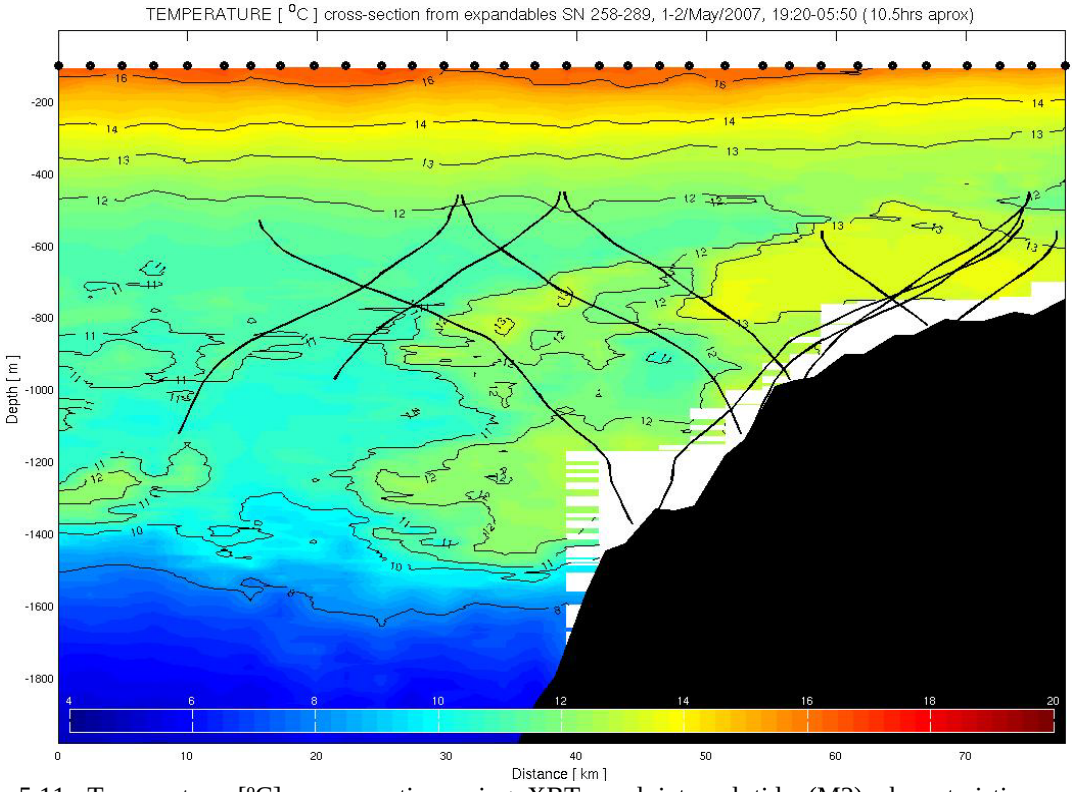

Figure 5.11: Temperature [ºC] cross section using XBTs and internal tide (M2) characteristics over the continental slope in the main seismic line. Rays plotted are over 500m to 1400m range but critical conditions can be found along the continental slope over shelf and outer slope as well.

Figure 5.12 shows a mechanistic view of mixing processes taking place over the MOW in the Gulf of Cadiz. Tides interact with topography generating baroclinic and bottom flows, and internal waves. MOW flow induces bottom friction leading to turbulence and mixing at the lower MOW-NACW interface. Internal waves break, inducing mixing over both MOW-NACW interfaces.

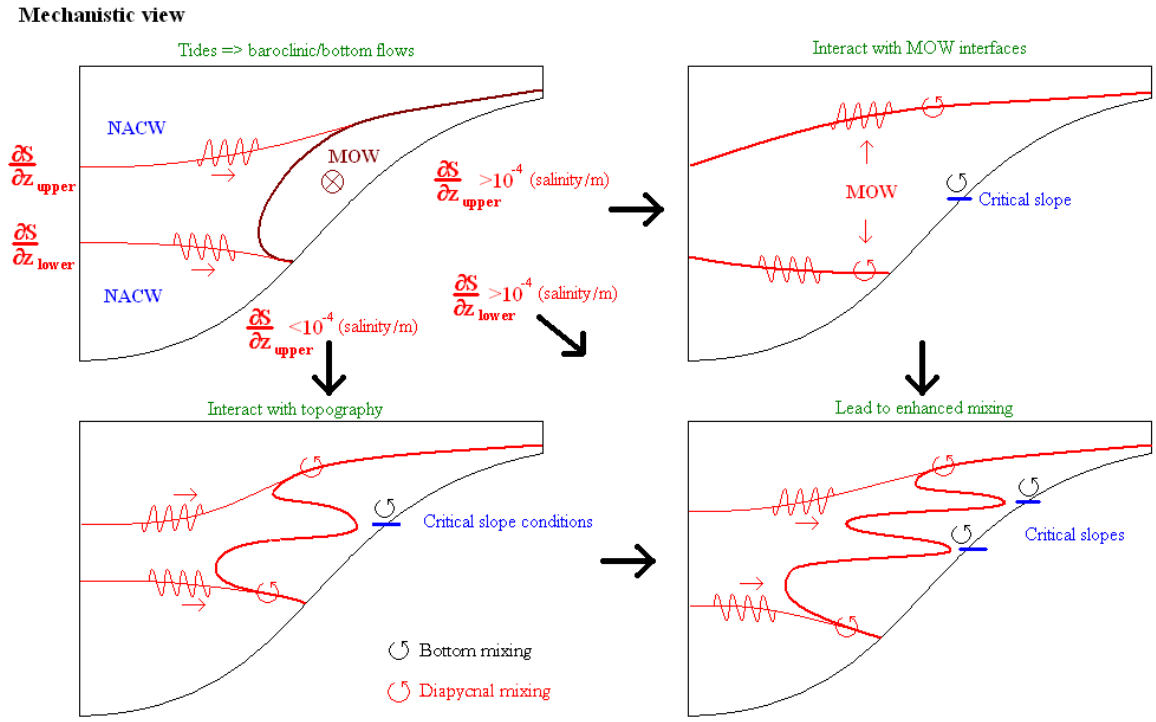

Figure 5.12: Schematic of mixing process that occurs in the Gulf of Cadiz. Turbulence from bottom friction on MOW flow and barotropic tidal currents mix the MOW. Internal waves propagate along the upper and lower interfaces, inducing turbulent mixing through internal wave breaking.

From time series analysis it is known that the internal wave field is active; internal tides are found to be the most important part of the internal wave field [M2 is largest] and influence the MOW as it travels along the Continental slope. Salinity [and temperature] gradients around the MOW and mid depths in the Gulf of Cadiz are strong and can be pathways for the internal wave breaking leading to mixing. The MOW flow is not stopped by the tide; the MOW flow is highly energetic and observations confirm the path travelling along the slope deflected by rotation as found in the literature. Also observations confirm that along the Continental Slope the current can be faster (> 0.5 m s^{-1}) at mid depths (900m-1000m, sites A3 and A4) and background stratification in the area can be critical for the M2 internal tide; then enhanced bottom friction can take place and conditions for strong mixing can be present.

From our analysis of finescale parameterizations of diapycnal mixing it is found that diffusivity can be enhanced inside the MOW and at MOW interfaces with NACW, however the diapycnal mixing inside of the MOW is patchy almost everywhere; MOW has some salinity/temperature gradients. MOW over the Continental Slope has been discussed in the literature; it splits in cores affected by internal waves. Cross sections of salinity/temperature contours (section 5.2 and chapters 2 and 3) in this study show that the MOW signal at mid-depths (800m-1100m) has a vertical salinity gradient which can be as strong as those found in the MOW-NACW interfaces [O(10^{-4}, salinity per metre)]. However, MOW flow interacting with topography has enhanced bottom stress that can result in strong mixing.

In the previous section (5.2), cross sections (figure 5.2 and chapter 2 figure 2.3.3) show a clear signal of MOW splitting in cores at similar depth to where our mooring observations recorded the highest velocities (> 0.5 m s^{-1}). Ambar *et al* (2008) confirm the present of many cores at different depths along the continental slope prior to penetrating into the Atlantic, just before the MOW flow reaches the Portimao Canyon. Conditions for a critical internal tide can vary along the Continental Slope; if the MOW water mass properties vary, then buoyancy forces will guide MOW to different “mid-depths”.

5.5 Summary

The present chapter discussed the link between the internal wave field, mixing and local circulation. The MOW undercurrent and tidal currents are highly energetic, and are considered to be the two principal mechanical generators of mixing. The internal tide is a contributor of enhanced diapycnal mixing. The mechanism of how the MOW water is displaced by the internal tide is also discussed. The early stage travel of the MOW along the slope which dilutes the MOW can determine the stratification (vertical salinity gradients $>10^{-4}$ salinity m^{-1}) in the GO study area. Overall the finescale estimates over the continental slope reveal enhanced mixing. Also finescale parameterizations calculated from XBT profiles using inferred salinity provide a regional view on where mixing is enhanced.

Chapter 6 Water mass transformation (Box model)

6.1 Introduction

This chapter presents an analysis of the variability of MOW flow in terms of water mass transformations within a box model. High salinity has been shown to be a tracer of MOW water in the Gulf of Cadiz, and Chapter 4 suggests that mixing is enhanced at the MOW upper and lower interfaces. Salinity differences are found to be large providing vertical gradients of (> 0.01 per 10 metres) at NACW-MOW interfaces and also differ for each MOW signal. In chapter 2, results showed that salinity in the MOW undercurrent is modified in transit from Gibraltar Strait; before it arrives at Portimao Canyon, the MOW undercurrent has increased volume and diluted salinity. Salinity differences can provide more information about mixing inside the MOW and with adjacent NACW.

Hydrographic cross sections (*Hill and Mitchelson-Jacob, 1993*) of a well defined NACW core of salinity have been used to show a salinity decrease. The MOW travelling northward along the west side of the Iberian Peninsula (*Huthnance* 1995; *Huthnance et al*, 2002) has been studied using a similar approach where salinity changes reveal the variability of MOW along the continental slope. A well defined reference for distinguishing water masses can be obtained from the density field, however, for MOW the strong salinity excess can provide an alternative way to study the flow distribution in the cross sections.

In this chapter alternative estimates of diapycnal mixing are attempted by using an approach of salinity fluxes in a box model. Fine-scale parameters discussed in Chapter 4 and 5 will be compared with effective values on a large scale from the box model.

6.2 Volume transport and salinity considerations

Chapter two summarised the analysis applied to the historical data from the SEMANE programme. Three cross sections over the Gulf of Cadiz were highlighted which enclosed the path of the MOW undercurrent. Figure 6.1 defines the study area where the box is built and where data are available for most of the analysed years. There are three faces to consider. The East face (1) is where MOW enters the box, travelling from East to West. The South face (2) also has water coming into the Gulf of Cadiz, water travelling from South to North. In the literature there are examples of more complex local circulation: NACW can

enter the box with lower salinity and there have been occasional events when a (MOW) meddy travelled south out of the box. However our sections only reveal a volume flux directed from South to North. The West face (3) is where the MOW undercurrent leaves the box, travelling (as at the East face 1) from East to West. The MOW is found to have increased in volume and is highlighted by the salinity contours. This face (3) is considered as the only place where water is leaving the box. Inside the box, there are found three characteristic layers, the MOW layer and two NACW layers (above and below the MOW). To distinguish the three layers, the maximums of vertical salinity gradient are used; it is found to be strong O(10^{-3} m^{-1}) in both interfaces.

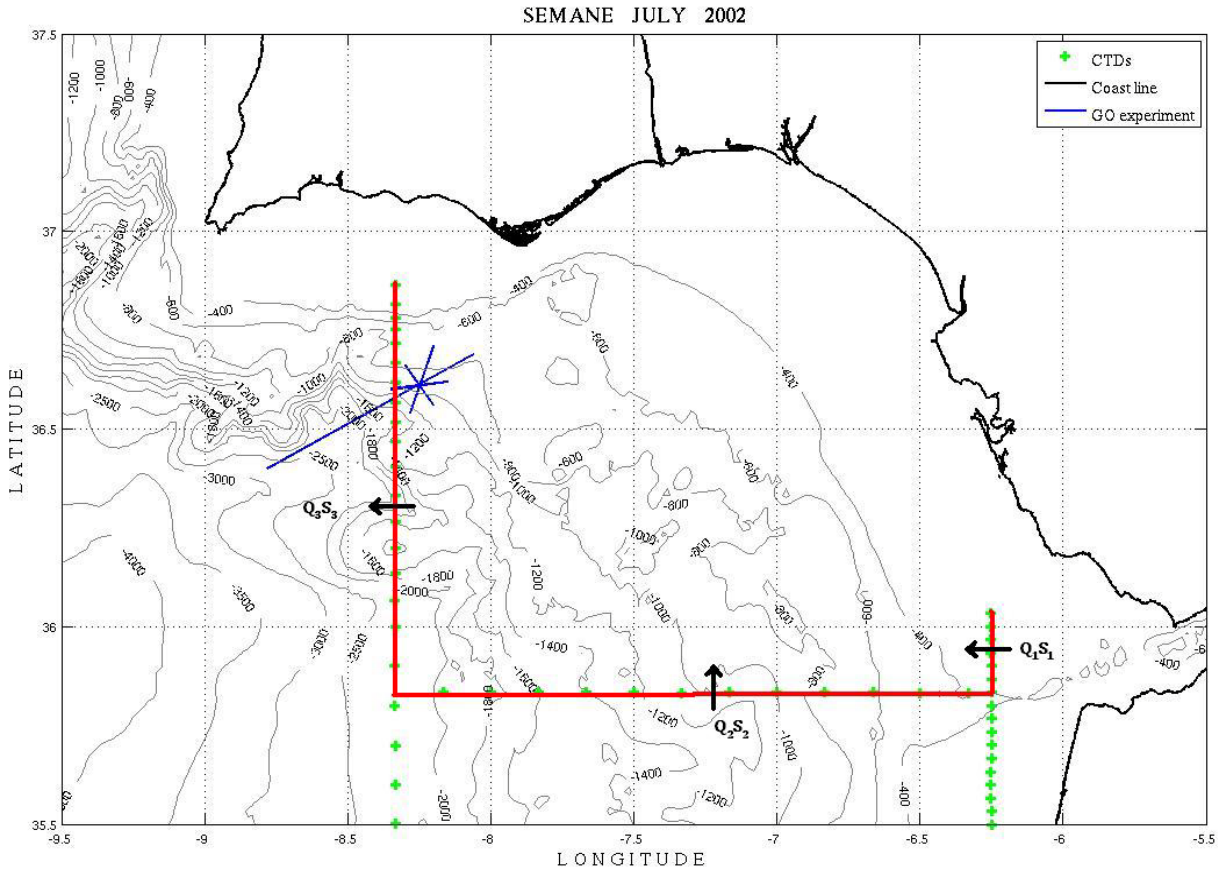

Figure 6.1: Map of data collection from the SEMANE used in the box model's three faces. Side 1 is the East face located near to Gibraltar Strait, Side 2 is the South face and Side 3 is the West face.

Figure 6.2 shows the box used in the Gulf of Cadiz. The dimensions of the box are as follows: East face (1) length of 20 km, South face (2) length of 185 km and West face (3) of 102 km, approximately. Interfaces between layers are taken where the vertical salinity gradient is maximum near the expected depth, also a horizontal salinity gradient is estimated (not shown) to account for salinity differences inside and outside the box. Salinity gradients imply diapycnal and horizontal diffusivity effects which in our system are part of the

unknowns. The volume flux through each face at every layer is multiplied by an average salinity to obtain the salinity flux [known]. The average of salinity is formed by taking all the profiles in the cross sections and the respective salinity in each layer [known], trying to avoid the interface area with a distinctive signal of the MOW undercurrent.

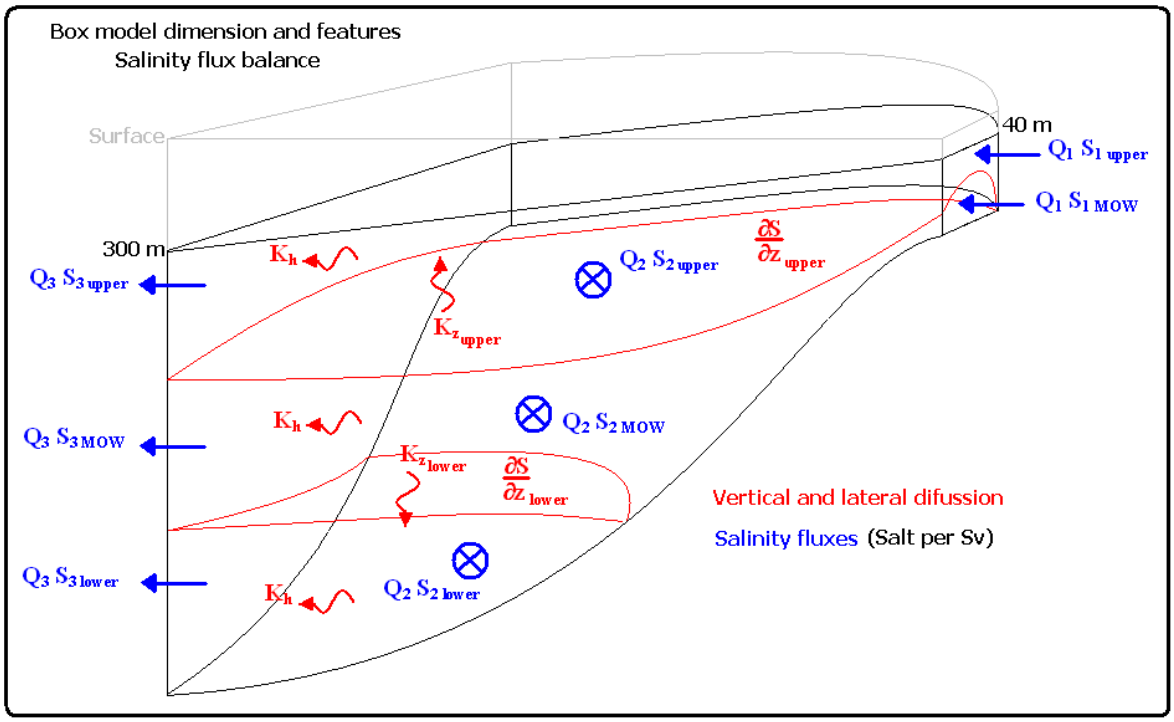

Figure 6.2: Sketch of Box model for balanced salinity fluxes in the Gulf of Cadiz using available cross sections from SEMANE program.

The balance of volume and salinity flux is done by the following horizontal flux statements:

$$Q_3 = Q_1 + Q_2 \qquad (6.1)$$

Q is the volume transport (Sv). Equation (6.1) is the initial condition to maintain volume flux balance.

Volume flux (Sv) was calculated by using geostrophic velocity considerations (from SEMANE program results summarised in Chapter 2). A level of no-motion was originally calculated to be used for water mass flux analysis and was found over the NACW upper layer. In our study we were interested in the effect of the MOW and its contributions to the surrounding waters; it was looking to omit the influence of the surface mixed layer. The choice of where to start to integrate in the water column and calculate a geostrophic shear comes from where current speed was found to be minimum confirming by evidence on records of Vessel Mounted and Lowered ADCP data from GO experiment; shown that

velocities at those depths (~300m) were small (< 3cm/s). Also, salinity gradients (variability 10-20m depth range) were minimum after leaving surface mixed layer depths (0-250m). Uncertainties of volume flux were considered by adding the speed to found (3 cm/s) to the standard deviations to calculated shear considered on volume flux results. Also uncertainties consider the use of alternating CTD profiles along the cross section.

A first consideration is to form a volume flux balance for the box as a whole, adding a barotropic velocity only on face (2) to complete the volume flux balance; this barotropic velocity is expected to be northward, because the original (faces 1 and 2) volume flux into the box was not big enough to complete the volume flux balance. Table (6.1) shows the volume fluxes of each face to keep the balance that is proposed.

Table 6.1: Volume flux [Sv] in box model, before (and after) adding a balancing barotropic velocity to Q_2.

Volume flux [Sv]	Box faces		
	Q_3	Q_2	Q_1
June-July 2001	5.02	1.04(4.56; 0.037m/s)	0.46
July 2002	3.07	1.78(2.78;0.011m/s)	0.29
1995-2002	4.44	1.41(4.07;0.028m/s)	0.37

Figure 6.3 shows water mass properties profiles used in the box model and regions where vertical gradients were calculated. The box model uses three layers, MOW and two for NACW. The top NACW layer starts where the level of no-motion is assumed around 300 m [where current speed was found minimal] and ends at interface with MOW [where salinity and temperature can increase more than half unit and one unit respectively in hundred metres, on selected profiles]. The bottom NACW layer is from the lower interface of MOW [where salinity and temperature can decrease more than a unit and four units respectively in hundred metres] to the actual bottom of the Gulf of Cadiz. Salinity vertical gradients over interfaces are *O(10^{-3}-10^{-4} salinity per metre)*, and strongest *O(10^{-3}, salinity per metre)* at the lower interface. Temperature gradients shown to be around *(10^{-2}-10^{-3} ^{o}C per metre)* and strongest *(10^{-2} ^{o}C per metre)* at the lower interface as well. Numerical modifications (80-160 db range) of these values were used to estimate uncertainties for box model outputs.

Horizontal fluxes from water mass properties were calculated by using available CTD data from inside and outside the box. Horizontal salinity gradients were found to be *O(10^{-6}-10^{-7} salinity per metre)* in the NACW layer and *O(10^{-5} salinity per metre)* in the MOW layer. Horizontal temperature gradients were found to be *O(10^{-6} ^{o}C per metre)* in the NACW layer

and *O(10^{-5} ^{o}C per metre)* in the MOW layer. NACW bottom layer horizontal gradients are higher than in the NACW upper layer by a factor of two overall.

The volume flux in each layer of the box needs to be in balance and this is done by adding a barotropic velocity on each face (as distinct from just one face). On faces (1) and (3) barotropic velocities were found small enough O(10^{-4} ms^{-1}) to be neglected. On face (2) respective values (2001-0.037ms^{-1}; 2002-0.011ms^{-1}; historical-0.028ms^{-1}) were added for barotropic velocity.

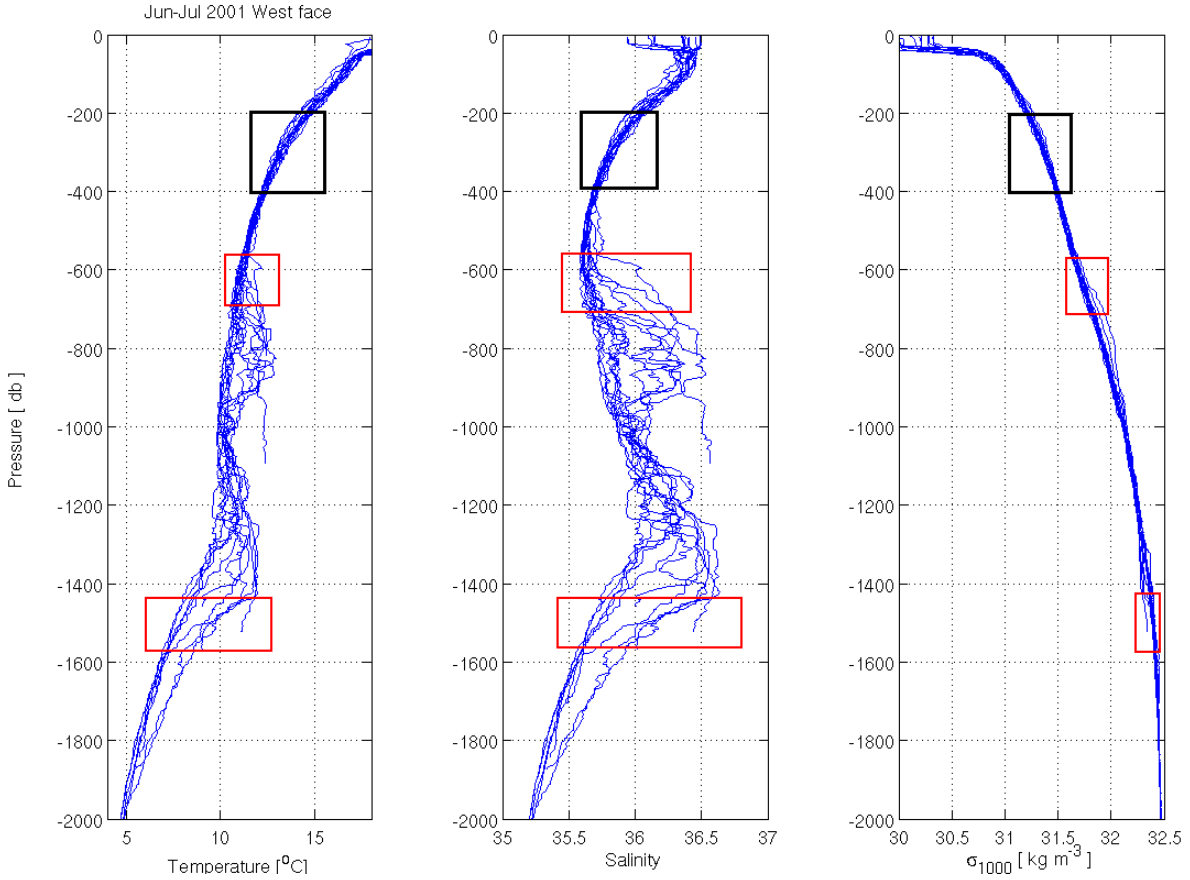

Figure 6.3: Temperature, salinity and potential density (σ_{1000}) profiles from West face during June-July 2001 experiment used to show the sensitivity of S_z (Red boxes) calculation over the TOP and BOTTOM interfaces, T_z was calculated at similar depths. The level of no-motion was calculated (black boxes) where current speed was minimum and confirmed with VMADCP and LADCP records for minimal speed (< 3cm/s).

The salinity flux term is expressed (*QS*) by multiplying the volume flux by the salinity average over the face or layer. Tables (6.2 and 6.3) show the inputs for the balanced volume flux as determined by equation (6.1) and the average salinities respectively. In table (6.4) are presented the salinity fluxes for each box.

Table 6.2: Volume fluxes [Sv] integrated over layers in the Box model and balanced.

Volume Flux [Sv]	Face 3, Lon 8.3º			Face 2, Lat 35.83º			Face 1, Lon 6.25º		
	TOP	MOW	BOT	TOP	MOW	BOT	TOP	MOW	BOT
June-July 2001	0.75±0.45	3.02±1.80	1.25±0.75	0.60±0.45	2.71±2.10	1.25±0.75	0.15±0.08	0.31±0.24	-
July 2002	0.46±0.39	1.84±1.76	0.77±0.75	0.37±0.34	1.64±1.90	0.77±0.67	0.09±0.05	0.20±0.18	-
1995-2002	0.67±0.43	2.66±1.73	1.11±0.72	0.54±0.48	2.42±1.98	1.11±0.66	0.13±0.06	0.24±0.22	-

Note: Uncertainties from volume flux were determined by alternating CTD profiles over cross sections.

Table 6.3.: Salinity averages.

Salinity average in sections	Face 3, Lon 8.3º			Face 2, Lat 35.83º			Face 1, Lon 6.25º		
	TOP	MOW	BOT	TOP	MOW	BOT	TOP	MOW	BOT
June-July 2001	35.7307	36.0967	35.7996	35.7523	35.9855	35.8807	36.1501	38.0509	-
July 2002	35.7304	36.0944	35.7293	35.6971	35.9894	35.9325	36.1509	38.3633	-
Aug-Sept 2000	35.7029	36.0941	35.7017	-	-	-	-	-	-
July 2000	35.6968	36.0953	35.7937	-	-	-	-	-	-
July 1999	35.7277	36.0949	35.7237	-	-	-	-	-	-

Note: Differences between years provide an idea of error for each layer.

Table 6.4: Salinity fluxes (Sv) used in the Box model faces.

Salinity average by sections	Q_3S_3			Q_2S_2			Q_1S_1		
	TOP	MOW	BOT	TOP	MOW	BOT	TOP	MOW	BOT
June-July 2001	26.7980	108.6511	44.7495	23.2390	97.1609	44.8509	3.6151	11.7958	-
July 2002	16.4360	66.4136	27.5116	14.2788	59.0226	27.6680	2.1691	7.6727	-
1995 – 2002	23.9257	95.9356	39.6714	21.4320	87.0474	39.7801	2.5305	9.1608	-

6.3 Water mass fluxes and salinity budget with diapycnal diffusivity

Following Huthnance *et al* (2002), a box model for salinity can be expressed by considering a balanced volume flux (equation 6.1 applied to each layer) and the concentration of salt and its variability at each face. For the proposed box model this can be expressed by:

$$\text{TOP LAYER} \quad Q_3S_3 = Q_1S_1 + \sum Q_2S_2 + \int K_{z\,upper}\left[\frac{\partial S}{\partial z}\right]_{Upper}^{120db} dA \tag{6.2}$$

$$\text{MOW LAYER} \quad Q_3S_3 = Q_1S_1 + \sum Q_2S_2 - \int K_{z\,upper}\left[\frac{\partial S}{\partial z}\right]_{Upper}^{120db} dA + \int K_{z\,lower}\left[\frac{\partial S}{\partial z}\right]_{Lower}^{120db} dA \tag{6.3}$$

$$\text{BOTTOM LAYER} \quad Q_3S_3 = Q_1S_1 + \sum Q_2S_2 - \int K_{z\,lower}\left[\frac{\partial S}{\partial z}\right]_{Lower}^{120db} dA \tag{6.4}$$

where Q_n, S_n are volume flux and salinity at face n for the layer in question, K_z is the diapycnal diffusivity (m^2s^{-1}) in the upper and lower interface, $\frac{\partial S}{\partial z}$ is the vertical salinity gradient (salinity per metre) at the interface indicated (the gradient is estimated from maximal salinity difference over 120db of data range), z increases downwards and dA is the integrated horizontal area of interface (m^2). In these equations only the diapycnal diffusivities are considered as unknowns. Solutions of equations (6.2) and (6.4) are presented and compared against least squares results. The least squares method involves squaring and summing the expressions for imbalance of the over-determined set of equations (6.2, 6.3 and 6.4) and

obtaining the derivatives with respect to both unknowns, obtaining two linear equations with two degrees of freedom.

Table 6.5 shows that the lower and upper interfaces have different values for diffusivity, which is slightly larger for the lower interface. Basically in the vertical, salinity is diffused from the MOW layer to the upper and lower layers; both are gaining salinity through the transfer across their interfaces with MOW.

Table 6.5: Diapycnal diffusivities from box model (equations 6.2 and 6.4) balance over three layers and solution from least squares (LS).

$K_z\ [10^{-4}\ m^2\ s^{-1}]$	K_{z_upper}		K_{z_lower}	
	Eq.(6.2)	LS	Eq.(6.4)	LS
June-July 2001	4.39±1.43	4.47±2.76	6.78±1.39	6.99±2.91
July 2002	3.64±1.46	5.63±2.72	5.26±1.42	6.69±2.59
1995 – 2002	4.48±1.66	4.54±2.98	7.67±1.65	7.83±2.82

Note: Uncertainties in diapycnal diffusivity values were estimated by modifying the range used in calculating the salinity gradient between 50 db and 150db.

Results from least squares (LS) confirmed that the results for $K_{z\ upper}$ and $K_{z\ lower}$ are similar (Table 6.5) to those found by solving equations separately. The apparent larger diapycnal diffusivity on the lower interface than the upper interface is found by applying LS, however uncertainties are broad and both methods give consistent mixing estimates. Uncertainties in LS are estimated by considering the degrees of freedom of the two linear equations and the related 95% confidence interval.

6.4 Water mass fluxes and salinity budget with diapycnal and lateral diffusivities

An alternative set of equations is proposed to include both diapycnal and lateral diffusion for each layer face. The inflows and outflows can be expressed as:

$$\text{TOP LAYER} \quad Q_3S_3 = Q_1S_1 + \sum Q_2S_2 + \int K_{z\ upper}\left[\frac{\partial S}{\partial z}\right]_{Upper}^{120db} dA + A_iK_h\frac{\partial S}{\partial n_o} \tag{6.5}$$

$$\text{MOW LAYER} \quad Q_3S_3 = Q_1S_1 + \sum Q_2S_2 - \int K_{z\ upper}\left[\frac{\partial S}{\partial z}\right]_{Upper}^{120db} dA + \int K_{z\ lower}\left[\frac{\partial S}{\partial z}\right]_{Lower}^{120db} dA + A_iK_h\frac{\partial S}{\partial n_o} \tag{6.6}$$

$$\text{BOTTOM LAYER} \quad Q_3S_3 = Q_1S_1 + \sum Q_2S_2 - \int K_{z\ lower}\left[\frac{\partial S}{\partial z}\right]_{Lower}^{120db} dA + A_iK_h\frac{\partial S}{\partial n_o} \tag{6.7}$$

where K_h is the lateral diffusivity (m^2s^{-1}), A_i is the vertical face area (m^2), $\frac{\partial S}{\partial n_o}$ is the horizontal salinity gradient (m^{-1}) out of the box. The equations system is solved and uncertainties are estimated for salinity fluxes by using the volume flux errors. (Uncertainties in volume flux from geostrophic velocities were calculated in Chapter 2 from difference of baroclinic shear by using different pairs of CTD profiles).

The alternative set of three equations was used: (6.5), (6.6) and (6.7) with the lateral diffusion term [three unknowns]. Table 6.6 shows the results for $K_{z\ upper}$, $K_{z\ lower}$ and K_h. Diapycnal diffusivity values are slightly less than those found in table (6.5) and uncertainties are tighter. When the lateral diffusion K_h is retained in equations (6.5) to (6.7), salinity flux is larger (~0.44 salinity Sv) overall because lateral diffusion with the horizontal gradient is stronger than diapycnal diffusion. Horizontal and vertical salinity gradients play an important role in the estimation of diffusivities; both of them are found to be large due to the amount of MOW passing through the box. To understand the vertical and lateral effects over the different faces, the sketch of the box model previously used to explain salinity fluxes is used to understand each face and layer (Figure 6.3).

Table 6.6: Diffusivities from box model adding lateral diffusion.

$K_i\ [\ m^2s^{-1}\ ]$	$K_{z\ upper}[10^{-4}]$	$K_{z\_lower}[10^{-4}]$	K_h
June-July 2001	3.38±1.11	4.73±0.95	248.97±30.56
July 2002	3.35±0.98	5.75±0.91	237.35±21.91
1995 – 2002	3.54±0.99	6.25±1.17	225.57±18.34

Note: Uncertainties in diapycnal diffusivities values were estimated by modifying the range used in calculating the salinity gradient between 50 db and 150db. For lateral diffusivity uncertainties the horizontal gradient was modified as well by using alternative profiles to estimate the horizontal salinity gradient.

In figure 6.3 for 2001, the salinity fluxes show that the upper and lower layers are gaining salinity from the MOW layer, however, more salinity is diffused laterally from the MOW layer. Also salinity loss by lateral diffusion in the upper and lower layers is found to be smaller (~0.03 salinity Sv) than the gain by diapycnal diffusion. In figure 6.4 for 2002, salinity flux is lower overall than in 2001, however the upper and lower layers are still gaining salinity from the MOW layer. In 2002, vertical effects seem to be larger, and there is a very similar diapycnal diffusivity as in 2001 (using equations with unknows, Table 6.5 and 6.6), and the amount of salt lost through the lower interface to the lower layer is larger (~0.15 salinity Sv).

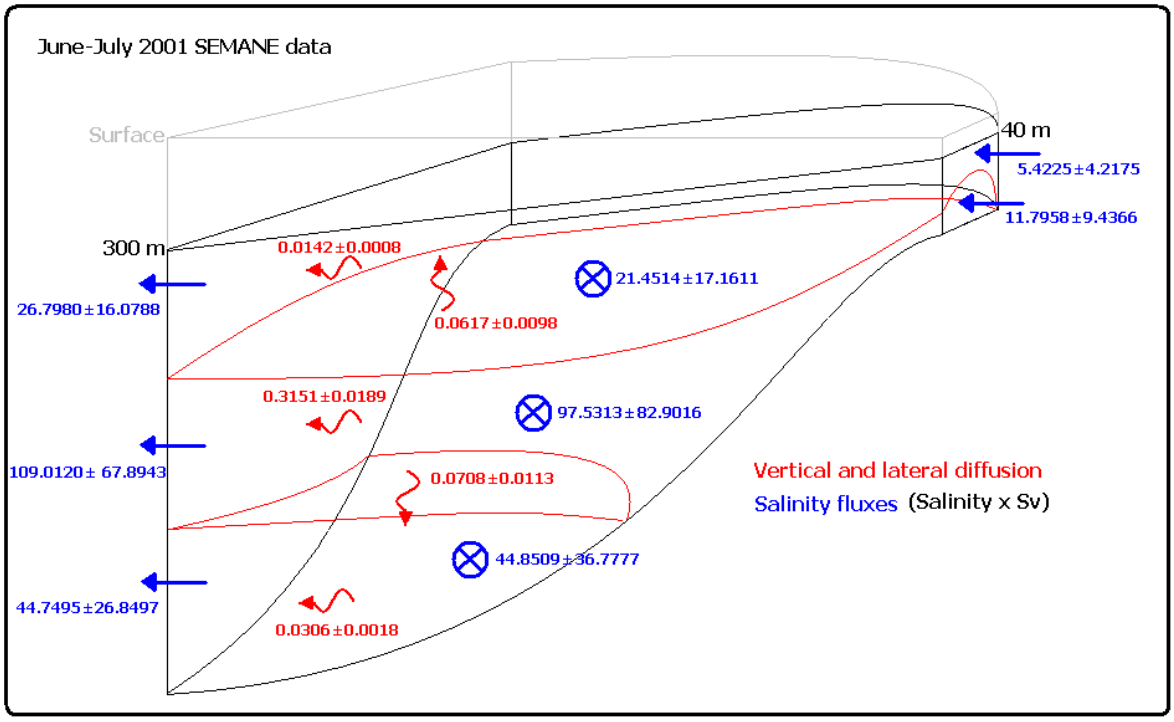

Figure 6.3: Sketch of salinity fluxes from box model results applied to SEMANE data in June-July 2001, with diapycnal and lateral mixing (red arrows). Uncertainties were estimated by taking volume flux uncertainties on each side, diapycnal diffusivity uncertainties were estimated by using their results from the different approaches (i.e. different sets of equations) and lateral diffusivity uncertainties from variation of horizontal salinity gradient.

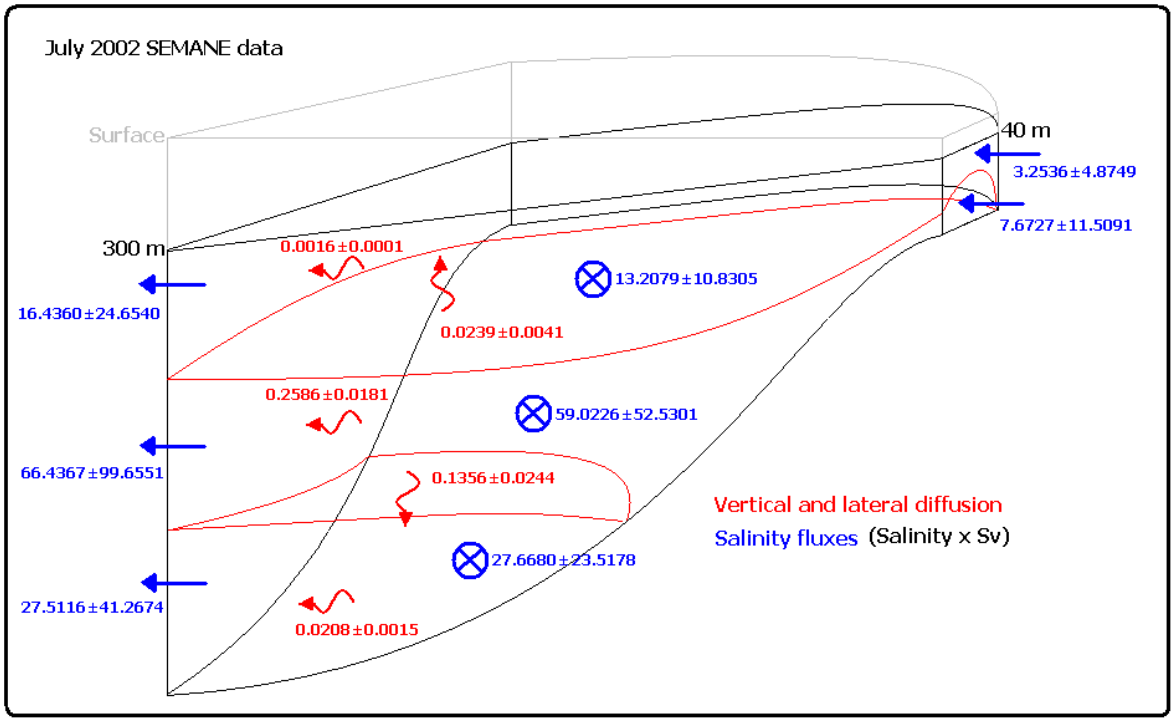

Figure 6.4: Sketch of salinity fluxes from box model results applied to SEMANE data in July 2002, with diapycnal and lateral mixing imposed (red arrows). Uncertainties were estimated by taking volume flux uncertainties on each side, diapycnal diffusivity uncertainties were estimated by using their results from the different approaches (i.e. different sets of equations) and lateral diffusivity uncertainties from variation of horizontal salinity gradient.

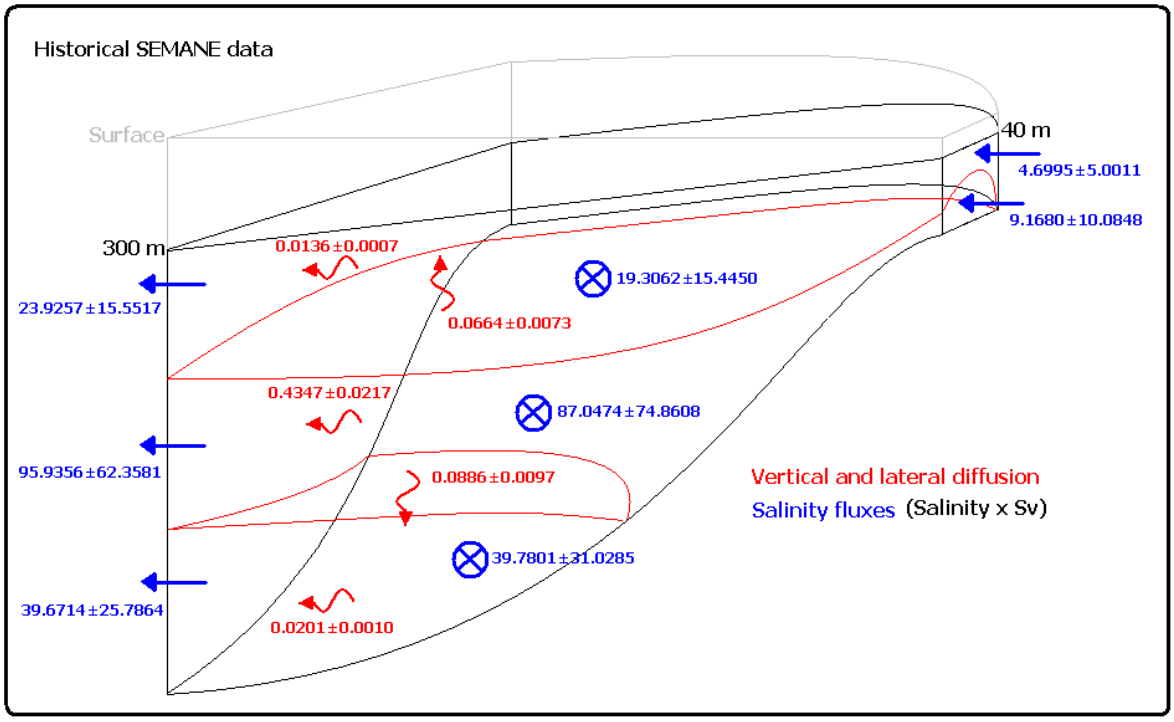

Figure 6.5: Sketch of salinity fluxes from box model results applied to SEMANE historical data (average of 1999, 2x2000, 2001 and 2002 years on face 3) with diapycnal and lateral mixing imposed (red arrows). Uncertainties were estimated by taking volume flux uncertainties on each side, diapycnal diffusivity uncertainties were estimated by using their results from the different approaches (i.e. different sets of equations) and lateral diffusivity uncertainties from variation of horizontal salinity gradient.

In figure 6.5 for the historical, the salinity fluxes results over face (3) are very similar to those found during 2001; probably 2002 had a weak MOW signal on face (3) as discussed later. Also, results confirm that vertical transfers are larger in the lower interface than the upper interface, and the upper and lower layers gain salinity through these interfaces. The MOW layer diffuses most salinity laterally.

A similar test of the box model was done by using the heat flux (Tables 6.6, 6.7 and 6.8). Results for vertical diffusivities were very similar to those found with salinity, only overall the vertical diffusivity at the upper interface is found to be slightly less than the diffusivity found for salinity. In fact, there are fluxes [heat and salt] from the mixed layer and their effect will be represented by a change in the calculated vertical diffusivity. Heat flux is coming from the MOW layer to the NACW which is another restriction of the water mass transformations that happens at the Gulf of Cadiz.

To summarise, the present analysis is done by using salinity and temperature cross sections over the study region, demonstrating the MOW as a source of heat and salt for the NACW [where vertical and lateral fluxes are both important]. If this analysis were done by

using only potential density gradients, flux direction will be miss-interpreted. Salinity and temperature increasing downwards at the upper interface and decreasing downwards at the lower interface determine that fluxes are coming out from the MOW layer.

Table 6.6: Temperature averages from selected layers (TOP and BOTTOM layers of NACW and MOW layer).

Temperature Averages	West face Lon 8.3°			South face Lat 35.83°			East face Lon 6.5°		
	TOP	MOW	BOT	TOP	MOW	BOT	TOP	MOW	BOT
Jul 2002	12.0723	11.2318	6.4555	12.1103	11.5836	6.6766	13.0100	13.5456	-
Jun-Jul 2001	12.2516	11.2622	6.6596	12.1356	11.3621	6.8716	13.2002	13.7581	-
Jul 2000	12.1727	11.2525	6.4575	-	-	-	-	-	-
Aug 2000	12.0632	11.4074	6.4890	-	-	-	-	-	-
Jul 1999	12.2401	11.4400	6.9864	-	-	-	-	-	-

Table 6.7: Vertical diffusivities from equations with 2 unknowns by using temperature gradients.

$K_z\ 10^{-4}$ [$m^2\ s^{-1}$]	$K_{z\ upper}$	$K_{z\ upper}$ LS	$K_{z\ lower}$	$K_{z\ lower}$ LS
Jul 2002	3.579±1.010	3.961±1.200	6.389±1.349	6.822±1.455
Jun-Jul 2001	2.415±0.784	4.113±0.977	5.812±1.454	6.222±1.342
Historical	3.530±0.987	3.423±1.015	7.487±1.400	6.690±1.450

Table 6.8: Vertical diffusivities from equations with 3 unknowns by using temperature gradients.

$K_z\ 10^{-4}$ [$m^2\ s^{-1}$]	$K_{z\ upper}$	$K_{z\ lower}$	K_h
Jul 2002	2.892±0.780	4.503±1.120	234.143±25.67
Jun-Jul 2001	2.144±0.566	5.176±1.432	227.508±14.35
Historical	3.305±0.865	6.663±1.103	233.816±18.94

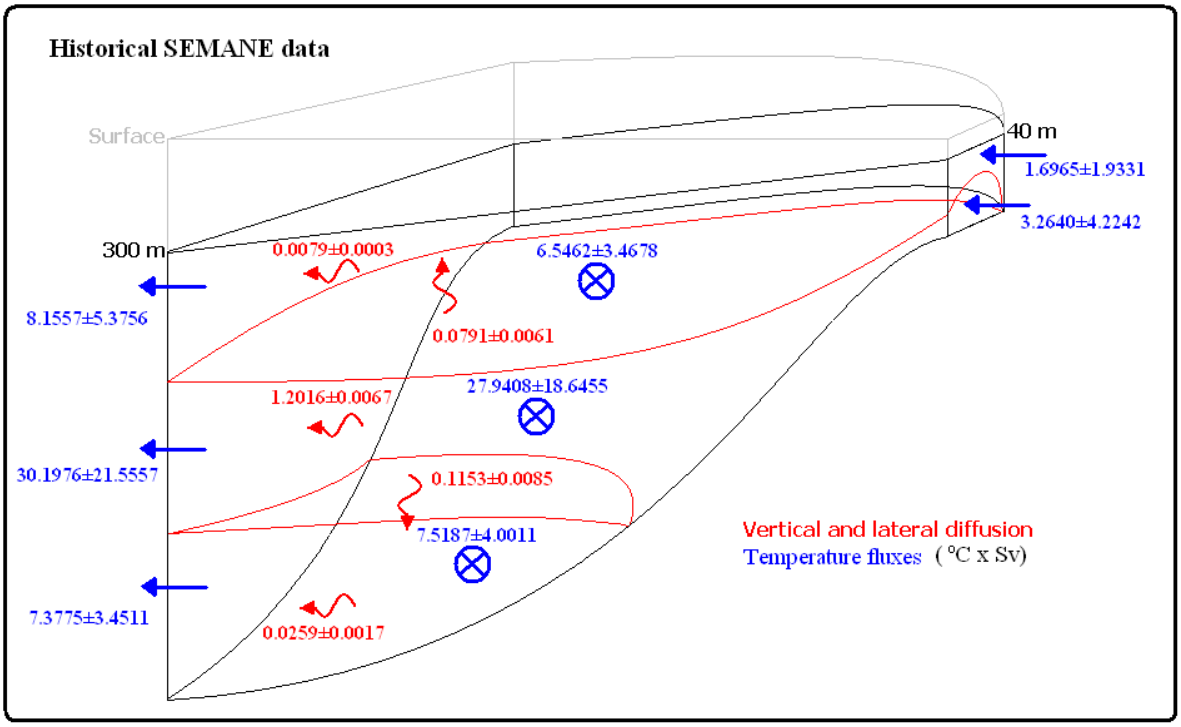

Figure 6.6: Sketch of temperature fluxes from box model results applied to SEMANE historical data (average of 1999, 2x2000, 2001 and 2002 years on face 3) with diapycnal and lateral mixing imposed (red arrows). Uncertainties were estimated by taking volume flux uncertainties on each side, diapycnal diffusivity uncertainties were estimated by using their results from the different approaches (i.e. different sets of equations) and lateral diffusivity uncertainties from variation of horizontal temperature gradient.

Figure 6.6 shows sketch of temperature fluxes of the whole data available from historical sources. The temperature fluxes show that around 0.2^{o}CxSv are lost though vertical diffusion and 1.2^{o}CxSv are lost through lateral diffusion from the MOW. In terms of energy units, upper interface 0.08^{o}CxSv and 0.11^{o}CxSv can be expressed as 32.2 W m^{-2} and 46.3 W m^{-2} on each interface over all study region. It is clear that, most of the MOW heat lost is lateral. The heat budget using the large scale effective values of vertical diffusivity can be balanced from in (East and South) and out (West) fluxes around three days (~70 hours).

6.5 Discussion

Results from the box model have shown that by using large scale balances for salinity and volume effective values of diapycnal diffusivity can be diagnosed, which are comparable with those derived from fine structure (in Chapters 4 and 5). In the box model system, the MOW layer is losing salt through its interfaces to the upper and lower layers where NACW is located, but also loses more salt by lateral diffusion out of the box. Diapycnal diffusivity is found to be larger but comparable with the Chapter 5 estimates based on fine-structure.

The upper interface has diapycnal diffusivity values, by the strain method using extensive temperature profiles with inferred salinity, of around O(2.1x10^{-4} m^{2} s^{-1}), and in the present box model the value is around O(3.5x10^{-4} m^{2} s^{-1}). The difference is less than a factor of two and covered by the uncertainties from both analyses. In the lower interface the diapycnal diffusivity is slightly larger than in the upper interface: box model values are around O(5.8x10^{-4} m^{2} s^{-1}) and fine-structure observations lead to a value around O(4.8x10^{-4} m^{2} s^{-1}); the difference is again covered by the uncertainties. Both results confirm that mixing is enhanced at the interfaces and is stronger at the lower interface.

Conditions of mixing for internal waves along the continental slope can be observed only in MOW structures. In the lower interface region, enhanced mixing is taking place and well mixed conditions over the deep section of the MOW layer can be found. In both interfaces salinity gradients were found to be strong O(10^{-3} salinity/m) and enhanced mixing was associated. At the upper interface, there were some weak salinity gradients O(10^{-4} salinity/m) and some enhanced mixing, but weaker than in regions with strong salinity gradients.

Lateral diffusivity is analysed in the present work using the box model. In Chapter 2, the MOW undercurrent is emphasized as being a continuous flow (>0.2 ms^{-1}), strongly influenced by tides, but not arrested by them, and carries most of the salinity flux. Now it is confirmed by the box model: salinity fluxes by advection drive most (~0.44 salinity Sv) of the salinity, and the salinity flux by diapycnal diffusion drives the remainder (~0.15 salinity Sv). Similar results were found by using heat flux [upper layer $k_z = 3x10^{-4}\ m^2\ s^{-1}$ and lower layer $k_z = 6x10^{-4}\ m^2\ s^{-1}$].

Previous analysis has shown that inside the MOW rapid changes of density are taking place, and the effect is for the MOW undercurrent to increase in volume flux downstream with diluted salinity. Also the MOW in the Gulf of Cadiz is known to separate from the continental slope, although most of the original flow remains along continental slope (as cited in Chapter 1 and Chapter 2).

Some box model assumptions are needed to come across due to the introduction of lateral effects, one is that the influence of MOW signal which inside of the box model is still in the process of getting split or to become a proper mesoscale eddy, however it as account as a baroclinic flow. Another important issue is that horizontal salinity and temperature gradients from box model region and outside [West side or towards face 3] are highly diluted from the original source by the combination of mixing process taking place.

Results from the box model here can be compared also with results from previous studies. Daniault *et al* (1994) reported a volume flux of around 5 Sv passing around Cape St Vincent (about 60 km from face 3) and mainly related with the MOW undercurrent. In the present work a similar volume flux is found through face 3 (~5 Sv). Mixing transformations from face (3) to Portimao Canyon are less (<0.2 Sv, most of the transformation has already taken place). Baringer and Price (1997 a,b) reported that around 0.5 Sv is passing through Gibraltar Strait and, by using a few cross sections (mostly on the Eastside of our box) at the early stage of the MOW undercurrent travelling down slope, they found entrainment is the main mechanism for enhancing the strength of the undercurrent by mixing MOW with NACW. The box model approach that is provided by the present research obtains the effect of mixing by considering salinity and temperature gradients but is likewise a large scale view.

6.6 Summary

A box model for salinity concentration has been built; salinity was used as a tracer of the MOW undercurrent. A volume flux balance is imposed in order to set consistent conditions for salinity concentration. A set of equations was proposed with three unknowns, those were the lateral and two diapycnal diffusivities. Results from solving the equations have found diapycnal diffusivities very similar to those derived by fine-scale parameterizations in chapters 4 and 5. Also, it is found that even though vertical effects are relevant around the MOW flow, lateral diffusion is the most important for MOW salinity loss in the study area. NACW layers, above and below the MOW, are gaining salinity from the MOW undercurrent by diapycnal diffusion.

Chapter 7

Final remarks and conclusions

7.1 Introduction

This Chapter provides a summary of the results and discussion of this research on the dynamics and mixing of water masses in the Gulf of Cadiz. The influence of the internal wave field, mostly associated with the internal tide, is described in relation to the local circulation. Different methodologies are used to diagnose the diapycnal mixing of the MOW signal. Final remarks on the discussions from previous chapters are provided and conclusions from the research. Future possibilities for research work on the circulation in the Gulf of Cadiz, diapycnal mixing and the related internal wave field are discussed.

Baroclinic flows in the Gulf of Cadiz are made up of two dominant water masses, MOW and NACW, which are shown to be strongly affected by enhanced mixing. The generation of internal waves, related with the internal tide, and their breaking leading to mixing, are discussed. Bottom slopes in water depths 1000 - 1500 metres can be critical for semi-diurnal internal waves, however the real evidence for waves enhancement comes from measurement of the waves over the continental slope. Internal tide energy over a critical slope can transfer to shorter internal waves and turbulence leading to enhanced mixing. This mechanistic view and fine-structure mixing diagnostics over the region are compared with the balanced Salinity budget from the box model; both provide a broadly consistent view of the mixing rates (within their error bars).

7.2 Final remarks

Observations revealed the spreading of the MOW in different forms: MOW cores or Meddies were detected at different depth ranges, but not all the four cores identified in other studies (*Ambar et al,* 2008) were detected. Salinity was shown to be a key variable to reveal the MOW and its dynamics.

MOW forms a strong continuous flow (~0.20 ms^{-1}) over the mid slope, although there is temporal variability including a tidal influence (~ 0.05 ms^{-1}, mostly semidiurnal) through depth, and the MOW can reach a maximum speed >0.40 ms^{-1}. The MOW signal (from

temperature time series in chapter 2) is correlated along and across the slope as seen in mid slope measurements (moorings spanning 20 km); the MOW signal varies with location of mooring down the slope. Measurements over the study area showed the presence of stratification supporting waves for energy transfer on the slope, leading to turbulence and mixing. The internal waves in the MOW have many candidate energy generation sources, but the MOW shear due to bottom friction and the internal tide are the most energetic.

Bottom stress is found to be strong and turbulence can also be strong, causing mixing mostly inside and at interfaces of the MOW. Internal wave characteristics for the M2 tide reveal a critical slope condition (Figure 5.10). Critical slopes lead us to expect that in mid slope regions bottom stress is strong and where salinity gradient is weak enable MOW separation [from XBTs cross sections of mixing estimations in Chapter 5]. Vertical mixing associated with internal wave breaking happens around the MOW structure when MOW separation is taking place (*Serra and Ambar,* 2002; *Serra et al* 2005). Surface stress also was found to be strong; however, the thick upper layer of NACW bars the surface stress from acting on MOW located over the continental slope.

The observation data (CTDs) show that the MOW signal is variable, but also that MOW temperature and salinity can co-vary in certain regions (500m-1500m depth) in the Gulf of Cadiz. Temperature and salinity inside the MOW have a loose relationship; however, both follow similar structures (decreasing or increasing downwards together) over their profiles; this enables us to reconstruct salinity to exploit an extensive source of temperature profiles (XBTs). Background stratification increases inside the MOW and decreases in the main NACW layers over the large scale O(400m). On small scales O(50m) stratification reveals rapid changes with depth as was shown by CTD profiles. Small scale stratification was used to analyse the strain (finescale structures), which was found to be strong at MOW-NACW interfaces and on some occasions inside the MOW. Temperature profiles with inferred salinity profiles were shown to provide additional information for the water mass finescale structures, especially for the MOW.

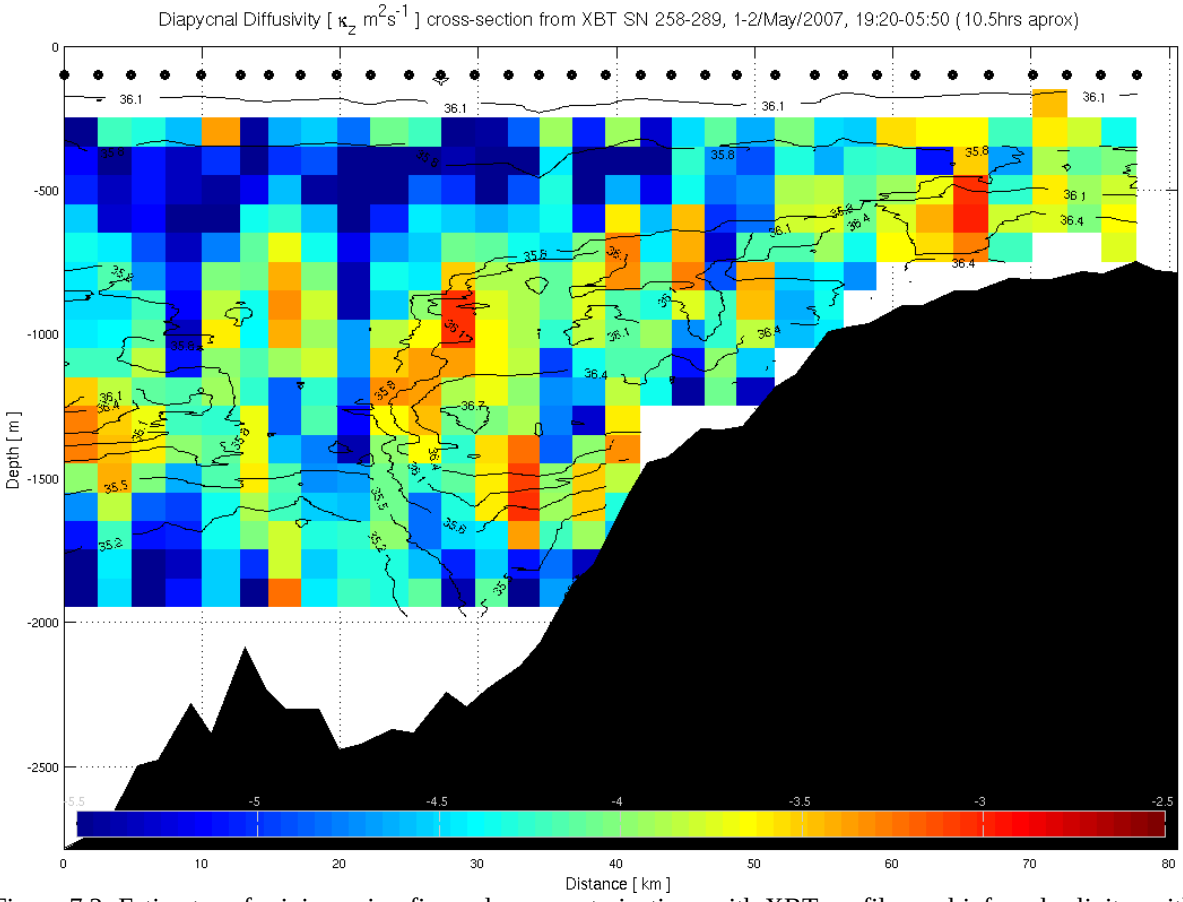

Figure 7.2: Estimates of mixing using finescale parameterizations with XBT profiles and inferred salinity, with salinity contoured in the background. Diapycnal diffusivity [$Log_{10}(\kappa_z$ in $m^2s^{-1})$] along the continental slope (see Chapter 5) calculated using *Osborne* (1980) parameterization.

Estimates of finescale parameterizations suggest that strong mixing (Figure 7.2) is taking place in both MOW-NACW interfaces (using the strain method with either CTD profiles or XBTs temperature and inferred salinity profiles). The diapycnal diffusivity reached $O(2x10^{-4}\ m^2s^{-1})$, at the upper interface. This strong mixing occurred along the continental slope and particularly where MOW structures (cores) are located. The diapycnal diffusivity reached $O(5x10^{-4}\ m^2s^{-1})$ at the lower interface and well-mixed conditions [temperature and salinity uniform] over a large depth range can be found. Also enhanced mixing took place inside the MOW with a diapycnal diffusivity as large as $O(>5x10^{-4}\ m^2s^{-1})$ over mid slopes. Both interfaces can be influenced by the semi-diurnal internal tide as happens inside the MOW [from current measurements]. The finding of enhanced mixing along the upper and lower MOW-NACW interfaces is supported by the mixing estimates required to balance a large scale salinity budget in a box model in the Gulf of Cadiz.

The mid-depths in the Gulf of Cadiz are the regions where water masses are getting warmer and saltier (*Potter and Lozier, 2004; Lozier and Sindlinger, 2009; Bozec et al 2011*),

also where MOW is located. MOW leaving the Strait of Gilbraltar is already warmer and saltier than NACW. However, when MOW arrives at mid-depths driven by buoyancy forces, it entrains surrounding water which is already warmer and saltier than proper NACW mid-depth water [as confirmed by our observations].

The fact that the surrounding water is already warm and salty could affect any calculation or parameterization of vertical and lateral diffusivity, modifying the background stratification. Two cases could arise: 1) if the accumulation of heat and salt from previous MOW affects the overall water column in the Gulf of Cadiz, salinity and temperature gradients will be weaker. 2) If those accumulations only affect the MOW layer, salinity and temperature gradients in the vertical will be strong.

In terms of MOW core generation, the accumulation of water mass properties in the Gulf of Cadiz could determine the resulting cores and meddies further in the Atlantic. Salt and heat will be advective-diffusive driven by buoyancy forces at large scale and will clearly affect the local circulation in the Gulf of Cadiz.

7.2.1 Mechanistic View

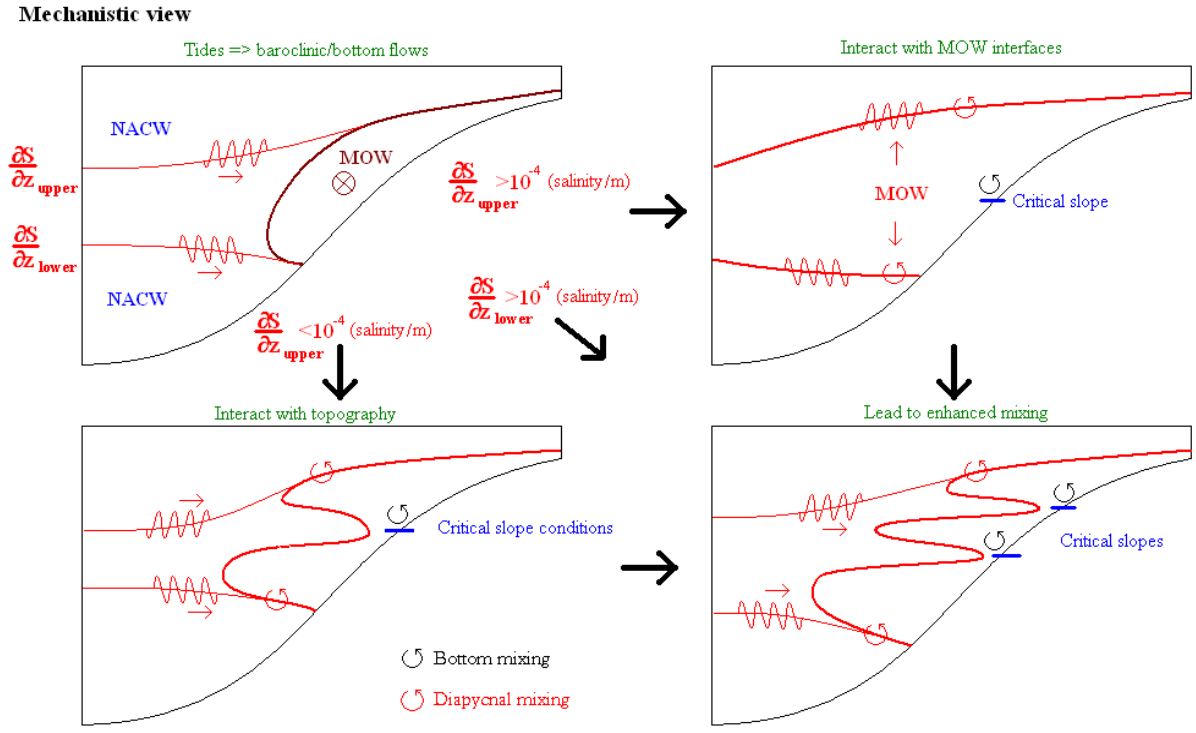

Figure 7.3: Schematic of mixing processes that occur in the Gulf of Cadiz. Turbulence from MOW flow and bottom friction on barotropic tidal currents mix the MOW. Internal waves propagate along the upper and lower interfaces, inducing turbulent mixing through shear instabilities and internal wave breaking.

The mechanistic view (Figure 7.3) is formed by considering the baroclinic and bottom flows generated by MOW flow and tides interacting with the topography to generate internal waves which eventually break leading to mixing. Mixing from bottom friction and internal wave breaking maintain well-mixed conditions inside the MOW [top left]. However diapycnal mixing over strong density gradients O(>10^{-4} salinity m^{-1}) is enhanced [top right]: over weak salinity gradients O(<10^{-4} salinity m^{-1}) mixing can be enhanced [relative to some basic open ocean value O(2x10^{-5} m^2s^{-1})] but its effects are related more with diffusivities around MOW structures [bottom left, based on XBTs cross sections with mixing estimates in Chapter 5]. Critical slope conditions for strong bottom currents occur at depths where MOW is separated and when the salinity gradient is weak O(<10^{-4} salinity m^{-1}) [bottom right]. Also most of the MOW splitting seems to happen over mid slope and not over deep regions (>1200m), however deeper MOW structures are thicker (>300m) than shallower-depth ones.

7.2.2 Salinity budget and box model

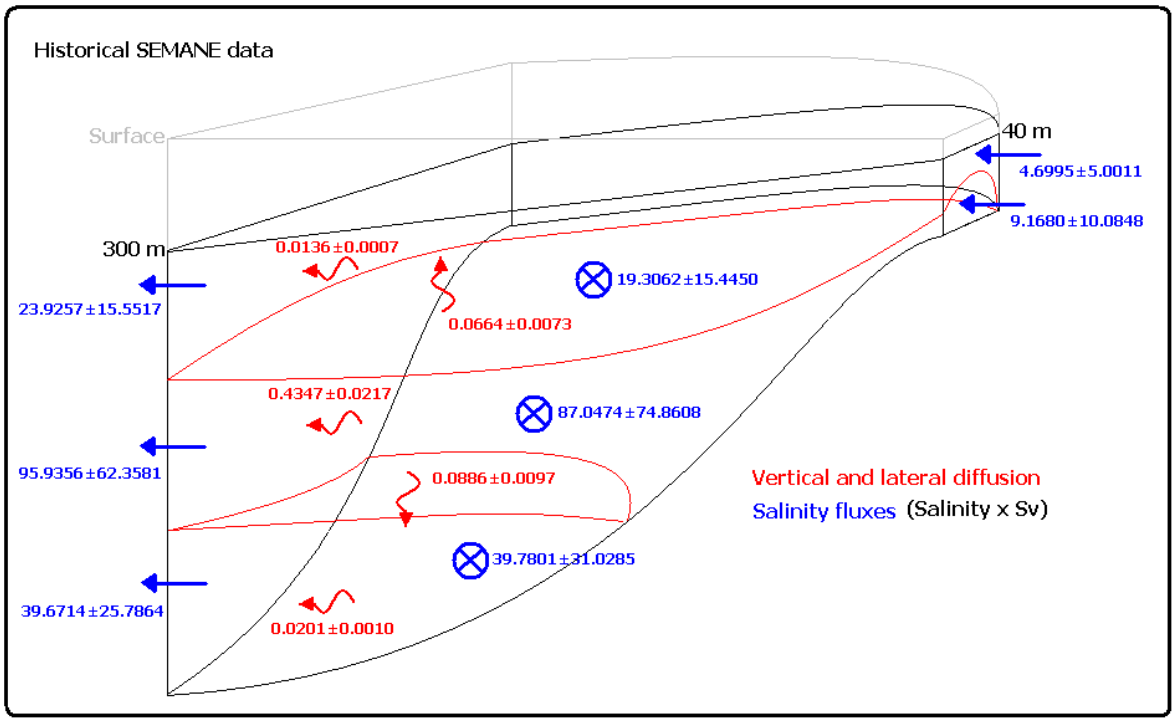

Figure 7.4: Sketch of salinity fluxes from box model results applied to SEMANE historical data (average of different years on face 3) with vertical and lateral mixing.

The box model analysis for mixing at the interfaces has shown that salinity diffuses vertically from the MOW to the NACW layers; however, most of the salinity diffusion from MOW is lateral (Figure 7.4) and remains in the MOW layer. Vertical mixing over the region

needs to be enhanced to maintain the conditions of salinity loss from the MOW layer, however most of the MOW salinity excess remains in the layer.

7.3 Conclusions

Following the previous remarks the study concludes the following:

- The internal wave field inside the MOW is energetic and MOW stratification allows the propagation of the internal waves, which are found in the GO mooring measurements along the mid slope in the Gulf of Cadiz.
- Internal waves occur at the MOW-NACW interfaces and inside the MOW where strong salinity gradients are present.
- Mixing estimates are found to be enhanced around the MOW structures and over different salinity gradients their effects can differ; both strong and weak gradients have enhanced mixing [relative to some basic open ocean value $O(2x10^{-5}\ m^2s^{-1})$] and over weak salinity gradients MOW can be displaced.
- Enhanced mixing is mostly found over the mid slope in the MOW, where conditions for critical slope are found.
- Strong bottom stress can provide mixing to contribute to well-mixed conditions inside the MOW over the mid slope.
- Most of the energy flux to generate internal waves comes from the MOW flow and internal tide.
- The internal wave field, mixing and local circulation are related by the effects on them of salinity gradients which determine internal wave breaking leading to mixing.
- Diapycnal mixing needs to be enhanced to maintain the loss of salinity from the MOW flow; however most of the loss is due to lateral diffusion.

7.4 Future work

The knowledge learned from the present research could provide valuable information for mixing studies, fine-structure parameterization methods were modified and this can have broad applications for research studies. For future work, the most important contributions from the present work are as follows:

- Inferring salinity to associate with temperature profiles. Extensive sources of data can be used to analyse fine-structure by using the salinity-inference approach, and also to apply to other data sets lacking salinity measurements.
- Finescale parameterizations by using strain analysis with temperature profiles and inferred salinity. A new alternative for mixing studies where vertical effects are important but with a lack of CTD measurements.
- Diapycnal mixing in the Gulf of Cadiz. This is found to be enhanced and now needs to be considered in future studies, especially those where MOW is modelled.
- Box modelling using salinity as a tracer. The approach of using salinity to delimit a box model was used due to the strong salinity highlighting of the MOW in the region. The approach of salinity gain and loss in the Gulf of Cadiz is effective. This approach can be applied to models where a water mass flows along/across the continental slope.
- The separation of MOW into cores and the generation mechanism of the MOW eddies have been studied in the Gulf of Cadiz and here discussed, but are not fully understood. More observational work is needed to address the controlling mechanisms.

Bibliography

Ambar, I., Serra, N., Nieves, F., Ferreira, T., Observations of the Mediterranean Undercurrent and eddies in the Gulf of Cadiz during 2001, Journal of Marine Systems vol. 71, 195-220, 2008.

Alford, M.H., Energy available for ocean mixing redistributed though long-range propagation of internal waves, Nature423, 159-163, 2003.

Alford, M.H., Internal swell generation: The spatial distribution of energy flux from the wind mixed layer near-inertial motions, Journal of Physical Oceanography, 31, 2359-2368, 2001.

Azevedo, A., da Silva, J.C.B., New, A.L., On the generation and propagation of internal solitary waves in the southernBay of Biscay, Deep-Sea Research Part I vol. 53, 927-941, 2006.

Baines, P.G., The generation of inertial tide by flat-bump topography. Deep-Sea Research, 20, 179-205, 1973.

Baringer, M.O., and Price J.F., A review of the physical oceanography of the Mediterranean outflow, Marine Geology, 155, 63-82, 1999.

Baringer, M.O., and Price, J.F., Mixing and spreading of the Mediterranean Outflow, Journal of Physical Oceanography vol.27, 1654-1677, 1997a.

Baringer, M.O., and Price, J.F., Momentum and Energy Balance of the Mediterranean Outflow, Journal of Physical Oceanography vol.27, 1678-1692, 1997b.

Bell, C., Vassie, J.M., Woodworth, P.L., POL/PSMSL Tidal Analysis Software Kit 2000 (Task-2000), Permanent Service for Mean Sea Level CCMS Proudman Oceanographic Laboratory, 2000.

Borenas, K., Wahlin, A., Ambar, I. Serra, N., The Mediterranean outflow splitting – a comparison between theoretical models and CANIGO data. Deep-Sea Research vol. 49 (19), 4195-4205, 2002.

Bower, A., Serra, N., Ambar, I., Structure of the Mediterranean Undercurrent and Mediterranean water spreading sround the south-wetern Iberian Peninsula, Journal of Geophysical Research vol. 107 (C10), 2002.

Bozec, A., Lozier, M.S., Chassignet E.P., and Halliwell G.R., On the variability of the Mediterranean Outflow Water in the Atlantic Ocean from 1948 to 2006. Journal of Geophysical Research – Oceans, submitted.

Bray, N.A., Foffonof N.P., Available potential energy for MODE eddies, Journal of Physical Oceanography Vol. 11, 30-47 p 1981.

Cacchione, D., Pratson L.F., Ogston, A.S., The shaping of Continental slopes by internal tides. Science 296, 724-727, 2002.

Cacchione, D., Wunsch C., Experimental study of internal waves over a slope. Journal of Fluid Mechanics 66, 223-239, 1974.

Cartwright, D.E., Tidal prediction and modern time scales. International Hydrographic Review, LXII (1), p 127-138, 1985.

Carton, X., Daniault., Alves, J., Cherubin, L., Ambar, I., Meddy dynamics and interaction with neighboring eddies southwest of Portugal: observations and modelling, Journal of Geophysical Research, 2010.

Cherubin, L., Carton., X., Paillet, J., Morel, Y., Serpette, A., Instability of the Mediterranean water undercurrents southwest of Portugal: effects of baroclinicity and of topography. Oceanologica Acta, 23, 551-573, 2000.

D'Asaro, E,. Eriksen, E.C., Levine, M., Niller, P., Paulson, C., van Meurs, P., Upper-ocean inertial currents forced by a strong storm. Part I: Data comparisons with linear theory, Journal of Physical Oceanography, 25, 2909-2936, 1995.

D'Asaro, E,. The energy flux from the wind to near-inertial motions in the mixed layer, Journal of Physical Oceanography, 15, 943-959, 1985.

da Silva, J.C.B., New, A.L., Azevedo, A., On the role of SAR for observing "Local Generation" of internal solitary waves off the Iberian Peninsula, Canadian Journal of Remote Sensing July, 2007.

Daniault, N., Maze, J.P., Arhan, M., Circulation and mixing of Mediterranean Water west of the Iberian Peninsula, Deep-Sea Research vol. 41, 1685-1713, 1994.

Dillon, T.M., Vertical overturns: a comparison of Thorpe and Osmidov length scales. Journal of Geophysical Research 87, 9601-9613, 1982.

Egbert, G.D., and Ray, R.D, Significant dissipation of tidal energy in the deep ocean inferred from satellite altimeter data, Nature, 405, 775-778, 2000.

Emery, W.J., and Thomson, R.E., Data analysis methods in physical oceanography, Elsevier Science B.V. second and revised edition 621pp, 2001.

Eriksen C.C., Implications of ocean bottom reflection for internal wave spectra and mixing, Journal of Physical Oceanography, 15, 1145-1156, 1985.

Eriksen C.C., Deep Currents and their interpretation as Equatorial Waves in the Western Pacific Ocean, Journal of Physical Oceanography Vol. 11, 48-70, 1981.

Dengler, M., and Quadfasel,D., Equatorial deep jest and abysal mixing in the Indian Ocean.,Journal of Physical Oceanography Vol.32, 1165-1180, 2002.

Galbraith, P.S., and Kelley, D.E., Identifying overturns in CTD profiles. Journal of Atmospheric and Ocean Technology 13, 688-702, 1996.

Garrett, C.J.R., and Kunze, E., Internal tide generation in the deep ocean, Ann. Rev. Fluid Mech., 39, 57-87, 2007.

Garrett, C.J.R., Marginal mixing theories, Atmosphere-Ocean, 29 313-339, 1991.

Garrett, C.J.R., and Munk, W.H., Space-time scales of internal waves: a progress report. Journal of Geophysical Research 80, 291-297, 1975.

Garrett, C.J.R., and Munk, W.H., Space-time scales of internal waves, Geophysical Fluid Dynamics, 2, 1972.

Gill, A., On the behaviour of internal waves in the wakes of the storms, Journal of Physical Oceanography, 14, 1129-1151, 1984.

Gill, A., Atmosphere - Ocean dynamics. International geophysics series vol. 30, Academic press 1982.

Gonella, J., A rotary-component method for analysing meteorological and oceanographic vector time series, Deep-Sea Research vol.19, 833-846, 1972.

Gregg, M.C., Sanford, T.B., Winkel, D.P., Reducing mixing from breaking internal waves in equatorial waters. Nature 422, 513-515, 2003.

Gregg, M.C., Scaling turbulent dissipation in the Thermocline, Journal of Geophysical Research, 94(C7), 9686-9698, 1989.

Grundlingh, M.L. On the observation of a solitary event in the Mediterranean Outflow west of Gibraltar. Meteor Forsh.-Ergebnisse, No 23, 15-46p 1981.

Henyey, F.S., Wright, J., Flatte, S.M., Energy and action flow through the internal wave field: an eikonal approach. Journal of Geophysical Research 91, 8487-8495, 1986.

Hernandez-Molina J., Llave.E., Somoza, L., Fernandez-Puga, M.C., Maestro, A., Leon, R., Medialdea, T., Barnolas A., Garcia, M., Diaz del Rio, V., Fernandez-Salas, L.M., Vazquez, J.T., Lobo, F., Alveirinho Dias, J.M., Rodero, J., Gardner, J., Looking for clues to paleoceanographic imprints: A diagnosis of the Gulf of Cadiz contourite depositional systems, Geology, 31, 19-22, 2003.

Hill, A.E., and Mitchelson-Jacob E.G., Observations of a poleward-flowing saline core on the continental slope west of Scotland, Deep-Sea Research 40, No. 7, 1521-1527, 1993.

Huthnance, J.M., Van Aken, H.M, White, M., Barton, E.D., Le Cann, B., Ferreira Coelho, E., Alvarez Fanjul, E., Miller, P., Vitorino, J., Ocean margin exchange – water flux estimates, 32, 107-137, 2002.

Huthnance, J.M., Circulation, exchange and water masses at the ocean margin: the role of physical processes at the shelf edge, Progress in Oceanography 35, 353-431, 1995.

Jayne, S.R., The impact of abyssal mixing parameterizations in an ocean general circulation model, Journal of Physical Oceanography, 39, 1756-1775, 2009.

Jayne, S.R., and St Laurent, Parameterizing tidal dissipation over rough topography, Geophys. Res. Lett., 28, 811-814, 2001.

Johnson, H.L., Garrett, M.C., Effects of noise on Thorpe Scales and run lengths. Journal of Physical Oceanography, 34, 2359-2372, 2004.

Käse, R.H., H.-H. Hinrichsen and T.B. Sanford, Inferring density from temperature via a density-ratio relation. J. Atmos. and Oceanic Tech., 13, 1202-1208, 1996.

Klymak, J.M., and Legg, S., A simple mixing scheme for models that resolve breaking internal waves, 2010, in review.

Kunze, E., Firing, E., Hummon, J.M., Chereskin, T.K., Thurnherr, A.M., Global abyssal mixing inferred from lowered ADCP shear and CTD strain profiles, Journal of Physical Oceanography, 36, 1553-1576, 2006.

Lanczos, C., Applied Analysis, Prentice - Hall, Englewood Cliffs, NJ. (Reprinted in 1988, Dover, New York), 1956.

Legg, S., and Klymak, J.M., Internal hydraulic jumps and overturning generated by tidal flow over a steep ridge, Journal of Physical Oceanography, 38, 1949-1964, 2008.

Legg, S., Internal tides generated on a corrugated continental slope. Part I: Cross-slope barotropic forcing, Journal of Physical Oceanography, 34, 156-173, 2004.

Ledwell, E.T., Montgomery, K.L., Polzin ,L.C., St. Laurent L.C., Schmitt R.W., Toole, J.M., Evidence for enhanced mixing over rough topography in the abyssal ocean, Nature vol. 403, 2000.

Levine, M.D., A modification of the Garret-Munk Internal Wave Spectrum, Journal of Physical Oceanography vol 32, 3166-3181, 2002.

Llewellyn Smith, S., and Young, W.R., Conversion of the barotropic tide, Journal of Physical Oceanography, 32, 1554-1566, 2002.

Lozier, M.S. and Sindlinger L., On the source of Mediterranean Overflow Water property changes, Journal of Physical Oceanography, 39, 1800-1817, 2009

Mackinnon, J.A., and Winters, K., Subtropical catastrophe: significant loss of low-mode tidal energy at 28.9 degress, Geophys. Res. Lett., 32, doi:10/1029/2005GL023, 376, 2005.

Mauritzen, C., Polzin K.L., McCartney, M.C., Millard, R.C., West-Mark D.E., Evidence in hydrography and density fine structure for enhanced vertical mixing over the Mid-Atlantic Ridge in the western Atlantic. Journal of Geophysical Research 107 (C103147), 2002.

McComas, C.H., and Muller, P., The dynamic balance of internal waves. Journal of Physical Oceanography 11, 970-986, 1981.

Mountfield D. Sea systems and operations from D318 GO experiment 17 April – 14 May 2007 report. National Marine Facilities, sensors and moorings group, June 2007.

Müller, P. and Melbourne, B., Diapycnal mixing and internal waves, Oceanography, Vol. 13 No.2, 98-103. 2000.

Munk, W.H., Abyssal recipes, Deep-Sea Research vol.13, 707-730, 1966.

Munk, W.H., Evolution of a physical oceanography scientific survey in honor of Henry Stommel, edited by Bruce A. Warren and Carl Wunsch , 1980.

Munk, W.H., Internal waves and small-scale processes. Evolution of physical Oceanography, Warren B.A. and Wunsch C. Eds., The MIT press, 264-290, 1981.

Nash, J.D., Alford, M.H., Kunze, E., Martini, K., Kelly, S., Hotspots of deep ocean mixing on the Oregon continental slope. Geophys. Res, Lett., Vol.34 L01605, doi:10.1029/2006GL028170, 2007.

Nash, J.D., Kunze, E., Toole, J.M., Schmitt, R.W., Internal tide reflection and turbulent mixing on the continental slope, Journal Physical Oceanography, 34, 1117-1134, 2004.

Naveira Garabato, A.C., Polzin K.L., King, B.A., Heywood, K.J.,Visbeck, M., Widespread intense turbulence mixing in the Southern Ocean. Sciense 303, 210-213, 2004a.

Naveira Garabato, A.C., Oliver K.I.C., Watson A.J., 2004b. Turbulent diapycnal mixing in the Nordic seas. Journal of Geophysical Research 109 (C12010), 2004b.

New, A.L., da Silva, J.C.B., Remote-sensing evidence for the local generation of internal soliton packets in the central Bay of Biscay, Deep-Sea Research Part I vol. 49, 915-934, 2002.

Osborn T.R., Estimates of the local rate of vertical diffusion from dissipation measurements. Journal of Physical Oceanography 10, 83-89, 1980.

Ozdimov, R.V., On the turbulent exchange in a stably stratified ocean. Izvestiya Academy of Science, USSR, Atmosphere and Ocean Physics 1, 861-871, 1965.

Phillips, O.M., The dynamics of the Upper Ocean, 2nd ed. Cambridge University Press, 336pp, 1977.

Pingree, R.D., The droguing of meddy pinball and seeding with alace floats, Journal of Marine Biology Assoc. UK vol. 75, 235-252, 1995.

Polzin, K.L., A heuristic description of internal waves dynamics, Journal of Physical Oceanography, 34, 214-230, 2004.

Polzin, K., Kunze, E., Hummon, J., Firing , E., The finescale response of Lowered ADCP velocity profiles, Journal of Atmospheric and Ocean Technology vol. 19, 205-224, 2002.

Polzin, K., Toole, J., Ledwell, J., Schmitt, R., Spatial variability of turbulent mixing in the abyssal ocean, Science, 276, 93-96, 1997.

Polzin, K.L., Oakey, N.S., Toole, J.M., Schmitt, R.W., Fine structure and microstructure characteristics acrossthe northwest Atlantic Subtropical Front, Journal of Geophysical Research, 101, 14, 111-14, 121, 1996.

Polzin, K.L., Tool, J.M., Schmitt, R.W., Finescale parameterizations of turbulent dissipation. Journal of Physical Oceanography 25, 306-328, 1995.

Pond, S., Pickard, G.L., 'Introductory Dynamical Oceanography'. 2nd edition, Elsevier 1983.

Potter, R.A. and Lozier M.S., On the warming and salinification of the Mediterranean Outflow Waters in the North Atlantic. Geophysical Research Letters, 31, L01202, doi:10.1029/2003GL018161, 2004.

Price, J.F., Mediterranean Outflow and mixing dynamics, Science, 259, 1277-1282, doi:10.1126/science259.5099.1277, 1993.

Prinsenberg S.J., Wilmot W.L., Rattray, M., Generation and dissipation of coastal internal tides, Deep-Sea Research, 21, 263-281, 1974.

Serra N., and Ambar, I., Eddy generation in the Mediterranean Undercurrent. Deep-Sea Research vol. 49(19), 4225-4243, 2002.

Serra N., Ambar, I., Käse, R.H., Observations and numerical modelling of the Mediterranenan outflow splitting and eddy generation, Deep-Sea Research II ,52, 383-408, 2005.

Smithson, M., Discovery 318 POL instruments deployments report. Observational group – Proudman Observational Laboratory, July 2007.

St Laurent, L.C., Thurnherr, A.M., Intense mixing of lower thermocline water on the crest of the Mid-Atlantic Ridge. Nature Vol. 448, doi:10.1038/nature06043, 2007.

St Laurent, L.C., and Nash J.D., On the fraction of internal tide energy dissipated near topography, in Near-Bourndary processes and their parameterization, proceedings of the 13th 'Aha Huliko' a Hawaiian winter workshop, edited by P. Müller and D. Henderson, 45-58, 2004.

St Laurent, L.C., and Garrett, C., The role of internal tides in mixing the deep ocean. Journal of Physical Oceanography, 32, 2882-2899, 2002.

St Laurent, L.C., Simmons, H.L., Jayne, S.R., Estimating tidally driven mixing in the deep ocean, Geophys. Res. Lett. 29, 2106, 2002

Thorpe, S.A., Turbulence and mixing in a Scottish Loch. Philosophical Transactions of the Royal Society of London A, 286, 125-181, 1977.

Timmermans, M.L., Garrett, M.C, Carmack, E., The thermohaline structure and evolution of the deep waters in the Canadian Basin, Artic Ocean. Deep-Sea Research I 50, 1305-1321, 2003.

Toole, J.M., Temporal characteristics of abyssal finescale motions above rough bathymetry, Journal of Physical Oceanography vol. 37, 409-427, 2007.

Toole, J.M., Polzin K.L., Schmitt R.W., Estimates of diapycnal mixing in the abyssal ocean, Science vol. 264, 1120-1123, 1994.

Wunsch, C., and Ferrari, R., Vertical mixing, energy and the general circulation of the oceans, Ann. Rev. Fluid Mech., 36, 281-314, 2004.